



The University of
Nottingham

UNITED KINGDOM • CHINA • MALAYSIA

Application of Shakedown Theory in the Structural Design of Bituminous Pavements

by

Shu Liu *BEng, MSc*

Thesis submitted to the University of Nottingham for
the degree of Doctor of Philosophy

July 2016

ABSTRACT

Excessive rutting, one of the major distress modes of bituminous pavements, is mainly caused by the accumulation of load-induced permanent deformation. However, current pavement design approaches against the excessive rutting are mainly developed using the theory of elasticity. Recently, a new pavement design approach based on the shakedown concept has attracted lots of attention because it can consider plastic properties of pavement materials. However, most of the existing shakedown solutions were developed for pavement foundations composed of granular materials and soils. Very limited work has been reported on bituminous pavements. Besides, current studies usually assume homogeneous, isotropic pavement materials obeying an associated plastic flow rule (termed as standard materials in the present study), which may not be realistic for pavement materials.

In the present research, a step-by-step numerical approach was used to obtain numerical shakedown limits of pavement structures under repeated moving loads. Both two-dimensional and three-dimensional problems were considered. It was found that, under the assumption of standard materials, the obtained numerical shakedown limits and residual stress fields agreed well with the available theoretical data.

A static (i.e. lower bound) shakedown approach for pavements with anisotropic, heterogeneous materials was developed based on Melan's lower bound theorem

and the critical residual stress method of Yu and Wang (2012). The influence of material plastic flow rules on pavement shakedown limits was also evaluated both numerically and theoretically. It was found that neglect of the inherent material properties (i.e. anisotropy, heterogeneity and non-associated plastic flow) could overestimate the real shakedown limits of bituminous pavements.

A series of tests were conducted to validate the shakedown concept for the responses of bituminous pavements under traffic loads. Two distinct phenomena corresponding to shakedown and non-shakedown were observed. Triaxial tests and uniaxial compression tests were also undertaken to obtain the stiffness and strength parameters, from which the theoretical shakedown limits can be calculated. Comparison between the experimental results and the theoretical solutions revealed that the current 3D shakedown approach for standard materials may overestimate capacities of bituminous pavements.

Finally, the lower bound shakedown approach was employed to design a typical bituminous pavement. A direct comparison was made between the shakedown-based design and the current UK design method. It demonstrated that the shakedown-based design for bituminous pavements can be conducted considering the maximum contact pressure and a relatively high air temperature.

ACKNOWLEDGEMENTS

First, I would like to express my sincere gratitude to my supervisors, Dr Dariusz Wanatowski, Professor Hai-Sui Yu and Dr. Juan Wang for their patience, motivation and continuous support of my Ph.D study over these years.

In addition, I need to thank Dr. Mostapha Boulbibane for the opportunity provided by him.

I also would like to thank Dr. Nick Thom, Dr. James Grenfell and all the technicians in the Nottingham Transportation Engineering Centre (NTEC) and L2 at the University of Nottingham who gave valuable advice in experimental design and specimen preparation.

I am also appreciative to express my gratitude to all my colleagues and friends for their sincere help and continuous encouragement.

Furthermore, I would like to acknowledge the financial support provided by the faculty of Engineering and the Graduate school at the University of Nottingham UK and Malaysia.

Finally, huge appreciation goes to my family and my boyfriend for their generous dedication and endless love.

CONTENTS

ABSTRACT	i
ACKNOWLEDGEMENTS.....	iii
CONTENTS	iv
LIST OF FIGURES	x
LIST OF TABLES.....	xix
NOTATION.....	xxii
CHAPTER 1 INTRODUCTION.....	1
1.1 Background.....	1
1.2 Aims and objectives	4
1.3 Thesis outline.....	4
CHAPTER 2 LITERATURE REVIEW	7
2.1 Introduction	7
2.2 Notion of shakedown in pavements	7
2.3 Shakedown theorems.....	8
2.3.1 Melan's static shakedown theorem.....	9

2.3.2	Koiter's kinematic shakedown theorem	9
2.4	Bituminous pavements	10
2.4.1	Typical structure of bituminous pavements.....	10
2.4.2	Failure modes of bituminous pavements	12
2.4.3	Current pavement design methods.....	15
2.5	Properties of pavement materials	18
2.5.1	Granular materials	18
2.5.2	Asphalt.....	20
2.5.3	Associated and non-associated plastic flow rule	24
2.5.4	Material anisotropy	25
2.5.5	Material heterogeneity	26
2.6	Previous studies of shakedown in pavement engineering	27
2.6.1	Experimental observation of shakedown behaviour.....	27
2.6.2	Shakedown analyses in pavement engineering.....	35
2.7	ABAQUS.....	40
CHAPTER 3 SHAKEDOWN ANALYSIS OF PAVEMENTS WITH STANDARD MATERIALS.....		43
3.1	Introduction	43
3.2	Two-dimensional pavement problems	44
3.2.1	Problem definition	44

3.2.2	Numerical approach.....	45
3.2.3	Review of the lower bound shakedown approach for a half-space with standard materials (Yu and Wang 2012; Wang and Yu 2013b).....	46
3.2.4	Model description	48
3.2.5	Model validation	49
3.2.6	Solutions and discussions	54
3.3	Three-dimensional pavement problems	70
3.3.1	Problem definition	70
3.3.2	Model description and verification	70
3.3.3	Solutions and discussions	72
3.4	Summary.....	77
CHAPTER 4 SHAKEDOWN ANALYSIS OF PAVEMENTS WITH MATERIALS FOLLOWING NON-ASSOCIATED PLASTIC FLOW		80
4.1	Introduction	80
4.2	Numerical shakedown analysis	81
4.2.1	General introduction	81
4.2.2	Solutions of single-layered pavements	82
4.2.3	Solutions of multi-layered pavements	89
4.3	Static shakedown analysis	95
4.3.1	Introduction.....	95

4.3.2	Static shakedown approach for pavements with materials following non-associated plastic flow	95
4.3.3	Solutions of single-layered pavements	97
4.3.4	Solutions of multi-layered pavements	101
4.4	Summary.....	104
CHAPTER 5 EFFECT OF MATERIAL CROSS-ANISOTROPY AND HETEROGENITY ON SHAKEDOWN SOLUTIONS OF PAVEMENTS.. 105		
5.1	Introduction	105
5.2	Effect of material cross-anisotropy	106
5.2.1	Problem definition	106
5.2.2	Review of the lower bound shakedown approach for a half-space with anisotropic materials (Wang and Yu 2014).....	111
5.2.3	2D FE model.....	112
5.2.4	3D FE model.....	113
5.2.5	2D solutions and discussions of single-layered problems	113
5.2.6	Solutions and discussions of two-layered pavements.....	117
5.3	Effect of material heterogeneity	131
5.3.1	Problem definition	131
5.3.2	Solutions and discussions of single-layered pavements	131
5.3.3	Solutions of two-layered pavements.....	134
5.4	Summary.....	138

CHAPTER 6 EXPERIMENTAL STUDY OF SHAKEDOWN CONCEPT FOR BITUMINOUS PAVEMENTS	140
6.1 Introduction	140
6.2 The Materials	141
6.2.1 Asphalt mixture	141
6.2.2 Granular material	142
6.3 Determination of Material Characterisatics.....	144
6.3.1 Compaction-related tests on crushed granite.....	144
6.3.2 Monotonic triaxial tests on crushed granite.....	147
6.3.3 Monotonic triaxial tests on asphalt	158
6.3.4 Unconfined uniaxial tests on asphalt	161
6.4 Wheel Tracking Test	168
6.4.1 Wheel tracking facility	168
6.4.2 Specimen preparation	169
6.4.3 Test procedures	172
6.4.4 Determination of contact area and contact pressure	173
6.4.5 Experimental results	174
6.4.6 Comparisons with theoretical solutions.....	175
6.4.7 Summary.....	178

CHAPTER 7 A COMPARISON BETWEEN THE SHAKEDOWN DESIGN APPROACH AND THE ANALYTICAL DESIGN APPROACH IN THE UK FOR FLEXIBLE PAVEMENTS.....	179
7.1 Introduction	179
7.2 A typical pavement problem	180
7.3 Thickness design	181
7.4 Influence of temperature.....	183
7.5 Summary.....	189
CHAPTER 8 CONCLUDING REMARKS	190
8.1 Conclusions	190
8.2 Suggestions for future research	192

LIST OF FIGURES

Figure 2-1 Typical shakedown behaviours of pavement materials under cyclic loading.....	8
Figure 2-2 Typical configuration of bituminous pavements (after Thom 2008)	12
Figure 2-3 Ideal force distribution through the bituminous pavement (Sharma et al. 2013)	12
Figure 2-4 Rutting characteristics.....	13
Figure 2-5 Measurement of the depth and width of the rut on pavement surface (Pedro and Serigos 2012).....	14
Figure 2-6 Fatigue cracking of pavements	14
Figure 2-7 Critical locations in bituminous pavements	18
Figure 2-8 Mohr circles and failure envelope.....	19
Figure 2-9 Idealised strain response of an asphalt mixture (Gibb 1996).....	21
Figure 2-10 Accumulation of permanent deformation of asphalt mixture under repeated load (Khanzada 2000)	22
Figure 2-11 Vertical permanent strain rate versus vertical permanent strain in log scale (Werkmeister et al. 2004).	29

Figure 2-12 Schematic of Large-scale model equipment used for prototype testing at the University of Wisconsin-Madison (Kootstra et al. 2010)	30
Figure 2-13 Measured residual stresses in soil after rolling passes (Radovsky and Murashina 1996)	31
Figure 2-14 Sydney pavement testing facility	32
Figure 2-15 A small wheel tracker at the University of Nottingham (Juspi 2007)	33
Figure 2-16 Diagram of the Nottingham Slab Test Facility (Juspi 2007)	34
Figure 2-17 Variation of the vertical permanent deformation of Crushed Granite Portaway Sand with number of passes for various wheel pressures (Juspi 2007).....	34
Figure 2-18 The Nottingham pavement test facility (Juspi 2007).....	35
Figure 2-19 Two-dimensional linear elements	42
Figure 2-20 Two-dimensional quadratic elements	42
Figure 2-21 A 3D reduced integrated quadratic solid element (C3D20R).....	42
Figure 3-1 Idealised pavement model and 2D Hertz load distribution.....	44
Figure 3-2 Model sketch and boundary conditions	46
Figure 3-3 FE model of plane strain half-space under moving surface load....	52
Figure 3-4 Residual stresses in Region A upon the removal of load when $\phi = 20^\circ$; $\psi = 20^\circ$; $p_0 = 7.56c$, single layer model	53
Figure 3-5 Residual stress fields after 20 load passes when $\phi = 20^\circ$; $\psi = 20^\circ$; $p_0 = 7.56c$, single layer model	53

Figure 3-6 Comparison between FE calculated residual stress field and critical residual stress fields when $\phi = 20^\circ; \psi = 20^\circ; p_0 = 7.56c$	54
Figure 3-7 Indication of yielding areas in Region A before and after loading passes	59
Figure 3-8 Development of plastic normal strain	60
Figure 3-9 Development of plastic shear strain	61
Figure 3-10 Development of horizontal residual stresses.....	62
Figure 3-11 Comparison between critical and numerical residual stress fields in a two-layered pavement	64
Figure 3-12 Shakedown limits versus stiffness ratio $h_1/a = 2$ and $\phi_1 = \psi_1 = 30^\circ$	65
Figure 3-13 Numerical shakedown limits in two-layered pavements with varying strength ratio	66
Figure 3-14 Layer thickness and materials design of a four-layered pavement	68
Figure 3-15 Mesh distribution in Region A for four-layered pavement model	68
Figure 3-16 Comparison between critical and numerical residual stress fields in a four-layered pavement	69
Figure 3-17 3D Hertz pressure distribution	70
Figure 3-18 3D model sketch	71
Figure 3-19 3D FE model for numerical shakedown analysis	74
Figure 3-20 Location of yielding areas in a 3D model	75
Figure 3-21 Distributions of the residual stresses after four load passes when $\phi = 0^\circ$	75
Figure 3-22 Residual stresses after four load passes when $\phi = 0^\circ$	76

Figure 3-23 Residual stress fields after four load passes when $p_0 = 4.5c$ and $\phi = 0^\circ$ when $y = 0$	77
Figure 3-24 Development of horizontal residual stress σ_{xx}^r under successive load passes when $\phi = 0^\circ$	78
Figure 3-25 Plastic strain fields at $y = 0$ after four load passes when $p_0 = 4.5c$ and $\phi = 0^\circ$	79
Figure 3-26 Residual distortions (deformation scale 600)	79
Figure 4-1 Indication of yielding areas in Region A subjected to a static load following 10 load passes ($p_0 = 10.6c$, $\phi = 30^\circ$)	84
Figure 4-2 Development of horizontal residual stress field	85
Figure 4-3 Influence of dilation angle on horizontal residual stress field when $\phi = 30^\circ$; $p_0 = 10.6c$	87
Figure 4-4 Influence of dilation angle on horizontal residual stress field when $\phi = 20^\circ$; $p_0 = 7.5c$	88
Figure 4-5 Comparison between FE calculated residual stress field and critical residual stress fields when $\phi = 30^\circ$; $\psi = 10^\circ$; $p_0 = 10.0c$	89
Figure 4-6 Development of plastic normal strains	90
Figure 4-7 Development of plastic shear strains	91
Figure 4-8 Comparison of numerical and theoretical shakedown limits for layered pavements when $\phi_1 = 30^\circ$; $\phi_2 = 0^\circ$; $c_1/c_2 = 1$	93
Figure 4-9 Influence of plastic flow rule on residual stress field in layered pavements when $\phi_1 = 30^\circ$; $\psi_1 = 0^\circ$; $c_1/c_2 = 1$, $E_1/E_2 = 3$, $p_0 = 6.7c_2$	94

Figure 4-10 Comparison between FE calculated residual stress field and critical residual stress fields for a layered pavement when $\phi_1 = 30^\circ$; $\psi_1 = 0^\circ$; $\phi_2 = \psi_2 = 0^\circ$; $c_1/c_2 = 1$, $E_1/E_2 = 3$, $p_0 = 5.5c_2$	94
Figure 4-11 Comparison of theoretical and numerical shakedown limits for single layered pavements	98
Figure 4-12 Dual-wheel Hertz pressure distribution	99
Figure 4-13 Comparison of theoretical and numerical shakedown limits with varying stiffness ratio when $\phi_1 = 30^\circ$; $\phi_2 = \psi_2 = 0^\circ$; $c_1/c_2 = 1$...	102
Figure 4-14 Comparison of theoretical and numerical shakedown limits in two-layered pavements with varying strength ratio when $\phi_1 = 30^\circ$; $\phi_2 = \psi_2 = 0^\circ$; $E_1/E_2 = 5$	102
Figure 4-15 Comparison of theoretical and numerical shakedown limits in two-layered pavements with varying first layer thickness when $\phi_1 = 30^\circ$; $\phi_2 = \psi_2 = 0^\circ$; $E_1/E_2 = 3$, $c_1/c_2 = 1$	103
Figure 5-1 2D problem definition and Hertz normal and shear stress distribution (Wang 2011)	106
Figure 5-2 3D Problem definition (Wang 2011)	109
Figure 5-3 3D FE model	113
Figure 5-4 Lower bound shakedown limits versus c_v/c_h for single-layered pavements with cross-anisotropic materials	115
Figure 5-5 Influence of frictional coefficient on shakedown limits of single-layered pavements with cross-anisotropic materials when $\phi = 0^\circ$	116

Figure 5-6 Design of a two-layered pavement system with cross-anisotropic materials	117
Figure 5-7 Influences of the factor of anisotropy in a 3D sand-clay system..	122
Figure 5-8 Influences of the factor of anisotropy in a 3D asphalt-clay system	123
Figure 5-9 Influence of the factor of anisotropy in a 2D sand-clay system ...	124
Figure 5-10 Influence of the factor of anisotropy in a 2D asphalt-clay system	125
Figure 5-11 Influences of plastic cross-anisotropy in a 3D sand-clay system	127
Figure 5-12 Influences of plastic cross-anisotropy in a 3D asphalt-clay system	128
Figure 5-13 Definition of heterogeneity problems	131
Figure 5-14 Influence of material heterogeneity on 2D shakedown limits of single-layered pavements	133
Figure 5-15 Influence of material heterogeneity on 3D shakedown limits of single-layered pavements when $\mu = 0$	134
Figure 5-16 Influence of material heterogeneity in 3D two-layered pavements when $E_1/E_2 = 1.39$, $c_1/c_2 = 20$, $\nu_1 = 0.4$, $\nu_2 = 0.3$, $\phi_1 = \phi_2 = 30^\circ$	136
Figure 5-17 Influence of material heterogeneity in 2D two-layered pavements when $E_1/E_2 = 1.39$, $c_1/c_2 = 20$, $\nu_1 = 0.4$, $\nu_2 = 0.3$, $\phi_1 = \phi_2 = 30^\circ$	137
Figure 6-1 Current gradation relation of the aggregate in asphalt (refer to BS EN 12679-5 2009)	142
Figure 6-2 Photo of crushed granite (Taken by author 2015)	143
Figure 6-3 Particle size distribution of crushed granite sample	143

Figure 6-4 Stress and strain characteristics of sands (Goetz 1989)	144
Figure 6-5 Performance of sand under contraction	145
Figure 6-6 General set-up of a soil specimen inside a triaxial cell (Rees 2013)	149
Figure 6-7 Illustration of triaxial test.....	149
Figure 6-8 GDS triaxial automated system	150
Figure 6-9 Preparation of the specimen.....	151
Figure 6-10 Stress and strain responses for dry specimens under different confining pressures	153
Figure 6-11 Confining pressures against stiffness moduli for dry specimens	154
Figure 6-12 Mohr circles and the failure line for dry specimens	155
Figure 6-13 Stress and strain responses for fully-saturated specimens under different magnitudes of confining pressure	157
Figure 6-14 Confining pressures against stiffness moduli for fully-saturated specimens	157
Figure 6-15 Mohr circles and the failure line of fully-saturated specimens...	158
Figure 6-16 Instron apparatus at the University of Nottingham.....	159
Figure 6-17 Photographs of the triaxial chamber for the Instron apparatus at the University of Nottingham (Taken by author 2015)	160
Figure 6-18 Mohr circles and the failure line of asphalt mixture	161
Figure 6-19 Asphalt specimen set-up for axial compression test	164
Figure 6-20 Determination of the stiffness modulus of asphalt during loading or unloading period when $t_s = 0.05s$	165

Figure 6-21 Effect of loading and unloading time on stiffness modulus of asphalt	166
Figure 6-22 Stress-strain response of asphalt under dynamic load with a frequency of 2Hz.....	167
Figure 6-23 Effect of loading frequency on stiffness modulus of asphalt.....	168
Figure 6-24 Nottingham wheel tracking facility	170
Figure 6-25 Measurement of the wheel load applied on the specimen surface (Taken by author 2015).....	171
Figure 6-26 Photographic of special designed LVDT (Taken by author 2015)	171
Figure 6-27 Bituminous pavement structure	172
Figure 6-28 Length of contact patch against contact load.....	173
Figure 6-29 Development of surface deformation under different magnitudes of moving surface load.....	176
Figure 6-30 Change of permanent vertical strain rate against surface deformation	178
Figure 7-1 A flexible pavement structure and material properties	180
Figure 7-2 Comparison of DBM thickness designs.....	185
Figure 7-3 Comparison of HRA thickness designs	185
Figure 7-4 Comparison between analytical design curves and shakedown-based design	186
Figure 7-5 Influence on temperature on asphalt stiffness.....	186
Figure 7-6 Pavement shakedown limits for various values of asphalt cohesion and stiffness (kPa).....	188

Figure 7-7 Influences of asphalt stiffness and layer thickness on the shakedown	
limit ($c_1 = 150\text{kPa}$)	188

LIST OF TABLES

Table 2-1 Summary of Mohr-Coulomb parameters of asphalt.....	23
Table 3-1 Material parameters for model validation	50
Table 3-2 Influence of model dimension.....	50
Table 3-3 Influence of mesh density in the 2D FE model.....	55
Table 3-4 Comparison of numerical shakedown limits for single-layered pavements	56
Table 3-5 Comparison of numerical shakedown limits for multi-layered pavements	57
Table 3-6 Parameters for the two layered soil material.....	58
Table 3-7 Influence of mesh density on 3D numerical shakedown limits	71
Table 4-1 Material parameters and shakedown limits for single-layered pavements	83
Table 4-2 Dimensionless lower bound shakedown limit parameters	100
Table 4-3 Shakedown limits for single layered-pavement under dual-wheel pressure	100
Table 5-1 Comparison of shakedown limits for cross-anisotropic Winnipeg Clay	114

Table 5-2 Summary of material properties and shakedown limits in consideration of elastic cross-anisotropy in a 3D sand-clay system	120
Table 5-3 Summary of material properties and shakedown limits in consideration of elastic cross-anisotropy in a 3D asphalt-clay system	121
Table 5-4 Summary of material properties and shakedown limits in consideration of plastic cross-anisotropy in a 2D sand-clay system	129
Table 5-5 Summary of material properties and shakedown limits in consideration of plastic cross-anisotropy in a 2D asphalt-clay system	130
Table 5-6 Effect of material heterogeneity on 2D shakedown limits of single- layered pavements.....	135
Table 5-7 3D shakedown limits for two-layered pavements with heterogeneous materials when $E_1/E_2 = 1.39$, $\nu_1 = 0.4$, $\nu_2 = 0.3$, $\phi_1 = \phi_2 = 30^\circ$.	138
Table 5-8 2D shakedown limit for two-layered pavements with heterogeneous materials when $E_1/E_2 = 1.39$, $c_1/c_2 = 20$, $\nu_1 = 0.4$, $\nu_2 = 0.3$, $\phi_1 = \phi_2$ $= 30^\circ$	138
Table 6-1 Compaction degree and density index (Djellali et al. 2012)	147
Table 6-2 Stiffness moduli and peak axial stresses during shear under different confining pressures for dry specimens.....	154
Table 6-3 Stiffness moduli and axial stresses for fully-saturated specimens under different magnitudes of confining pressure	158

Table 6-4 Maximum axial stress under different confining pressure for asphalt	160
Table 6-5 Summary of the stiffness moduli for asphalt specimens tested under static loads	165
Table 6-6 Measurements of the stiffness of asphalt specimens with different load frequencies	167
Table 6-7 transformational relation between the wheel load and the applied weights on the loading hanger	169
Table 6-8 Calculations of the contact length under different magnitudes of load	174
Table 6-9 Theoretical shakedown solutions obtained from the present study for comparison with the experimental results	177
Table 7-1 Shakedown limit of each layer for a DBM pavement	187
Table 7-2 Shakedown limit of each layer for a HRA pavement	187

NOTATION

a	half contact width for two-dimensional surface loads and radius of circular contact area for three-dimensional surface loads
AASHO	American Association of State Highway Officials
AASHTO	American Association of State Highway and Transportation Officials
c	cohesion
c_h	cohesion on horizontal plane
c_n	cohesion of n^{th} layer
c_v	cohesion on vertical plane
c_θ	cohesion on a plane inclines at an angle to the horizontal plane
c^*	modified cohesion considering non-associated plastic flow
$d\varepsilon_{ij}^P$	plastic strain rate
CBR	California Bearing Ratio
CSR	Cyclic Stress Ratio
DBM	dense bitumen macadam

HRA	hot rolled asphalt
E	Young's modulus (or stiffness modulus)
E_h	Young's modulus in horizontal direction
E_m	stiffness modulus of asphalt
E_n	Young's modulus (or stiffness modulus) of n^{th} layer
E_T	stiffness modulus of asphalt at a specified temperature
E_v	Young's modulus in vertical direction
E_0	Young's modulus at the top surface
E_{0n}	Young's modulus at the top surface of n^{th} layer
FE	finite element
f	yield condition
G	shear modulus
G_{vh}	shear modulus in VH plane
H	height
h_n	thickness of n^{th} layer
I_D	density index
k	dimensionless lower bound shakedown limit
k_n	dimensionless lower bound shakedown limit of the n^{th} layer

L	length of loading area
L'	length of unloading area
m_g	maximum dry mass
N	number of load application to failure
P	total normal load
p	normal contact pressure
p_0	maximum normal contact pressure
P_{sd}	actual shakedown limit
PIr	recovered penetration index
Q	total shear load
q	shear contact stress
q_0	maximum shear contact stress
S_T	structure surface area where external load are applied
SP_r	softening point
T_{0i}	external load
T	temperature
t	time
t^{-1}	frequency

\dot{u}_t	displacement velocity
V	volume
V_m	maximum volume reading
V_B	volume of binder in asphalt
V_v	volume of air voids in asphalt
VMA	voids in mixed aggregate
x, y, z	global coordinates
x', y', z'	local coordinates
ε_{xz}	shear strain
ε_t	tensile strain at the bottom of the asphalt layer
ε_z	normal strain on the top of the subgrade
ε_{ij}^p	plastic strain tensor
$\dot{\varepsilon}_{ij}^k$	kinematically admissible plastic strain rate cycle
$\hat{\varepsilon}_p^n$	accumulated permanent strain after n load cycles
λ	dimensionless load parameter
λ_{sd}	lower bound shakedown limit parameter
λ_{sd}^n	lower bound shakedown limit parameter for n^{th} layer

μ	surface frictional coefficient
σ_{ij}	total stress tensor
σ_{ij}^e	elastic stress tensor
σ_{ij}^r	residual stress tensor
σ_1	maximum principle stress/axial stress
σ_3	minimum principle stress/confining pressure
ρ_d	average density of specimen
$\rho_{d \max}$	maximum possible dry density
$\rho_{d \min}$	minimum possible dry density
ρ	heterogeneity factor
ρ_n	inhomogeneous ratio of the n^{th} layer
ϕ	friction angle
ϕ_n	friction angle of n^{th} layer
ϕ^*	modified friction angle considering non-associate plastic flow
ψ	dilation angle
ψ_n	dilation angle of n^{th} layer
ν	Poisson's ratio

ν_{hh}	Poisson's ratio regarding the effect of horizontal strain on complementary horizontal strain
ν_{vh}	Poisson's ratio regarding the effect of vertical strain on horizontal strain
ν_n	Poisson's ratio of n^{th} layer
$\delta\epsilon_{ij}$	strain increments
$\delta\sigma_{ij}$	stress increments
2D	two-dimensional
3D	three-dimensional

CHAPTER 1

INTRODUCTION

1.1 Background

Shakedown is concerned with the responses of an elastic-plastic structure subjected to cyclic or repeated loads. According to Yu (2006), when the applied cyclic load is above the yield limit but lower than a critical load limit, termed as ‘shakedown limit’, the structure may exhibit some initial plastic deformation; however, after a number of load cycles, the structure ceases to experience any further plastic strain and responds purely elastically to the subsequent load. This phenomenon is called ‘shakedown’. Otherwise, if the load is higher than the shakedown limit, the structure will continue to exhibit plastic strains (known as ratchetting) for however long the load cycles are applied.

Pavement structural design is a process intended to find the most economical combination of layer thicknesses and material types against design traffic. One major distress form considered in the design of bituminous pavements is excessive rutting, which is mainly caused by the accumulation of permanent deformation under repeated traffic loads. Shakedown analysis, based on elastic-

plastic theory, can obtain the maximum admissible load (shakedown limit) of a structure against unlimited increasing of permanent deformation under repeated loads; therefore, it is possible to be applied to the structural design of bituminous pavements (Brown et al. 2012).

Actually the shakedown phenomenon has been observed in field tests (Radovsky and Murashina 1996; Sharp and Booker 1984), triaxial tests (e.g. Brown et al. 2008; Larew and Leonard 1962; Lekarp and Dawson 1998; Werkmeister et al. 2001, 2005; Werkmeister 2003; Ravinda and Small 2008) and wheel tracking tests (Brown 2008; Juspi 2007; Kootstra et al. 2010). The range of shakedown limit can be roughly estimated by evaluating the developing tendency of permanent vertical deformation.

Besides, shakedown limits can be determined by using either direct theoretical shakedown analysis or numerical elastic-plastic analysis. In the past few decades, theoretical solutions for shakedown limits of pavements were developed mainly based on two fundamental shakedown theorems (i.e. Melan's static shakedown theorem and Koiter's kinematic shakedown theorem). On the one hand, different methods based on Melan's static shakedown theorem were developed for Tresca or Mohr-Coulomb materials subjected to two-dimensional (2D) and three-dimensional (3D) repeated moving surface loads (e.g. Johnson 1962; Sharp and Booker 1984; Yu and Hossain 1998; Shiau and Yu 2000; Yu 2005; Krabbenhøft et al. 2007; Zhao et al. 2008; Wang 2011; Yu and Wang 2012; Wang and Yu 2013a, 2013b, 2013c, 2014). On the other hand, shakedown analyses using Koiter's kinematic shakedown theorem have been carried out for 2D and 3D pavement problems (Collins and Cliffe 1987; Collins et al. 1993a, 1993b; Ponter

et al. 1985; Collins and Boulbibane 1998; Collins and Boulbibane 2000; Ponter and Engelhardt 2000; Boulbibane et al. 2005; Boulbibane and Ponter 2005a, 2005b; Ponter et al. 2006; Li and Yu 2006). It should be noted that the static and kinematic shakedown solutions provide lower and upper bounds to the true shakedown limit respectively. This is because the static shakedown theorem satisfies the internal equilibrium equations and the stress boundary conditions, while the kinematic shakedown theorem satisfies the compatibility condition for plastic strain rate and boundary conditions for velocity instead. Nevertheless, some identical solutions have been noticed. For instance, when a 2D Mohr-Coulomb half-space is subjected to a repeated moving pressure, the lower bound shakedown solutions (Yu 2005; Yu and Wang 2012) are identical to the upper bound shakedown solutions (Collins and Cliffe 1987). Therefore, upper and lower bound solutions provide exact shakedown limits for those problems. In terms of numerical elastic-plastic analysis, a numerical step-by-step approach was developed by investigating the development of residual stress field in cohesive-frictional half-space under repeated moving surface loads (e.g. Wang 2011; Wang and Yu 2013a).

However, most of the existing solutions are for pavement foundations composed of granular materials and soils. Very limited work has been reported on bituminous pavements. Besides, previous studies usually assume homogeneous, isotropic pavement materials obeying an associated plastic flow rule which is not true in reality.

1.2 Aims and objectives

The research objectives can be concluded as follows:

- To give a clear perspective of the shakedown concept and highlight the pivotal role of residual stress field in shakedown analysis.
- To obtain shakedown limits of multi-layered pavements and examine the effect of layer configuration on the shakedown limits.
- To reveal the influence of non-associated plastic flow rule of materials on the shakedown limits of pavements.
- To study the effect of anisotropy and heterogeneity of materials on the shakedown limits by further developing a lower bound shakedown approach.
- To validate the shakedown concept in layered bituminous pavements by wheel tracking tests.
- To directly compare the shakedown-based pavement design approach and the analytical design approach adopted in the UK Design Manual for Roads and Bridges HD26/06 (Highways Agency 2006).

1.3 Thesis outline

This thesis is divided into eight chapters. A brief outline is given below:

Chapter 1 provides necessary background information and key objectives of the present study.

Chapter 2 gives literature reviews including the notion of shakedown, key aspects of bituminous pavements (typical structure of bituminous pavements, principle distress modes, properties of pavement materials), fundamental shakedown theorems and previous research on pavement shakedown.

Chapter 3 presents a step-by-step approach using 2D and 3D finite element analysis in order to obtain numerical shakedown limits and investigate the development of residual stresses and plastic strains. The effect of layer configuration is also assessed.

Chapter 4 develops both numerical and theoretical shakedown solutions for pavements with materials following a non-associated plastic flow rule. These solutions are compared with numerical shakedown solutions.

Chapter 5 extends the theoretical shakedown approach to pavements with cross-anisotropic or heterogeneous materials.

Chapter 6 presents an experimental work showing responses of a bituminous pavement structure under moving loads. Triaxial and uniaxial compression tests were also conducted to obtain the stiffness and strength parameters which were used to calculate the theoretical shakedown limit, then compared with the experimental shakedown limit.

Chapter 7 applies the lower bound shakedown approach to design layer thicknesses of a typical bituminous pavement and then compares with the existing analytical design approach in the UK.

Chapter 8 summarises the major findings in the present study and gives suggestions on future research.

CHAPTER 2

LITERATURE REVIEW

2.1 Introduction

In this chapter, the basic shakedown concept and two fundamental shakedown theorems are first presented, followed by an introduction to bituminous pavements. Then experimental observations of the shakedown phenomenon and recent shakedown studies in the field of pavement engineering are summarised. Finally, the commercial finite element software ABAQUS is briefly introduced.

2.2 Notion of shakedown in pavements

Three distinct behaviours, known as purely elastic, shakedown, and incremental collapse respectively, can be recognised when a pavement structure is subjected to different levels of repeated load (Figure 2-1).

Purely elastic behaviour will occur only when the load level is sufficiently small so that no permanent deformation can be observed after unloading.

When the applied load is above the yield limit, but lower than a critical load; the structure may deform plastically in initial load cycles, but respond purely elastically to subsequent load cycles. This phenomenon is called ‘shakedown’, and the critical load is termed as the ‘shakedown limit’.

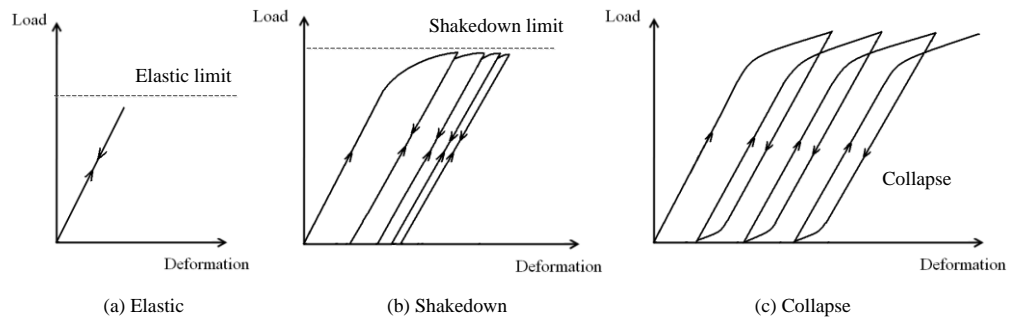


Figure 2-1 Typical shakedown behaviours of pavement materials under cyclic loading

In terms of the incremental collapse, also known as ratchetting, this is caused by the increase of plastic strain after each cycle of load when the applied load level is relatively high. Ratchetting can result in excessive rutting and thus should be avoided.

2.3 Shakedown theorems

In the past few decades, shakedown analyses were generally carried out based on two fundamental shakedown theorems, known as Koiter’s kinematic (upper bound) shakedown theorem and Melan’s static (lower bound) shakedown theorem respectively. The advantage of using the shakedown theorems is that detailed stress and strain history are not required during calculation.

2.3.1 Melan's static shakedown theorem

Melan's static shakedown theorem (Melan 1938) states that an elastic-perfectly plastic structure under cyclic or variable loads will shakedown if a time-independent residual stress field exists such that its superposition with a load-induced elastic stress field does not exceed the yield criterion anywhere in the structure.

$$f(\lambda \sigma_{ij}^e + \sigma_{ij}^r) \leq 0 \quad (2.1)$$

where σ_{ij}^e is the elastic stress field due to applied unit pressure p_{0u} , λ is a scale parameter, σ_{ij}^r is the self-equilibrated residual stress field and $f(\sigma_{ij}) = 0$ is the material yield criterion.

By searching all possible self-equilibrated residual stress fields under pressure λp_0 , the largest value of λ (defined as λ_{sd}) can be obtained to ensure the stresses in the structure satisfy Equation (2.1). Thus, λ_{sd} is termed as the 'shakedown limit parameter' and accordingly, $P_{sd} = \lambda_{sd} p_0$ is the actual shakedown limit.

2.3.2 Koiter's kinematic shakedown theorem

Koiter's kinematic shakedown theorem (Koiter 1960) states that shakedown cannot occur for an elastic-perfectly plastic structure subjected to cyclic or variable loads if the rate of plastic dissipation power is less than the work rate of external forces for any admissible plastic strain rate cycle. It can be expressed as

$$\int_0^t dt \iint_{S_T} p_{0i} \dot{u}_i^k dS_T > \int_0^t dt \iiint_V \sigma_{ij}^k \dot{\epsilon}_{ij}^k dV, \quad (2.2)$$

where

\dot{u}_i is displacement velocity,

p_{0i} is external load,

S_T is the structure surface area where external load is applied,

σ_{ij} is stress on the yield surface,

V is structure volume,

$\dot{\epsilon}_{ij}^k$ is any kinematically admissible plastic strain rate cycle.

Therefore, it can be known that the structure may shakedown if the inequality sign in Equation (2.2) is reversed:

$$\lambda \int_0^t dt \iint_{S_T} p_{0i} \dot{u}_i^k dS \leq \int_0^t dt \iiint_V \sigma_{ij}^k \dot{\epsilon}_{ij}^k dV, \quad (2.3)$$

which provides an upper bound to shakedown load multiplier λ_{sd} and therefore the upper shakedown limit is λp_0 .

2.4 Bituminous pavements

2.4.1 Typical structure of bituminous pavements

A typical structure for a bituminous pavement is given in Figure 2-2. The surface course, also known as wearing course, is comprised of asphalt (e.g. Hot Rolled Asphalt (HRA), Dense Bitumen Macadam (DBM), Stone Mastic Asphalt (SMA) and so on), so that it can withstand direct loading. Due to the high expenditure,

the typical thickness of this layer is relatively thin, varying from 20mm to 50mm. The base layer provides the pavement most of its strength and distributes the imposed wheel load to the pavement foundation; therefore it must be with sufficient quality and sufficient thickness. The thickness of this layer is typically 200mm or more. Generally, larger particle sizes tend to be used, whether the layer is of asphalt (e.g. HRA or DBM) or granular materials. The use of larger particles makes the surface of this layer uneven and therefore the direct application of the wearing course layer may reduce the quality of the finished road surface. Insertion of a binder course layer, made of asphalt with particle size larger than those in course layer, but smaller than those in the base layer, acts a transition between the wearing course layer and the base layer, of which the thickness ranges from 50mm to 80mm typically. The subbase layer is beneath the base layer and serves as the foundation for the overall pavement structure, transmitting traffic loads to the subgrade and providing drainage and frost protection. A typical thickness of 150mm is recommended. Capping layer, a subgrade-improvement layer, is always made of cheap and locally available materials and constructed for poor subgrade only. Generally, crushed gravels and rockfill may be the suitable options of capping materials. Overall, the goal of the bituminous pavement is to distribute the traffic loads down to the subgrade over a sufficiently large area as shown in Figure 2-3 to minimise the stress level on the top of the subgrade (Sharma et al. 2013).

Surface course -asphalt	20-50mm
Binder course -asphalt	50-80mm
Base – granular materials (often in more than one layer)	200mm
Sub-base – granular materials	200mm
Capping (lower sub-base) granular materials (used over poor subgrade; often in more than one layer)	
Subgrade (substrate) - soil	

Figure 2-2 Typical configuration of bituminous pavements (after Thom 2008)

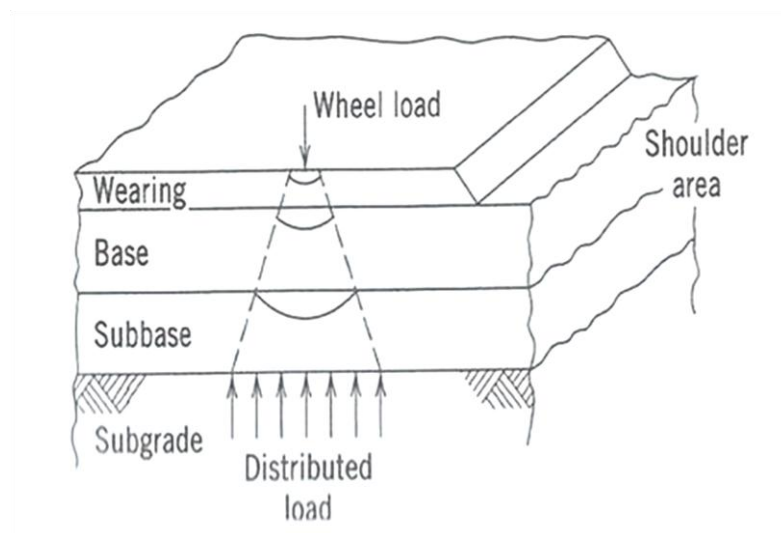


Figure 2-3 Ideal force distribution through the bituminous pavement (Sharma et al. 2013)

2.4.2 Failure modes of bituminous pavements

Two principal failure modes are of most concern in the design of bituminous pavements: excessive rutting and fatigue cracking.

Rutting is recognised as a permanent downward deformation on the pavement surface induced by repeated wheel loads, which may badly affect comfort, ride

quality, motorist safety and some other general performance characteristics of pavements (Haas et al. 1994). Excessive rutting can eventually occur if irrecoverable deformation of pavements keeps rising with increasing number of load passes (Witezak et al. 1997; Fwa et al. 2004). In the UK, the limiting rut depth is often taken to be 25 mm and pavements with rut depth varying from 15 to 20 mm should be considered for remedial work, such as the provision of an overlay or replacement of the surfacing (Croney and Croney 1991). In other countries, the limiting rut depth varies from 15mm to 25mm (De Pont et al. 1999; Jameson and Sharp 2004; Maji and Das 2005).

Measurements of ruts are usually conducted by placing a straight edge across the wheel path as shown in Figures 2-4 and 2-5. Generally speaking, the rut depth reflects the degree of rutting, and the rut width can be used as a sign of which layer has failed; normally a very narrow rut corresponds to a surface failure, while a wide one is indicative of a subgrade failure (Adlinge and Gupta 2013).

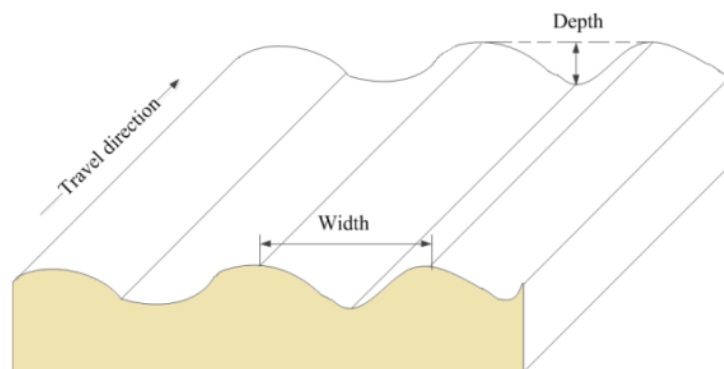


Figure 2-4 Rutting characteristics



Figure 2-5 Measurement of the depth and width of the rut on pavement surface
(Pedro and Serigos 2012)

Fatigue cracking occurs due to repeated wheel loading, and perhaps assisted by climatic factors such as low-temperature stress (Thom 2008). The generation of cracks may reduce the ride quality and provide pathways for water to flow into the pavement foundation. Fatigue cracks may start at the bottom of the bituminous layer which is usually considered to be the most critical place where the highest tension stress is expected to occur in the analytical pavement approach in the UK. Then the cracks may propagate to the pavement surface or connect with adjacent cracks (Figure 2-6) and eventually leading to failure of pavements. As the wheel loading continues, more cracks are formed.



Figure 2-6 Fatigue cracking of pavements

2.4.3 Current pavement design methods

Nowadays, pavement structural design can be conducted using an empirical approach or a mechanistic-empirical approach. Normally, the empirical approach is achieved by charts and equations developed from experimental and field work. In the aspect of the mechanistic-empirical approach, the concepts of mechanics are utilised together with the empirical equations to predict the performance of pavement structures. In this subsection, some representative methods are reviewed.

The CBR (California Bearing Ratio) method is one of the earliest empirical pavement design approaches developed by California Division of Highways in around 1930 as a result of surveys made during 1928 to 1929 (Yoder and Witczak 1975). CBR is expressed as a percentage of the penetration resistance to that of a standard value for crushed stone. The CBR value can be regarded as a sign of the quality of pavement materials. Some thickness design charts were developed based on the empirical relations established between the CBR value and the thickness. In 1944, this method was adopted by the U.S. Corps of Engineers for the design of airfield pavements (Porter 1950, Corps of Engineers 1945). Following that, the CBR approach was applied in highway design (e.g. Brown and Ahlvin 1961; Highways Agency 2009). Hveem and Carmany (1949) modified the traditional CBR design approach by further considering the cohesion and friction of granular materials.

The empirical design approach recommended by the American Association of State Highway Transportation Officials (AASHTO) was developed based on the

test results of the American Association of State Highway Officials (AASHO) road in-situ tests conducted in Ottawa, Illinois from 1956 to 1958. These in-situ tests involved observations of the performance of pavements at the end of selected time periods. Some physical features of the pavements, including longitudinal roughness, rutting depth in wheel tracks and extent of cracking and patching, were assessed (AASHTO 1972). The AASHO design equations were developed based upon a statistical analysis of the test data. Even though the AASHO tests provide a significant contribution to pavement design, their limitations are obvious. The design formula is applicable to specific pavement structures under a specific environment only. Again, it is difficult to predict the twenty-year performance of a pavement from a two-year test.

The mechanistic-empirical design is achieved by first obtaining elastic data (e.g. stress, strain, deflection) of a pavement structure under design loads, then inputting these data into selected empirical models to predict pavement responses (e.g. rutting, fatigue cracking, low-temperature cracking or smoothness) over the pavement design life. By using this approach, the designer should first select a 'trial pavement' with a specified layer configuration and material properties (from laboratory or field tests); then the critical stress and/or strain of the trial pavement due to the design traffic load are analysed to predict the critical life of the pavement based on the empirical models.

The rise of the mechanistic-empirical approach in pavement design can be traced back to 1962, in which year an international conference on the structural design of pavements attracted great attention and laid the foundation for the development of the mechanistic-empirical design approach. Until now, plenty of

work has been reported regarding the mechanistic-empirical approach (e.g. Jones 1962; Peutz 1968; Finn et al. 1977; Powell et al. 1984; Brown et al. 1985; Seeds 2000; Nunn 2004). For example, according to the Design Manual for Roads and Bridges HD26/06 (Highways Agency 2009), TRRL Report LR1132 provides guidance that should be considered in the preparation of mechanistic-empirical design for bituminous pavements, also known as analytical design approach in the UK. Two principal failure modes are considered in this approach: fatigue cracking and excessive rutting. While the excessive horizontal tensile strain at the bottom of the bound layer ϵ_r leads to fatigue cracking, the excessive vertical compressive strain at the top of subgrade ϵ_z is related to pavement rutting (Figure 2-7). Empirical equations are used to link the pavement life with the critical strains. Report LR1132 suggested the following empirical correlations for Dense Bitumen Macadam (DBM) and Hot Rolled Asphalt (HRA) at 20 °C:

Criterion against fatigue:

$$\log N = -9.38 - 4.16 \log \epsilon_r, \text{ for DBM (100pen)} \quad (2.4)$$

$$\log N = -9.78 - 4.32 \log \epsilon_r, \text{ for HRA (50pen)} \quad (2.5)$$

Criterion against rutting:

$$\log N = -7.21 - 3.95 \log \epsilon_z, \quad (2.6)$$

where N is the number of standard axles (in millions).

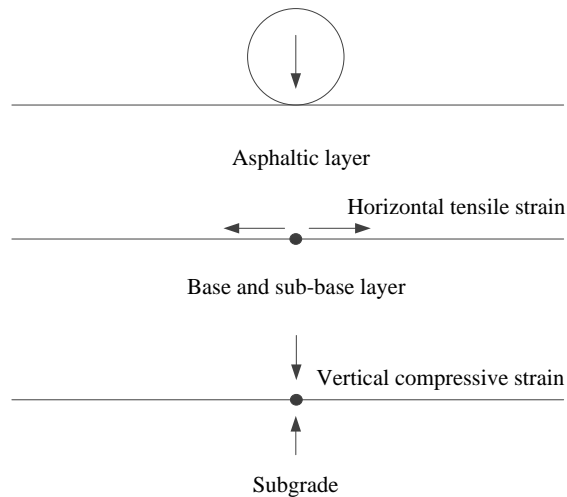


Figure 2-7 Critical locations in bituminous pavements

2.5 Properties of pavement materials

2.5.1 Granular materials

Properties of granular materials can be described in two aspects: stiffness and strength. Stiffness is the ratio of the applied stress to the induced strain. Stiffness of granular material is not like that of linear elastic materials; it may vary depending on the stress condition. In the aspect of strength, friction angle and cohesion are two main factors used to describe the shear strength of granular materials.

Both the stiffness and the strength of granular materials can be measured by the triaxial test. Since the granular material does not behave purely elastically under a pressure, a secant modulus is recommended to be used as the stiffness modulus of granular material. This is done by taking the slope of a secant between two points on the stress-strain curve (Poulos and Davis 1980; Briaud 2001; Ranjan

and Rao 2007). Lambe and Whitman (2008) stated that normally the stiffness modulus is the secant modulus from zero to a deviator stress $(\sigma_1 - \sigma_3)$ equal to one-third to one-half of the peak deviator stress. Besides, Briaud (2001) proposed that the stiffness modulus can be calculated by:

$$E = \frac{\sigma_1 - 2\nu\sigma_3}{\epsilon_{zz}}, \quad (2.7)$$

in which E is the stiffness modulus, σ_1 is the axial stress, σ_3 is the confining pressure, ϵ_{zz} is the vertical strain and ν is the Poisson's ratio. If a maximum Poisson's ratio (0.5) is selected, the secant modulus agrees with that in Lambe and Whitman (2008).

c and ϕ can be determined by seeking a well-matching failure line for couples of Mohr circles plotted by using the triaxial test data (Figure 2-8). By simplifying the Mohr-Coulomb envelope as a straight line, the Mohr-Coulomb yield criterion can be written in a linear form relating to c and ϕ . It is considered that any stress state exceeds this line is considered to be yield.

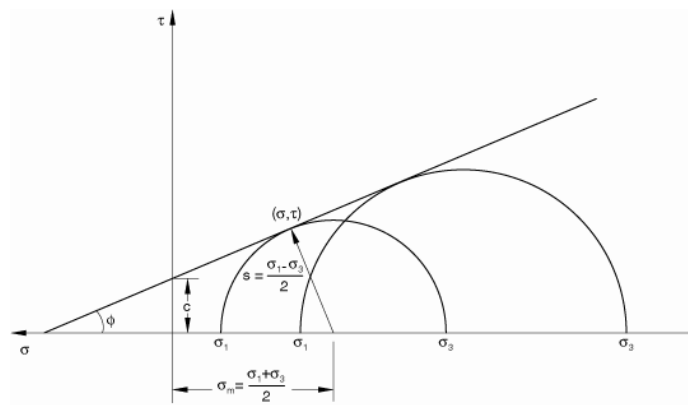


Figure 2-8 Mohr circles and failure envelope

However, stiffness modulus measured by means of triaxial test under repeated loads (Elliot and Thornton 1988; Puppala et al. 1996; CEN 2004; AASHTO 2007) is more realistic for pavement design. It was found that the stiffness modulus increase slightly after each load cycle, but to a first approximation it can be considered to be constant (Thom 2008). Therefore, in a relatively loose sense, stiffness modulus obtained from monostatic triaxial test is reasonable to be used in pavement design.

2.5.2 Asphalt

Asphalt is basically a granular material with an added binding ingredient (i.e. bitumen). The addition of bitumen affects the property of asphalt undeniably. Therefore, it is necessary to know the properties of bitumen and how do they affect the properties of asphalt. Bitumen behaves as an elastic solid under quick loading or at low temperatures, while acts as a viscous fluid at high temperature or under slow loading. Due to the addition of bitumen, deformation of asphalt should be concerned with the elasticity, visco-elasticity, viscosity and plasticity (Figure 2-9).

The uniaxial compression test has been employed in determining the stiffness modulus of asphalt. Deng (2000) indicated that asphalt performs purely elastically at a low temperature or under a very quick loading (last around 10^{-8} s to 10^{-6} s). However, most tests are conducted at a considerably slow errate due to the limitation of test equipment. Stiffness modulus actually involves the combined effects of elasticity and visco-elasticity. More details about the uniaxial compression test will be mentioned in Section 6.3.4.

Deformation of asphalt consists of two parts: recoverable deformation and permanent deformation (Figure 2-9). The recoverable part can be instantaneously recovered or gradually recovered. The gradually recovered deformation is due to visco-elasticity of asphalt.

Thom (2008) indicated that the magnitude of strain taking place within the aggregate skeleton is relatively small compared with those encountered in unbound materials as the binder takes much of the stress away from the particle contacts. With an increase of temperature, the stresses across particle contacts increase and result in an increased danger of inter-particle slips (from particle rotation and separation). Accumulation of the permanent deformation in asphalt is illustrated in Figure 2-10.

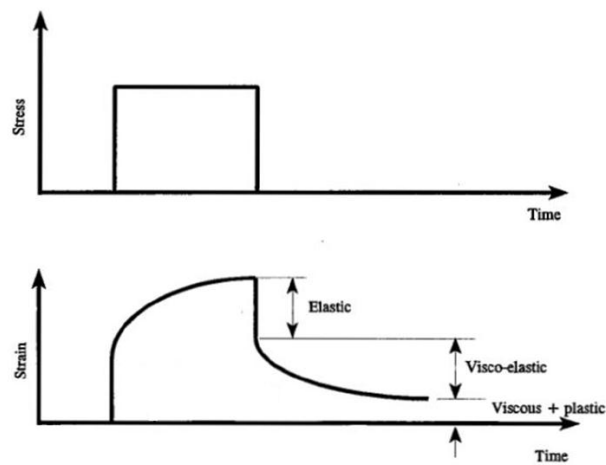


Figure 2-9 Idealised strain response of an asphalt mixture (Gibb 1996)

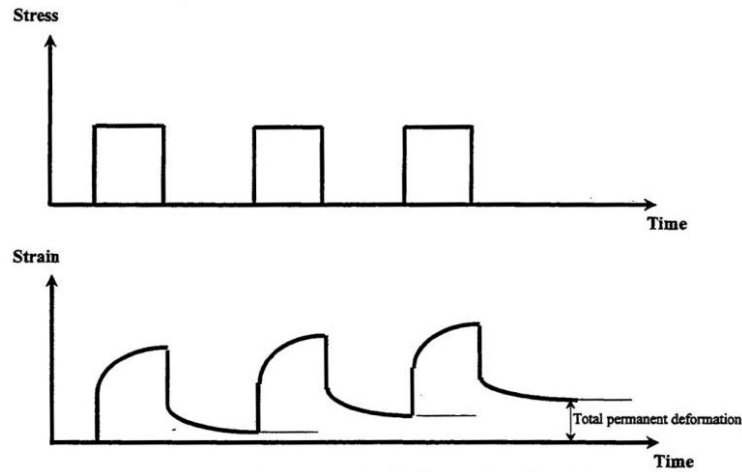


Figure 2-10 Accumulation of permanent deformation of asphalt mixture under repeated load (Khanzada 2000)

The Mohr-Coulomb yield criterion has also been suggested to describe the strength of asphalt (e.g. McLeod and Ricketts 1950; Endersby 1951; Goetz 1989, Smith 1951; McLeod 1952; Road Research Laboratory 1962; Fwa et al. 2001, 2004; Witzcak 2002; Airey and Prathapa 2013). Hence, the plastic properties of asphalt can be described by friction angle (ϕ) and cohesion (c) at a specified temperature. Table 2-1 summarises the strength data for standard hot mix asphalt (HMA). Some experimental results of the friction angle and cohesion of hot rolled asphalt at 30 °C from triaxial tests were given in the report of Road Research Laboratory (1962). The results demonstrate that the change of the aggregate type from sand to stone may increase the cohesion of asphalt to some extent, while decreasing the friction angle. Moreover, the decrease of binder content may increase the cohesion; however its effect on the friction angle is minor. Furthermore, Chen et al. (2009) reported that there exist two optimum binder contents which can provide the maximum cohesion and the maximum frictional angle respectively. They also noted that increasing binder viscosity

may lead to higher values of cohesion and friction angle. Fwa et al. (2004) carried out triaxial tests on three types of asphalt at different temperatures. The results show that higher temperature may reduce the cohesion but increase the friction angle. However, Chen et al. (2009) reported that the increasing temperature may lead to smaller cohesion as well as smaller friction angle. In summary, the effect of temperature on the friction angle is uncertain. Nevertheless, it can be found from both Fwa et al. (2004) and Chen et al. (2009) that the change of temperature does not influence the friction angle very much. This agrees with Goetz's (1989) statements which indicate that the friction angle is affected minimally by test temperature. In summary, the strength properties of the asphalt mixture depend on various factors. For example, aggregate grading obviously affects the friction angle, while the binder (bitumen) content and grade influence the material cohesion. This may explain the wide range of values in Table 2-1.

Table 2-1 Summary of Mohr-Coulomb parameters of asphalt

Reference	Type of asphalt mixture	T (°C)	c (kPa)	ϕ (°)
Airey and Prathapa (2013)	SMA	NA	NA	34.6
	DBM	NA	NA	41
Bindu and Beena (2013)	SMA	60	109	35
	SMA	25	420	43.3
Chen et al. (2009)		40	245	42.8
		60	204.4	38.6
Christensen et al. (2002)	NA	20	571-933	20.4-44.8
	NA	28	1768.8	15.1
Fwa et al. (2004)		40	616.4	33.4
		60	290.0	36
Zofka et al. (2014)	NA	25	760-1110	13.8-57.5

2.5.3 Associated and non-associated plastic flow rule

Determining the amount of plastic strain relates to a concept in plasticity known as plastic flow. It is well known that the failure surface defines the boundary of elastic deformation. When the stress state reaches the failure surface, further loading induces plastic flow. For an elastic-perfectly-plastic model, the stress state satisfying the yield condition will become unchanged, but will cause unlimited plastic strain. Clearly, there is no straightforward relationship between the yield stress and the plastic strain. Therefore, a strain rate is introduced which is defined as the rate at which the strain increases with respect to time.

Two rules were established to define the relation between the components of plastic stresses and the corresponding plastic strain rates, named as associated plastic flow rule and non-associated plastic flow rule.

An associated plastic flow rule has been confirmed by many experiments on frictionless materials (e.g. metals), of which the vector of plastic strain rate is normal to the yield surface. Therefore, the plastic strain rate ($d\varepsilon_{ij}^p$) can be described as a function relating to the yield criterion (f):

$$d\varepsilon_{ij}^p = d\lambda \frac{\partial f}{\partial \sigma_{ij}} \quad (2.8)$$

in which the scalar $d\lambda$ represents a proportional coefficient that can change with loading.

However, the associated plastic flow has not been successfully implemented for cohesive-frictional materials (e.g. soil and rocks), as its application in granular materials may overestimate the volume changes during plastic failure (Scott

2013). Non-associated plastic flow is therefore proposed by assuming that the plastic strain rate is not normal to the yield surface, but to a plastic potential surface of which the function is in a form very similar to the yield function as shown in Equation (2.9) (Nova and Wood 1978; Lade et al. 1987, 1988).

$$d\varepsilon_{ij}^p = d\lambda \frac{\partial Q}{\partial \sigma_{ij}} \quad (2.9)$$

For Mohr-Coulomb materials, the plastic potential surface is defined by replacing the friction angle (ϕ) with a dilation angle (ψ). In other words, if an associated plastic flow rule is applied, the dilation angle (ψ) is equal to the friction angle (ϕ); otherwise, the dilation angle is smaller than the friction angle and may be close to 0.

2.5.4 Material anisotropy

The materials which are assumed to have a single vertical axis of symmetry with the same properties in any horizontal direction, but different properties in the vertical direction are known as cross-anisotropic or transverse isotropic materials. According to Wang and Yu (2014), E_v/E_h and c_v/c_h can be regarded as the two main indexes to evaluate the elastic anisotropy and plastic anisotropy of materials, in which E is Young's modulus and c is cohesion, h and v relate to the horizontal plane and vertical plane respectively.

Elastic properties of anisotropic soils have been widely explored. For example, typical values of E_v/E_h for clays may range from 0.25 to 1.11 (e.g. Yu and Dakoulas 1993; Lings et al. 2000; Yimsir and Soga 2011). Experimental results for sands and gravel also show some degree of inherent anisotropy with E_v/E_h

from 1.06 to 2 (e.g. Hoque et al. 1996; Jiang et al. 1997; Kuwano and Jardine 2002). The property of anisotropy is also an inherent characteristic of asphalt concrete caused by the non-uniform distribution of aggregates. Experimental data (Wang et al. 2005) show that the anisotropy of asphalt concrete under field compaction might also be approximated as cross-anisotropy with $E_v/E_h \approx 3.33$.

Laboratory tests performed on soil specimens cut at different orientations have also demonstrated the directional dependence of soil shear strength (e.g. Lo 1965; Arthur and Menzies 1972; Guo 2008). It has been suggested that the variation of soil cohesion with direction due to inherent anisotropy is much more significant than the anisotropy of friction angles (Arthur and Menzies 1972). The value of c_v/c_h may relate to the value of E_v/E_h . For example, when the soil is heavily compressed, $E_v/E_h > 1$ and $c_v/c_h > 1$ (Jiang G L et al. 1997). Chen (2013) indicated that the value of c_v/c_h is within 0.75 to 2 for clay.

2.5.5 Material heterogeneity

As a layered structure, material properties of these layers are diverse. Even within a single type of material, the material property may also vary at different locations. Typically, the stiffness of soil increases with depth. Some relations have been suggested to describe the change of stiffness modulus with depth. For example, Gibson (1967) assumed that the stiffness modulus changes linearly with depth:

$$E_z = E_0 + kz, \quad (2.10)$$

in which E_z is the Young's modulus at depth 'z' and k is a constant). This kind of soil is known as Gibson-type soil. This Gibson soil has been widely applied to solve footing problems (Boswell and Scott 1975; Stark and Booker 1997). Apart from that, some researchers also assumed a power law relation: $E_z = E_0 z^k$ (where $0 \leq k < 1$ is a non-dimensional exponent) (Carrier and Christian 1973) or an exponential law relation: $E_z = E_0 e^{\alpha z}$ ($E_0 > 0$ and α can be either positive or negative) (Rowe and Booker 1981; Giannakopoulos and Suresh 1997).

2.6 Previous studies of shakedown in pavement engineering

2.6.1 Experimental observation of shakedown behaviour

At the beginning, the shakedown phenomenon was observed from triaxial tests. Larew and Leonard (1962) did some undrained repeated triaxial tests on partly-saturated (around 80% saturation degree) granular materials. Results were reported by plotting the permanent deformation against the number of load cycles. A shakedown limit of around 84% to 91% of the maximum compression stress (critical limit $\sigma_{1\max}$) was presented for silty clay. Undrained triaxial tests were also conducted by Sangrey et al. (1969) and Lashine (1971) on consolidated saturated clay and consolidated Keuper Marl respectively. The obtained shakedown limits ranged from 67% to 85% of $\sigma_{1\max}$.

Tang et al. (2015) conducted undrained tests on fully-saturated clay with selected confining pressure varies from 56 kPa to 85 kPa. The specimens were collected

from different depths of the test field. The shakedown or non-shakedown behaviours are classified by introducing a cyclic stress ratio (CSR) which is defined as the ratio between the cyclic shear stress $\tau = (\sigma_1 - \sigma_3)/2$ and the consolidated undrained shear strength τ_{cu} obtained through monotonic triaxial tests. The results were analysed by plotting the number of load cycles against pore pressure or axial strain. Results demonstrated that the shakedown limits of the clay collected at any depth were all at around CSR = 0.03 and the critical cyclic ratio was at around CSR = 0.44.

Lekarp and Dawson (1998) conducted repeated load triaxial tests on five different aggregates under drained condition to examine the relations between the development of permanent axial strain and the number of load applications. Results indicated that at low levels of shear stress (defined as $q_{\max}/(p_{\max} + p^*)$, in which q_{\max} is the maximum deviator stress, p_{\max} is the maximum mean normal stress and p^* is defined by the intersection of the static failure line and the p -axis in p/q space), the growth of permanent strain eventually levels off and reaches an equilibrium condition, whereas large load level may cause gradual failure. The equilibrium condition is similar to the shakedown phenomenon. They also indicated that the model proposed by Paute et al. (1996) can successfully predict the relations between the permanent axial strain and the number of load applications under shakedown condition.

Drained triaxial tests were also conducted on diverse granular materials by Werkmeister et al. (2001, 2004, 2005) and Werkmeister (2003) under different magnitudes of loads. Three behaviours were observed as shown in Figure 2-11,

in which three different phenomena were defined: plastic shakedown (labelled as A), plastic creep (labelled as B) and incremental collapse (labelled as C). Again, they defined the boundaries for those three ranges as follows, and they have been included in European Standard EN-13286-7.

$$A: (\hat{\varepsilon}_p^{5000} - \hat{\varepsilon}_p^{3000}) < 0.045 \times 10^{-3}, \quad (2.11)$$

$$B: 0.045 \times 10^{-3} < (\hat{\varepsilon}_p^{5000} - \hat{\varepsilon}_p^{3000}) < 0.4 \times 10^{-3}, \quad (2.12)$$

$$C: (\hat{\varepsilon}_p^{5000} - \hat{\varepsilon}_p^{3000}) > 0.4 \times 10^{-3}, \quad (2.13)$$

in which, $\hat{\varepsilon}_p^{3000}$ and $\hat{\varepsilon}_p^{5000}$ are accumulated permanent strains after 3000 and 5000 load cycles.

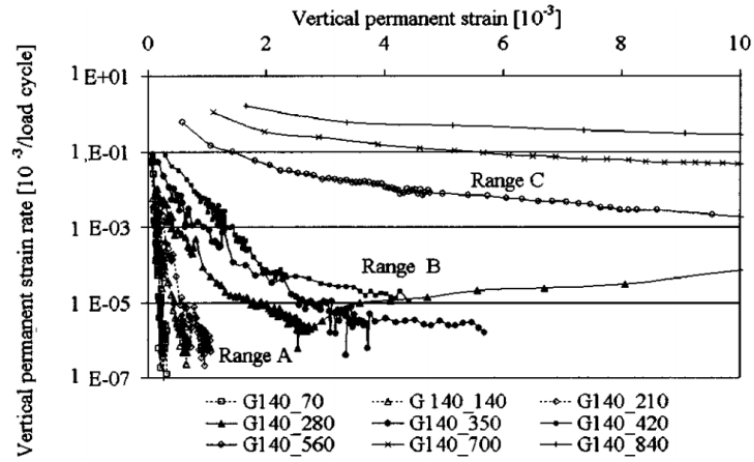


Figure 2-11 Vertical permanent strain rate versus vertical permanent strain in log scale (Werkmeister et al. 2004).

Apart from the repeated triaxial tests, Kootstra et al. (2010) conducted large-scale tests on two-layered specimens by applying repeated cyclic loads (700kPa) (Figure 2-12). The shakedown phenomenon was observed in the base layer of some particular cases.

Considering the moving nature of traffic loads, Radovsky and Murashina (1996) performed a full-scale test to validate the shakedown concept in soil under a rolling strip of 310kPa. Pressure cells were installed beneath the subgrade surface at different depths to measure the horizontal residual stresses. The subgrade soil contained 10% sand, 77% silt and 13% clay and the moisture content was 15%. Results indicated that the horizontal residual stresses increased with the number of repeated loads and became constant eventually after 12 rolling passes. The measured residual stresses are plotted in Figure 2-13 which indicates that the most critical residual stress was beneath the surface at a depth of around $z = 7\text{cm}$ ($z/a = 0.52$, where a is half of the tyre contact length). The most critical depth is consistent with Wang and Yu (2013a)'s numerical solutions.

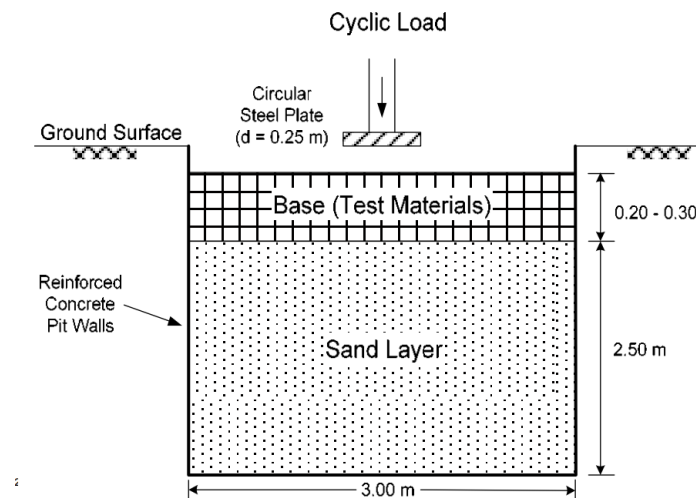
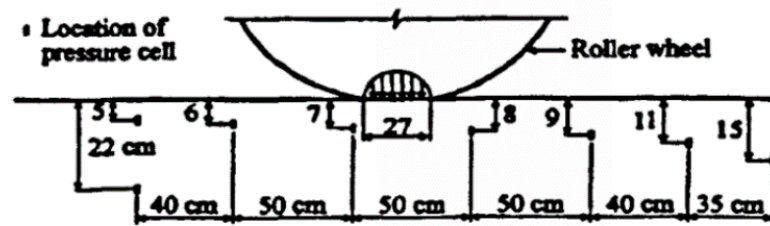
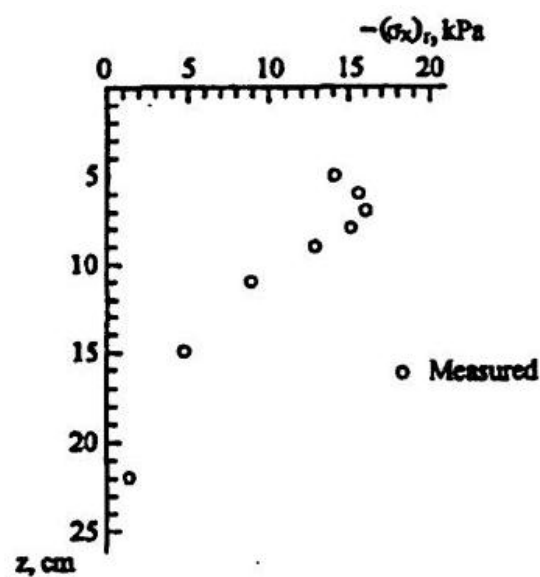


Figure 2-12 Schematic of Large-scale model equipment used for prototype testing at the University of Wisconsin-Madison (Kootstra et al. 2010)



(a) Location of pressure cell



(b) Measured residual stresses with depth

Figure 2-13 Measured residual stresses in soil after rolling passes (Radovsky and Murashina 1996)

Ravinda and Small (2008) utilised the Sydney pavement testing facility (Figure 2-14) to investigate the shakedown phenomenon of three kinds of unbound pavement configuration sealed with bitumen emulsion under moving wheel load. Results showed that wheel load lower than the shakedown limit for a large

number of load passes results in less deformation than that under a lower number of load cycles of a load larger than the shakedown limit.

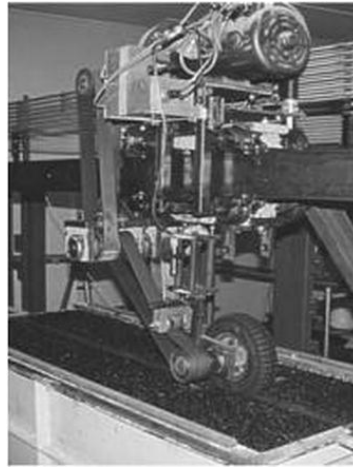


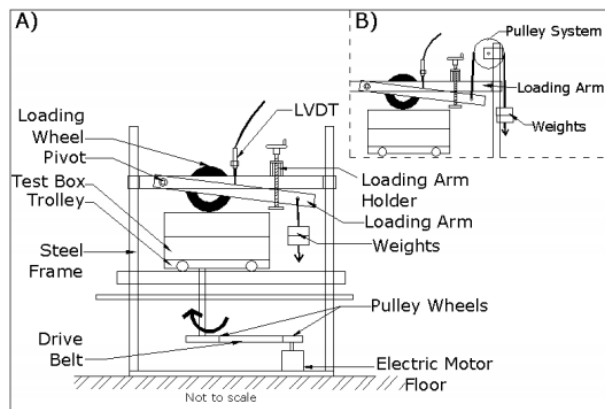
Figure 2-14 Sydney pavement testing facility

Brown et al. (2008) carried out tests on four types of soil and granular materials by using a small wheel tracking apparatus or a slab test facility at the University of Nottingham (Figure 2-15 and Figure 2-16). For soil like silty-clay, of which the particle size is relatively small, the small wheel tracking apparatus was employed. All the specimens were contained in a mould of 400mm in length, 280mm in width and 125mm in depth. Wheel loadings were applied by a 200mm diameter steel wheel with a solid rubber tyre of 50mm width. In terms of the slab test facility, it was utilized to test specimens like crushed rock of which the particle size is relatively large. Certainly, a larger specimen needed to be prepared which is 1m long \times 0.6m wide \times 0.18m deep. The results also revealed three types of phenomenon as shown in Figure 2-17, in which Type 1 is known as shakedown, Type 3 is definitely much in excess of shakedown and the intermediate case is defined as Type 2. The obtained experimental shakedown limit is compared with theoretical predictions and the results show that the

theoretically predicted shakedown limits were generally 20% lower than the experimental shakedown limit. The experiments were extended to two-layered or three-layered granular systems by Brown et al. (2012).



(a)



(b)

Figure 2-15 A small wheel tracker at the University of Nottingham (Juspi 2007)

Furthermore, Brown et al. (2012) also conducted some full scale wheel tracking tests by using the pavement test facility at the University of Nottingham. This facility is on a large scale in which the specimen is 2.5m long \times 1.25m wide \times

1.4m depth (Figure 2-18). The wheel was operated at a speed of 2.5km/h. Experimental results of multi-layered pavements were also compared with the theoretical solutions. Results showed that the theoretical prediction on two-layered pavement structures matched well with the test results; while for three-layered problems, the theoretically predicted shakedown limit was much smaller than the experimental measured amount.

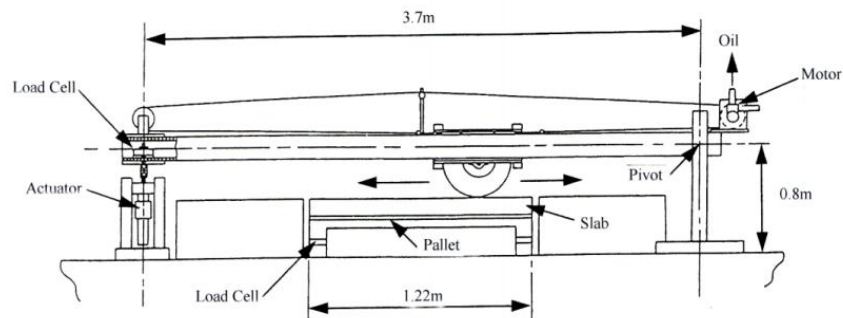


Figure 2-16 Diagram of the Nottingham Slab Test Facility (Juspi 2007)

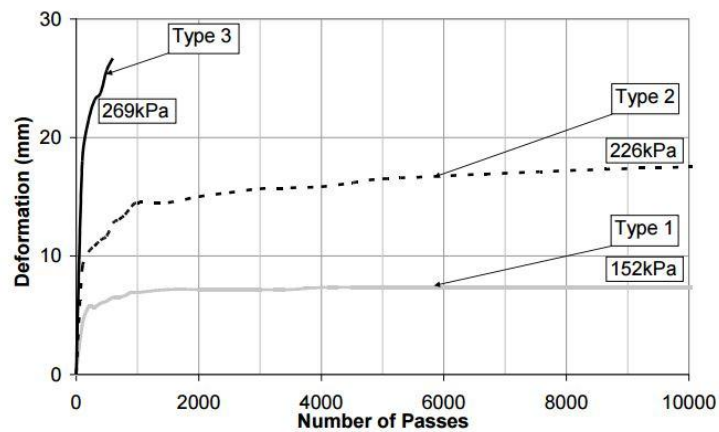


Figure 2-17 Variation of the vertical permanent deformation of Crushed Granite Portaway Sand with number of passes for various wheel pressures (Juspi 2007)



Figure 2-18 The Nottingham pavement test facility (Juspi 2007)

2.6.2 Shakedown analyses in pavement engineering

Sharp and Booker (1984) first stated that shakedown analysis can be used as a useful tool in pavement design. In their study, 2D single-layered and multi-layered pavement structures with elastic-perfectly-plastic Mohr-Coulomb materials subjected to trapezoidal pressure were studied by using a so-called method of conic. The effects of material properties, surface sliding and layer configuration on the shakedown limits were presented.

Raad et al. (1988, 1989a) applied a numerical approach developed based on lower bound shakedown theorem to a two-layered pavement system consisting of a surface layer (cement or asphalt concrete) overlying a clay subgrade. The numerical approach involved a discretization of the pavement structure using the finite element method as well as a mathematical optimization technique. This approach was then applied to shakedown analysis of granular materials considering the non-linear stress-dependent resilient properties (Najm 1987; Raad et al. 1989b). Further studies were conducted by Raad and Weichert (1995)

and Boulbibane et al. (2000) by considering different layer configurations and material anisotropy. A finite element formulation was presented by Yu and Hossain (1998) on the basis of Melan's static shakedown theorem using 2D triangular stress elements for the shakedown analysis of multi-layered structures. A linearizing Mohr-Coulomb yield surface lying within the classic Mohr-Coulomb yield surface was adopted so that this problem could be solved as a linear programming problem. Shiau and Yu (2000) and Shiau (2001) utilized a similar approach by simplifying Yu and Hossain (1998)'s assumptions in which the residual stresses were constrained to satisfy the yield condition and equilibrium. The calculated shakedown limits were relatively higher than those of Yu and Hossain (1998), while very close to Sharp and Brown (1984)'s solutions.

Radovsky and Murashina (1996) proposed an analytical approach based on the static shakedown theorem to solve 2D shakedown problems with materials following the Mohr-Coulomb yield criterion. By assuming a critical plane in a 3D pavement problem, a similar approach was also developed by Yu (2005). The solutions showed good agreements with the upper bound solutions of Ponter et al. (1985) and Collins and Cliffe (1987) because the self-equilibrium condition of the residual stress field was not strictly applied.

Krabbenhøft et al. (2007) obtained 2D shakedown solutions by considering that both total stresses and residual stresses satisfy the equilibrium and yield constraints. Evaluations of the influence of different constraints were also made. It was found that the relaxation of the yield constraint of residual stresses may lead to an overestimation of the shakedown limit when the surface friction was

high, i.e. the failure mode of the pavement structure is surface failure rather than sub-surface failure. Zhao et al. (2008) further discussed the effects of different types of load distributions on the 2D shakedown limits.

Nguyen (2008) proposed an interior-point method based on the lower bound shakedown theorem and finite element method. Both 2D and 3D problems with Mohr-Coulomb or Tresca materials were considered. Nguyen (2008) also mentioned that this approach can be extended to more complicated material properties including the viscosity of asphalt, non-associated flow rules, and the presence of pore-water.

Yu and Wang (2012) solved the 3D lower bound shakedown problem by introducing a critical self-equilibrated residual stress field and a simple optimisation procedure. The shakedown problem was reduced to a formulation in terms of a load parameter only. Further studies were carried out by considering more complicated cases, such as the multi-layered pavement problems, pavements with anisotropic materials and so on (Wang 2011; Wang and Yu 2013b, 2014; Yu et al. 2015). By using this method, the range of possible residual stress fields can be obtained.

Concerning shakedown analysis based on Koiter's kinematic shakedown theorem, Collins and Cliffe (1987) demonstrated that the method of conics (Sharp and Booker 1984) can be interpreted from a kinematic viewpoint. The approach was extended by Collins et al. (1993a) to 3D problems and the results agreed well with Ponter et al. (1985)'s upper bound solutions when Tresca materials and Hertz pressure were used in the analysis. It should be noticed that

this approach assumes a failure mode of subsurface slip. More failure modes, such as rut deformation and surface slip, were considered by Collins and Boulbibane (1998), Collins and Boulbibane (2000) and Boulbibane et al. (2005).

Li and Yu (2006) proposed a nonlinear programming approach based on the kinematic shakedown theorem and a finite element technology. The upper bound of the shakedown limit can be calculated by minimizing the plastic dissipation power function (a nonlinear function with respect to stress and plastic strain rate) to satisfy the geometric compatibility and velocity boundary conditions.

Another approach which has been widely used in solving shakedown problems based on the kinematic shakedown theorem is known as the linear matching method. This approach was first proposed by Ponter and Engelhardt (2000) for the shakedown analyses of metal materials, and then extended to geotechnical problems by Boulbibane and Ponter (2005b) using the Drucker-Prager yield criterion. According to Boulbibane and Ponter (2006), the basic idea of this method is that the stress and strain fields for non-linear material behaviour may be simulated by solving linear problems where the moduli are chosen to vary linearly with time and space.

Although some converged shakedown limits have been obtained using the static and kinematic shakedown theorems, most of them are calculated on the basis of an associated flow rule (i.e. the plastic strain rate is normal to the yield surface). However, it is well known that granular materials, such as soil and pavement materials, exhibit non-associated plastic behaviour (Lade et al. 1987; Lade and Pradel 1990). Until now, very limited results have been reported on this topic.

Boulbibane and Weichert (1997) proposed a theoretical framework for shakedown analysis of soils with a non-associated plastic flow. It was reported by Nguyen (2007) that this framework can be applied to shakedown analysis of footing problems. Using the linear matching method, Boulbibane and Ponter were able to give 3D upper bound shakedown solutions for non-dilatant Drucker-Prager materials, although they did not evaluate the influence of dilation angle. Numerical studies of Li (2010) extended the 2D upper-bound shakedown solutions by Li and Yu (2006) to materials with a non-associated plastic flow and suggested that the pavement upper-bound shakedown limit is reduced due to the use of non-associated flow rule.

For heterogenous materials, a 2D rolling contact problem was considered when subjecting metal to a one point contact load or a Hertz pressure by assuming that the hardness and yield strength varied with depth (Kapoor and Williams 1996). The effect of soil heterogeneity on shakedown limits was studied by Zhao (2008) in a 2D Mohr-Coulomb half-space by using an analytical shakedown approach based on lower bound shakedown theorem.

In terms of material anisotropy, Boulbibane et al. (1999) applied the static shakedown theorem to 2D layered pavement structures whose cohesion (of soil) changed with direction, i.e. strength anisotropy. Results showed that a higher ratio of c_h/c_v (in which c_h is the cohesion in the horizontal direction and c_v is the cohesion in the vertical direction) resulted in a higher shakedown limit. Wang and Yu (2014) extended the lower bound shakedown approach by Wang and Yu (2013b) to obtain 3D shakedown solutions of pavement structures with anisotropic materials.

An advantage of the shakedown approach based on two fundamental shakedown theorems (static and kinematic shakedown theorem) is that the details of the successive elastic-plastic stress fields are not required. However, it is still necessary to know the developments of residual stress and plastic strain under repeated moving surface load which may help to understand the lower bound shakedown theorem. Wang (2011) and Wang and Yu (2013a) developed a step-by-step approach using the finite element method to monitor the development of the residual stress field in a 2D half-space. It was found that the residual stresses cease to develop after a limited number of load passes and the fully developed residual stress field can be entirely bracketed by two critical residual stress fields (known as maximum smaller roots (MSR) and minimum larger root (MLR) respectively) obtained by the analytical approach proposed by Wang and Yu (2013b) when the applied load did not exceed the shakedown limit. Details of these two approaches will be introduced in Chapter 3 and Chapter 4.

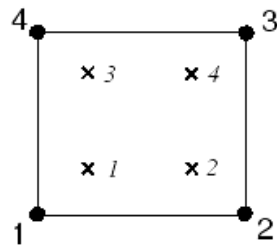
2.7 ABAQUS

ABAQUS is a commercial finite element (FE) software package developed by SIMULIA. It can be used to solve both linear and non-linear problems. Nonlinear problems are always solved incrementally, so that each increment can be considered as a linear problem. ABAQUS provides several plastic models including Drucker-Prager and Mohr-Coulomb models which can be used in geotechnical problems. In addition, user subroutines can customise ABAQUS solvers for particular applications; for example, a user subroutine UMAT allows user constitutive models to be added to the program, and DLOAD can be used

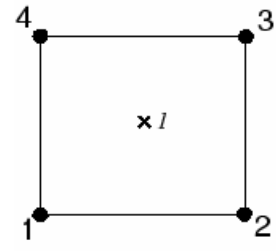
to define the variation of the distributed load magnitude as a function of position, time, element number, and load integration point numbers and so on. The user subroutines can be written in FORTRAN or C++ languages.

The element library in ABAQUS provides a wide range of element types, like solid (continuum) elements, structural elements and rigid elements and so on to different applications. In the present work, solid elements were used. The ABAQUS/Standard solid element library includes first-order (linear) interpolation elements and second-order (quadratic) interpolation elements in one, two, or three dimensions. Linear elements (Figure 2-19) are with nodes at corners only, while quadratic elements (Figure 2-20) have one more node in the middle of each edge. The expression “fully-integration” refers to the number of integration points required to integrate during the polynomial terms in an element’s stiffness matrix exactly when the element has a regular shape. As shown in Figure 2-19(a) and Figure 2-20(a), the fully-integrated linear element has the same number of integration points in each direction as the nodes in that direction, and the reduced-integrated has one less integration point in each direction compared with the nodes in that direction (Figure 2-19(b) and Figure 2-20(b)).

Choosing an element for a particular analysis can be simplified by considering solid element characteristics, i.e. linear (first order) or quadratic (second order); full integration or reduced integration. According to the ABAQUS manual, quadratic reduced-integration elements in ABAQUS/Standard generally yield more accurate results than the corresponding fully integrated elements. . avoid hour-glassing and interlocking problems.

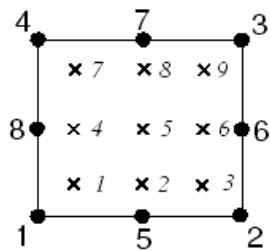


(a) Fully integration

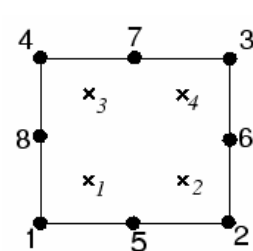


(b) reduced integration

Figure 2-19 Two-dimensional linear elements



(a) Fully integration



(b) reduced integration

Figure 2-20 Two-dimensional quadratic elements

In ABAQUS, each element comes with a unique name which identifies primary characteristics of the element. The elements will be applied to the 3D analyses in the present study are C3D20R which stands for Continuum, 3D, 20 noded reduced integrated elements (Figure 2-21); and the one used in 2D problems is CPE8R which means 8 noded, reduced-integrated, quadrilateral, plain strain elements (Figure 2-20b).

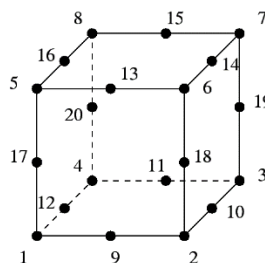


Figure 2-21 A 3D reduced integrated quadratic solid element (C3D20R)

CHAPTER 3

SHAKEDOWN ANALYSIS OF PAVEMENTS WITH STANDARD MATERIALS

3.1 Introduction

As noted above, the shakedown limit can be determined by either numerical elastic-plastic analysis or two fundamental shakedown theorems. However, there is very limited information on the development of plastic strains and residual stresses. And the comparison between the theoretical solutions and numerical simulation results is urgently needed, especially for layered pavements. In this chapter, a numerical elastic-plastic step-by-step approach is applied to capture shakedown limits of pavements in a visible way. Comparisons are given between the numerical shakedown solutions and the theoretical shakedown solutions calculated through the method proposed by Wang and Yu (2013b) (refer to subsection 3.2.3 for the details). Both two-dimensional (2D) and three-dimensional (3D) analyses were conducted. Through the numerical approach, the developments of plastic strains and residual stresses in pavement structures can be investigated in detail for different load levels. All materials considered in

this chapter are standard materials, defined as isotropic, homogeneous, elastic-perfectly plastic materials following an associated plastic flow rule.

3.2 Two-dimensional pavement problems

3.2.1 Problem definition

For 2D problems, it is considered that a layered pavement is repeatedly subjected to a rolling long cylinder, as shown in Figure 3-1. This can be simplified as an idealised plane strain pavement model with a moving contact load P . The normal load distribution p can be assumed as:

$$p = p_0 \sqrt{1 - (x/a)^2} \quad (-a \leq x \leq a) \quad (3.1)$$

where a is half of contact length; $p_0 (= 2P/\pi a)$ is the maximum vertical stress located at $x = z = 0$. This load distribution is also known as a 2D Hertz load distribution (Johnson 1985).

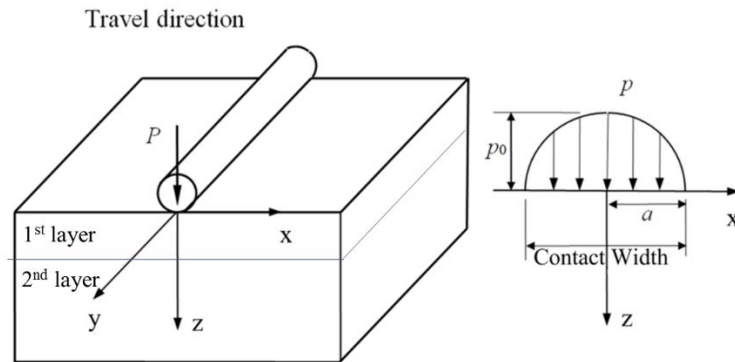


Figure 3-1 Idealised pavement model and 2D Hertz load distribution

3.2.2 Numerical approach

Finite element (FE) elastic-plastic analyses were carried out to obtain actual residual stresses developed in pavement structures under repeated moving traffic loads. By using the finite element software ABAQUS, shakedown limits of pavements can be obtained through a step-by-step approach:

- (1) As illustrated in Figure 3-2, for a given pavement structure, the load moves on the pavement surface repeatedly from point B to point C. At the end of each load pass, the applied load is removed thoroughly to investigate stresses remaining in the pavement (known as residual stresses).
- (2) After a few load passes, a static load with the same magnitude on the moving load is applied in the middle on the pavement surface. If no yielding point can be found in the pavement (i.e. the total stress state of each point in the pavement does not violate the yield criterion), a steady state (termed as ‘shakedown state’) is achieved. In contrast, any yielding point would indicate that the applied load is above the shakedown limit of the pavement and the whole structure is in a non-shakedown state.
- (3) Several numerical simulations with different load magnitudes are performed to determine the shakedown limit of the pavement.

It should be noted that this numerical approach requires great computation effort in order to obtain results with a reasonable accuracy. This problem has been solved to a great extent by using High Performance Computing (HPC) facilities at the University of Nottingham, UK. The HPC consists of a cluster of computer,

which work together to drastically reduce the time required to perform large scale calculations.

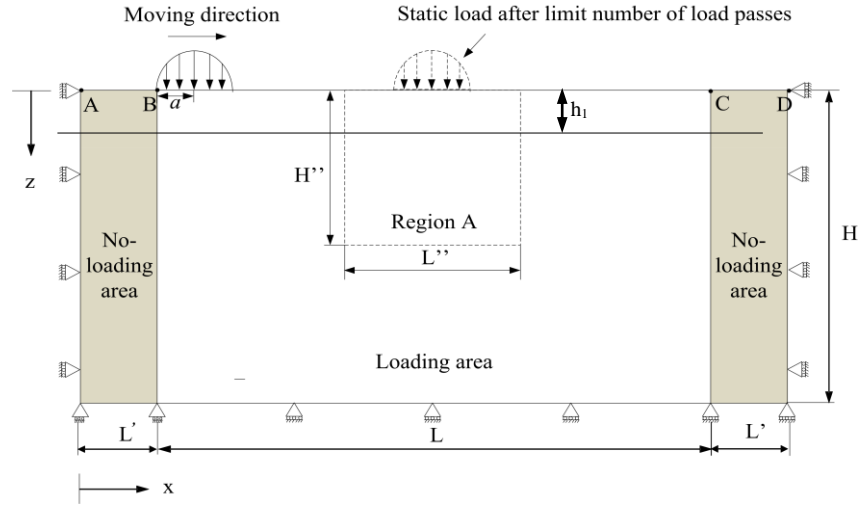


Figure 3-2 Model sketch and boundary conditions

3.2.3 Review of the lower bound shakedown approach for a half-space with standard materials (Yu and Wang 2012; Wang and Yu 2013b)

A lower bound shakedown approach, which aims to find the maximum admissible load of pavement structures against rutting, has been developed by Yu (2005), Wang (2011), Yu and Wang (2012), Wang and Yu (2013b). The pavement materials are assumed to be isotropic homogenous Mohr-Coulomb materials. For a 2D problem, it was found that only the horizontal residual stresses (along the wheel moving direction) can exist as a result of boundary conditions and equilibrium conditions. Those residual stresses together with the elastic stresses induced by a load p have to fulfil the Mohr-Coulomb yield criterion according to Melan's static shakedown theorem. This leads to the lower bound shakedown condition for pavements:

$$f = (\sigma_{xx}^r + M)^2 + N \leq 0, \quad (3.2)$$

in which,

$$M = \lambda \sigma_{xx}^e - \lambda \sigma_{zz}^e + 2 \tan \phi_n (c_n - \lambda \sigma_{zz}^e \tan \phi_n),$$

$$N = 4(1 + \tan^2 \phi_n)[(\lambda \sigma_{xx}^e)^2 - (c_n - \lambda \sigma_{zz}^e \tan \phi_n)^2].$$

In the Equation 3.2, λ is a dimensionless load factor; ϕ is material friction angle, c is material cohesion; σ^e is load-induced elastic stress; $f(\sigma_{ij}) = 0$ is the yield condition for the material. σ^r is residual stress; the subscript n ($n = 1, 2, 3 \dots$) means the n^{th} layer of the pavement structures; the subscripts x , y and z correspond to traffic moving direction, pavement transverse direction and vertical direction respectively. Tension positive notation is applied throughout this thesis.

According to the condition of self-equilibration, a critical residual stress field is conceived by calculating $\min(-M_i + \sqrt{-N_i})$ (referred to as ‘minimum larger root’) or $\max(-M_i - \sqrt{-N_i})$ (referred to as ‘maximum smaller root’) at each depth $z = j$ (i is the node number). The present shakedown problem can be written as a mathematical formulation:

$$\begin{aligned} & \max \lambda, \\ & \text{s.t.} \begin{cases} f(\sigma_{xx}^r(\lambda \sigma^e), \lambda \sigma^e) \leq 0, \\ \sigma_{xx}^r(\lambda \sigma^e) = \min_{z=j} (-M_i + \sqrt{-N_i}) \text{ or } \sigma_{xx}^r(\lambda \sigma^e) = \max_{z=j} (-M_i - \sqrt{-N_i}). \end{cases} \end{aligned} \quad (3.3)$$

For each layer of a pavement structure, one maximum admissible λ could be found, marked as λ_{sd}^n , and therefore λ_{sd}^n is the shakedown limit of the n^{th} layer.

The minimum value among all λ''_{sdP} is then recorded as the shakedown limit of the pavement structure which is usually normalised by material cohesion.

This method can be also applied to solve 3D problems by considering that one of the vertical planes along the wheel moving direction is the most critical plane (Yu 2005; Yu and Wang 2012).

3.2.4 Model description

A pavement model is established using ABAQUS. During every load pass, the load is gradually applied at the start point, then translated in the horizontal direction at a constant speed, and finally removed at the end point. The loading process is controlled by a user subroutine DLOAD. Figure 3-2 shows a sketch of a two-layered pavement used in this study. A restraint on horizontal movement is applied at two vertical boundaries, and a restraint on vertical movements is applied on the bottom boundary. In order to minimise the influence of two vertical boundaries on the numerical results, no load is applied near the vertical boundaries. Eight-noded, reduced-integrated, quadratic elements (CPE8R) are selected. Material properties of each layer are described by linear elastic parameters (Young's modulus E and Poisson's ratio ν) and Mohr-Coulomb criterion parameters (cohesion c , friction angle ϕ and dilation angle ψ). The materials are assumed to be homogenous, isotropic, and elastic-perfectly-plastic with associated plastic flow (i.e. $\phi = \psi$). In this thesis, subscript 'n' of E , ν , c , ϕ and ψ represents the n^{th} layer. For single-layered pavement problems, identical materials are assigned to both layers. In addition, tension is positive in the following results. It should be noted that the Mohr-Coulomb

model in ABAQUS uses a smooth plastic flow potential proposed by Menéndez and Willam (1995) which is very close to the classical Mohr-Coulomb model with associated flow potential, especially when mean pressure is high (refer to ABAQUS manual).

3.2.5 Model validation

3.2.5.1 Model dimensions

Material properties used for model validation are listed in Table 3-1. Table 3-2 shows different model dimensions used for sensitivity study and their corresponding results. Model A was used by Wang and Yu (2013a) for a homogeneous half-space, but required lots of computational effort. From Model B and Model C, it can be seen that some reduction in height and length of the model only slightly change the shakedown limit while saving a lot of computation time. Therefore, model dimensions of $40a$ (length of loading area L) \times $25a$ (depth H) were selected. As mentioned before, no-loading areas were applied near vertical boundaries. Their influences were checked by Model D in which the moving load gradually entered through the left boundary and finally exited through the right boundary, and Model E in which the length of the no-loading area L' was increased from $3a$ to $10a$. The results demonstrate the length of the no-loading area barely affects shakedown limits. However, for some two-layered cases, it was found that $L' = 3a$ was not enough to prevent yielding near the vertical boundaries. Therefore, Model E was finally chosen.

Table 3-1 Material parameters for model validation

Model type	Layer	E_1/E_2	c_1/c_2	ν	ϕ (°)	ψ (°)
Single-layered	n/a	n/a	n/a	0.3	20°	20°
Multi-layered	1 st	0.5	1	0.2	30°	30°
	2 nd			0.49	0°	0°

Table 3-2 Influence of model dimension

Model	L	H	L'	Theoretical shakedown limit	Numerical shakedown limit	Average elapsed time per load pass (s)
A	78a	30a	3a	7.56c	7.5c	13854
B	40a	30a	3a		7.4c	3607
C	40a	25a	3a		7.4c	3576
D	40a	25a	0		7.5c	3480
E	40a	25a	10a		7.5c	3475

3.2.5.2 Mesh density

Sensitivity studies on mesh density were also carried out to ensure that mesh distribution can obtain numerical results with a reasonable accuracy. High mesh density was applied in the first layer and near the interface between two layers due to high stress and strain gradient. As shown in Table 3-3, the shakedown limit barely changes when the number of elements exceeds 16000 for both single-layered and multi-layered models. Therefore, the mesh density in case 3 was selected. In this case, elements are distributed uniformly along $10a \leq x \leq 50a$ (the loading area) and small elements ($0.25a \times 0.1a$) are applied in the region near the surface ($z \leq 2a$). The mesh is also fine just beneath the interface, and it becomes coarser with increasing depth (Figure 3-3).

3.2.5.3 *Residual stress field*

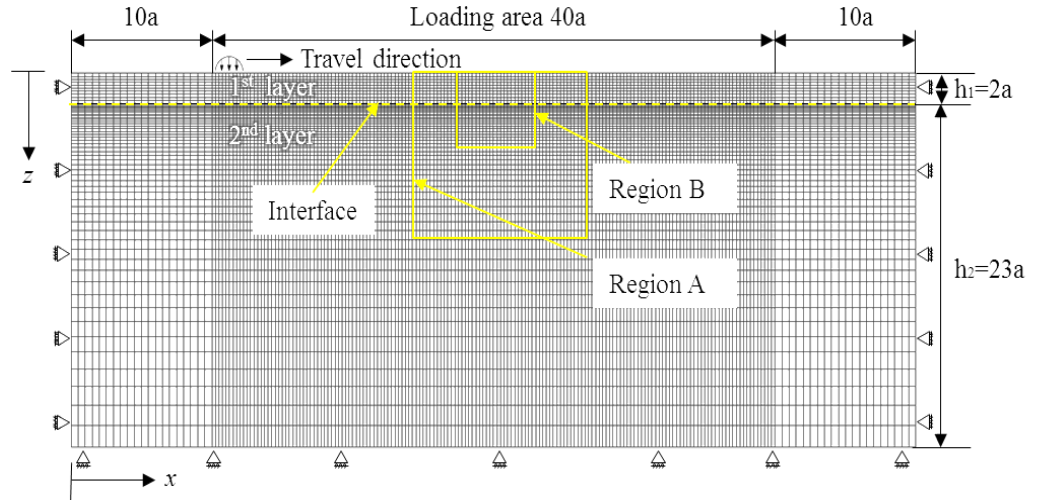
According to the lower bound shakedown theorem, residual stress field σ_{ij}^r (i and j denote the x axis, y axis or z axis) plays an important role in helping the structure reach shakedown status. Ideally, elements at the same depth experience the same loading history, therefore the resulting residual stress distribution should be independent of x (Yu and Wang 2012). Figure 3-4 demonstrates that the residual stresses in Region A after 10 load passes barely change in the horizontal direction (i.e. x axis). Slight fluctuations may exist due to boundary conditions in the numerical model.

Johnson (1962) noted that σ_{xz}^r and σ_{zz}^r should be zero for the 2D pavement problem due to the self-equilibrium condition. This agrees well with numerical results in Figure 3-5. In addition, Wang (2011) indicated that the actual horizontal residual stress field σ_{xx}^r should lie between two critical residual stress fields (i.e. MLR and MSR as mentioned in section 3.2.3) when the applied load is no larger than the shakedown limit. Therefore, the residual stress field obtained by the numerical shakedown analysis can be checked by comparing with critical residual stress fields obtained by Wang (2011). Figure 3-6 demonstrates a very good agreement.

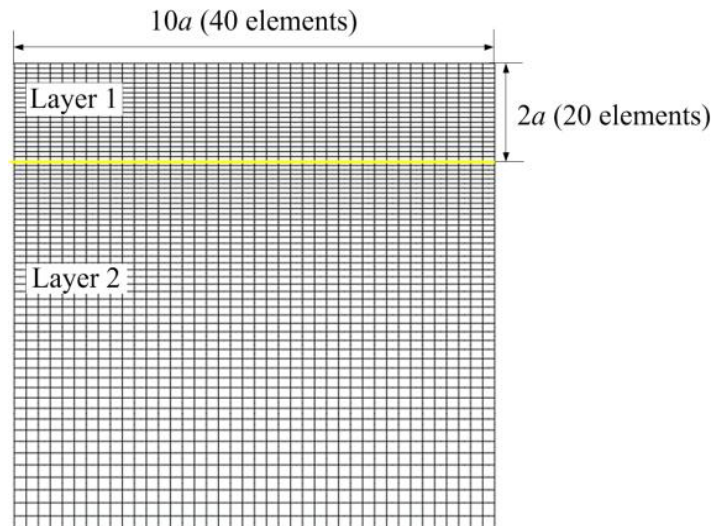
3.2.5.4 *Comparison of shakedown limits*

Shakedown limits obtained by the numerical step-by-step approach are also compared with shakedown solutions of other researchers. Those shakedown solutions were developed based on the classical shakedown theorems and they all assumed that an associated plastic flow rule is applied to pavement materials.

Table 3-4 and Table 3-5 demonstrate that the differences between shakedown limits of the current study and those in the references are within 4.8%. The comparison between Case 1 and Case 3 shows that the application of trapezoidal load distribution results in smaller shakedown limits compared with those obtained under a Hertz load distribution.



(a) 2D two-layered pavement model



(b) Mesh distribution in region A

Figure 3-3 FE model of plane strain half-space under moving surface load

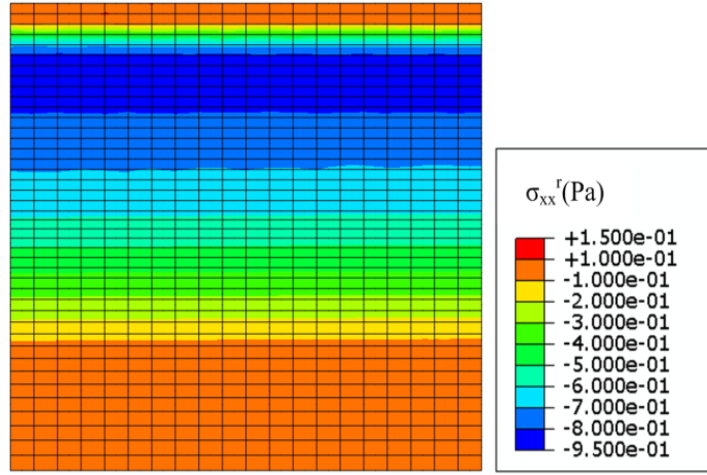


Figure 3-4 Residual stresses in Region A upon the removal of load when $\phi = 20^\circ$, $\psi = 20^\circ$, $p_0 = 7.56c$, single layer model

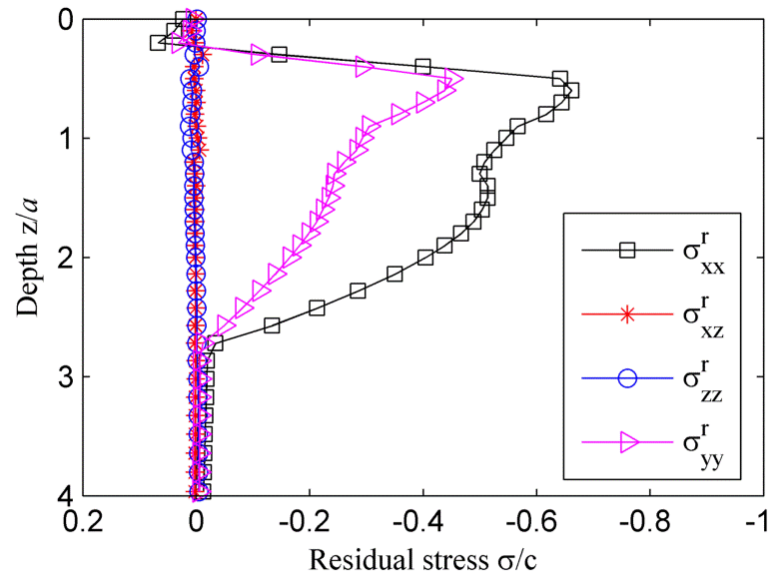


Figure 3-5 Residual stress fields after 20 load passes when $\phi = 20^\circ$, $\psi = 20^\circ$, $p_0 = 7.56c$, single layer model

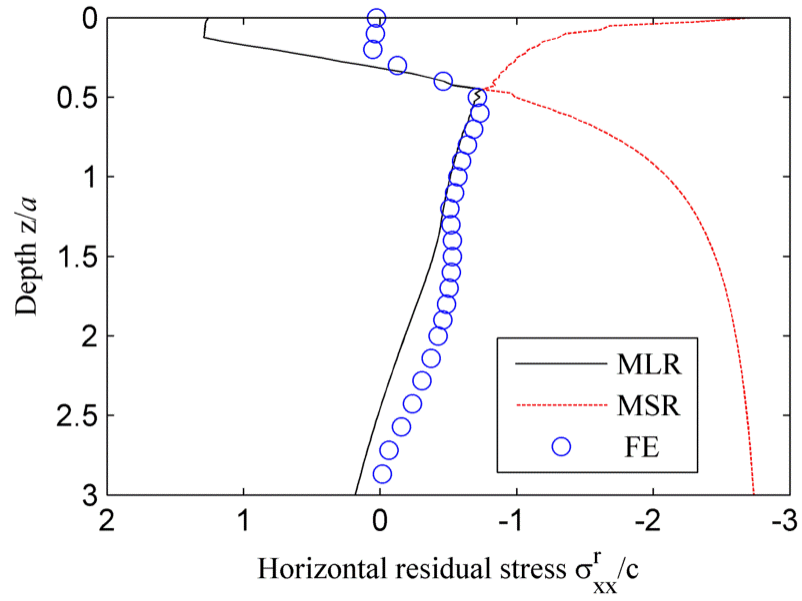


Figure 3-6 Comparison between FE calculated residual stress field and critical residual stress fields when $\phi = 20^\circ$; $\psi = 20^\circ$; $p_0 = 7.56c$

3.2.6 Solutions and discussions

3.2.6.1 Shakedown and non-shakedown

A two-layered pavement example is given in Table 3-6 of which the theoretical shakedown limit is $18.9c_2$. The theoretical shakedown limit was calculated by using the lower bound shakedown approach proposed by Wang and Yu (2013b) which will be further introduced in Chapter 4. Figure 3-7 gives the yielding areas in Region A before and after the loading passes when $p_0 = 18.7c_2$ and $p_0 = 19.3c_2$. Clearly, when $p_0 = 18.7c_2$, large and non-continuous yielding areas were generated under the static load before the application of any moving load (Figure 3-7a) but no yielding area can be found after a limited number of loading passes (Figure 3-7c).

Table 3-3 Influence of mesh density in the 2D FE model

	Model	Number of Elements	Theoretical shakedown limit	Numerical shakedown limit	Average elapsed time per load pass (s)
Single-layered	1	1500	7.56c	7.2c	125
	2	2500		7.2c	320
	3	16000		7.5c	3475
	4	18000		7.4c	3603
	5	21600		7.4c	4714
Two-layered	2	2500	8.48c ₂	8.5c ₂	344
	3	16000		8.5c ₂	4279
	6	20000		8.5c ₂	4561

Table 3-4 Comparison of numerical shakedown limits for single-layered pavements

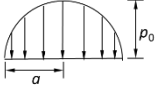
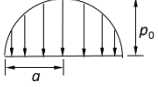
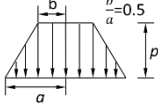
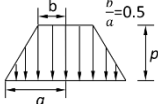
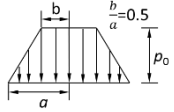
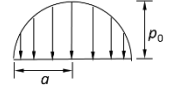
Case	Load distribution	ϕ (°)	ψ (°)	ν	Shakedown limit		Difference (%)
					This study	References	
1		0	0	0.4	4.0c	4.00c (Johnson 1962; Yu, 2005; Wang, 2011)	0
2		30	30	0.3	10.6c	10.82c (Collins and Cliffe 1987; Yu 2005; Krabbenhoj et al. 2007; Wang, 2011)	1.8
3		0	0	0.4	3.7c	3.8c (Zhao et al. 2008)	2.6
4		15	15	0.3	5.9c	6.2c (Zhao et al. 2008)	4.8

Table 3-5 Comparison of numerical shakedown limits for multi-layered pavements

Case	Load distribution	Layer	ϕ (°)	ψ (°)	ν	E_1/E_2	c_1/c_2	Shakedown limit		Difference (%)
								This study	References	
5		1 st	40	40	0.3	5	5	11.6c ₂	11.7c ₂	0.8
		2 nd	0	0	0.4				(Yu and Hossain 1998)	
6		1 st	30	30	0.2	10	1	3.3c ₂	3.2c ₂	3.0
		2 nd	0	0	0.49				(Wang and Yu, 2013b)	

However, when $p_0 = 19.3c_2$, relatively larger yielding areas were generated before the moving loads (Figure 3-7b) and two small yielding areas are still observed after the moving loads (Figure 3-7d). Therefore, for such a two-layered pavement system, $p_0 = 18.7c_2$ leads to the shakedown state, whereas $p_0 = 19.3c_2$ results in a non-shakedown state. This means the shakedown limit should be in between $18.7c_2$ and $19.3c_2$. Finally, the numerical shakedown limit ($18.9c_2$) is determined by undertaking more simulations using different magnitudes of load between $18.7c_2$ and $19.3c_2$ and it shows a good agreement with the theoretical shakedown limit.

3.2.6.2 Development of plastic strain

Figure 3-8 and Figure 3-9 demonstrate the development of plastic normal strain and plastic shear strain under different load levels in the two-layered pavement. It can be seen that, when the applied load is above the shakedown limit, the amounts of plastic normal strain and plastic shear strain increase at each load cycle and this will lead to structure failure. However, when the load applied is at the shakedown limit, plastic normal strain and plastic shear strain cease to develop after a limited number of load passes.

Table 3-6 Parameters for the two layered soil material

Layer	Friction Angle $\phi (^{\circ})$	Dilation Angle $\psi (^{\circ})$	Stiffness Ratio E_1/E_2	Strength Ratio c_1/c_2	Poisson's Ratio ν	1 st Layer Thickness (h_1/a)
1 st Layer	30	30	10	10	0.2	2
2 nd Layer	0	0			0.49	

(Note: The location of the 1st layer and the 2nd layer can refer to Figure 3-2.)

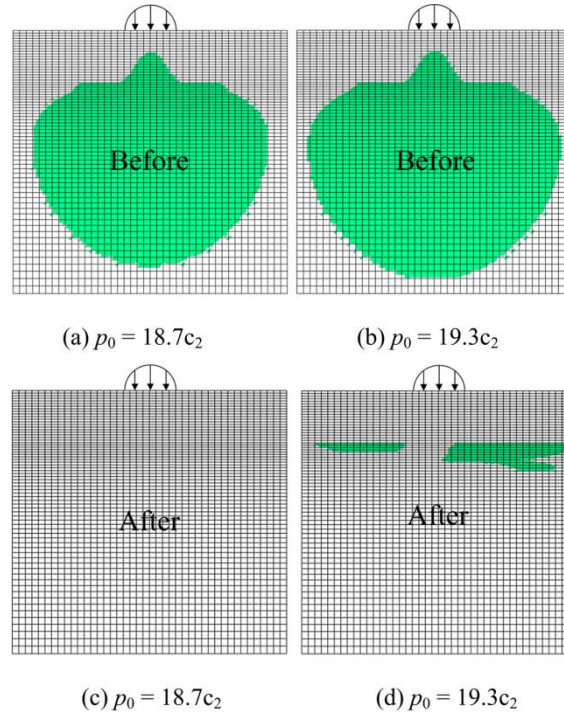
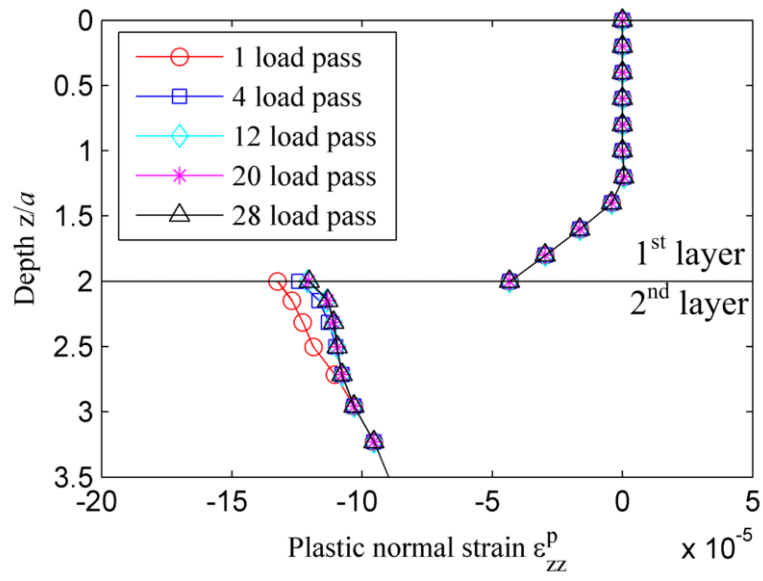


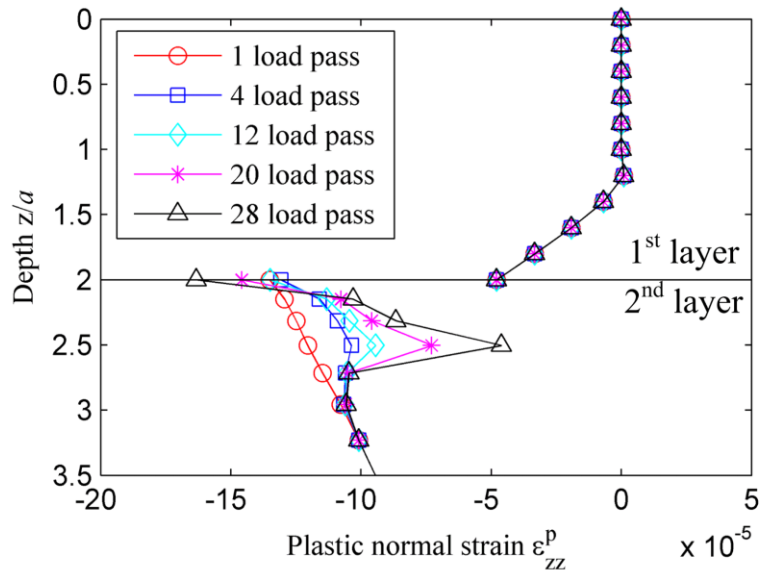
Figure 3-7 Indication of yielding areas in Region A before and after loading passes

3.2.6.3 Residual stress fields

It has been noted by Wang (2011) that in a pavement structure, the horizontal residual stress field in the travel direction may increase at the most critical points to help the structure shake down; thus in this chapter, the development of the horizontal residual stress field is analysed. Figure 3-10 shows the horizontal residual stress field in the middle section of the pavement model when the load is at or above the theoretical shakedown limit ($p_0 = 18.7c_2$). Here, the residual stresses of each layer are normalised with respect to their own cohesion respectively. From these figures, it is clear that the residual stress fields in the first layer barely change with increasing loading passes, while some changes are observed in the second layer near the interface. This means

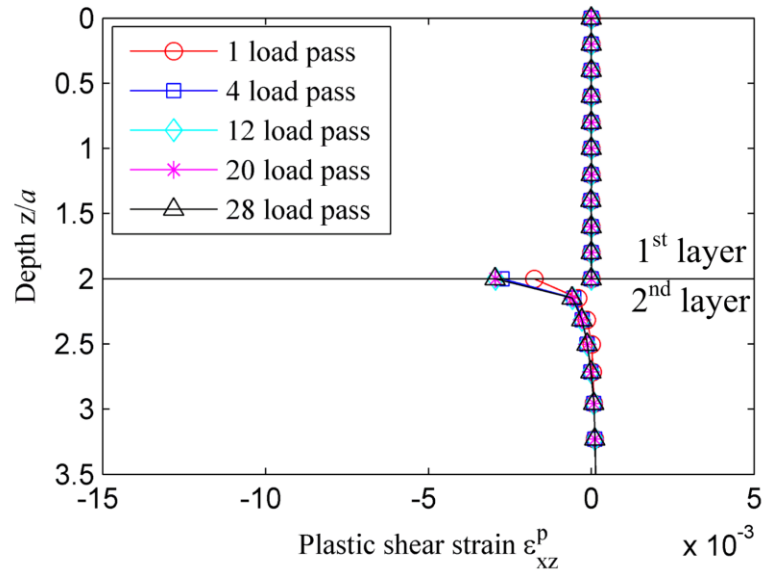


(a) $p_0 = 18.7c_2$

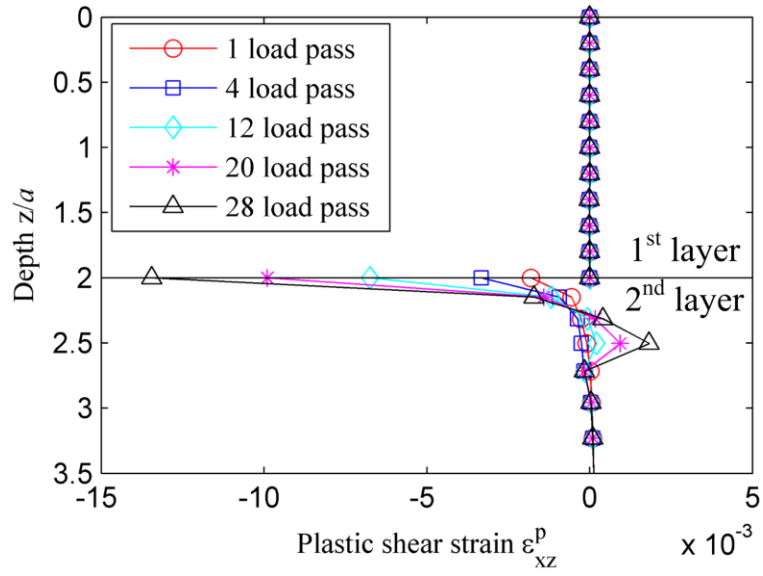


(b) $p_0 = 19.3c_2$

Figure 3-8 Development of plastic normal strain

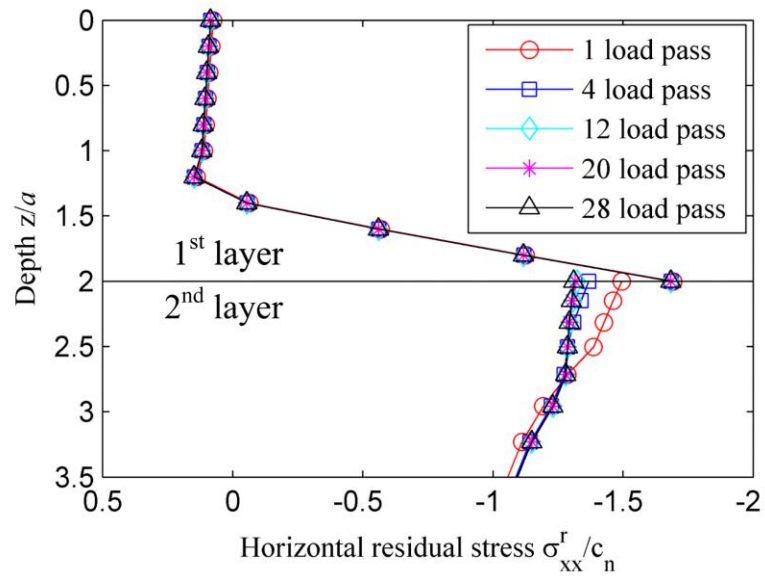


(a) $p_0 = 18.7c_2$

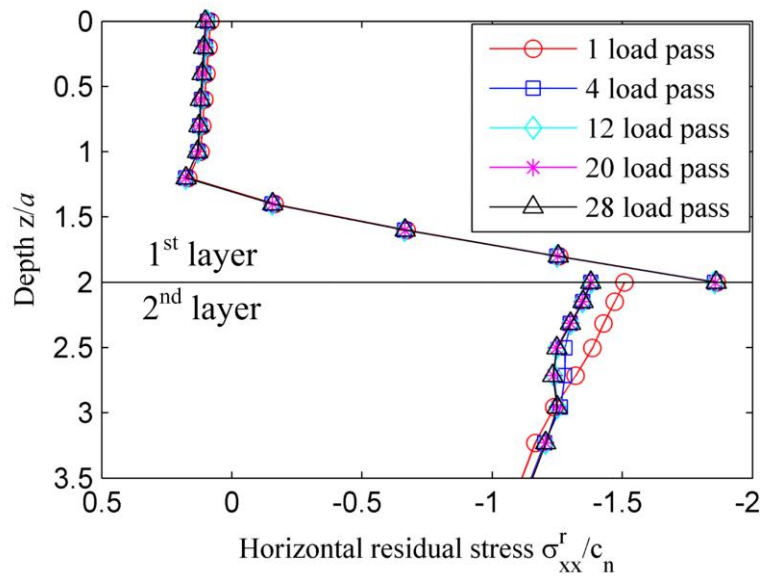


(b) $p_0 = 19.3c_2$

Figure 3-9 Development of plastic shear strain



(a) $p_0 = 18.7c_2$



(b) $p_0 = 19.3c_2$

Figure 3-10 Development of horizontal residual stresses

the second layer is more critical than the first layer and the critical point is close to the interface. This is in agreement with the theoretical finding where the critical point of this particular pavement structure is on the top of the second layer. It also can be recognized that, no matter whether the load applied is at or above the shakedown limit, the residual stress fields cease to develop after a limited number of load passes. Furthermore, the fully-developed residual stress field obtained by the numerical shakedown analysis is checked by comparing with the critical residual stress fields. As shown in Figure 3-11, the maximum smaller roots and minimum larger roots are calculated according to the theoretical method when $p_0 = 18.7c_2$. The solid curves indicate fully-developed horizontal residual stresses obtained by the numerical method with the same magnitude of load level. It lies between the two critical residual stress fields with some very minor exception.

3.2.6.4 *Effect of stiffness ratio and strength ratio*

A two-layered pavement structure with $h_1 = 2a$, $\phi_1 = 30^\circ$, $\nu_1 = 0.2$, $\phi_2 = \psi_2 = 0^\circ$, $\nu_2 = 0.49$ is taken as an example for the analyses. The shakedown limit of any layer in a multi-layered pavement is normalised by the cohesion of the first layer c_2 . Figure 3-12 and Figure 3-13 present the effect of stiffness ratio (E_1/E_2) and strength ratio (c_1/c_2) on the shakedown limit of the two-layered pavement structure.

It should be noted that the shakedown limit of the pavement structure is the minimum among shakedown limits of all layers. As shown in Figure 3-12 and Figure 3-13, the solid line and the dashed line correspond to the shakedown limit

of the first layer and the second layer respectively; therefore the intersection of these two curves indicates the change of failure mode from one layer failure to another layer failure. As can be seen, the numerical shakedown limits agree well with the theoretical shakedown limits. It is not difficult to find that there exists an optimum stiffness ratio for each case at which the shakedown limit is maximised. In terms of the effect of the strength ratio, the shakedown limit is maximized when the strength ratio reaches the value at the turning point and remains constant no matter how the strength ratio rises.

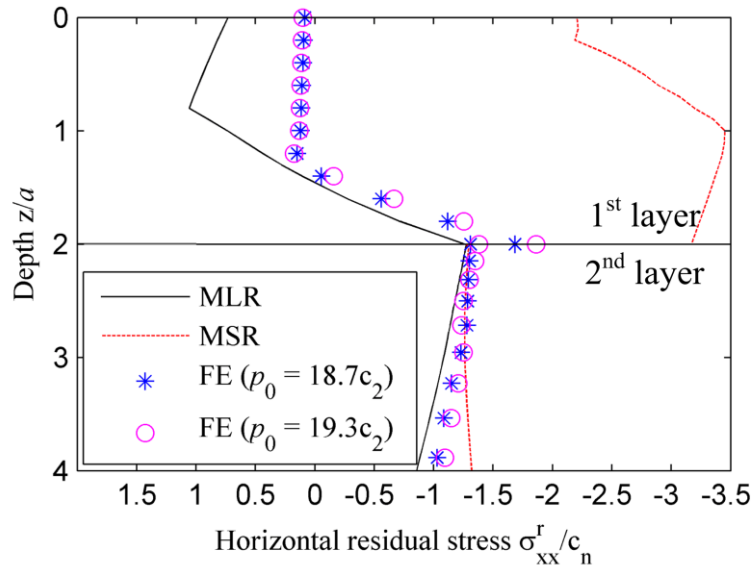
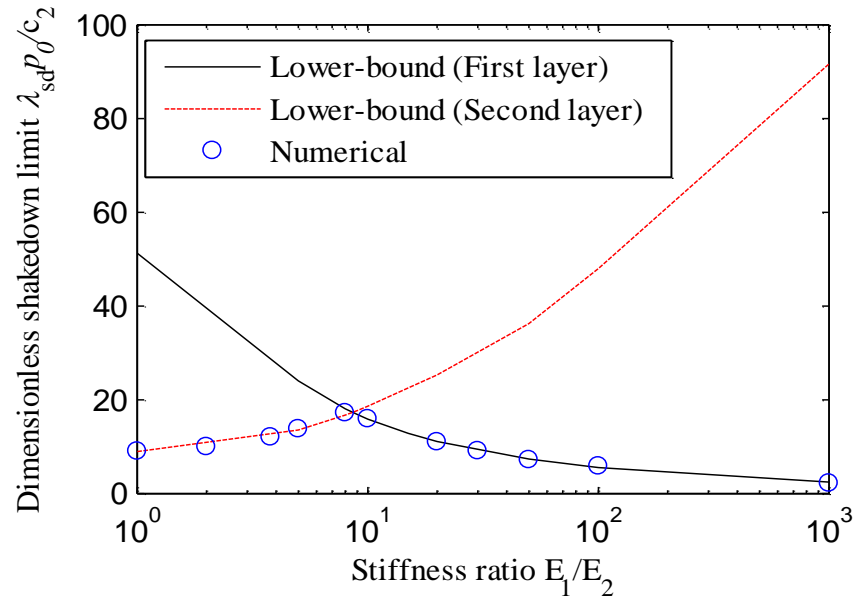
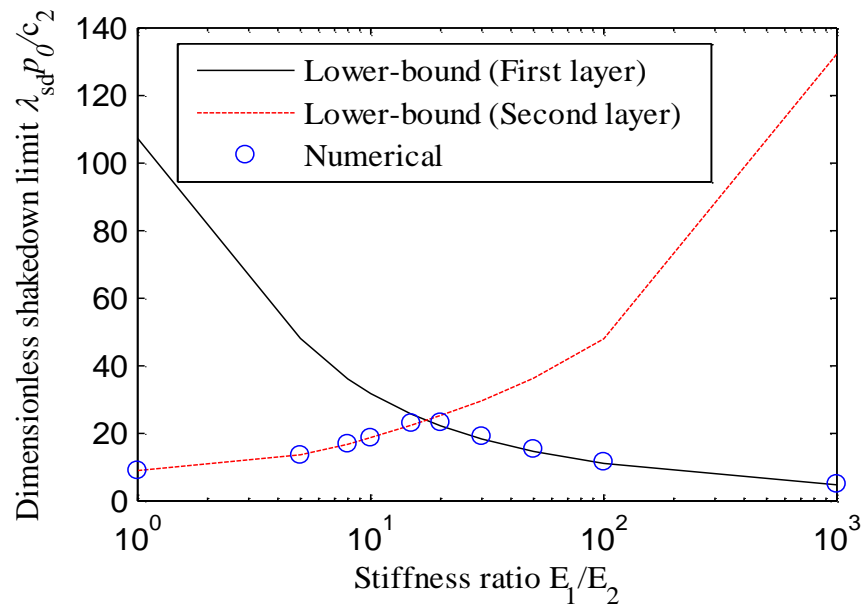


Figure 3-11 Comparison between critical and numerical residual stress fields in a two-layered pavement

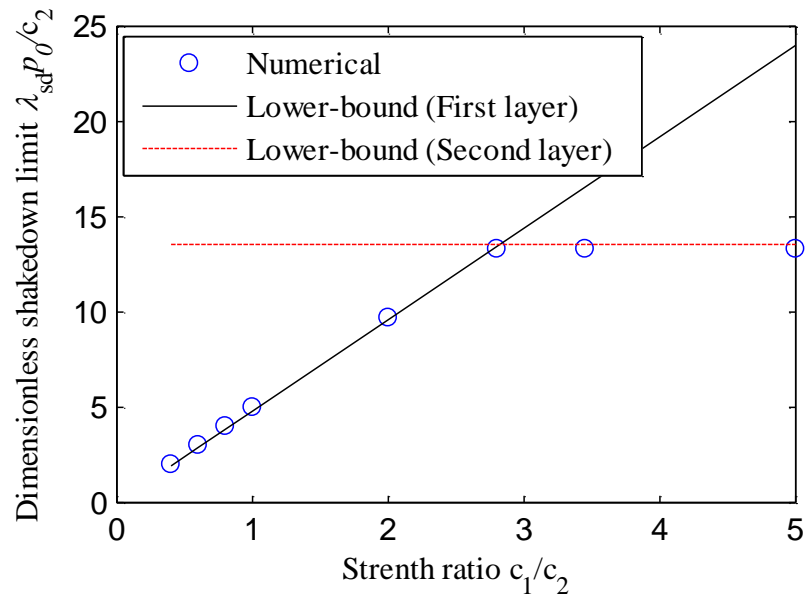


(a) $c_1/c_2 = 5$

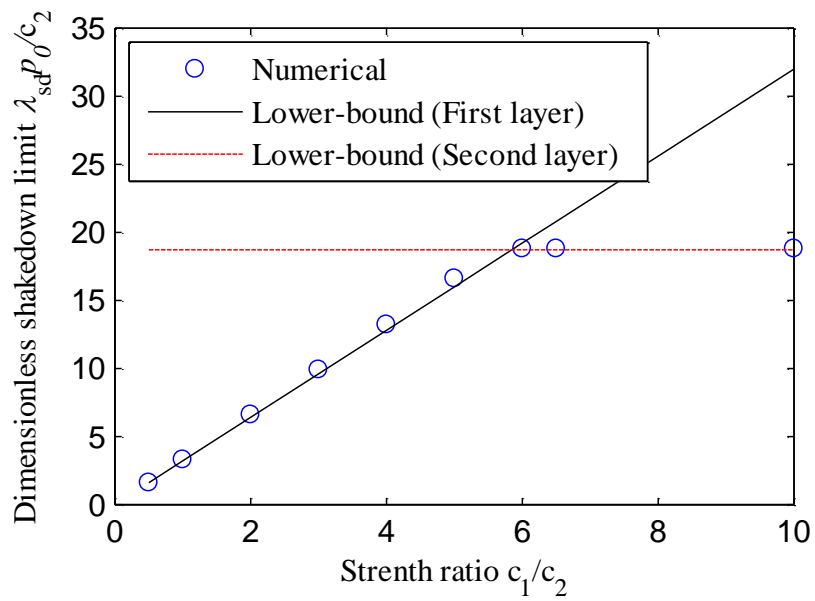


(b) $c_1/c_2 = 10$

Figure 3-12 Shakedown limits versus stiffness ratio $h_1/a = 2$ and $\phi_1 = \psi_1 = 30^\circ$



(a) $E_1/E_2 = 3$



(b) $E_1/E_2 = 10$

Figure 3-13 Numerical shakedown limits in two-layered pavements with varying strength ratio

3.2.6.5 *A typical bituminous pavement*

A typical bituminous pavement is shown in Figure 3-14 consisting of surfacing, base, sub-base and subgrade. Typical layer thickness and material parameters have been selected for each layer. The surfacing layer is assumed to be an asphalt mixture

For the four-layered problem, fine meshes are applied to the top layer and those areas in the vicinity of the interface between any two layers, especially for the first two layers (Figure 3-15).

The theoretical shakedown limit for this pavement is obtained as 632 kPa (i.e. $22.6c_2$) and yielding first occurs at the top of the second layer. By using the numerical step-by-step approach, it is found that the numerical shakedown limit is 583kPa (i.e. $20.8c_2$), 7.9% lower than the theoretical result.

Similar to two-layered pavements, when the applied load ($p_0 = 22.6c_2$) is above the numerical shakedown limit ($20.8c_2$), some fully-developed residual stresses lie outside two critical residual stress fields (Figure 3-16a). When the applied load is decreased to c_2 , the numerical residual stresses are all bracketed by two critical residual stress fields (Figure 3-16b).

More results for layered problems can be found in Liu et al. (2014, 2015a).

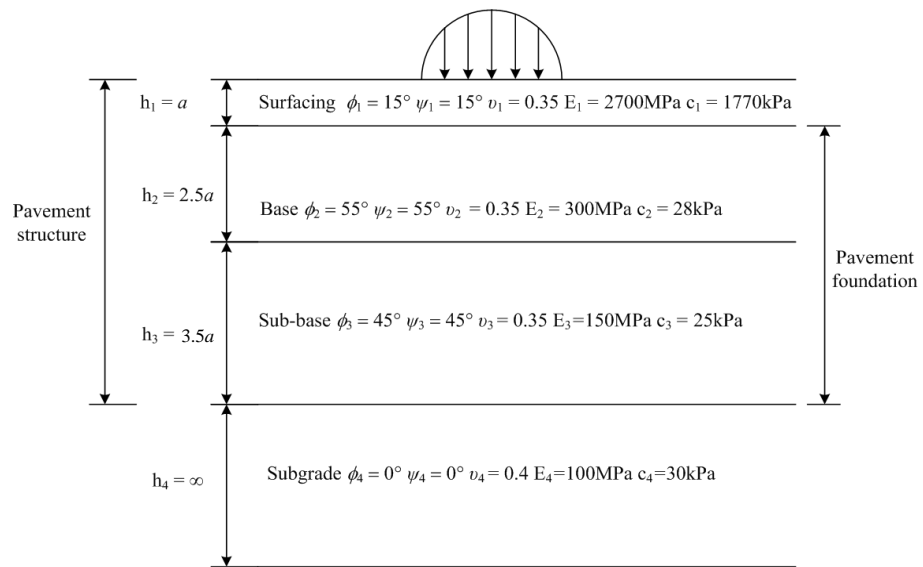


Figure 3-14 Layer thickness and materials design of a four-layered pavement

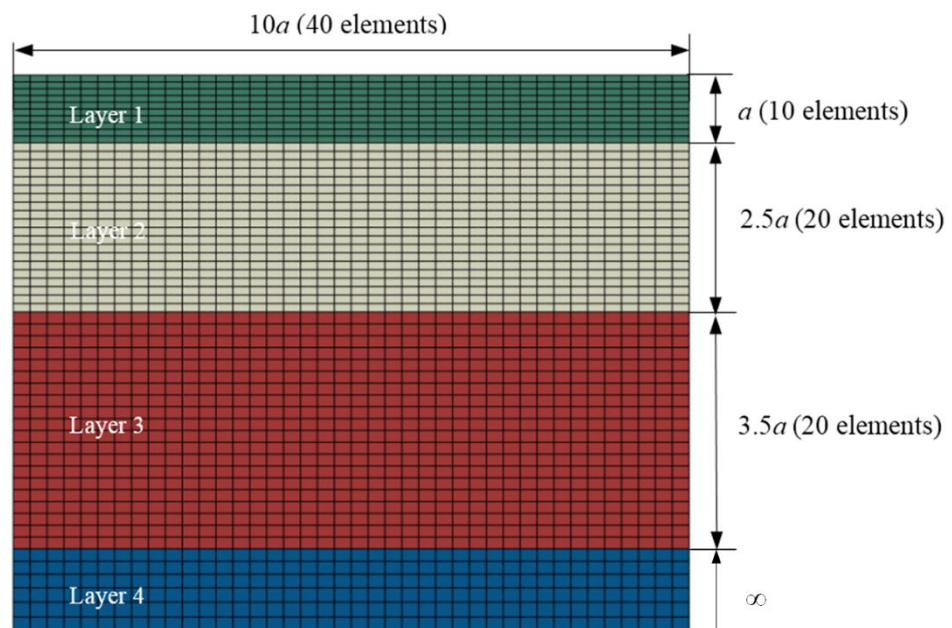
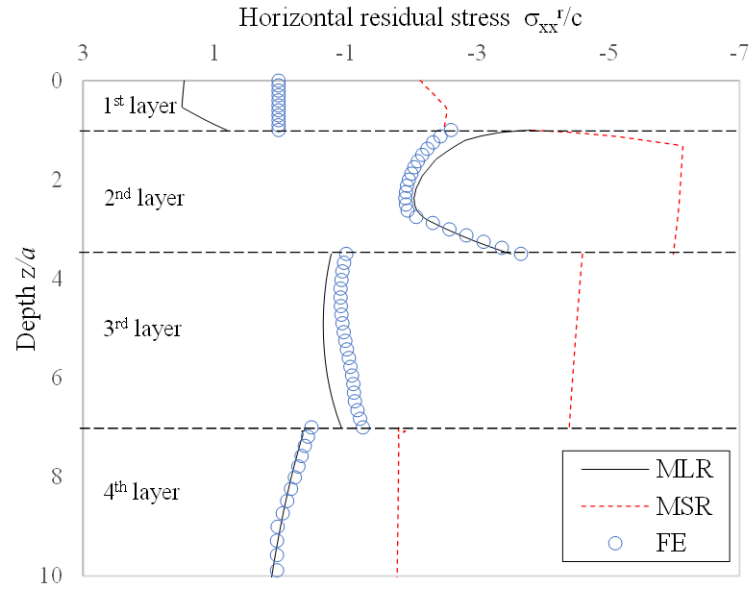
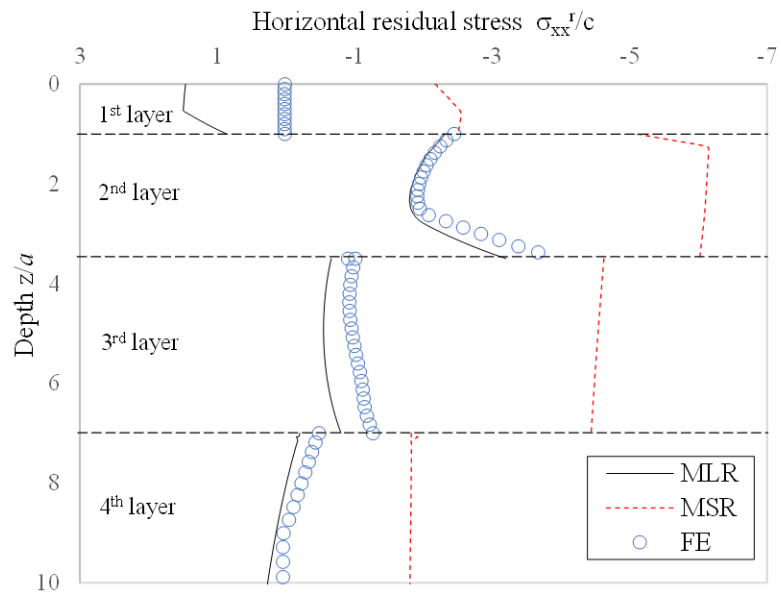


Figure 3-15 Mesh distribution in Region A for four-layered pavement model



(a) $p_0 = 22.6c_2$



(b) $p_0 = 20.8c_2$

Figure 3-16 Comparison between critical and numerical residual stress fields in a four-layered pavement

3.3 Three-dimensional pavement problems

3.3.1 Problem definition

In this subsection, a 3D surface contact load limited within a circle of radius a , is considered as shown in Figure 3-17. The pressure p on the contact surface is formulated as:

$$p = \frac{3P}{2\pi a^3} (a^2 - x^2 - y^2) \quad (3.4)$$

where P is the total normal load in the z -direction (i.e. the vertical direction). This load distribution is also known as the 3D Hertz load distribution. It has a maximum pressure $p_0 = 3P/2\pi a^2$ at the centre of the contact area.

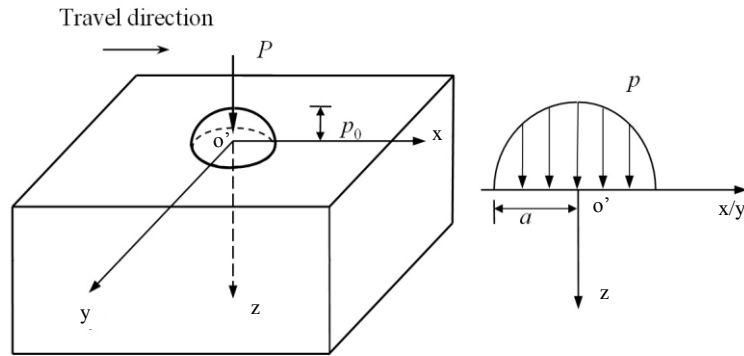


Figure 3-17 3D Hertz pressure distribution

3.3.2 Model description and verification

A semi-infinite body subjected to a quarter-spherical Hertz pressure is considered in the present work to curtail the working effort (Figure 3-18). The dimension of the 3D model is smaller than the one used in 2D numerical shakedown analyses because of the relatively small affected area. Symmetric boundary conditions are

applied on the plane of $y = 0$. Both vertical (i.e. z direction) movement and horizontal movement in the x direction are constrained on the cambered surface. Constraints on horizontal movements of the two sides are also applied. Table 3-7 shows different mesh densities used for sensitivity study and the corresponding results. The shakedown limits decrease with increasing mesh density. In the following study, the mesh with 7695 elements is used. It can be found that its 3D numerical shakedown limits are very close to the theoretical solutions of Yu and Wang (2012).

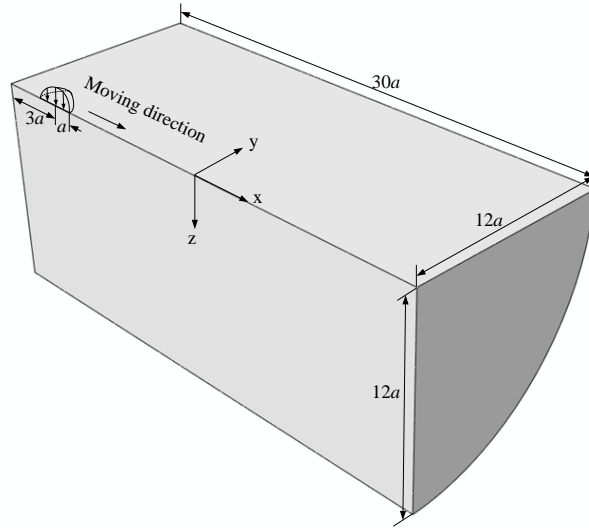


Figure 3-18 3D model sketch

Table 3-7 Influence of mesh density on 3D numerical shakedown limits

Model	Number of Elements	Friction angle	Theoretical shakedown limit (Ref)	Numerical shakedown limit	Average elapsed time per load pass (hr)
1	1920	0	4.68c	5.3c	0.05
2	4320	0		4.5c	0.78
3	7695	0		4.5c	2.21
4	4320	15	7.75c	7.8c	0.99
5	7695	15		7.7c	4.62

3.3.3 Solutions and discussions

3.3.3.1 Yielding areas

An example with Tresca materials is considered first. By using the procedure in the subsection 3.2.3, some yielding areas are observed under a static load following four load passes ($p_0 = 4.6c$). It is also demonstrated that the yielding area first generates on the plane $y = 0$ (Figure 3-20), which is consistent with the theoretical findings of Yu and Wang (2012). It should be noted that residual stresses obtained after four load passes are also independent of travel direction, as shown in Figure 3-21.

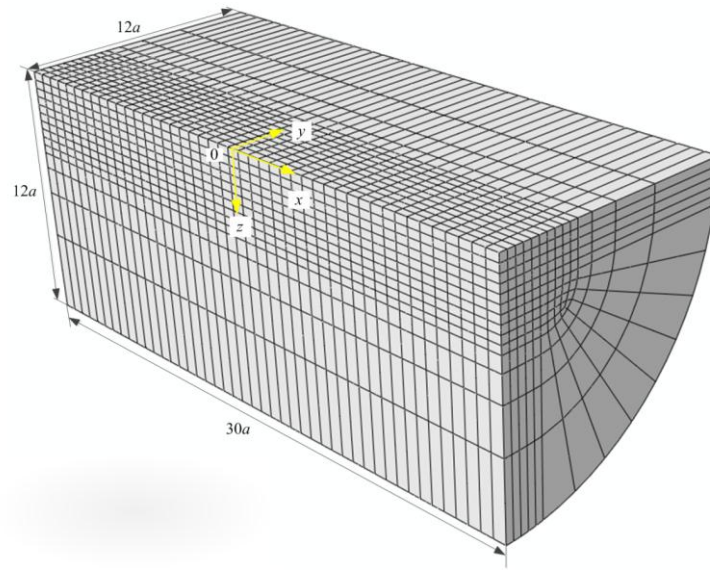
Compared to Figure 3-5, where only σ_{xx}^r and σ_{yy}^r exist in 2D problems, all six residual stress components could exist in 3D problems. However, on any x-z plane, σ_{zz}^r , σ_{xy}^r , σ_{xz}^r and σ_{yz}^r are very small compared with σ_{xx}^r and σ_{yy}^r (Figure 3-22). This agrees with Kulkarni et al. (1990) and Jiang et al.(2002)'s findings, in which the stress analyses were carried out on 3D rolling contact problems with Von-Mises materials. Figure 3-22 also indicates that σ_{xx}^r and σ_{yy}^r on all the planes normal to the y-axis attain their peak values at a depth of $z = 0.4a$. This agrees with Wang (2001)'s theoretical finding of $z = 0.36a$. The residual stress field is almost zero when $z \geq 1.2a$. In addition, the values of σ_{xx}^r and σ_{yy}^r are largest at the plane of $y = 0$. Figure 3-22 also demonstrates that σ_{yy}^r can be treated as the intermediate residual stress on the plane of $y = 0$.

Comparisons are also made between the horizontal residual stresses obtained by the numerical approach and the critical residual stresses calculated by the theoretical approach proposed by Wang (2011) (Figure 3-23). When $p_0 = 4.6c$,

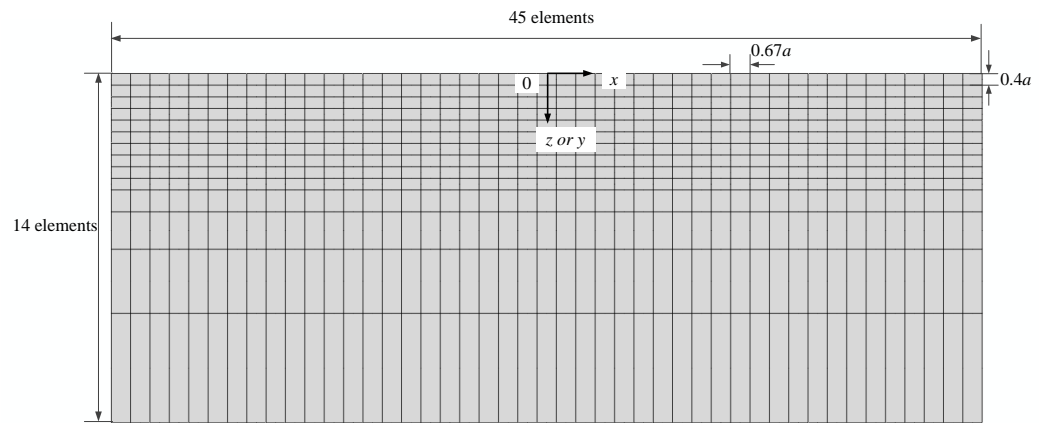
the FE calculated residual stress field deviates from the critical residual stresses at around $z = 0.4a$ (refer to Figure 3-24), which means the load applied is larger than the numerical shakedown limit. When the applied load is decreased to 4.5c (i.e. the numerical shakedown limit), the FE calculated residual stresses are bracketed by the critical residual stress fields.

3.3.3.2 Plastic strain

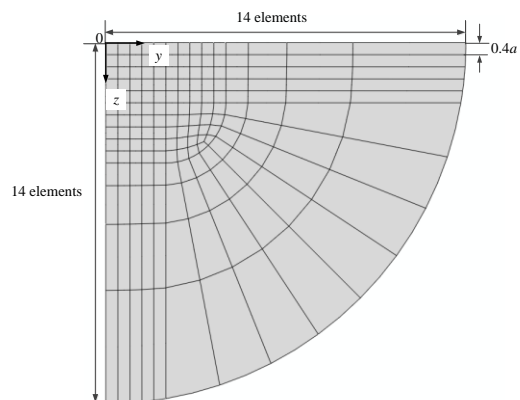
All the six components of strain are non-zero for the 3D analysis. The locations of the most critical depths of normal plastic strain are consistent with those of the normal stress, i.e. $z = 0.45a$. ϵ_{yy}^p is higher than ϵ_{xx}^p due to less constraints in the y direction. Since every point in the horizontal direction experiences the same loading history, the generation of the plastic strains in the horizontal direction is also related to the shear strains in x-z planes and x-y planes. In terms of the plastic normal strain ϵ_{yy}^p , it was zero in 2D analysis as the plane strain assumption was made, but becomes tensile in 3D analysis. The most significant normal strain is observed in the vertical direction, and the integration of the vertical strain over the depth indicates the vertical deformation on the surface, i.e. rutting. From Figure 3-25, shear strains ϵ_{xz}^p are more significant than ϵ_{yz}^p and ϵ_{xy}^p . The negative and positive values of ϵ_{xz}^p demonstrate forward and backward shear flows at different depths in the pavement. The shear strains ϵ_{xy}^p are related to different amount of shear flow at the same depth in the transverse direction. The shear strains ϵ_{yz}^p are attributed to different vertical deformations at the same depth in the transverse direction.



(a)



(b)



(c)

Figure 3-19 3D FE model for numerical shakedown analysis

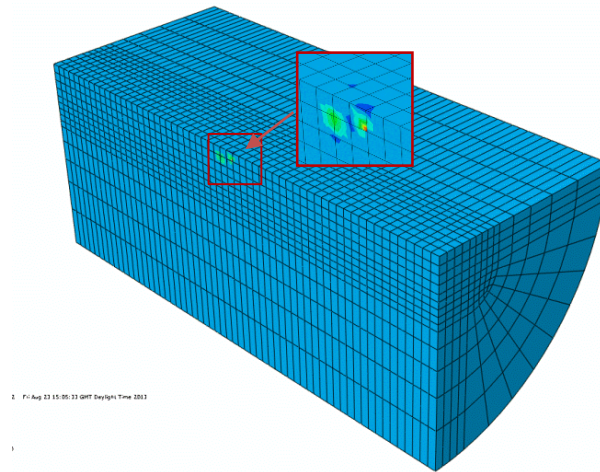
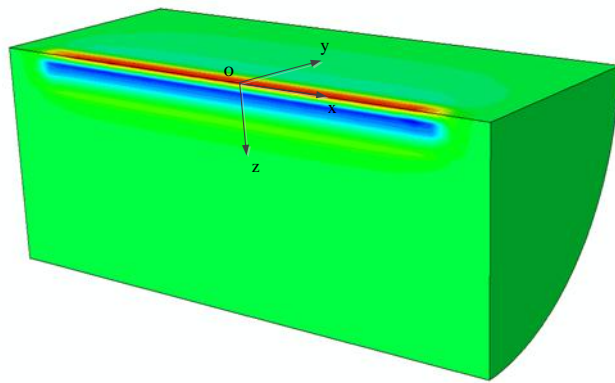
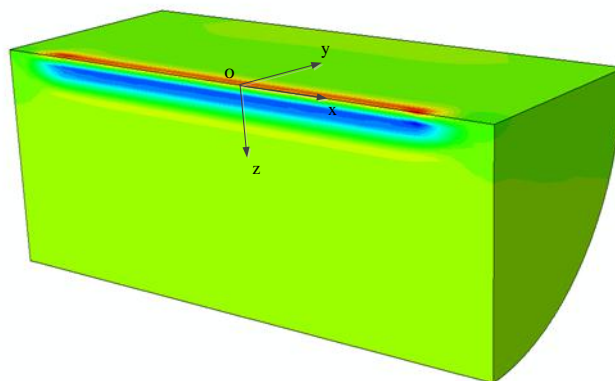


Figure 3-20 Location of yielding areas in a 3D model



(a) σ_{xx}^r



(b) σ_{yy}^r

Figure 3-21 Distributions of the residual stresses after four load passes when $\phi = 0^\circ$

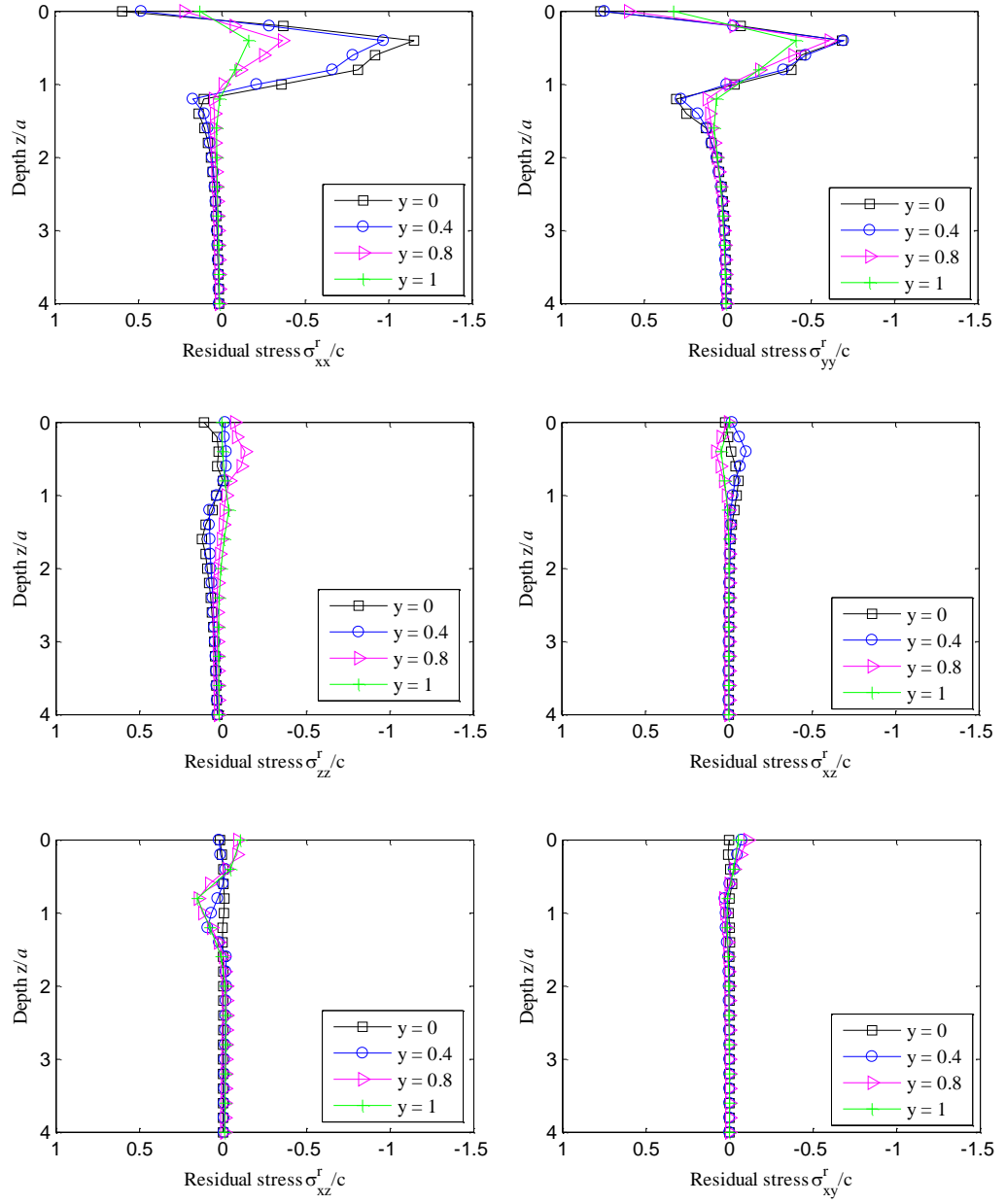


Figure 3-22 Residual stresses after four load passes when $\phi = 0^\circ$

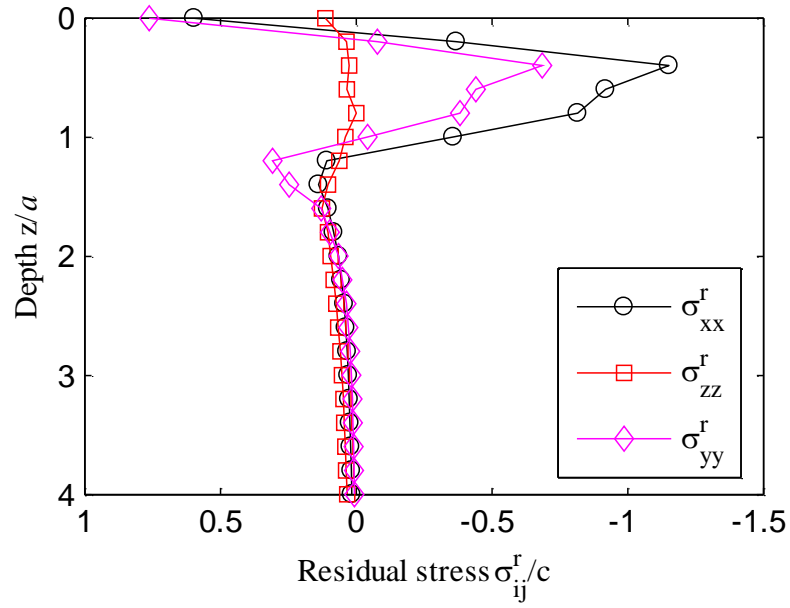


Figure 3-23 Residual stress fields after four load passes when $p_0 = 4.5c$ and $\phi = 0^\circ$ when $y = 0$

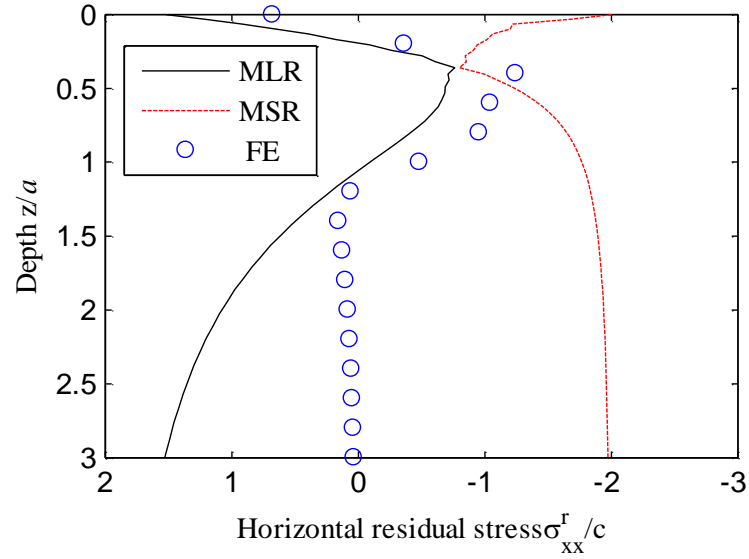
3.3.3.3 Deformation

Figure 3-28 presents the undeformed and deformed mesh in the 3D pavement model along and perpendicular to the moving direction after four load passes when $p_0 = 4.5c$. The deformations have been enlarged by 600 times. From Figure 3-28a, a uniformly distributed ploughing is observed on the surface of the pavement after four load passes. It also can be seen that the elements in the band of $0.4a \leq z \leq a$ on the plane $y = 0$ are the most seriously compressed.

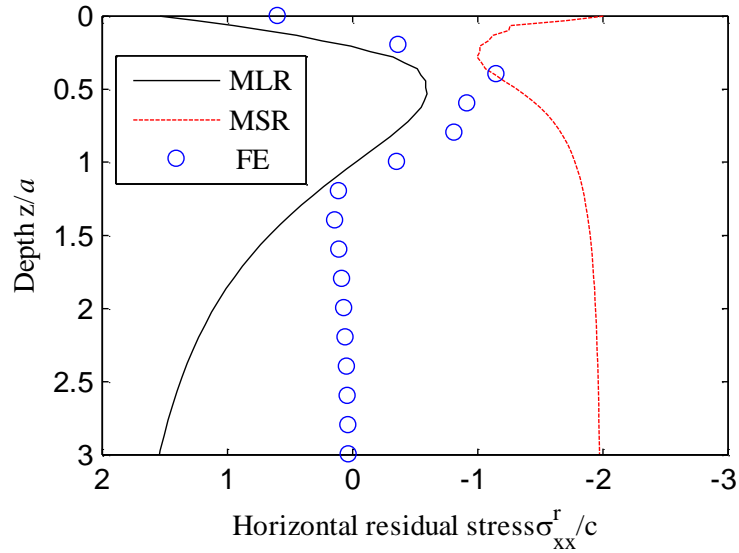
3.4 Summary

In this chapter, a numerical step-by-step approach was applied to 2D and 3D pavement problems. The numerical shakedown solutions generally agree with the theoretical shakedown solutions for multi-layered pavement structures. For

a 3D half-space under moving loads, it is found that the plane of $y = 0$ is the most critical plane; this is consistent with the theoretical findings of Yu and Wang (2012). Good agreements are also shown between the numerical and theoretical 3D shakedown limits.



(a) $p_0 = 4.6c$



(b) $p_0 = 4.5c$

Figure 3-24 Development of horizontal residual stress σ_{xx}^r under successive load passes when $\phi = 0^\circ$

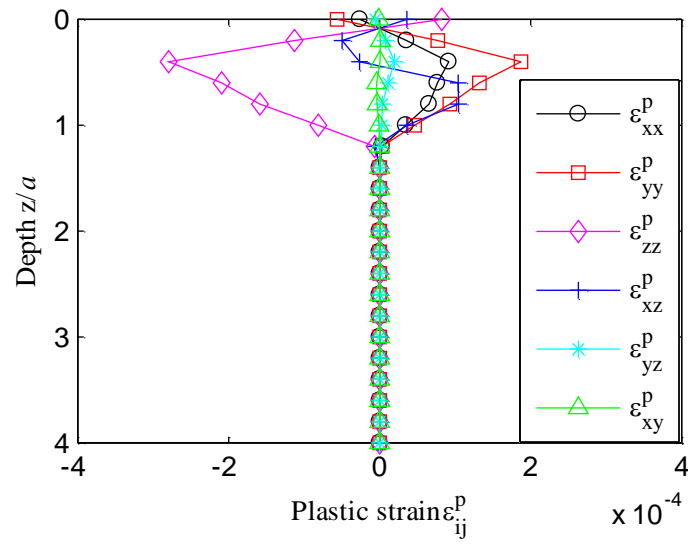
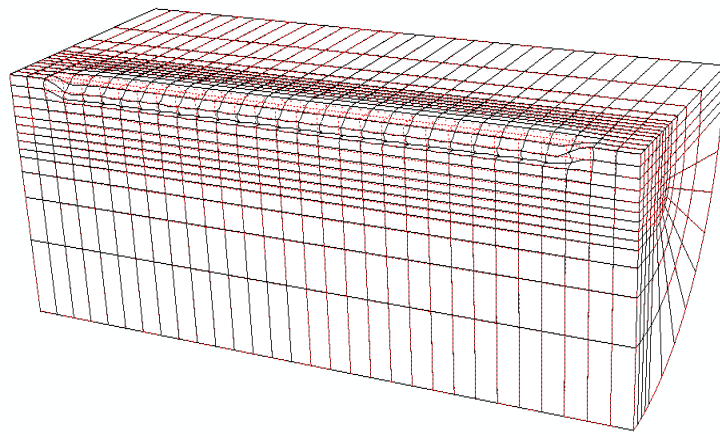
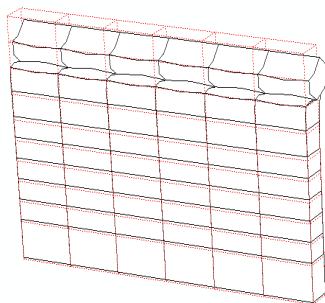


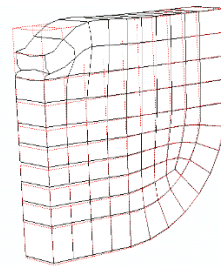
Figure 3-25 Plastic strain fields at $y = 0$ after four load passes when $p_0 = 4.5c$ and $\phi = 0^\circ$



(a) whole model



(b) x-z plane



(c) x-y plane

Figure 3-26 Residual distortions (deformation scale 600)

CHAPTER 4

SHAKEDOWN ANALYSIS OF PAVEMENTS WITH MATERIALS FOLLOWING NON- ASSOCIATED PLASTIC FLOW

4.1 Introduction

Most of the existing shakedown solutions were carried out based on the assumption of an associated flow rule (i.e. the plastic strain rate is normal to the yield surface). It is well known that granular materials, such as soil and pavement materials, exhibit a non-associated plastic behaviour (Lade et al. 1987; Lade and Pradel 1990). Until now, very limited results have been reported on this topic. Boulbibane and Weichert (1997) proposed the formulation of a constitutive law for the materials following a non-associated plastic flow rule and indicated that this formulation can be applied to solve shakedown problems on the basis of the lower bound shakedown theorem. By using this formulation, a direct shear test under two variable cyclic loads was modelled as a plane strain problem by Nguyen (2008) to investigate the effect of non-associated plastic flow rule on the shakedown limits. Results showed that the loading capacity decreased when the non-associated behaviour was taken into account. Also, decreases in the shakedown limits due to the consideration of material non-associated plastic

behaviour were also observed by Li (2010) who performed upper bound shakedown analysis on a 2D pavement model with non-associated materials subjected to Hertz pressure.

In this chapter, first, shakedown limits for 2D pavement problems are captured by using a step-by-step numerical approach. Both associated and non-associated flow rules will be considered for pavement materials. Then a direct method will be developed based on the previous work of Yu and Wang (2012) to estimate the lower bound shakedown limits of pavements using a non-associated plastic flow rule.

The 2D problem defined in the subsection 3.2.1 and the FE model given in Figure 3-3 are applied in this chapter.

4.2 Numerical shakedown analysis

4.2.1 General introduction

The materials are assumed to be homogenous, isotropic, and elastic-perfectly plastic with associated plastic flow (i.e. $\phi = \psi$) or non-associated plastic flow (i.e. $0 \leq \psi < \phi$). Subscript 'n' of E , ν , c , ϕ and ψ represents the n^{th} layer. For single-layered pavement problems, identical materials are assigned to both layers.

The step-by-step numerical approach for non-associated cases is similar to that used in Chapter 3. However, there exists some difference in the selection of the stiffness matrix type. According to ABAQUS Analysis User's Guide (2013), the type of the stiffness matrix of the materials following associated plastic flow is

automatically selected by the solver (symmetric or unsymmetric), while for non-associated cases, the unsymmetric stiffness matrix has to be selected by the user. The simulation is processed by means of ‘automatic incrementation control’ with a given maximum increment of 0.1.

4.2.2 Solutions of single-layered pavements

4.2.2.1 Shakedown limits

Table 4-1 presents numerical results for single-layered pavements and compares them with the shakedown limits of Wang (2011). If an associated flow rule ($\phi = \psi$) is assumed, the shakedown limits are only slightly lower than those in Wang (2011) with a maximum difference of 2.0%. However, if a non-associated flow rule ($\psi < \phi$) is used in the numerical model, the difference can be as high as 13.1%. Therefore, the effect of the plastic flow rule cannot be neglected, especially when the friction angle is high. Also, Table 4-1 shows that the dimensionless shakedown limit (defined as the shakedown limit normalised by material cohesion ‘c’) reduces acceleratively with decreasing dilation angle, and the maximum reduction occurs when the dilation angle ψ drops from 30 ° to 0 ° (friction angle ϕ remains 30 °).

4.2.2.2 Shakedown and non-shakedown

Figure 4-1 demonstrates the yielding area in region A of the pavement structure under a static load before and after a limited number of loading passes when $p_0 = 10.6c$ and $\phi = 30^\circ$. It can be seen that there exist large yielding areas under a static load without any previous moving passes. However, after a limited number

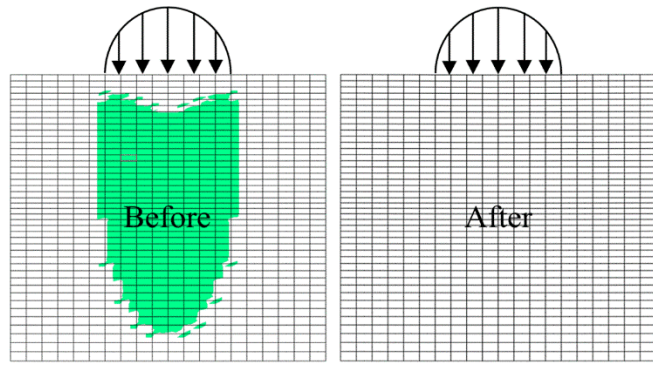
of load passes, the application of a static load ($p_0 = 10.6c$) does not result in any yielding areas for the case with materials following associated plastic flow, and some relatively smaller yielding areas are observed if $p_0 = 10.6c$ for the cases with materials following non-associated plastic flow. Figure 4-1 also reveals that the shakedown limits of the non-associated cases are lower than the associated cases.

Table 4-1 Material parameters and shakedown limits for single-layered pavements

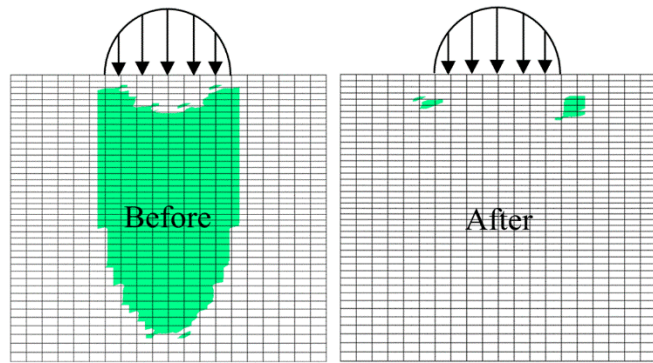
case	$\phi (^\circ)$	$\psi (^\circ)$	ν	Theoretical shakedown limit	Numerical Shakedown limit	Difference (%)
1	30	30	0.3	10.82c	10.6c	2.0
2	30	20	0.3		10.4c	3.8
3	30	10	0.3		10.0c	7.6
4	30	0	0.3		9.4c	13.1
5	25	25	0.3	8.89c	8.8c	1.0
6	25	10	0.3		8.6c	3.4
7	25	5	0.3		8.5c	4.7
8	25	0	0.3		8.1c	10.6
9	20	20	0.3	7.56c	7.5c	0.8
10	20	10	0.3		7.4c	2.1
11	20	0	0.3		7.2c	4.8
12	15	15	0.3	6.58c	6.1c	7.3
13	15	7.5	0.3		6.1c	7.3
14	15	0	0.3		6.1c	7.3

4.2.2.3 Residual stress fields

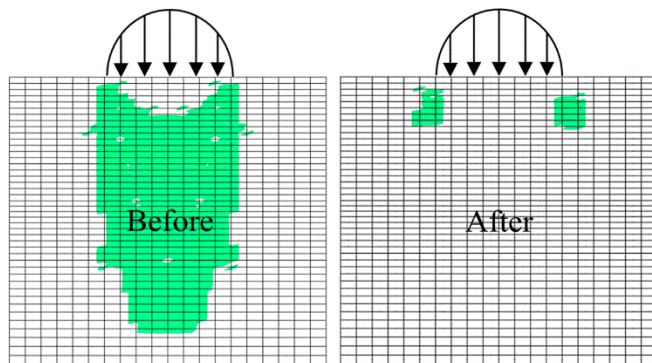
The development of horizontal residual stress fields with increasing number of load passes is shown in Figure 4-2 for cases with different dilation angles (i.e. associated or non-associated flow rule) and load magnitudes (at or above numerical shakedown limits). These fields barely change after several load passes. This coincides with the test report of Radovsky and Murashina (1996) in which the measured residual stresses ceased to increase after 12 wheel passes. Lower load level results in a smaller amount of residual stresses.



(a) $\phi = 30^\circ, \psi = 30^\circ$



(b) $\phi = 30^\circ, \psi = 20^\circ$



(c) $\phi = 30^\circ, \psi = 10^\circ$

Figure 4-1 Indication of yielding areas in Region A subjected to a static load following 10 load passes ($p_0 = 10.6c$, $\phi = 30^\circ$)

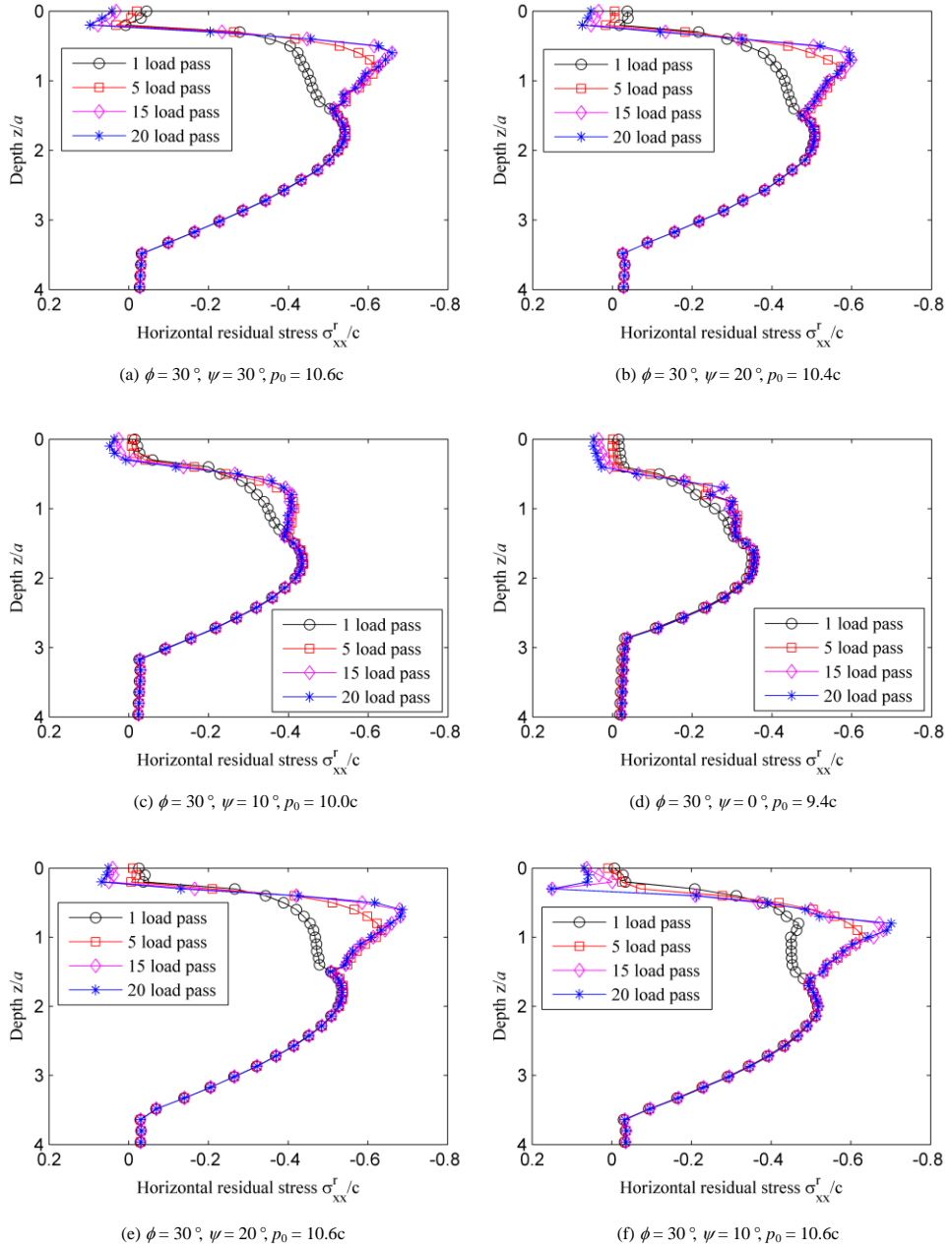


Figure 4-2 Development of horizontal residual stress field

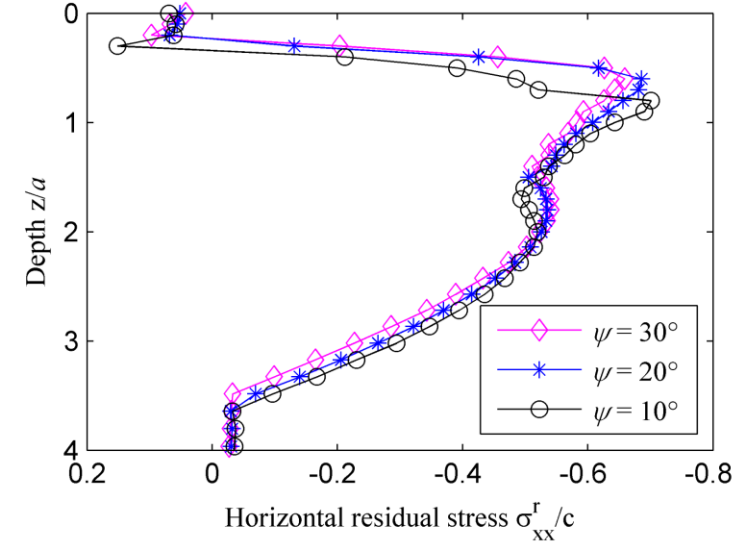
When the load magnitudes remain the same, the fully-developed residual stresses are compared in Figure 4-3(a) for the case of $\phi = 30^\circ$ and $p_0 = 10.6c$, and in Figure 4-4(a) for the case of $\phi = 20^\circ$ and $p_0 = 7.5c$. Figure 4-3(b) and Figure 4-4(b) further compare those residual stresses with MLR and MSR when $0 \leq z/a \leq 1$. It is evident that the numerical residual stresses are completely

bracketed by MLR and MSR when the materials obey the associated flow rule. It can also be observed that the use of smaller dilation angle drifts some residual stresses further away from the safe region bracketed by the two curves. Therefore there are some critical depths below the pavement surface representing locations for unlimited increasing plastic strains (Figure 4-6(a) and Figure 4-7(a)). Hence, if the load magnitude is higher than the shakedown limit, the structure will eventually fail due to excessive cumulative permanent deformation. However, if the load magnitude is reduced to the shakedown limit, plastic strains will cease to accumulate after a few load passes (e.g. Figure 4-6(b) and Figure 4-7(b)). This is because smaller load magnitude will result in a wider safe region between the two curves, so that the fully-developed horizontal residual stress field can be well contained (e.g. Figure 4-5). Locations of these critical depths also agree with yielding areas plotted in ABAQUS when a static load is further applied on the pavement surface, as shown in Figure 4-1.

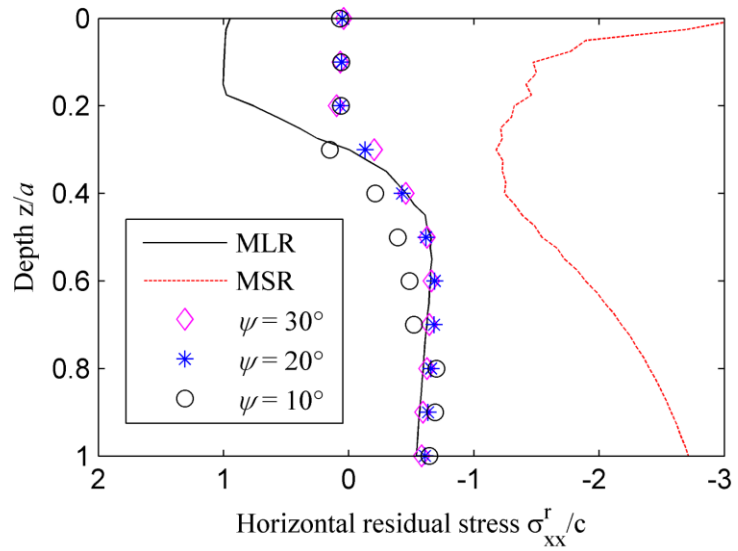
4.2.2.4 *Plastic strain*

When the dilation angle is non-zero, plastic normal strains in the half space are attributed to both material compression and dilatancy. Material compression results in negative plastic normal strains, while material dilation contributes to positive plastic strains. At shallow depths, the dilatancy effect due to shear overwhelms the compression effect; therefore positive normal strains occur. Moreover, further changes of plastic shear strains (Figure 4-7(a)) result in increasing positive plastic normal strains (due to dilation) at the same depths (Figure 4-6(a)). At greater depths, material compression dominates element

deformation thus negative normal strains occur. When the dilation angle is zero, plastic normal strains depend on material compression only.

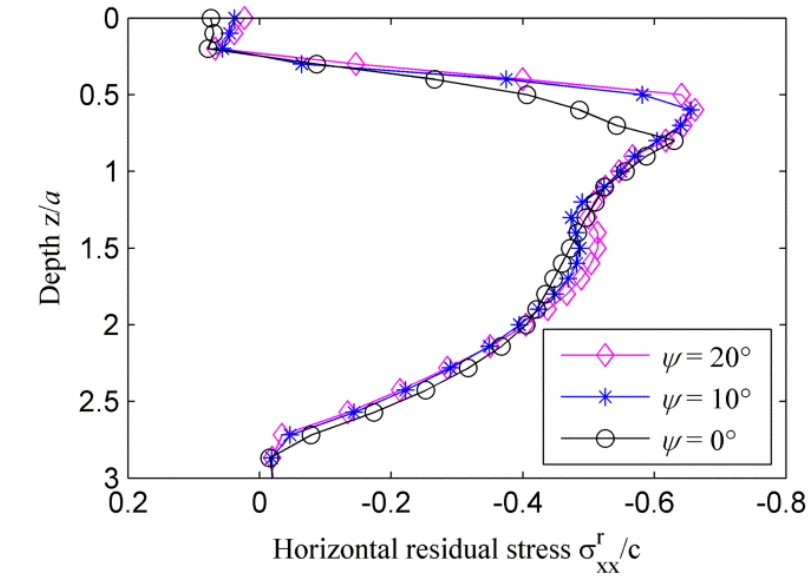


(a)

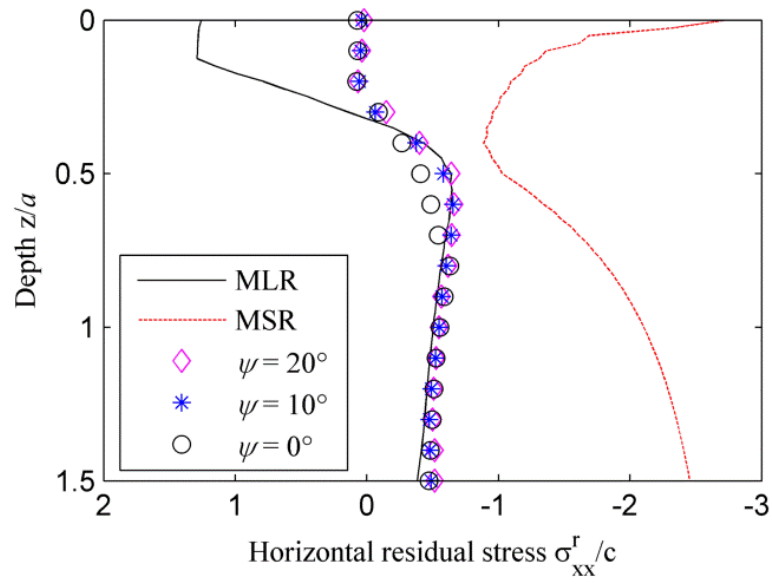


(b)

Figure 4-3 Influence of dilation angle on horizontal residual stress field when $\phi = 30^\circ$, $p_0 = 10.6c$



(a)



(b)

Figure 4-4 Influence of dilation angle on horizontal residual stress field when $\phi = 20^\circ$, $p_0 = 7.5c$

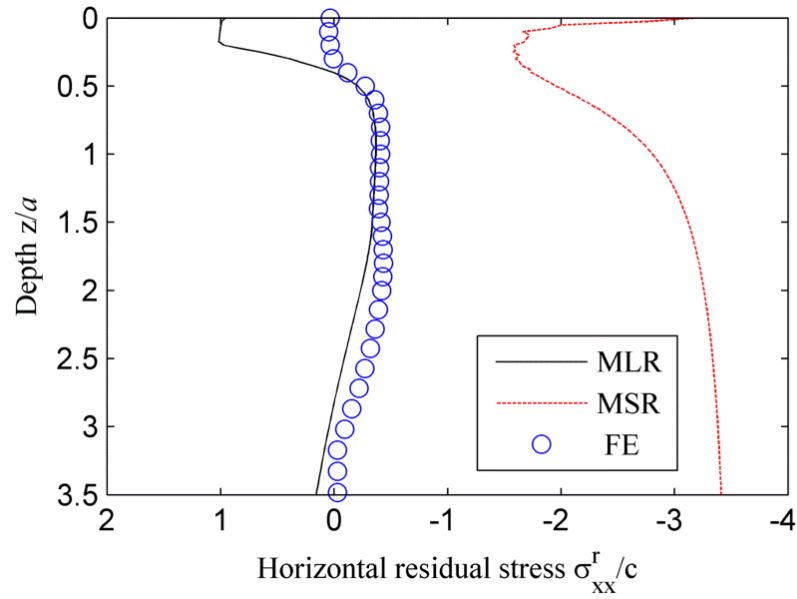
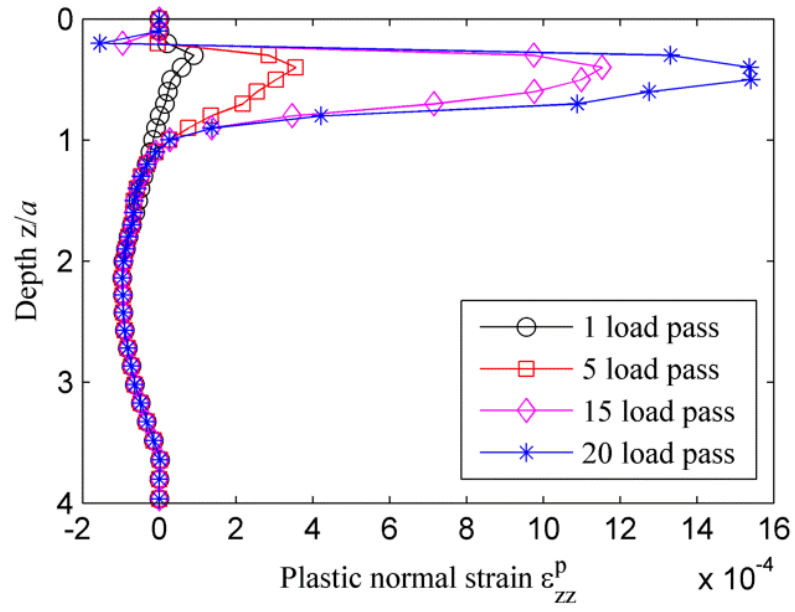


Figure 4-5 Comparison between FE calculated residual stress field and critical residual stress fields when $\phi = 30^\circ$, $\psi = 10^\circ$, $p_0 = 10.0c$

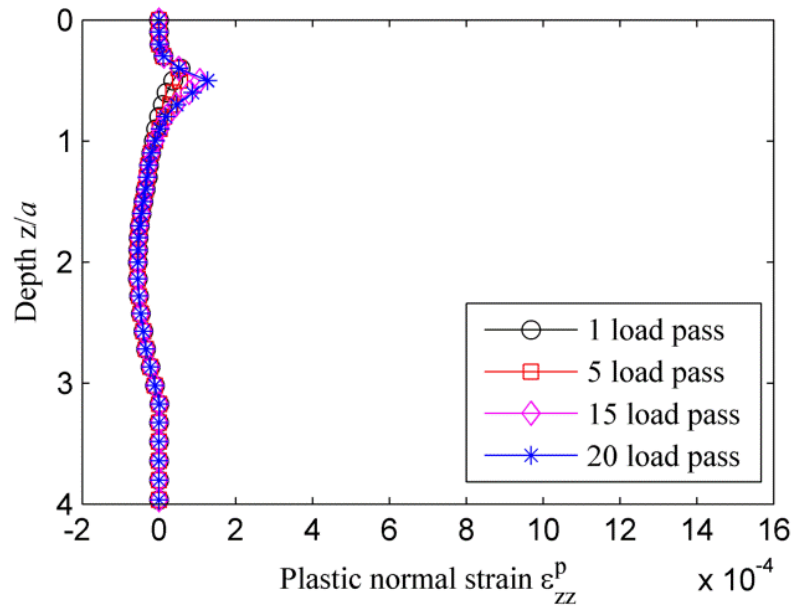
4.2.3 Solutions of multi-layered pavements

4.2.3.1 Effect of stiffness ratio

A two-layered pavement structure with $h_1 = 2a$, $\phi_1 = 30^\circ$, $\nu_1 = 0.2$, $\phi_2 = \psi_2 = 0^\circ$, $\nu_2 = 0.49$ is taken as an example for analysis. Results are obtained by using materials with either an associated flow rule ($\phi_1 = \psi_1 = 30^\circ$) or a non-associated flow rule ($\phi_1 = 30^\circ, \psi_1 = 0^\circ$). A direct comparison between these two cases is made in Figure 4-8 for various stiffness ratios E_1/E_2 . Shakedown limits calculated through the lower bound approach are also presented in this figure as a dashed line. Here, the shakedown limit of any layer in a multi-layered pavement is normalised by the cohesion of the second layer c_2 . It is noteworthy that there exists an optimum stiffness ratio at around $E_1/E_2 = 1.4$ at which the shakedown limit is maximised. The turning point also indicates the change of

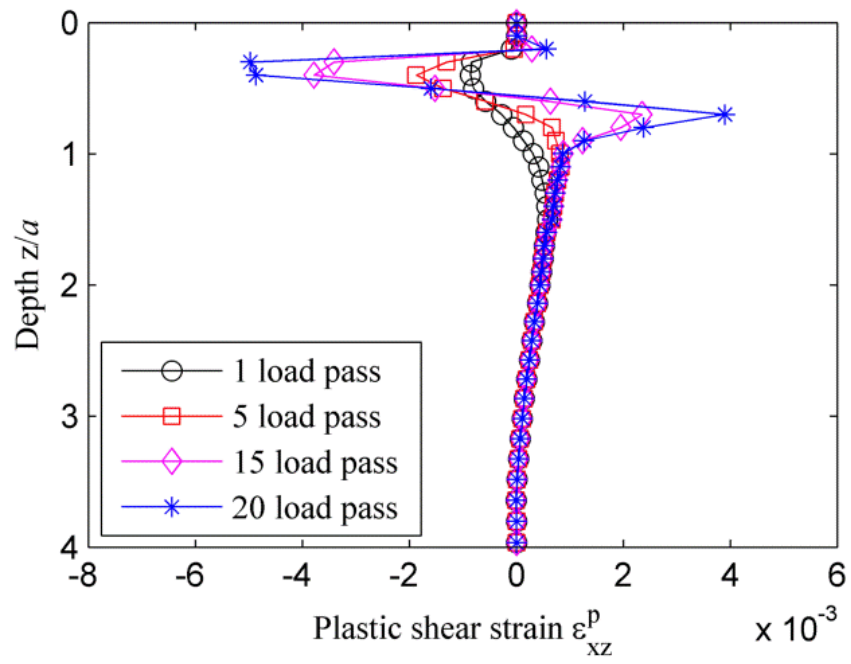


(a) $\phi = 30^\circ$, $\psi = 10^\circ$, $p_0 = 10.6c$

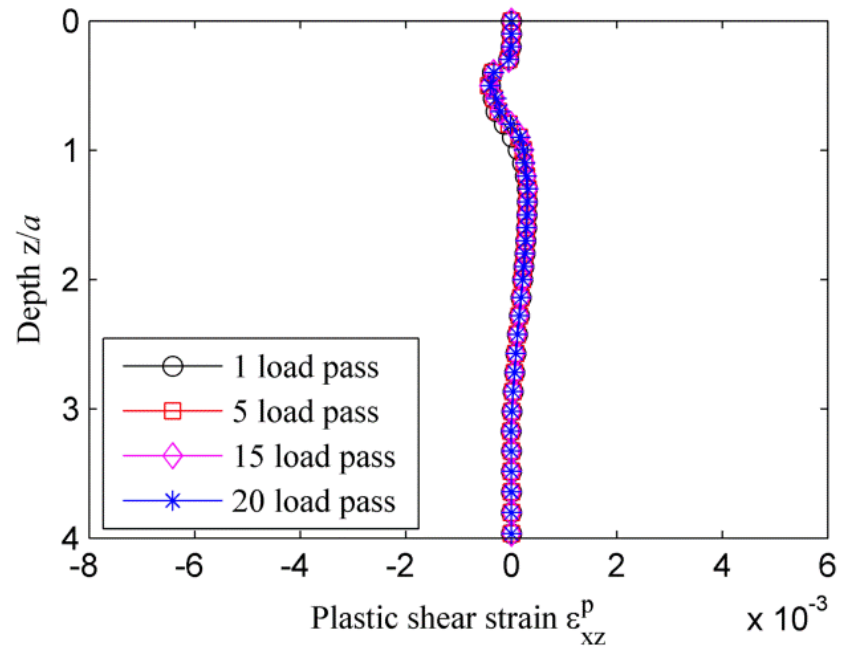


(b) $\phi = 30^\circ$, $\psi = 10^\circ$, $p_0 = 10.0c$

Figure 4-6 Development of plastic normal strains



(a) $\phi = 30^\circ$, $\psi = 10^\circ$, $p_0 = 10.6c$



(b) $\phi = 30^\circ$, $\psi = 10^\circ$, $p_0 = 10.0c$

Figure 4-7 Development of plastic shear strains

pavement failure mode from second layer failure to first layer failure. As can be seen, numerical results for cases with an associated flow rule agree well with the lower bound shakedown limits. However, when the non-associated flow rule is applied, numerical results are lower than the lower bound shakedown solutions when $E_1/E_2 \geq 0.8$.

4.2.3.2 *Residual stress fields*

Residual stresses also develop in multi-layered pavements. Taking a two-layered pavement with $E_1/E_2 = 3$ as an example, a fully-developed horizontal residual stress field exists not only in the first layer, but also at the top of the second layer, as shown in Figure 4-9. This means that the top of the second layer can also be critical. This agrees with the current pavement design approach (e.g. Brown 1996) in which the top of the soil subgrade is considered as one of the critical locations. Again, with the use of a non-associated flow rule, some fully-developed residual stresses cannot reach the safe region bracketed by MLR and MSR. Therefore, shakedown limits of the non-associated cases are smaller than those using $\phi_1 = \psi_1$. Further studies show that for a pavement with $\phi_1 = 30^\circ$, $\psi_1 = 0^\circ$; if the load is decreased from $6.7c_2$ to $5.5c_2$, the numerical residual stresses can lie totally within the safe region (Figure 4-10), and therefore the pavement will shakedown to a steady state.

It is also interesting to notice that (e.g. Figure 4-4, Figure 4-5, Figure 4-9 and Figure 4-10), the actual residual stresses within the plastic region are very close to the compressive (negative) MLR rather than MSR. This implies that the structure tends to a minimum of plastic work (i.e. as small a plastic deformation

as possible) subject to a certain level of load in order to achieve the shakedown state. Outside the plastic region, the actual residual stresses are almost zero; whereas the MLR are positive. This is because the assumption of yielding at all depths (Yu and Wang 2012) yields some positive artificial residual stresses. In reality, actual stress states at some depths will not touch the yield surface, reflected as zero residual stresses.

In summary, the numerical approach is a valid way to obtain shakedown limits of pavements with the assumptions of either an associated or a non-associated plastic flow rule. More numerical solutions considering different load cases, strength ratios and layer configurations will be presented in the following section in comparison with theoretical solutions.

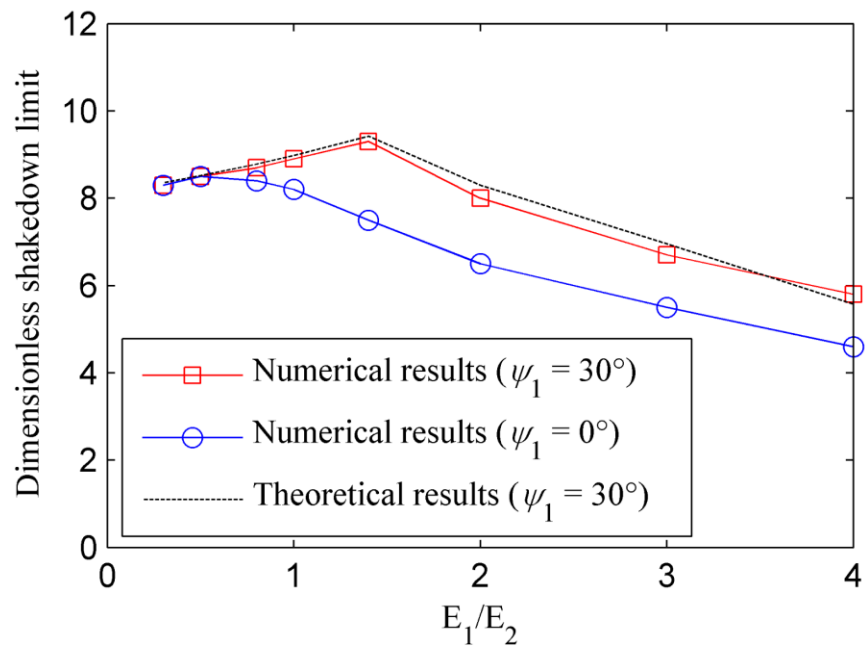


Figure 4-8 Comparison of numerical and theoretical shakedown limits for layered pavements when $\phi_1 = 30^\circ$; $\phi_2 = 0^\circ$; $c_1/c_2 = 1$

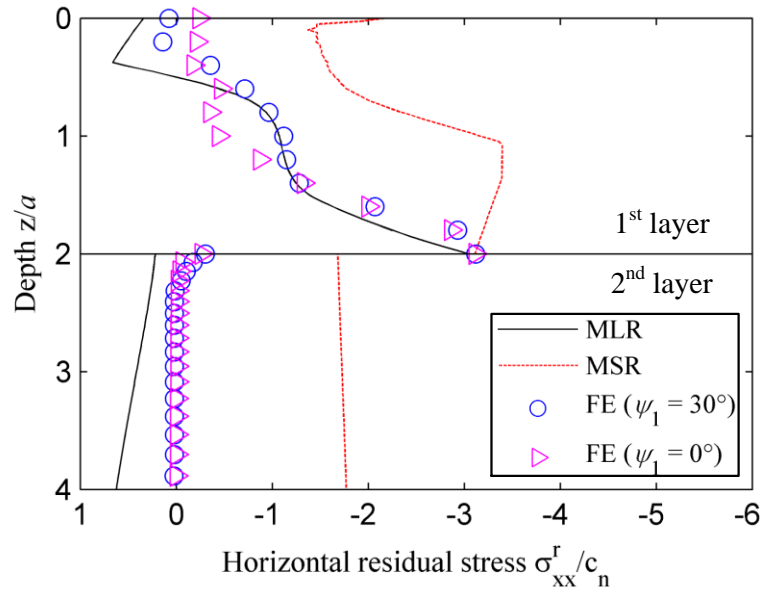


Figure 4-9 Influence of plastic flow rule on residual stress field in layered pavements when $\phi_1 = 30^\circ$, $\psi_1 = 0^\circ$, $c_1/c_2 = 1$, $E_1/E_2 = 3$, $p_0 = 6.7c_2$

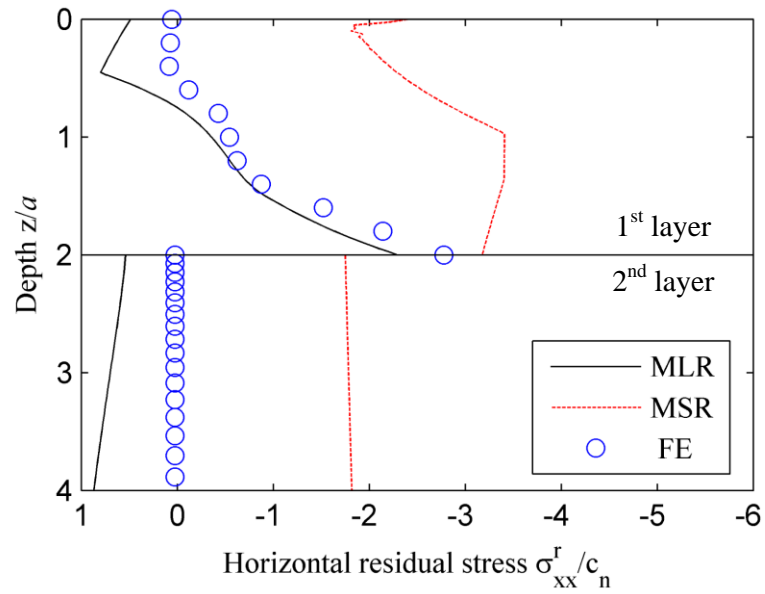


Figure 4-10 Comparison between FE calculated residual stress field and critical residual stress fields for a layered pavement when $\phi_1 = 30^\circ$, $\psi_1 = 0^\circ$, $\phi_2 = \psi_2 = 0^\circ$, $c_1/c_2 = 1$, $E_1/E_2 = 3$, $p_0 = 5.5c_2$

4.3 Static shakedown analysis

4.3.1 Introduction

The classical shakedown theorems follow the principle of maximum plastic work. Therefore, shakedown solutions using classical shakedown theorems were based on the assumption of an associated flow rule. However, as explained in the previous section, ignoring non-associated plastic flow may overestimate the real shakedown limits of pavements thus lead to an unsafe pavement design. The numerical approach developed in the previous section has been devoted to overcome this issue. Despite much effort, very limited results have been reported on this aspect due to computation cost. A direct method to address this issue would be more appealing to practitioners. For this purpose, the lower bound shakedown solutions of Yu and Wang (2013b) are further developed in this section to obtain approximate shakedown limits for pavements assuming non-associated plastic flow.

4.3.2 Static shakedown approach for pavements with materials following non-associated plastic flow

In consideration of non-associated plastic flow, the dilation angle ψ ($0 \leq \psi < \phi$) should be used. Davis (1968), Drescher and Detournay (1993) and Sloan (2013) suggested the use of reduced strength for the calculation of limit loads of structures in the case of materials obeying a non-associated flow rule. And this has been used for stability analysis of plane strain footing problems (e.g. Drescher and Detournay 1993; Michalowski 1997; Silvestri 2003; Shiau et al.

2003). In their analyses, the following modified friction angle ϕ^* and cohesion c^* were used:

$$\tan \phi^* = \eta \tan \phi, \quad (4.1)$$

$$c^* = \eta c, \quad (4.2)$$

$$\eta = \frac{\cos \psi \cos \phi}{1 - \sin \psi \sin \phi}. \quad (4.3)$$

By replacing ϕ and c in Equation (3.6) with ϕ^* and c^* and using the solution procedure in Yu and Wang (2012), shakedown limits of pavements with Mohr-Coulomb materials following a non-associated flow rule (defined by ϕ, ψ, c) can be obtained by solving the following mathematical formulation:

$$\begin{aligned} & \max \lambda, \\ & \text{s.t.} \begin{cases} f(\sigma_{xx}^r(\lambda \sigma^e), \lambda \sigma^e) \leq 0, \\ \sigma_{xx}^r(\lambda \sigma^e) = \min_{z=j} \left(-M_i^* + \sqrt{-N_i^*} \right) \text{ or } \sigma_{xx}^r(\lambda \sigma^e) = \max_{z=j} \left(-M_i^* - \sqrt{-N_i^*} \right) \end{cases} \end{aligned} \quad (4.4)$$

with

$$M^* = \lambda \sigma_{xx}^e - \lambda \sigma_{zz}^e + 2\eta^2 \tan \phi (c - \lambda \sigma_{zz}^e \tan \phi),$$

$$N^* = 4(1 + \eta^2 \tan^2 \phi) [(\lambda \sigma_{xz}^e)^2 - \eta^2 (c - \lambda \sigma_{zz}^e \tan \phi)^2].$$

A FORTRAN program was developed to solve this optimisation problem for single-layered pavement under single-wheel pressure; meanwhile a MATLAB program was developed for single-layered or multi-layered pavements subjected to a single-wheel pressure or a dual-wheel pressure. By substituting the load-induced elastic stress fields into these programs, lower bound shakedown limits for pavements with materials following associated or non-associated flow rules

can be obtained. Since FE calculated elastic stress fields are used in the MATLAB program, the shakedown limits obtained are not as accurate as those from the FORTRAN program where analytical elastic stress fields were utilised. However, differences between them are slight if a very fine mesh is applied to the FE model. Take the homogeneous case with $\phi = 30^\circ, \psi = 30^\circ$ as an example, FORTRAN gives a shakedown limit of $10.82c$, while MATLAB gives a lower value of $10.76c$; the difference is only 0.55% .

4.3.3 Solutions of single-layered pavements

For the problem studied here, where a homogeneous half-space is subjected to a moving 2D Hertz load, the elastic stress solutions under a static 2D Hertz pressure can be expressed in an analytical form (Johnson 1985):

$$\sigma_{xx}^e = -\frac{2P}{\pi a^2} \left\{ m \left(1 + \frac{z^2 + n^2}{m^2 + n^2} \right) - 2z \right\}, \quad (4.5)$$

$$\sigma_{zz}^e = -\frac{2P}{\pi a^2} m \left(1 - \frac{z^2 + n^2}{m^2 + n^2} \right), \quad (4.6)$$

$$\sigma_{xz}^e = \frac{2P}{\pi a^2} n \frac{m^2 - z^2}{m^2 + n^2}, \quad (4.7)$$

where

$$m^2 = \frac{1}{2} \left\{ \sqrt{(a^2 - x^2 + z^2)^2 + 4x^2 z^2} + (a^2 - x^2 + z^2) \right\},$$

$$n^2 = \frac{1}{2} \left\{ \sqrt{(a^2 - x^2 + z^2)^2 + 4x^2 z^2} - (a^2 - x^2 + z^2) \right\},$$

in which the signs of m and n are the same as the signs of z and x respectively.

By substituting the above elastic stress solutions into the optimisation FORTRAN program, the lower bound shakedown limit, denoted as a dimensionless parameter $k = \lambda_{sd} p_{0u}/c$, can be obtained. Figure 4-11 compares lower bound shakedown limits with those obtained from the numerical approach and upper bound solutions of Li (2010) for various values of friction angle and dilation angle. The results generally agree except the cases with high friction angle and low dilation angle. This kind of discrepancy is also noted by other researchers (e.g. Shiau 2001; Sloan 2013) when using the modified Mohr-Coulomb parameters (ϕ^* and c^*) to solve limit state problems. More dimensionless shakedown limit parameters are shown in Table 4-2 for the problem of a homogeneous Mohr-Coulomb half-space subjected to moving pressure.

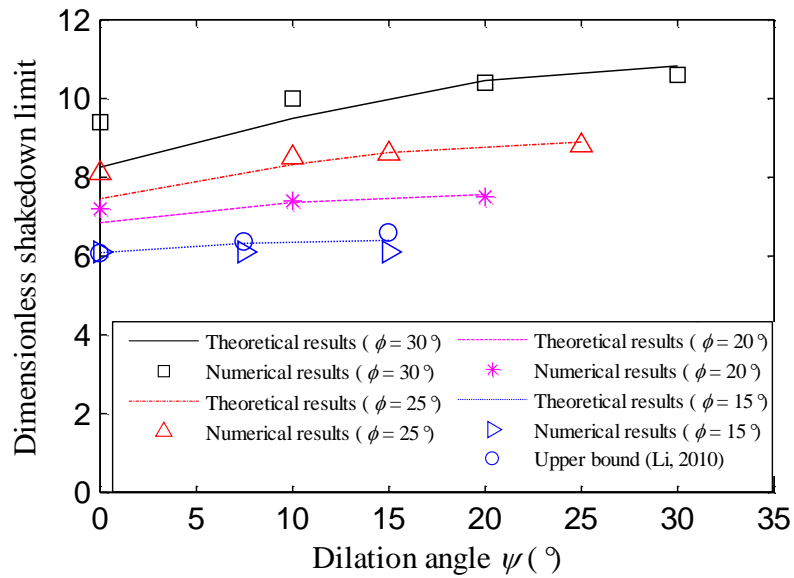


Figure 4-11 Comparison of theoretical and numerical shakedown limits for single layered pavements

If this fictitious material (Equation (4.1) to Equation (4.3)) is also applied to the upper bound shakedown solution of Collin and Cliffe (1987) where a tangential velocity jump $v \cos \phi$ is assumed, their solutions will give the same shakedown limits.

The problem of a homogeneous Mohr-Coulomb half-space subjected to a dual-wheel Hertz pressure with an axle distance (d) ranging from $3a$ to $8a$ is also considered (Figure 4-12). According to Table 4-3, the application of dual-wheel pressure results in lower shakedown limits than the single-wheel case due to the summation effects of the two neighbouring wheels. The most significant reduction (3.41% in the present study) occurs when the two wheels are very close to each other (e.g. $d = 3a$). With the increase of axle distance, the shakedown limits of dual-wheel cases gradually approach that of the single-wheel case. Even though the lower bound shakedown limits are not totally identical to the numerical shakedown limits, similar reductions are observed in the dual-wheel case (Table 4-3).

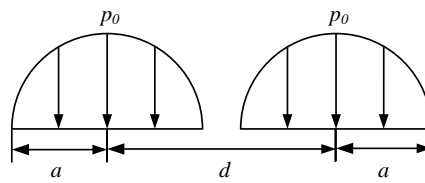


Figure 4-12 Dual-wheel Hertz pressure distribution

Table 4-2 Dimensionless lower bound shakedown limit parameters

ϕ	$\psi = 0^\circ$	$\psi = 5^\circ$	$\psi = 10^\circ$	$\psi = 15^\circ$	$\psi = 20^\circ$	$\psi = 25^\circ$	$\psi = 30^\circ$	$\psi = 35^\circ$	$\psi = 40^\circ$	$\psi = 45^\circ$
0°	4.00									
5°	4.64	4.66								
10°	5.34	5.42	5.45							
15°	6.08	6.25	6.36	6.40						
20°	6.84	7.14	7.36	7.51	7.56					
25°	7.58	8.03	8.43	8.73	8.93	9.00				
30°	8.25	8.90	9.50	10.02	10.44	10.72	10.82			
35°	8.81	9.67	10.51	11.31	12.03	12.62	13.02	13.16		
40°	9.21	10.28	11.39	12.51	13.60	14.60	15.44	16.02	16.24	
45°	9.41	10.68	12.05	13.51	15.03	16.53	17.96	19.19	20.06	20.39

Table 4-3 Shakedown limits for single layered-pavement under dual-wheel pressure

Case	d/a	$\phi = 25^\circ \psi = 25^\circ$		$\phi = 25^\circ \psi = 0^\circ$	
		Lower bound	Numerical	Lower bound	Numerical
1	3	8.64	8.5	7.29	7.9
2	4	8.76	8.8	7.39	8.1
3	8	8.89	8.8	7.49	8.1
4	Single wheel	8.9	8.8	7.49	8.1
Difference between case1 and 4		0.26	0.3	0.2	0.2

4.3.4 Solutions of multi-layered pavements

4.3.4.1 *Effect of stiffness ratio*

Comparisons between lower bound shakedown limits and numerical results for layered pavements (with $h_1 = 2a$) with various stiffness ratios and strength ratios also show good agreements in Figure 4-13 and Figure 4-14. Materials of the first layer have a friction angle $\phi = 30^\circ$ and a dilation angle $\psi = 30^\circ$ or 0° , while the second layer is a Tresca material (i.e. $\phi = \psi = 0^\circ$). It should be noted: (1) shakedown limit of the pavement structure is the minimum among the shakedown limits of all layers, and therefore the turning point indicates the change of failure mode from one layer failure to another layer failure; (2) the change of first layer dilation angle only changes static shakedown limits of the first layer. When the first layer dilation angle is decreased from 30° to 0° , lower bound shakedown limits of the first layer are slightly reduced. Since theoretical shakedown limits of the second layer do not change, the turning points for non-associated cases deviate from those of associated cases. Therefore, the shakedown limits for non-associated cases are smaller than those for associated cases when E_1/E_2 is relatively large ($E_1/E_2 \geq 0.8$ in Figure 4-13) or c_1/c_2 is relatively small ($c_1/c_2 \leq 2.8$ in Figure 4-14), but remain the same when E_1/E_2 is small enough or c_1/c_2 is large enough.

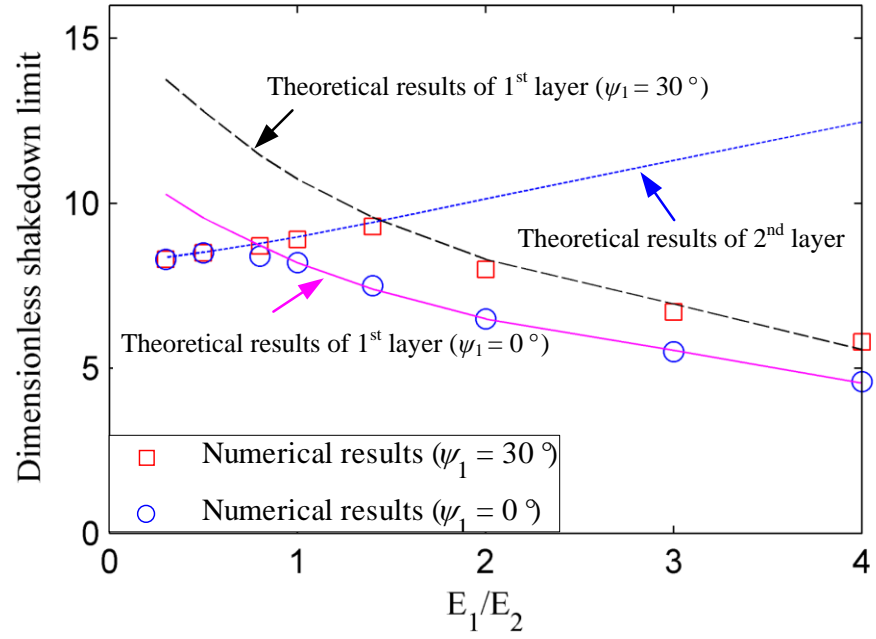


Figure 4-13 Comparison of theoretical and numerical shakedown limits with varying stiffness ratio when $\phi_1 = 30^\circ$, $\phi_2 = \psi_2 = 0^\circ$, $c_1/c_2 = 1$

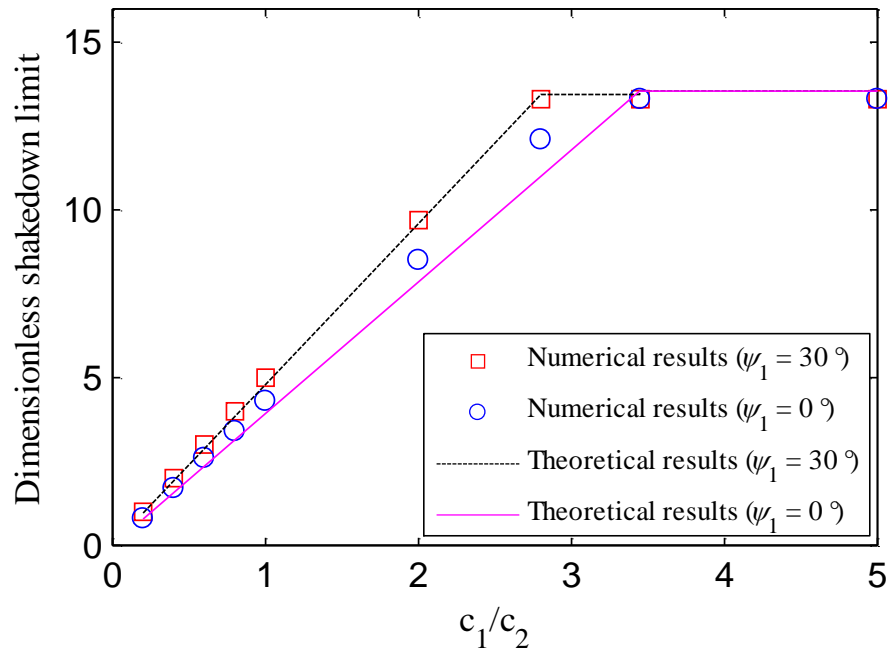


Figure 4-14 Comparison of theoretical and numerical shakedown limits in two-layered pavements with varying strength ratio when $\phi_1 = 30^\circ$, $\phi_2 = \psi_2 = 0^\circ$, $E_1/E_2 = 5$

4.3.4.2 Effect of first layer thickness

Two more models with $h_1 = 3a$ and $5a$ were established to evaluate the effect of layer configuration on shakedown limits. As shown in Figure 4-15, the numerical shakedown limits show good agreements with lower bound shakedown limits when an associated plastic flow rule is assumed. For non-associated cases, the numerical shakedown limits generally agree with the lower bound shakedown limits when $h_1/a = 2$ and $h_1/a = 3$. When the first layer is relatively thick (i.e. $h_1/a = 5$), the difference between theoretical and numerical solutions becomes more pronounced with decreasing dilation angle. Indeed, the increase of the first layer thickness leads to even more similar results to the homogeneous case.

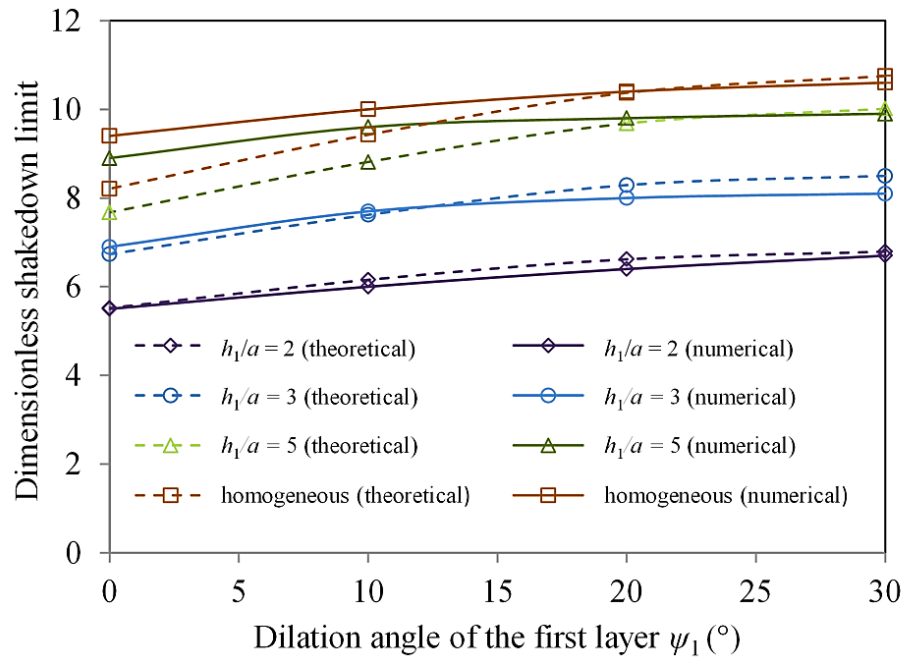


Figure 4-15 Comparison of theoretical and numerical shakedown limits in two-layered pavements with varying first layer thickness when $\phi_1 = 30^\circ$, $\phi_2 = \psi_2 =$

$$0^\circ; E_1/E_2 = 3, c_1/c_2 = 1$$

In summary, when the dilation angle is at or above one third of the friction angle or the friction angle is relatively low, the numerical and theoretical results generally agree well. Noticeable discrepancy occurs when the friction angle is high while the dilation angle is very small in a homogeneous or homogenous-like structure.

4.4 Summary

In this chapter, a numerical step-by-step approach and a static shakedown approach has been applied to obtain shakedown limits of single-layered and multi-layered pavements assuming either an associated or a non-associated flow rule. The static shakedown solutions agree with most shakedown limits obtained from the numerical approach and upper bound solutions of Li (2006). When the dilation angle is much smaller than the friction angle (e.g. $\phi = 30^\circ$ and $\psi = 0^\circ$), the static shakedown solutions may underestimate shakedown limits of pavements. Nevertheless, as a method to solve the pavement shakedown problem, the direct static shakedown solutions can be very useful for conservative pavement design. Solutions can be also found in Liu et al. (2016).

CHAPTER 5

EFFECT OF MATERIAL CROSS-ANISOTROPY AND HETEROGENEITY ON SHAKEDOWN SOLUTIONS OF PAVEMENTS

5.1 Introduction

Most of the existing shakedown analyses were carried out by assuming the pavement materials are isotropic and homogeneous. This chapter mainly concentrates upon the effects of material cross-anisotropy and heterogeneity on shakedown solutions.

3D shakedown solutions for an anisotropic half-space under moving loads were reported by Wang and Yu (2014), but the layered cases were not studied. In this chapter, the lower bound shakedown approach was extended to multi-layered pavement structures considering either 2D or 3D load distribution. Heterogeneous materials were also considered in the shakedown analysis by assuming depth-dependent stiffness of pavement materials.

5.2 Effect of material cross-anisotropy

5.2.1 Problem definition

5.2.1.1 2D problem

Both normal and shear forces (i.e. P and Q) are considered in this study (Figure 5-1). The distribution of surface traction (Equation (5.2)) is linked with the Hertz pressure (Equation (5.1)) by a frictional coefficient $\mu (= q/p)$.

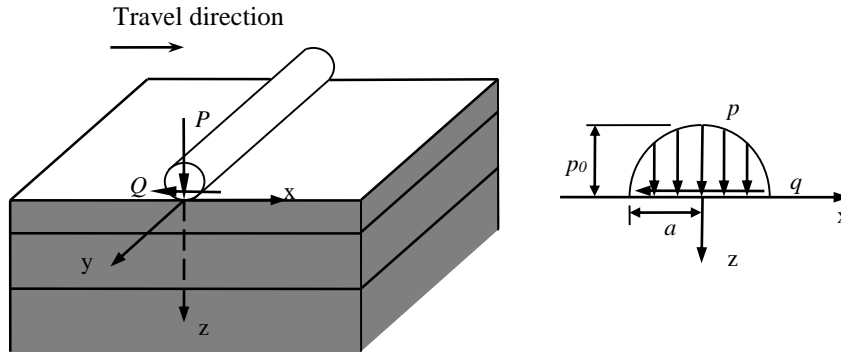


Figure 5-1 2D problem definition and Hertz normal and shear stress distribution (Wang 2011)

$$p = \frac{2P}{\pi a^2} (a^2 - x^2)^{1/2}, \quad (5.1)$$

$$q = \frac{2Q}{\pi a^2} (a^2 - x^2)^{1/2}. \quad (5.2)$$

In a cross-anisotropic plain strain problem, the relations between elastic stresses and elastic strains were given by Gazetas (1981) as below:

$$\begin{aligned}
\delta\sigma_{xx} &= D_{11}\delta\varepsilon_{xx} + D_{13}\delta\varepsilon_{zz}, \\
\delta\sigma_{yy} &= D_{12}\delta\varepsilon_{xx} + D_{13}\delta\varepsilon_{zz}, \\
\delta\sigma_{zz} &= D_{13}\delta\varepsilon_{xx} + D_{33}\delta\varepsilon_{zz}, \\
\delta\sigma_{xz} &= G_{vh}\delta\sigma_{xz}.
\end{aligned} \tag{5.3}$$

where

$$\begin{aligned}
D_{11} &= (E_h/e)(1 - \alpha^2\nu_{vh}^2), \quad D_{12} = (E_h/e)(\alpha^2\nu_{vh}^2 + \nu_{hh}), \quad D_{13} = (E_h/e)\nu_{vh}(1 + \nu_{hh}), \\
D_{33} &= (E_v/e)(1 - \nu_{hh}^2),
\end{aligned}$$

in which

$$\alpha^2 = E_h/E_v, \tag{5.4}$$

$$e = (1 + \nu_{hh})(1 - \nu_{hh} - 2\alpha^2\nu_{vh}^2). \tag{5.5}$$

In these equations, the stress increments $\delta\sigma_{ij}$ and strain increments $\delta\varepsilon_{ij}$ are referred to the Cartesian axes (i.e. i and j denote x axis, y axis or z axis), with the z axis being vertical; E_h is the Young's modulus in horizontal (H) direction; E_v is the Young's modulus in vertical (V) direction; G_{vh} is the shear modulus in VH plane; ν_{hh} is the Poisson's ratio regarding the effect of horizontal strain on complementary horizontal strain; ν_{vh} is the Poisson's ratio regarding the effect of vertical strain on horizontal strain. According to Graham and Houlsby (1983), ν_{hh} and ν_{vh} are related by a factor α ($\nu_{hh}/\nu_{vh} = \alpha$). The shear modulus G_{vh} is defined by Carrier (1964) as:

$$G_{vh} = \frac{D_{11}D_{33} - D_{13}^2}{D_{11} + 2D_{13} + D_{33}} \tag{5.6}$$

Equation 5.6 has been validated by a series of experimental results (Gazetas 1980). For isotropic materials, due to $E_h = E_v = E$ and $\nu_{hh} = \nu_{vh} = \nu$, Equation (5.6) can be written as $E(1+\nu)/2$; this relation has been widely adopted in isotropic materials. Equation (5.3) can be also simplified into a form which is suitable for isotropic materials.

In terms of strength anisotropy (i.e. plastic anisotropy), Arthur and Menzies (1972), Wong and Arthur (1985) and Kurukulasuriya et al. (1999) noted that the variation of cohesion with direction due to inherent anisotropy is more significant than the effect of anisotropy on the friction angle. Therefore, the present work lays emphasis on the effects of cohesive anisotropy only. According to Lo (1965), directional cohesion can be formulated as:

$$c_\theta = c_h + (c_v - c_h)\sin^2\theta \quad (5.7)$$

in which c_v and c_h are the cohesion on the vertical plane and the horizontal plane respectively, and c_θ indicates the value of cohesion on a plane inclined at an angle θ to the horizontal plane. Wang and Yu (2014) indicated that the consideration of plastic cross-anisotropy makes the conventional isotropic Mohr-Coulomb yield criterion a special case. A modified Mohr-Coulomb yield criterion has been proposed (Equation (5.8)).

$$f = (\sigma_{zz} - \sigma_{xx} - 2\sigma_{xz}\tan\phi)^2 + (c_v - c_h + 2\sigma_{xz} - \sigma_{xx}\tan\phi + \sigma_{zz}\tan\phi)^2 - (c_v + c_h - \sigma_{xx}\tan\phi - \sigma_{zz}\tan\phi)^2 \quad (5.8)$$

5.2.1.2 3D problems

A 3D cohesive-frictional system subjected to a point contact load (limited to a circle of radius a) is considered (Figure 5-2). The normal stress p and shear stress q are formulated as:

$$p = \frac{3P}{2\pi a^3} (a^2 - x^2 - y^2), \quad (5.9)$$

$$q = \frac{3Q}{2\pi a^3} (a^2 - x^2 - y^2), \quad (5.10)$$

where P is the total normal load applied in the z -direction and Q is the total shear load applied in the x -direction. This load distribution is known as the 3D Hertz load distribution. It has a maximum pressure $p_0 = 3P/2\pi a^2$ at the centre of the contact area ($x = y = z = 0$). The normal and shear loads are also assumed to be correlated by a frictional coefficient $\mu = q/p$.

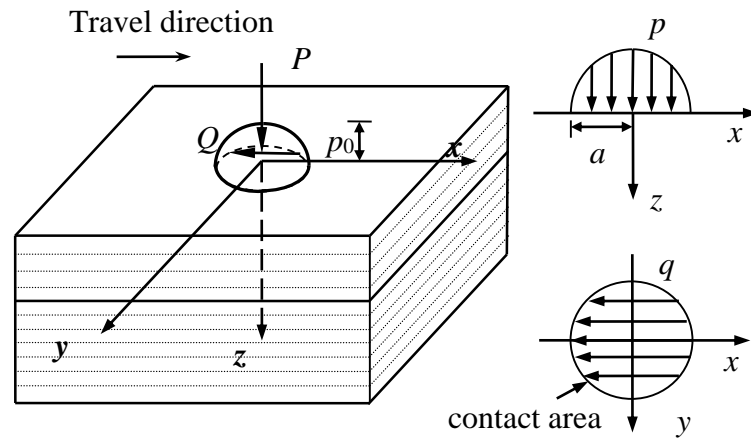


Figure 5-2 3D Problem definition (Wang 2011)

The stress and strain relations of a cross-anisotropic material in the elastic regime were formulated as:

$$\begin{bmatrix} \delta\epsilon_{xx} \\ \delta\epsilon_{yy} \\ \delta\epsilon_{zz} \\ \delta\epsilon_{xy} \\ \delta\epsilon_{xz} \\ \delta\epsilon_{yz} \end{bmatrix} = \begin{bmatrix} 1/E_h & -\nu_h/E_h & -\nu_{vh}/E_v & & & \\ -\nu_h/E_h & 1/E_h & -\nu_{vh}/E_v & & & \\ -\nu_{hv}/E_h & -\nu_{hv}/E_h & 1/E_v & & & \\ & & & 1/2G_h & & \\ & & & & 1/2G_{vh} & \\ & & & & & 1/2G_{vh} \end{bmatrix} \begin{bmatrix} \delta\sigma_{xx} \\ \delta\sigma_{yy} \\ \delta\sigma_{zz} \\ \delta\sigma_{xy} \\ \delta\sigma_{xz} \\ \delta\sigma_{yz} \end{bmatrix}, \quad (5.11)$$

where the stress increments $\delta\sigma_{ij}$ and strain increments $\delta\epsilon_{ij}$ are referred to the Cartesian axes (i.e. i and j denote x axis, y axis or z axis), with the z axis being vertical; E_h is the Young's modulus in horizontal (H) direction; E_v is the Young's modulus in vertical (V) direction; G_{hh} is the shear modulus in horizontal plane; G_{vh} is the shear modulus in VH plane; ν_{hh} is Poisson's ratio (effect of horizontal strain on complementary horizontal strain); ν_{vh} is Poisson's ratio (effect of vertical strain on horizontal strain); ν_{hv} is Poisson's ratio (effect of horizontal strain on vertical strain). There are another two correlations between these parameters:

$$G_{hh} = \frac{E_h}{2(1 + \nu_{hh})}, \quad (5.12)$$

$$\frac{\nu_{vh}}{\nu_{hh}} = \frac{E_v}{E_h}. \quad (5.13)$$

Graham and Houlsby (1983) proposed that the elastic anisotropy of natural clays can be described by three parameters: E^* and ν^* and α by giving the following definitions: $E_v = E^*$, $E_h = \alpha^2 E^*$, $\nu_{hh} = \nu^*$, $\nu_{vh} = \nu^*/\alpha$, $G_{vh} = \alpha E^*/(2+2\nu^*)$, $G_{hh} =$

$\alpha^2 E^*/(2+2\nu^*)$. In the plastic region, the anisotropic Mohr-Coulomb yield criterion given in Equation (5.8) was employed.

5.2.2 Review of the lower bound shakedown approach for a half-space with anisotropic materials (Wang and Yu 2014)

According to the lower bound shakedown theorem and the anisotropic Mohr-Coulomb yield criterion, the shakedown condition for the current problem can be expressed as:

$$\begin{aligned} f = & (\lambda\sigma_{zz}^e - \lambda\sigma_{xx}^e - \sigma_{xx}^r - 2\lambda\sigma_{xz}^e \tan \phi)^2 + \\ & (c_v - c_h + 2\lambda\sigma_{xz}^e - \lambda\sigma_{xx}^e \tan \phi - \sigma_{xx}^r \tan \phi + \lambda\sigma_{xx}^e \tan \phi)^2 \\ & - (c_v + c_h - \lambda\sigma_{xx}^e \tan \phi - \sigma_{xx}^r \tan \phi - \lambda\sigma_{zz}^e \tan \phi)^2 \leq 0, \end{aligned} \quad (5.14)$$

It also can be written as:

$$f = (\sigma_{xx}^r + M)^2 + N + P \leq 0, \quad (5.15)$$

where

$$\begin{aligned} M &= \lambda\sigma_{xx}^e - \lambda\sigma_{zz}^e + 2(c_h - \lambda\sigma_{zz}^e \tan \phi) \tan \phi, \\ N &= 4(\tan^2 \phi + 1)[(\lambda\sigma_{xz}^e)^2 - (c_h - \lambda\sigma_{zz}^e \tan \phi)^2], \\ P &= 4(c_v - c_h)[- \lambda\sigma_{xz}^e - (c_h - \lambda\sigma_{zz}^e \tan \phi)]. \end{aligned}$$

The self-equilibrium conditions require that the residual stress σ_{xx}^r at any depth $z = j$ is unique and must be bracketed by two critical residual stress fields:

$$\max_{z=j} (-M_i - \sqrt{-N_i - P_i}) \leq \sigma_{xx}^r \leq \min_{z=j} (-M_i + \sqrt{-N_i - P_i}), \quad (5.16)$$

where $\sigma_{xx}^r = \min_{z=j}(-M_i + \sqrt{-N_i - P_i})$ and $\sigma_{xx}^r = \max_{z=j}(-M_i - \sqrt{-N_i - P_i})$ are termed as minimum larger roots and maximum smaller roots respectively.

Therefore, the shakedown limit can be determined by searching the maximum load parameter λ subject to

Maximum λ

$$\begin{cases} f(\sigma_{xx}^r(\lambda\sigma^e, \lambda\sigma^e)) \leq 0, \\ \sigma_{xx}^r(\lambda\sigma^e) = \max_{z=j}(-M_i - \sqrt{-N_i - P_i}) \text{ or } \sigma_{xx}^r(\lambda\sigma^e) = \min_{z=j}(-M_i + \sqrt{-N_i - P_i}). \end{cases} \quad (5.18)$$

In the present research, the existing Matlab program for the searching of the maximum load parameter for isotropic cases (refer to subsection 4.3.2) was modified accordingly to solve Equation (5.18).

5.2.3 2D FE model

The 2D model given in Figure 3-3 was employed again. A UMAT user subroutine was developed using Equations (5.3) - (5.5) to describe the cross-anisotropic properties. It was then incorporated with ABAQUS to obtain elastic stress fields in anisotropic materials. The UMAT subroutine was verified by assuming material isotropy, i.e. $E_h = E_v$ and $\nu_{hh} = \nu_{vh}$. The obtained elastic stress fields were compared with those directly obtained by using the isotropic elastic model in ABAQUS. Completely identical stress and strain fields were observed. The modified MATLAB program was verified by giving identical value to c_h and c_v (i.e. plastic isotropy). The solutions agree well with the existing shakedown solutions given in Chapter 3. This MATLAB program is further verified in following subsection.

5.2.4 3D FE model

A two-layered 3D model was established as shown in Figure 5-3. Finer meshes are arranged in the loading area and its vicinities. The finite element model, the UMAT subroutine and the MATLAB program are verified by applying the same material parameters to those two layers and comparing the solutions with those of Wang and Yu (2014). All the results are summarised in Table 5-1. The maximum difference is only 3.2%.

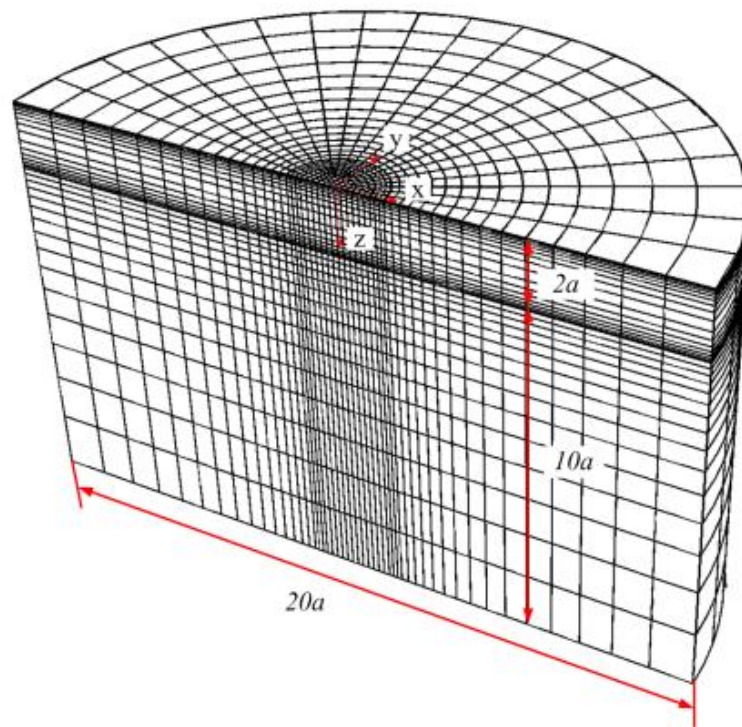


Figure 5-3 3D FE model

5.2.5 2D solutions and discussions of single-layered problems

In this subsection, the shakedown limits are normalised by the cohesion in the horizontal plane (i.e. c_h) for plastic anisotropic problems, or by c for plastic

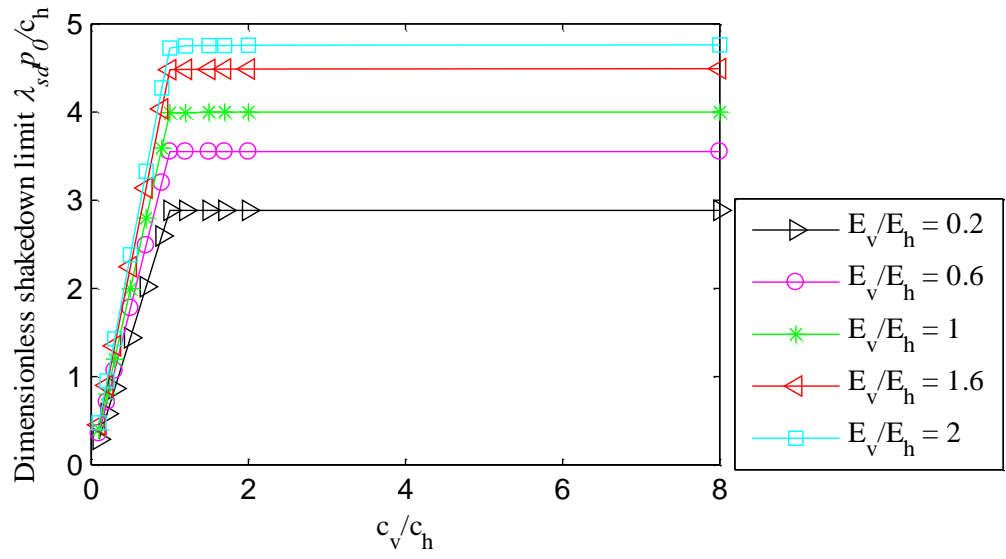
isotropic problems of which $c_h = c_v = c$. The normalised shakedown limits are termed as dimensionless shakedown limits.

Figure 5-4 reveals the effect of E_v/E_h and c_v/c_h on the shakedown limits of single-layered pavements. It can be seen that increasing E_v/E_h could result in larger shakedown limits. Also, the increase of c_v/c_h results in larger shakedown limits only when $c_v/c_h \leq 1$; the shakedown limits become unchanged whatever c_v/c_h increases to a value larger than 1. These agree with Wang and Yu (2014)'s findings where 3D problems were considered.

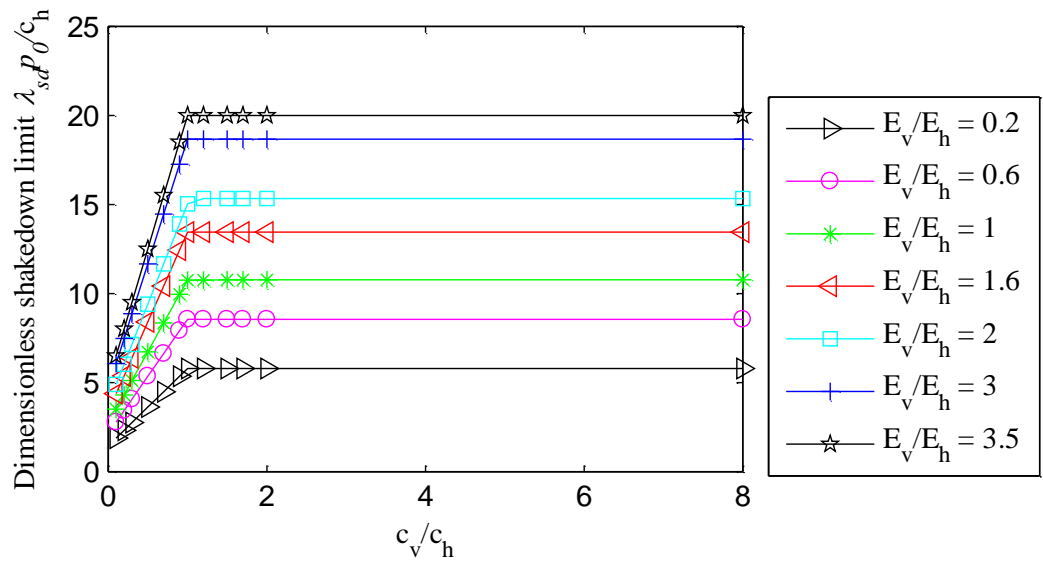
The effect of plastic anisotropy is further studied in consideration of surface shear stress. Figure 5-5 shows that when c_v is smaller than c_h , the maximum shakedown limit always occurs at $\mu = 0$; whereas, if c_v/c_h is larger than 1, there exists an optimum frictional coefficient corresponding to a maximum shakedown limit which is not equal to 0.

Table 5-1 Comparison of shakedown limits for cross-anisotropic Winnipeg Clay

case	E_h (MPa)	E_v/E_h	G_{vh}/G_h	ν_{vh}	ν_h	c_v/c_h	Shakedown limit		Difference
							Wang and Yu (2014)	this study	
1	9.35	0.53	0.73	0.17	0.23	1	$4.00c_h$	$3.87 c_h$	3.2%
2	6.96	0.41	0.64	0.08	0.12	1	$3.74 c_h$	$3.63 c_h$	2.9%
3	7.67	0.52	0.72	0.17	0.23	1	$3.97 c_h$	$3.85 c_h$	3.0%
4	5.76	0.76	0.87	0.23	0.27	1	$4.37 c_h$	$4.24 c_h$	3.0%
5	9.35	0.5	0.7	0.22	0.15	0.8	$3.14 c_h$	$3.05 c_h$	-2.8%
6	9.35	2	1.4	0.11	0.15	1.2	$5.31 c_h$	$5.18 c_h$	-2.4%
Isotropy							$4.68 c_h$	$4.61 c_h$	1.5%

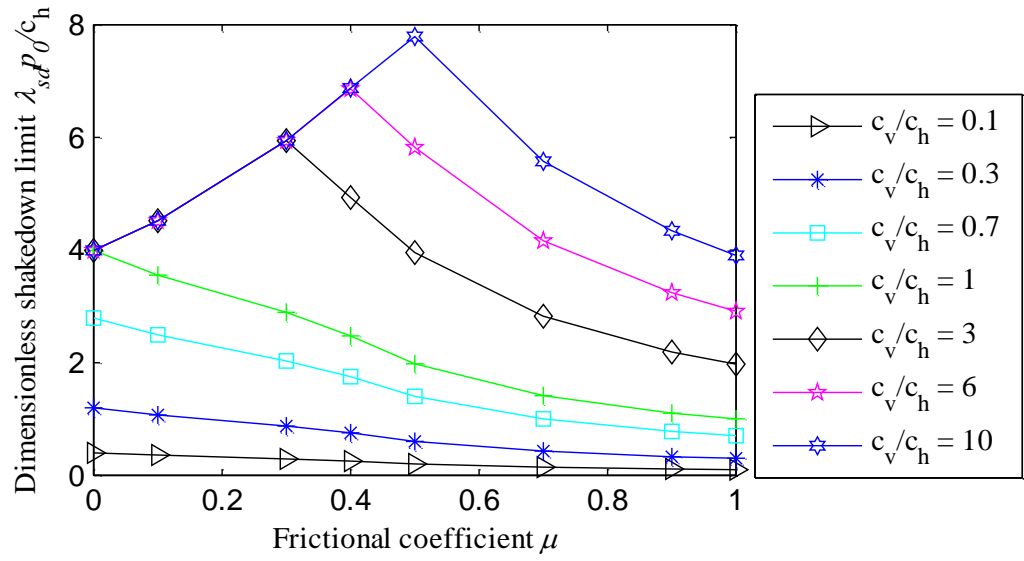


(a) $\phi = 0^\circ$, $\nu_{hh} = \nu_{vh} = 0.2$

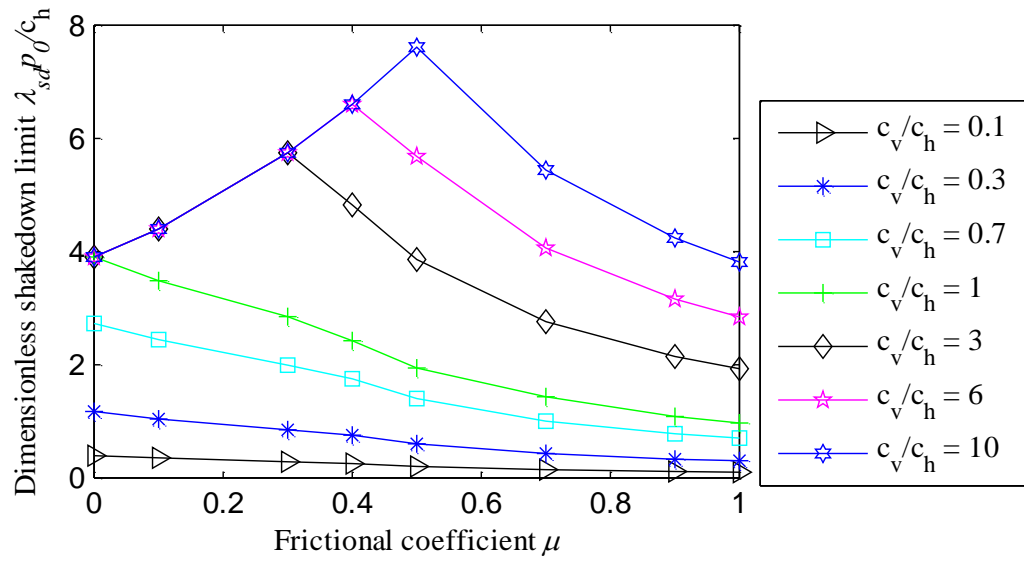


(b) $\phi = 30^\circ$, $\nu_{hh} = \nu_{vh} = 0.2$

Figure 5-4 Lower bound shakedown limits versus c_v / c_h for single-layered pavements with cross-anisotropic materials



(a) $E_v/E_h = 1$, $v_{hh} = v_{vh} = 0.2$

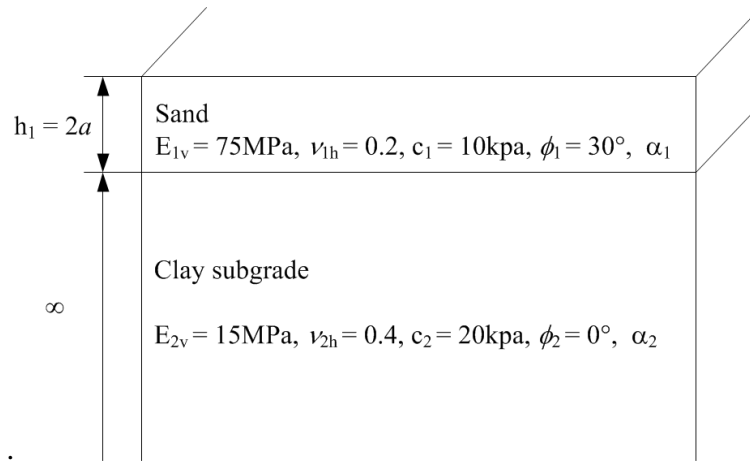


(b) $E_v/E_h = 0.8$, $v_{hh} = 0.2$, $v_{vh} = 0.35$

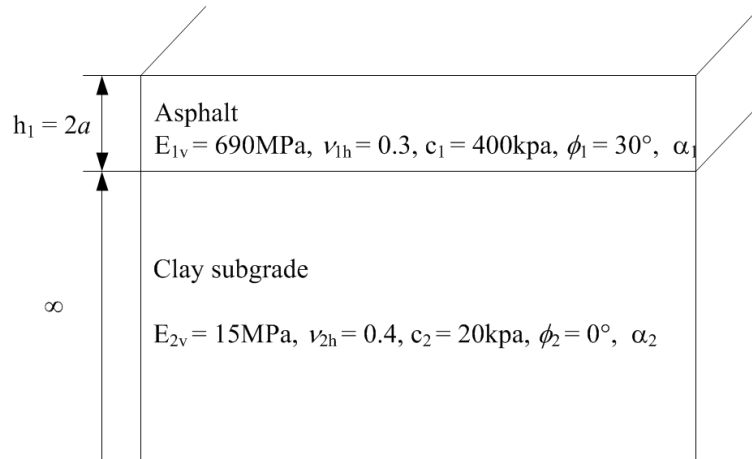
Figure 5-5 Influence of frictional coefficient on shakedown limits of single-layered pavements with cross-anisotropic materials when $\phi = 0^\circ$

5.2.6 Solutions and discussions of two-layered pavements

Two two-layered pavements are considered in the present study as shown in Figure 5-6: one is a sand-clay system and the other is asphalt-clay system. Shakedown limits are all normalised by the cohesion in the horizontal plane in the second layer, i.e. c_{h2} . α_n , which was introduced in the subsections 5.2.1.1 and 5.2.1.2 is termed as the factor of anisotropy in the n^{th} layer.



(a) Sand-Clay system



(b) Asphalt-Clay system

Figure 5-6 Design of a two-layered pavement system with cross-anisotropic materials

5.2.6.1 *Influence of elastic cross-anisotropy*

Table 5-2 summarises the material properties, the normalised shakedown limits of each layer k_n and the normalised shakedown limit of the layered system k for a 3D sand-clay system. Case 1 represents an isotropy assumption for both sand and clay layer; cases 2-7 assume a cross-anisotropic clay layer; and cases 8-13 consider the property of cross-anisotropy for both layers. Results show that the 3D lower bound shakedown limits k are all controlled by critical points in the first layer. Further studies show that all critical points are located beneath the surface. While sand is considered as an isotropic material, the rise of the anisotropic factor of clay leads to an obvious decrease of second layer shakedown limit and a slight increase of the first layer shakedown limit (Figure 5-7a). However, a reversed trend is observed for sand anisotropy (Figure 5-7b). The rate of change is relatively small in clay anisotropy cases.

Materials and shakedown limits of the second series of analyses for an asphalt-clay system is summarised in Table 5-3. Case 1 represents the isotropy case for both layers; cases 2-6 assume a cross-anisotropic clay layer only; and cases 7-12 also consider asphalt cross-anisotropy. Similar change trends are observed in Figure 5-7 and Figure 5-8. However, as two lines intersect at $E_v/E_h = 1.5$ in Figure 5-8, the shakedown limit of the layered system first rises and then drops with the increasing factor of clay anisotropy. In reality, because the factor of anisotropy α tends to be smaller than 1 for asphalt (i.e. $E_v/E_h = 1/\alpha^2 > 1$), but larger than 1 for clay (i.e. $E_v/E_h < 1$), the shakedown limit is more likely to be smaller than that under an isotropic assumption. That is to say, when the critical

point lies on the surface of the second layer, pavement design tends to be unsafe without a consideration of cross-anisotropy.

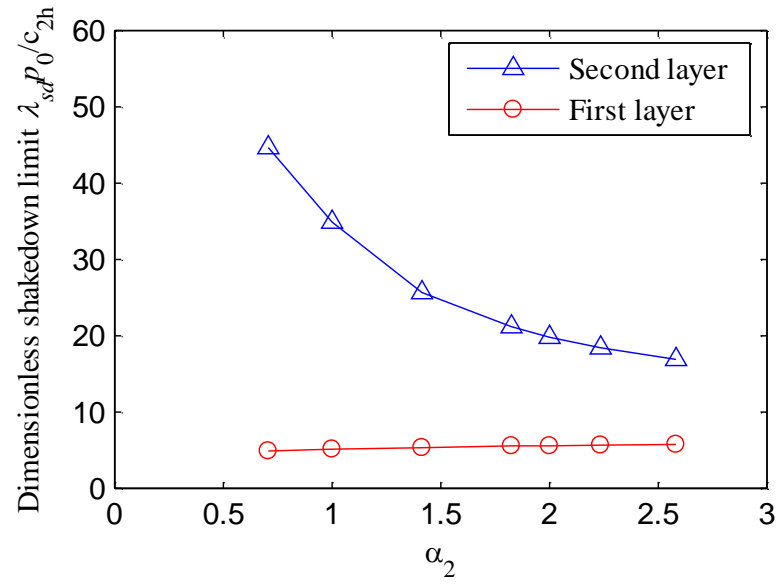
2D solutions are demonstrated in Figure 5-9 and Figure 5-10. It can be seen that even though the 2D shakedown solutions are much smaller than the 3D shakedown solutions, the same change tendencies are observed. Again, it is found that the optimum factors of anisotropy (α) for 2D and 3D problems are identical.

Table 5-2 Summary of material properties and shakedown limits in consideration of elastic cross-anisotropy in a 3D sand-clay system

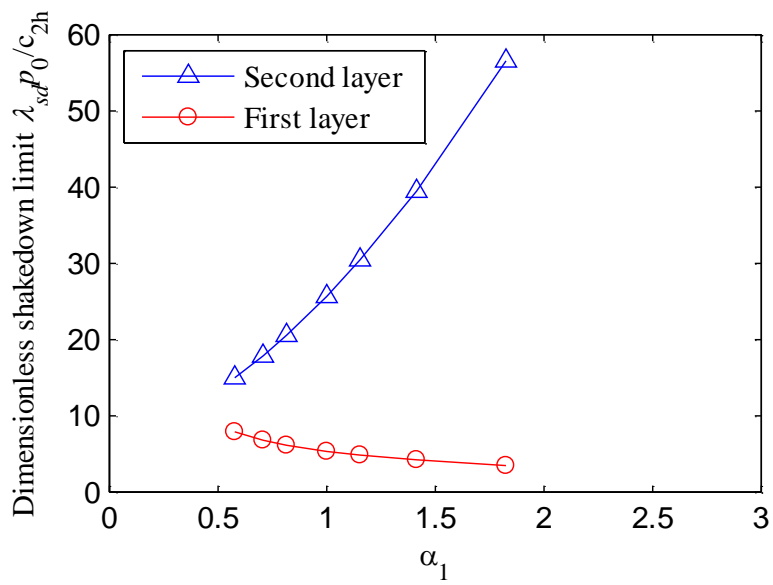
No.	1 st layer – sand					2 nd layer – clay					
	$E_{1v} = 75\text{MPa}, c_1 = 10\text{kPa}, \phi_1 = 30^\circ$					$E_{1v} = 15\text{MPa}, c_2 = 20\text{kPa}, \phi_2 = 0^\circ$					
	E_{1v}/E_{1h}	G_{1vh}/G_{1h}	ν_{1h}	ν_{1vh}	k_1	E_{2v}/E_{2h}	G_{2vh}/G_{2h}	ν_{2h}	ν_{2vh}	k_2	k
1	1	1	0.2	0.2	10.18	1	1	0.4	0.4	34.87	10.18
2	1	1	0.2	0.2	9.80	2	1.4	0.4	0.49	44.63	9.80
3	1	1	0.2	0.2	10.61	0.5	0.7	0.4	0.28	25.65	10.61
4	1	1	0.2	0.2	11.07	0.3	0.55	0.4	0.24	21.15	11.07
5	1	1	0.2	0.2	11.11	0.25	0.5	0.4	0.2	19.79	11.11
6	1	1	0.2	0.2	11.30	0.2	0.45	0.4	0.18	18.40	11.30
7	1	1	0.2	0.2	11.50	0.15	0.39	0.4	0.16	16.90	11.50
8	3	1.73	0.2	0.35	15.76	0.5	0.7	0.4	0.28	15.00	15.76
9	2	1.4	0.2	0.28	13.57	0.5	0.7	0.4	0.28	17.84	13.57
10	1.5	1.2	0.2	0.24	12.23	0.5	0.7	0.4	0.28	20.54	12.23
11	0.75	0.87	0.2	0.174	9.68	0.5	0.7	0.4	0.28	30.45	9.68
12	0.5	0.71	0.2	0.14	8.46	0.5	0.7	0.4	0.28	39.45	8.46
13	0.3	0.55	0.2	0.1	6.86	0.5	0.7	0.4	0.28	56.56	6.86

Table 5-3 Summary of material properties and shakedown limits in consideration of elastic cross-anisotropy in a 3D asphalt-clay system

No.	1 st layer - asphalt					2 nd layer – clay					k
	$E_{1v} = 690\text{MPa}, c_1 = 400\text{kPa}, \phi_1 = 30^\circ$					$E_{1v} = 15\text{MPa}, c_2 = 20\text{kPa}, \phi_2 = 0^\circ$					
	E_{1v}/E_{1h}	G_{1vh}/G_{1h}	ν_{1h}	ν_{1vh}	k_I	E_{2v}/E_{2h}	G_{2vh}/G_{2h}	ν_{2h}	ν_{2vh}	k_2	
1	1	1	0.3	0.3	148.20	1	1	0.4	0.4	178.55	148.20
2	1	1	0.3	0.3	145.40	2	1.4	0.4	0.49	263.55	145.40
3	1	1	0.3	0.3	151.60	0.5	0.7	0.4	0.28	115.35	115.35
4	1	1	0.3	0.3	155.40	0.3	0.55	0.4	0.24	83.35	83.35
5	1	1	0.3	0.3	156.00	0.25	0.5	0.4	0.2	75.30	75.30
6	1	1	0.3	0.3	157.60	0.2	0.45	0.4	0.18	65.97	65.97
7	3	1.73	0.3	0.49	157.20	0.5	0.7	0.4	0.28	47.91	47.91
8	2	1.4	0.3	0.42	153.60	0.5	0.7	0.4	0.28	65.50	65.50
9	1.5	1.2	0.3	0.36	152.20	0.5	0.7	0.4	0.28	82.43	82.43
10	0.75	0.87	0.3	0.261	151.00	0.5	0.7	0.4	0.28	147.55	147.55
11	0.5	0.71	0.3	0.213	144.80	0.5	0.7	0.4	0.28	211.50	144.80
12	0.3	0.55	0.3	0.165	130.80	0.5	0.7	0.4	0.28	337.00	130.80

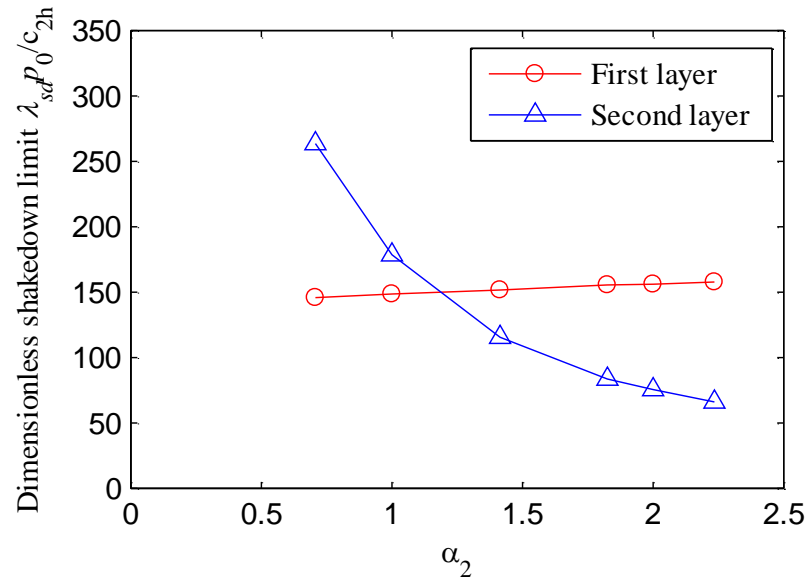


(a) Clay elastic anisotropy

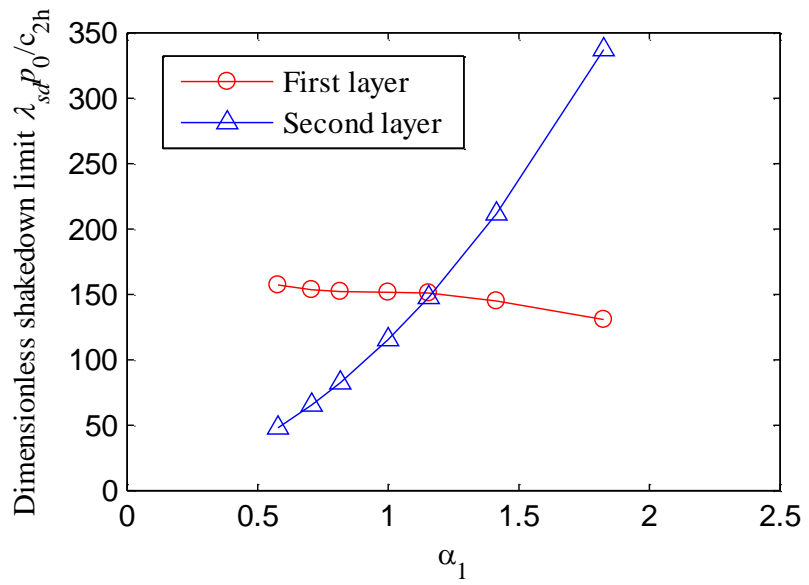


(b) Sand elastic anisotropy

Figure 5-7 Influences of the factor of anisotropy in a 3D sand-clay system

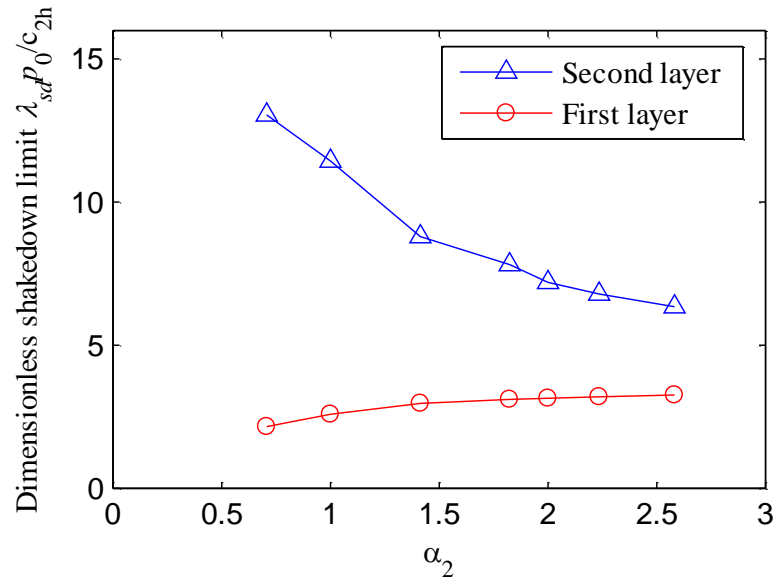


(a) Clay elastic anisotropy

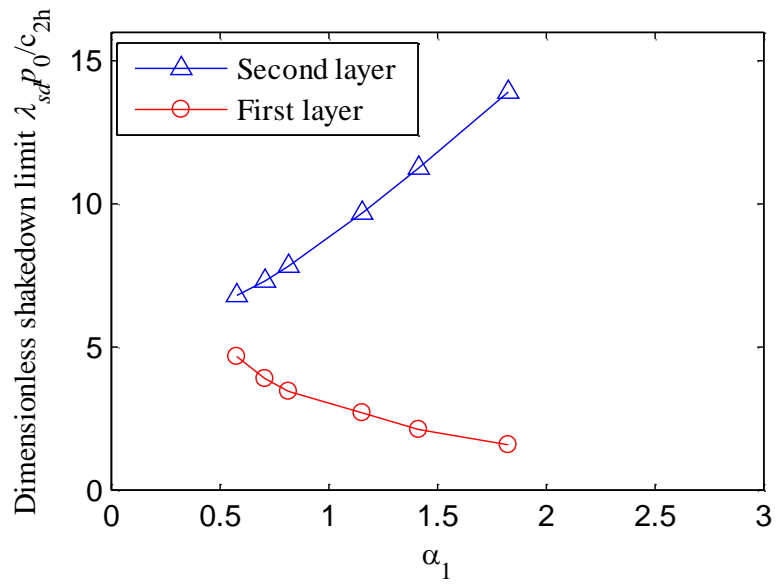


(b) Asphalt elastic anisotropy

Figure 5-8 Influences of the factor of anisotropy in a 3D asphalt-clay system

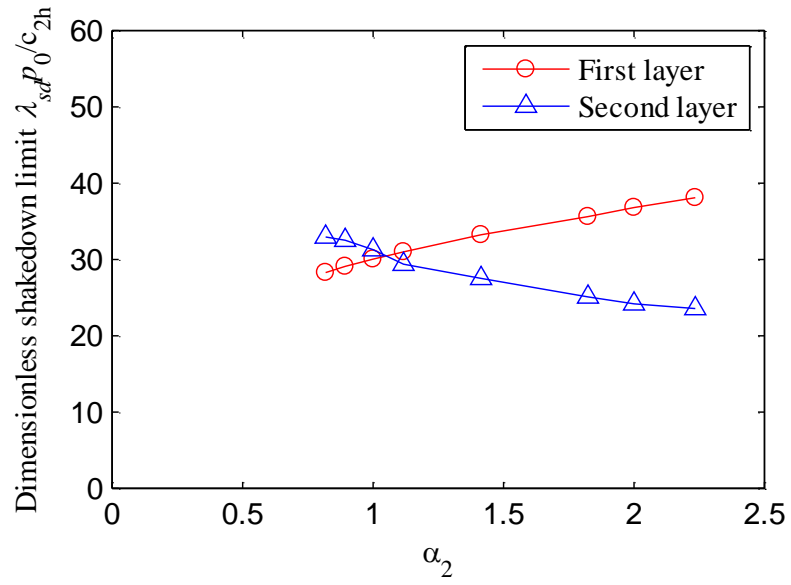


(a) Clay elastic anisotropy

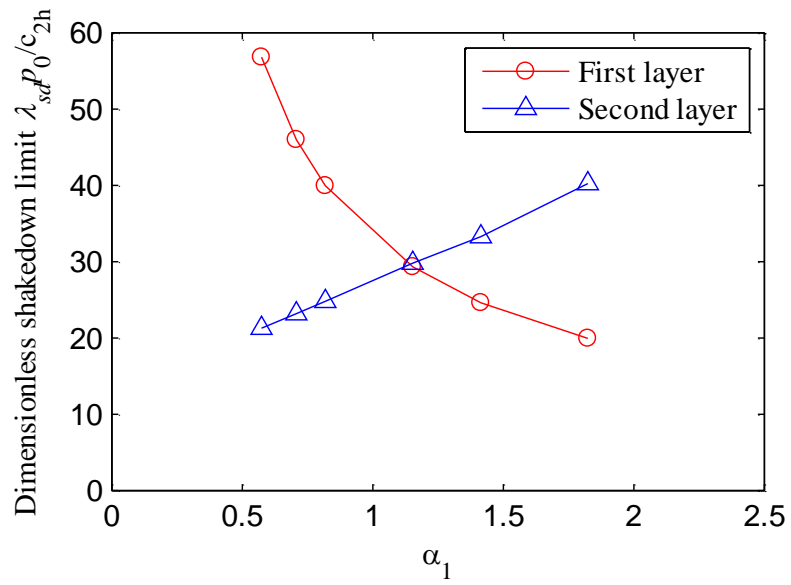


(b) Sand elastic anisotropy

Figure 5-9 Influence of the factor of anisotropy in a 2D sand-clay system



(a) Clay elastic anisotropy



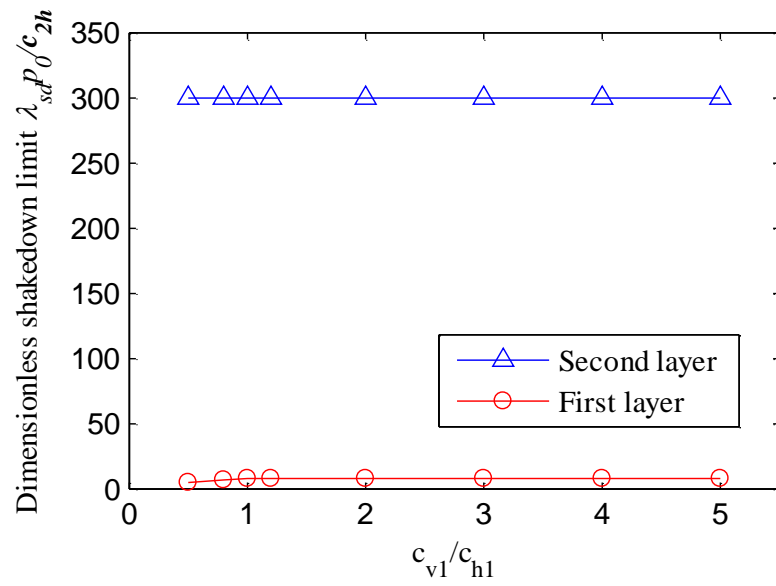
(b) Asphalt elastic anisotropy

Figure 5-10 Influence of the factor of anisotropy in a 2D asphalt-clay system

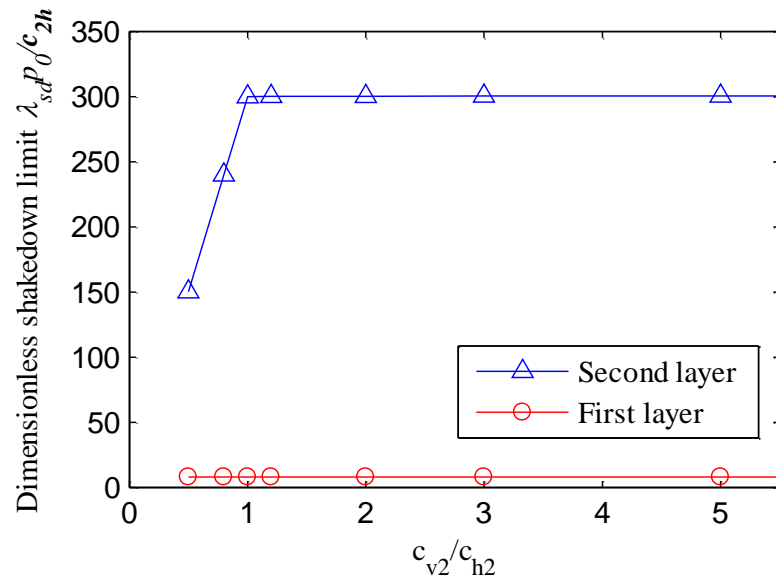
5.2.6.2 Influence of plastic cross-anisotropy

The above two material series are further studied by considering plastic anisotropy. Figures 5-11 and 5-12 also imply that the change of c_{vn}/c_{hn} in one layer does not cause any change in the shakedown limit of the other layer. In addition, it is found that the shakedown limits increase with rising c_{vn}/c_{hn} only when c_{vn} is smaller than c_{hn} ; this is same as the finding in the single-layered problem.

As mentioned before, for granular materials, the value of c_v/c_h corresponds to E_v/E_h , i.e. if $E_v/E_h > 1$ ($\alpha < 1$), then $c_v/c_h > 1$. It is assumed that the asphalt mixture meets the above relationship as well. By assuming that $c_{v1}/c_{h1} = 1.2$, $\alpha_1 = 0.58$, $c_{v2}/c_{h2} = 0.8$, $\alpha_2 = 1.43$, shakedown initially happens to the second layer and the shakedown limit of the asphalt-clay structure is $47.91c_{h2}$. However, consideration of isotropic materials in both layers gives a shakedown limit of $148.2c_2$ which is 67.7% higher than that of the anisotropic case. Therefore, the neglecting of material anisotropy may overestimate the capacities of road pavements. The 2D shakedown limits are also calculated for these cases, and a reduction of 38.3% is observed as compared with the isotropic cases. More 2D solutions are given in Table 5-4 and Table 5-5.

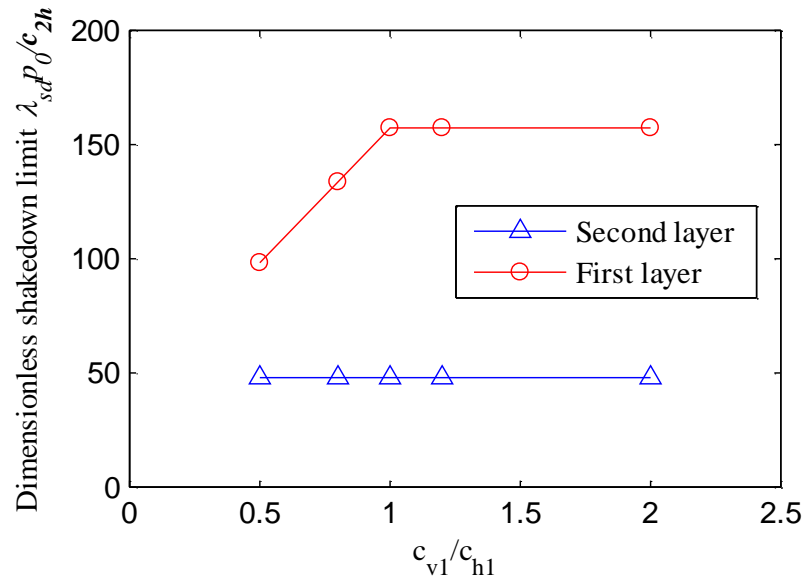


(a) Sand plastic anisotropy ($c_{v2}/c_{h2} = 1$, $\alpha_1 = 0.58$, $\alpha_2 = 1.43$)

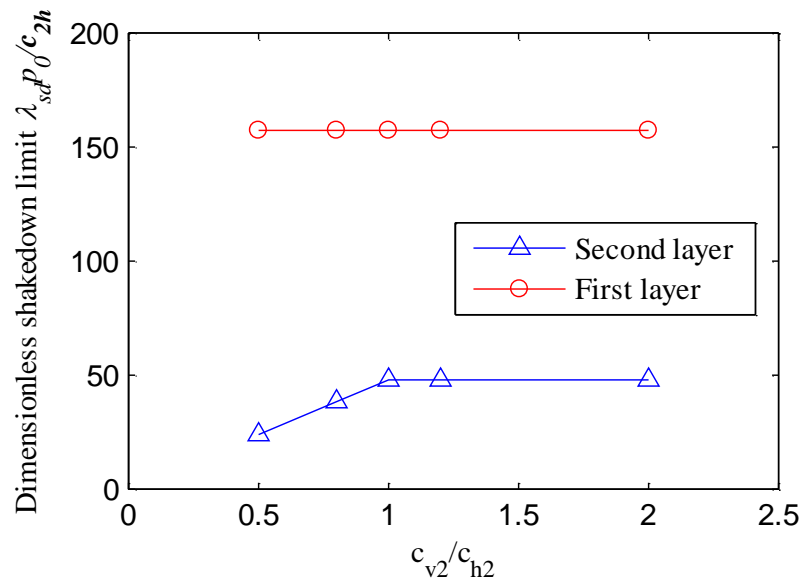


(b) Clay plastic anisotropy ($c_{v1}/c_{h1} = 1.2$, $\alpha_1 = 0.58$, $\alpha_2 = 1.43$)

Figure 5-11 Influences of plastic cross-anisotropy in a 3D sand-clay system



(a) Sand plastic anisotropy ($c_{v2}/c_{h2} = 1, \alpha_1 = 0.58, \alpha_2 = 1.43$)



(b) Clay plastic anisotropy ($c_{v1}/c_{h1}=1.2, \alpha_1 = 0.58, \alpha_2 = 1.43$)

Figure 5-12 Influences of plastic cross-anisotropy in a 3D asphalt-clay system

Table 5-4 Summary of material properties and shakedown limits in consideration of plastic cross-anisotropy in a 2D sand-clay system

No.	1 st layer - sand					2 st layer – clay					
	$E_{1v} = 75\text{MPa}, c_1 = 10\text{kPa}, \phi_1 = 30^\circ$					$E_{2v} = 15\text{MPa}, c_2 = 20\text{kPa}, \phi_2 = 0^\circ$					
	E_{1v}/E_{1h}	ν_{1h}	ν_{1vh}	c_{1v}/c_{1h}	k_1	E_{2v}/E_{2h}	ν_{2h}	ν_{2vh}	c_{2v}/c_{2h}	k_2	k
1	1	0.2	0.2	1	2.15	2	0.4	0.49	1	13.05	2.15
2	1	0.2	0.2	1	2.58	1	0.4	0.4	1	11.44	2.58
3	1	0.2	0.2	1	2.96	0.5	0.4	0.28	1	8.80	2.96
4	1	0.2	0.2	1	3.11	0.3	0.4	0.24	1	7.82	3.11
5	1	0.2	0.2	1	3.14	0.25	0.4	0.2	1	7.20	3.14
6	1	0.2	0.2	1	3.20	0.2	0.4	0.18	1	6.79	3.2
7	1	0.2	0.2	1	3.26	0.15	0.4	0.16	1	6.34	3.26
8	3	0.2	0.35	1	4.67	0.5	0.4	0.28	1	6.80	4.67
9	2	0.2	0.28	1	3.89	0.5	0.4	0.28	1	7.31	3.89
10	1.5	0.2	0.24	1	3.45	0.5	0.4	0.28	1	7.83	3.45
11	0.75	0.2	0.17	1	2.70	0.5	0.4	0.28	1	9.68	2.7
12	0.5	0.2	0.14	1	2.12	0.5	0.4	0.28	1	11.26	2.12
13	0.3	0.2	0.1	1	1.58	0.5	0.4	0.28	1	13.91	1.58
14	3	0.2	0.35	1.2	4.67	0.5	0.4	0.28	1	7.31	4.67
15	3	0.2	0.35	1.2	4.67	0.5	0.4	0.28	0.4	2.92	2.92
16	3	0.2	0.35	1.2	4.67	0.5	0.4	0.28	0.6	4.39	4.39
17	3	0.2	0.35	1.2	4.67	0.5	0.4	0.28	0.8	5.85	4.67

Table 5-5 Summary of material properties and shakedown limits in consideration of plastic cross-anisotropy in a 2D asphalt-clay system

No.	1 st layer - asphalt					2 st layer - clay					
	$E_{1v} = 690\text{MPa}, c_1 = 400\text{kPa}, \phi_1 = 30^\circ$					$E_{2v} = 15\text{MPa}, c_2 = 20\text{kPa}, \phi_2 = 0^\circ$					
	E_{1v}/E_{1h}	ν_{1h}	ν_{1vh}	c_{1v}/c_{1h}	k_1	E_{2v}/E_{2h}	ν_{2h}	ν_{2vh}	c_{2v}/c_{2h}	k_2	k
1	1	0.3	0.3	1	28.27	1.5	0.4	0.49	1	32.93	28.27
2	1	0.3	0.3	1	29.05	1.25	0.4	0.45	1	32.48	29.05
3	1	0.3	0.3	1	30.01	1	0.4	0.4	1	31.25	30.01
4	1	0.3	0.3	1	30.98	0.8	0.4	0.36	1	29.36	29.36
5	1	0.3	0.3	1	33.22	0.5	0.4	0.28	1	27.48	27.48
6	1	0.3	0.3	1	35.58	0.3	0.4	0.24	1	25.06	25.06
7	1	0.3	0.3	1	36.80	0.25	0.4	0.2	1	24.19	24.19
8	1	0.3	0.3	1	38.05	0.2	0.4	0.18	1	23.53	23.53
9	3	0.3	0.49	1	56.80	0.5	0.4	0.28	1	21.25	21.25
10	2	0.3	0.42	1	45.98	0.5	0.4	0.28	1	23.15	23.15
11	1.5	0.3	0.36	1	39.94	0.5	0.4	0.28	1	24.77	24.77
12	0.75	0.3	0.261	1	29.29	0.5	0.4	0.28	1	29.79	29.29
13	0.5	0.3	0.213	1	24.61	0.5	0.4	0.28	1	33.27	24.61
14	0.3	0.3	0.165	1	19.92	0.5	0.4	0.28	1	40.21	19.92
15	3	0.3	0.49	1.2	60.80	0.5	0.4	0.28	1	23.15	23.15
16	3	0.3	0.49	1.2	60.80	0.5	0.4	0.28	0.4	9.25	9.25
17	3	0.3	0.49	1.2	60.80	0.5	0.4	0.28	0.6	13.89	13.89
18	3	0.3	0.49	1.2	60.80	0.5	0.4	0.28	0.8	18.51	18.51

5.3 Effect of material heterogeneity

5.3.1 Problem definition

The effect of material heterogeneity on shakedown limits is studied for both single-layered and two-layered pavements. It is assumed that stiffness modulus on the surface of each layer is E_{0n} (n is layer number) and this modulus increases linearly with depth at a ratio of ρ_n/E_{0n} . This ratio is termed as ‘heterogeneous factor’ in the present study (Figure 5-13).

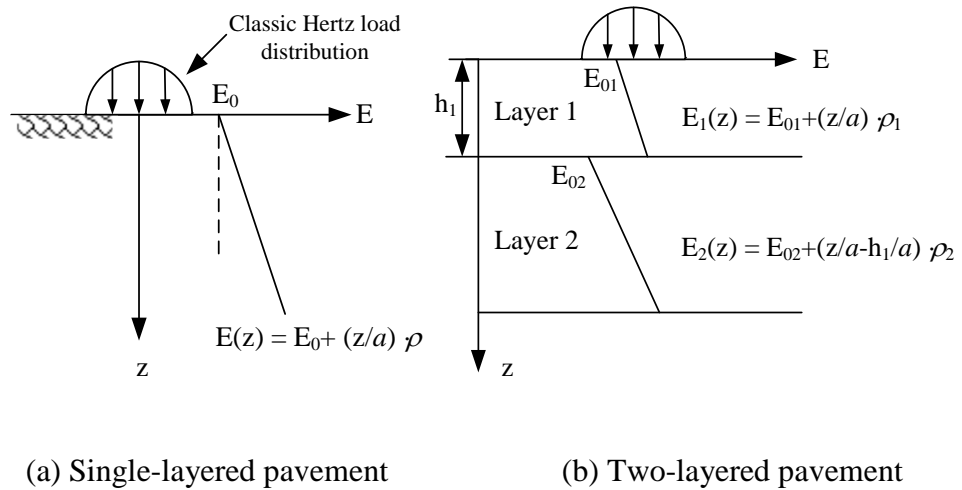
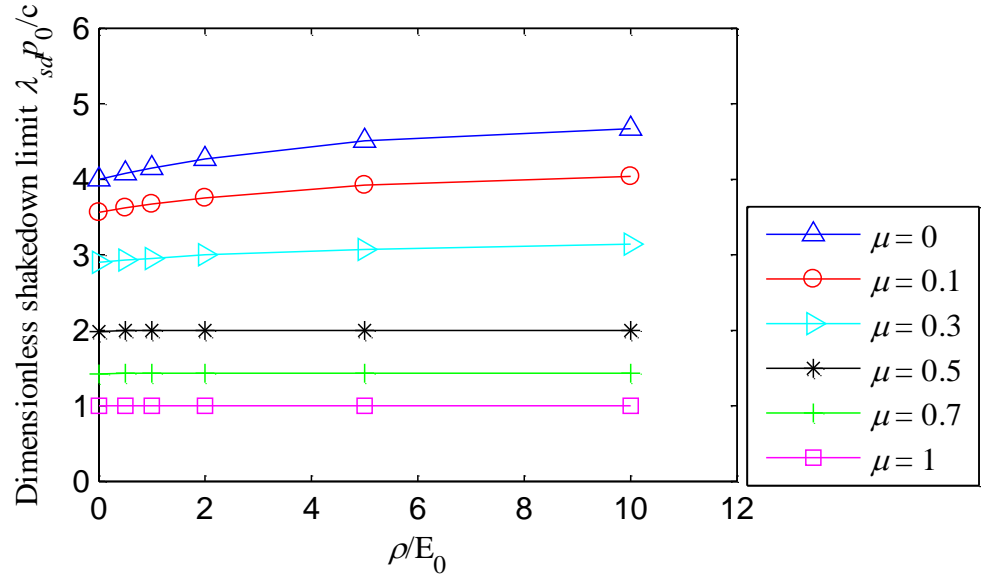


Figure 5-13 Definition of heterogeneity problems

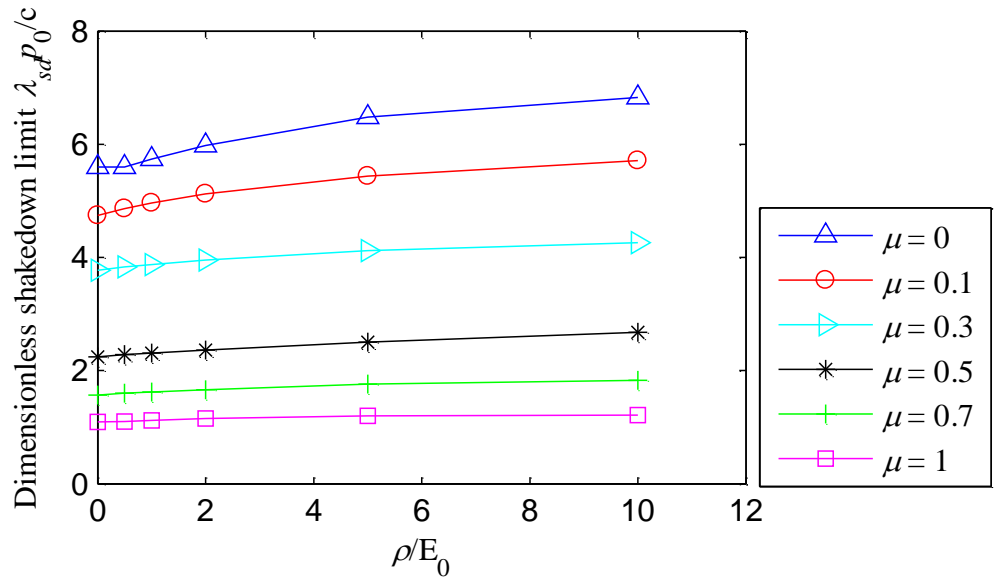
5.3.2 Solutions and discussions of single-layered pavements

Table 5-6 summarises the effect of material heterogeneity on the 2D shakedown solutions for single-layered problems. Figure 5-14 shows that more changes can be observed due to the increasing heterogeneous factor when the surface shear stress is relatively small. 3D analyses were also carried out by giving different values of friction angle as shown in Figure 5-15, which indicates that the

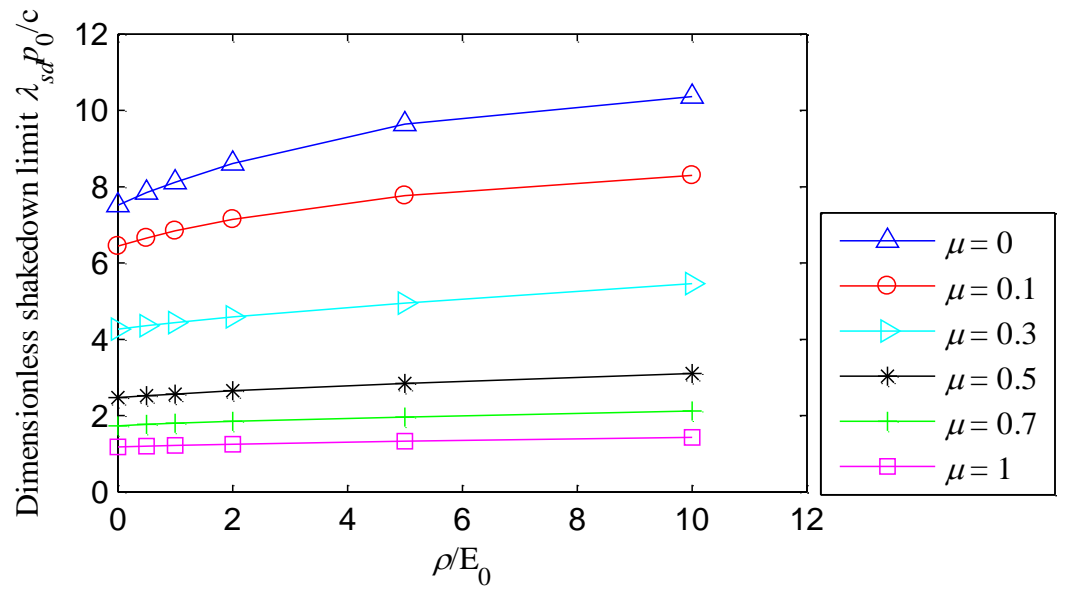
shakedown limit is sensitive to heterogeneous factor when the friction angle is high. This can also be observed in Figure 5-14 where 2D problems are considered.



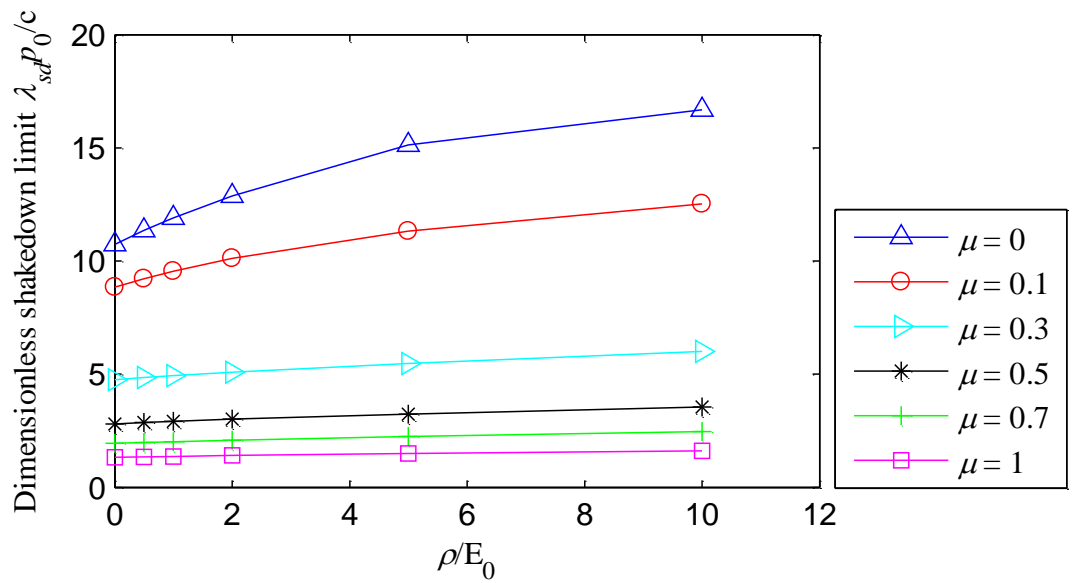
(a) $\phi = 0^\circ$



(b) $\phi = 10^\circ$



(c) $\phi = 20^\circ$



(d) $\phi = 30^\circ$

Figure 5-14 Influence of material heterogeneity on 2D shakedown limits of single-layered pavements

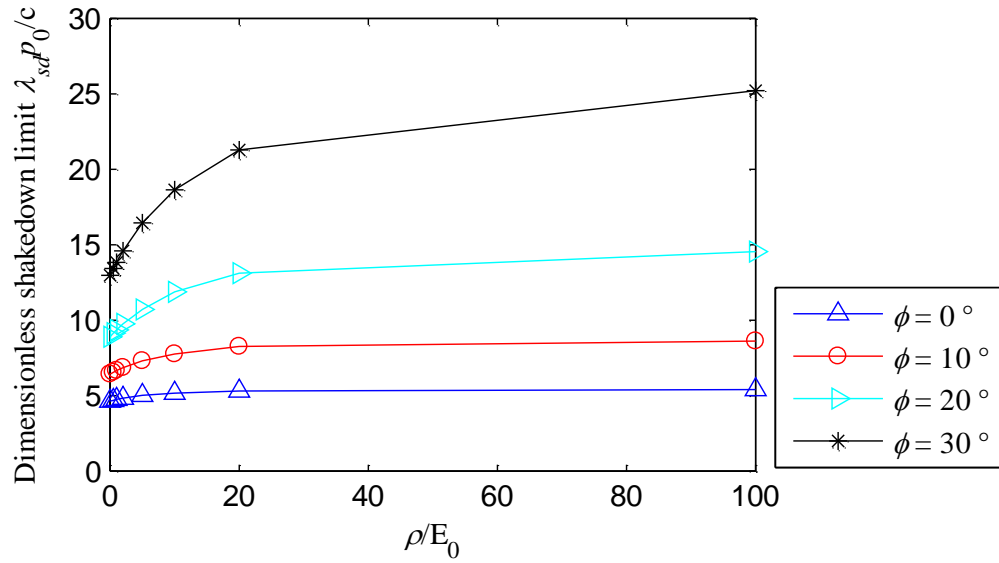


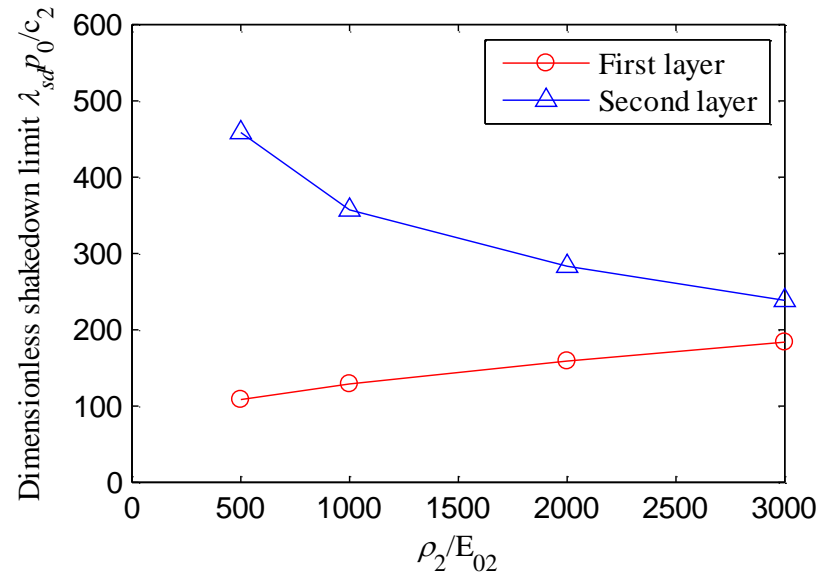
Figure 5-15 Influence of material heterogeneity on 3D shakedown limits of single-layered pavements when $\mu = 0$

5.3.3 Solutions of two-layered pavements

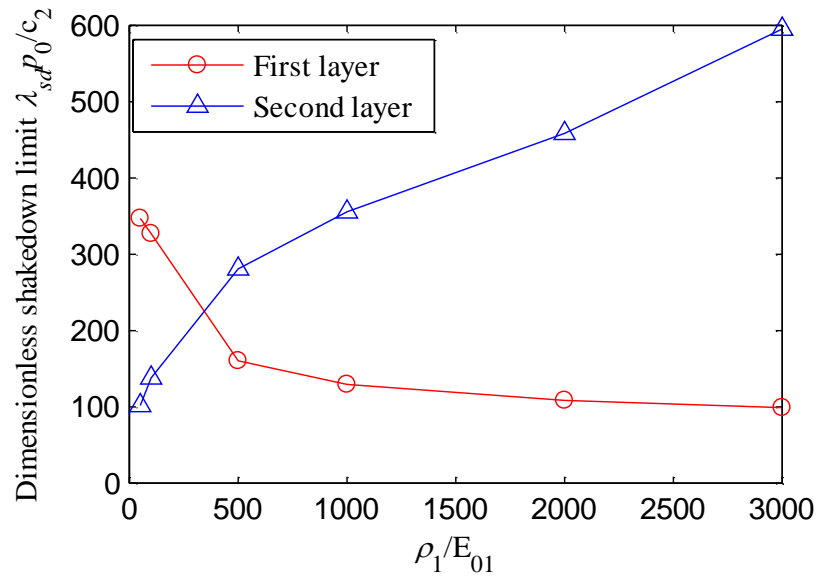
The effect of heterogeneous factor in a two-layered pavement structure is given in Figure 5-16 and Figure 5-17 for 3D and 2D problems respectively. All the results are given in Tables 5-7 and 5-8. These solutions demonstrate that increasing heterogeneous factor in one layer reduces the shakedown limit of that layer while it increases the shakedown limit of the other layer. Optimum heterogeneous factors are observed in Figure 5-16b and Figure 5-17; while the 2D and 3D solutions give different values. As the shakedown limit of the layered structure depends on the layer with lower shakedown limit, the consideration of material heterogeneity in a layered system may lead to either larger (refer to Table 5-7 when $c_1/c_2 = 20$) or smaller (refer to case 4-11 in Table 5-7 when $c_1/c_2 = 1$) shakedown limit when compared with the isotropic case.

Table 5-6 Effect of material heterogeneity on 2D shakedown limits of single-layered pavements

ρ/E_0	$\phi = 0^\circ$						$\phi = 10^\circ$					
	0	0.5	1	2	5	10	0	0.5	1	2	5	10
$\mu = 0$	4.00	4.08	4.15	4.27	4.51	4.67	5.60	5.60	5.74	5.98	6.48	6.83
$\mu = 0.1$	3.56	3.62	3.67	3.75	3.92	4.04	4.74	4.86	4.96	5.12	5.44	5.71
$\mu = 0.3$	2.9	2.93	2.95	3.00	3.07	3.14	3.77	3.83	3.87	3.95	4.12	4.26
$\mu = 0.5$	1.98	2.00	2.00	2.00	2.00	2.00	2.24	2.28	2.31	2.36	2.50	2.68
$\mu = 0.7$	1.42	1.43	1.43	1.43	1.43	1.43	1.57	1.60	1.62	1.66	1.76	1.83
$\mu = 1$	1.00	1.00	1.00	1.00	1.00	1.00	1.09	1.10	1.12	1.15	1.20	1.21
ρ/E_0	$\phi = 20^\circ$						$\phi = 30^\circ$					
	0	0.5	1	2	5	10	0	0.5	1	2	5	10
$\mu = 0$	7.51	7.84	8.12	8.61	9.64	10.36	10.73	11.35	11.9	12.87	15.13	16.68
$\mu = 0.1$	6.44	6.65	6.84	7.14	7.76	8.30	8.84	9.21	9.55	10.12	11.32	12.52
$\mu = 0.3$	4.27	4.36	4.44	4.59	4.95	5.46	4.76	4.86	4.94	5.09	5.48	6.01
$\mu = 0.5$	2.47	2.52	2.56	2.65	2.84	3.10	2.8	2.86	2.91	3.01	3.24	3.55
$\mu = 0.7$	1.73	1.77	1.80	1.85	1.96	2.12	1.94	1.98	2.02	2.08	2.24	2.46
$\mu = 1$	1.18	1.20	1.22	1.25	1.33	1.43	1.33	1.35	1.37	1.41	1.50	1.62

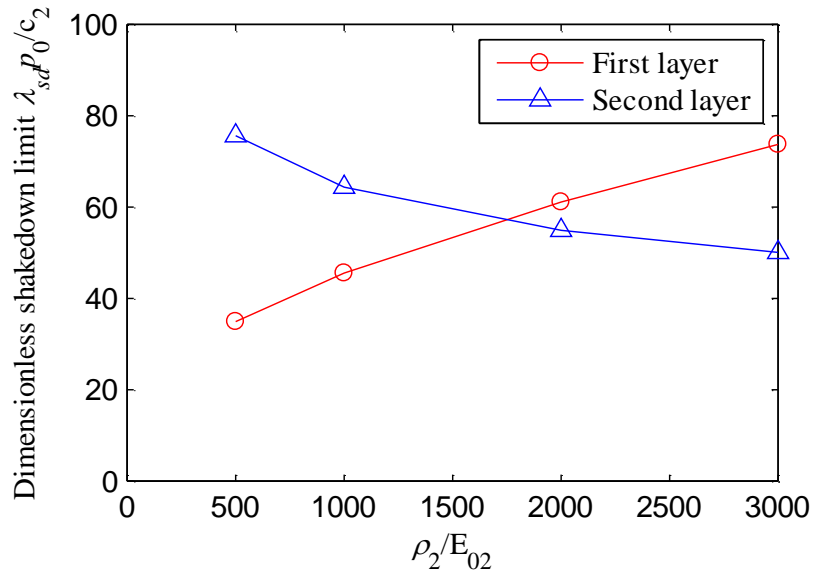


(a) $\rho_1/E_{01} = 2000$

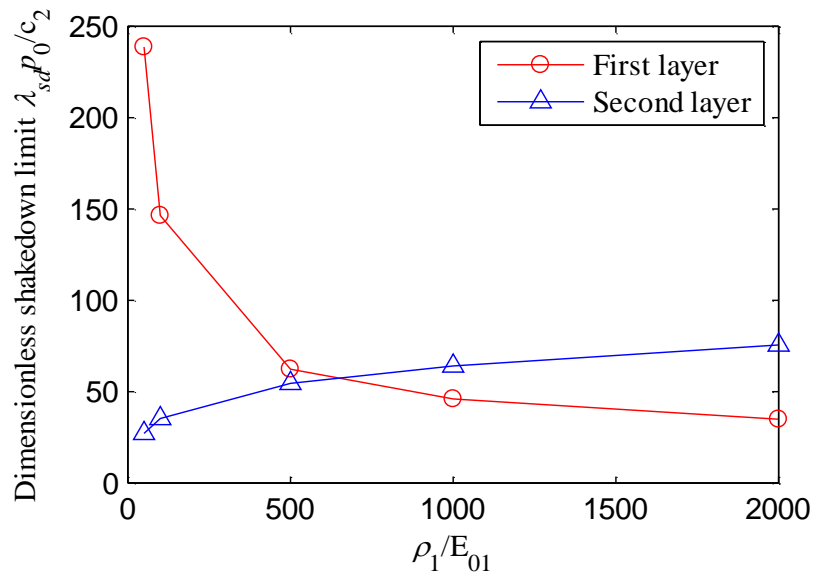


(b) $\rho_2/E_{02} = 500$

Figure 5-16 Influence of material heterogeneity in 3D two-layered pavements
when $E_1/E_2 = 1.39$, $c_1/c_2 = 20$, $\nu_1 = 0.4$, $\nu_2 = 0.3$, $\phi_1 = \phi_2 = 30^\circ$



(a) $\rho_1/E_{01} = 2000$



(b) $\rho_2/E_{02} = 500$

Figure 5-17 Influence of material heterogeneity in 2D two-layered pavements
when $E_1/E_2 = 1.39$, $c_1/c_2 = 20$, $\nu_1 = 0.4$, $\nu_2 = 0.3$, $\phi_1 = \phi_2 = 30^\circ$

Table 5-7 3D shakedown limits for two-layered pavements with heterogeneous materials when $E_1/E_2 = 1.39$, $\nu_1 = 0.4$, $\nu_2 = 0.3$, $\phi_1 = \phi_2 = 30^\circ$

Case	ρ_1/E_{01}	ρ_2/E_{02}	k_1		k_2	k_{sd}	
			$c_1/c_2 = 20$	$c_1/c_2 = 1$		$c_1/c_2 = 20$	$c_1/c_2 = 1$
1	0	0	250.65	12.53	57.46	57.46	12.53
2	50	500	347.01	17.35	101.53	101.53	17.35
3	100	500	326.70	16.34	137.69	137.69	16.34
4	500	500	160.03	8.00	280.81	160.03	8.00
5	1000	500	129.09	6.45	355.41	129.09	6.45
6	2000	500	108.19	5.41	458.32	108.19	5.41
7	3000	500	98.92	4.95	594.88	98.92	4.95
8	2000	500	108.19	5.41	458.32	108.19	5.41
9	2000	1000	128.61	6.43	356.73	128.61	6.43
10	2000	2000	158.92	7.95	283.18	158.92	7.95
11	2000	3000	183.42	9.17	238.38	183.42	9.17

Table 5-8 2D shakedown limit for two-layered pavements with heterogeneous materials when $E_1/E_2 = 1.39$, $c_1/c_2 = 20$, $\nu_1 = 0.4$, $\nu_2 = 0.3$, $\phi_1 = \phi_2 = 30^\circ$

Case	ρ_1/E_{01}	ρ_2/E_{02}	k_1	k_2	k_{sd}
1	0	0	182.40	18.93	18.93
2	50	500	238.52	27.18	27.18
3	100	500	146.36	35.21	35.21
4	500	500	62.18	54.53	54.53
5	1000	500	45.97	64.03	45.97
6	2000	500	34.86	75.57	34.86
7	3000	500	29.93	83.39	29.93
8	2000	1000	45.52	64.33	45.52
9	2000	2000	61.11	54.92	54.92
10	2000	3000	73.69	50.01	50.01

5.4 Summary

The existing lower bound shakedown approach has been extended to solve those problems considering non-standard properties of pavement materials. The effects of cross-anisotropy and heterogeneity on the shakedown limits of single-

layered or two-layered pavements were investigated. Results indicate that, for single-layered problems, the rise of stiffness and heterogeneous ratio will give larger shakedown limit. Increase of c_v/c_h can raise the shakedown limit only when it is not larger than 1. For two-layered systems, the increase of anisotropic or heterogeneous factor in one layer reduces the shakedown limit of that layer but increases the shakedown limit of the other layer. Solutions in this chapter can be found in Yu et al. (2015) and Liu et al. (2015).

CHAPTER 6

EXPERIMENTAL STUDY OF SHAKEDOWN CONCEPT FOR BITUMINOUS PAVEMENTS

6.1 Introduction

The shakedown concept involves the response of a structure to cyclic loads in a resilient manner without further permanent deformation. A series of shakedown concept validation tests were conducted by Juspi (2007) on both single-layered and multi-layered pavement foundations composed of different sorts of granular materials. However, shakedown in bituminous pavements was not examined. In the present study, a series of tests were carried out to investigate shakedown and non-shakedown phenomena of bituminous pavements using the Nottingham wheel tracking facility at the University of Nottingham. Monotonic triaxial tests and uniaxial compression tests were also performed on asphalt and granular materials to obtain the stiffness and strength parameters for theoretical shakedown analysis. Comparison between the experimental and theoretical shakedown limits is finally given.

6.2 The Materials

6.2.1 Asphalt mixture

Asphalt, a mixture of bitumen and graded granular materials, is one of the main materials used in bituminous pavements. Properties of the components (granular materials and bitumen) determine the behaviour of asphalt. Thom (2008) stated that permanent deformation of asphalt is closely related with the deformation of the aggregate skeleton due to particle contacts and inter-particle slipping. Generally speaking, when the temperature is low or moderate, plastic strain in the aggregate would be negligible as the binder takes much of the stress away from particle contacts and may self-heal after unloading; whereas, with the rise of temperature, the stress taken across particle contacts increases, encouraging inter-particle slipping and irreversible deformation. Consequently, strength of asphalt is determined by both the stability of the aggregate skeleton which is affected by particle shape, particle size, gradation, particle packing and properties of bituminous binder which are closely related to temperature and binder grade.

In the present study, an asphalt slab constituted of broadly graded aggregates and bitumen binder was used as the top layer of a two-layered specimen. According to the empirical database from the Nottingham Transportation Engineering Centre, two bounds, i.e. upper and lower grading limits (Figure 6-1), are generally used to adjudicate whether the aggregate is well graded. Figure 6-1 illustrates that the current gradation curve completely lies within these two bounds, i.e. the aggregate is well graded.

Bitumen (as the binder in an asphalt mixture) can be classified in different grades known as "penetration" or "pen" grades. The pen value is a manifestation of the depth to which a standard needle (100g) penetrates the surface of binder at a specified temperature (normally 25 °C). Penetration has a significant influence on workability and stiffness of asphalt. High penetration always gives soft material. In pavement engineering, 35-50pen bitumen is typically used as the binder in an asphalt wearing course. In the present test, 50pen bitumen was selected. The relatively soft bitumen can avoid rapid cracking at the bottom of the asphalt slab and minimise sliding between these two layers. The current asphalt mixture has 82.1% aggregate, 10.6% bitumen and 7.3% void by volume.

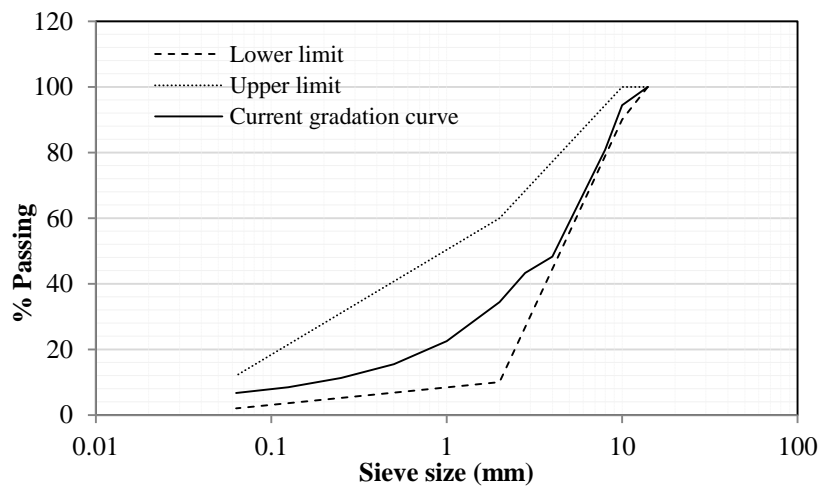


Figure 6-1 Current gradation relation of the aggregate in asphalt (refer to BS EN 12679-5 2009)

6.2.2 Granular material

Granite, an ideal paving material in pavement foundations, was selected for the base layer of the two-layered specimen. In pavement engineering, the maximum particle size is generally constrained by the thickness of the layer being

constructed; generally speaking, it should be less than 30% of the layer thickness. Since the scale of the specimen (Figure 6-27) employed in the present study is small, relatively fine granular materials were used to reduce possible discreteness and ensure a good contact between the asphalt layer and the granular layer. As shown in Figure 6-2, a well-graded crushed granite with a maximum particle size of 2.8 mm was selected. The material gradation is presented in Figure 6-3.



Figure 6-2 Photo of crushed granite (Taken by author 2015)

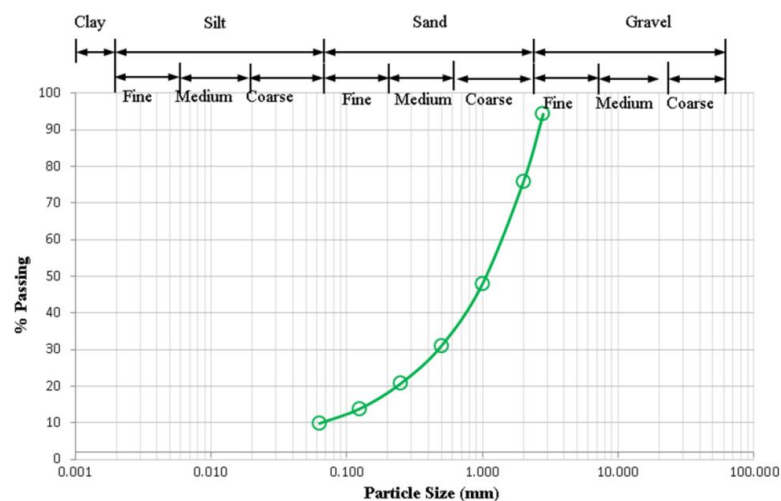


Figure 6-3 Particle size distribution of crushed granite sample

6.3 Determination of Material Characteristics

In this section, stiffness modulus and Mohr-Coulomb parameters of materials were obtained by monotonic triaxial tests and uniaxial compression tests. In addition, compaction related tests were carried out on the granular materials to determine the density index.

6.3.1 Compaction-related tests on crushed granite

Goetz (1989) indicated that the strength of granular materials is closely related to material density. A peak can be observed in axial load for densely compacted aggregates during shearing, while the force-deformation response for loose material does not exhibit such a peak (Figure 6-4). Additionally, loose materials undergo contraction all the time during shear, whereas the dense materials expand after some contraction at the beginning (Figure 6-5). The expansion behaviour is known as dilatancy. Density of crushed granite should lie between the maximum and minimum dry densities which can be measured by compaction-related tests.

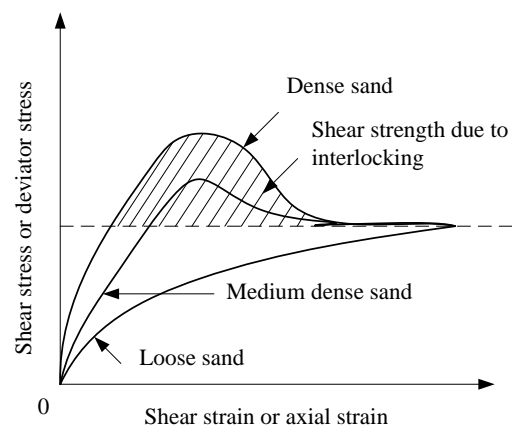


Figure 6-4 Stress and strain characteristics of sands (Goetz 1989)

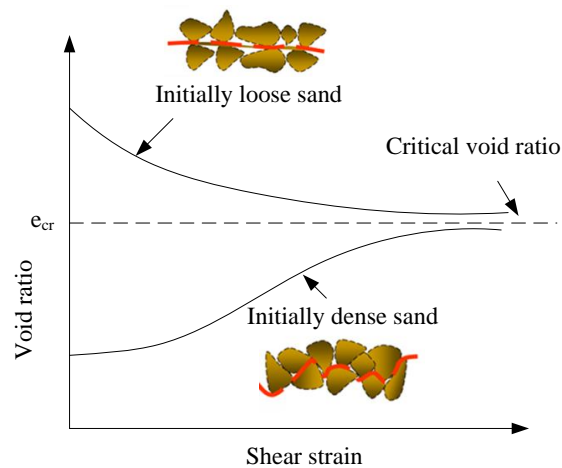


Figure 6-5 Performance of sand under contraction

6.3.1.1 *The maximum possible dry density*

Procedures for the determination of maximum possible density are given as below (BS 1377:4 1990).

(1) The crushed granite samples were poured into a bucket filled with warm water, accompanied by stirring thoroughly to remove the air bubbles. The samples were left submerged overnight.

(2) On the following day, the samples were compacted into a 1L CBR mould layer by layer with a 900W vibrating hammer under water until no more samples can be squeezed in. A straightedge was used to trim the soil surface.

(3) The granular materials were extracted from the mould into a small metal tray and left in an oven (105 °C) overnight to dry.

(4) The weight of the oven-dry sample was recorded on the next day.

BS 1377:4 (1990) requires the test to be conducted at least twice until the mass difference is less than 50g. In the present study, masses of two specimens were

measured to be 1938.6g and 1891.4g respectively with a difference of 47.2g (less than 50g). According to BS 1377:4 (1990), the maximum possible dry density can be calculated as

$$\rho_{d \max} = \frac{m_g}{V} = \frac{1938.6g}{1L} = 1938.6kg/m^3, \quad (6.1)$$

where m_g is the maximum dry mass.

Nevertheless, the actual maximum possible dry density may be larger than this value due to a certain amount of loss in the process of extracting and weighting.

6.3.1.2 *The minimum possible dry density*

Procedures for determining minimum possible density are shown below (BS 1377:4 1990):

- (1) 1000g granular samples were sealed into a 1 L glass measuring cylinder.
- (2) The cylinder was shaken up and down and inverted a few times to loosen the materials.
- (3) The volume readings were taken as fast as possible to avoid stacking caused by self-gravity of granular materials.
- (4) The test was repeated ten times.

According to Equation 6.2, the minimum possible dry density ($\rho_{d \min}$) was determined according to the maximum volume reading (V_m), i.e. 680ml in the present study.

$$\rho_{d \min} = \frac{m}{V_m} = \frac{1kg}{0.68dm^3} = 1470.0kg/m^3. \quad (6.2)$$

6.3.1.3 Derivation of density index

A number of cylindrical crushed granite specimens, 25mm in radius and 100mm in height, were prepared for monotonic triaxial tests. It was found that the average mass of the specimens after heavy compaction was around 370g, corresponding to an average density (ρ_d) of 1885kg/m³. Therefore, the density index can be calculated as:

$$I_D = \left(\frac{\rho_d - \rho_{d\min}}{\rho_{d\max} - \rho_{d\min}} \right) \left(\frac{\rho_{d\max}}{\rho_d} \right) = \left(\frac{1885 - 1470}{1936 - 1470} \right) \left(\frac{1936}{1885} \right) = 0.91. \quad (6.3)$$

According to Table 6-1 (Djellali et al. 2012), the specimens for triaxial tests were compacted very densely.

Table 6-1 Compaction degree and density index (Djellali et al. 2012)

Density index	≥ 0.85	0.85-0.65	0.65-0.35	0.35-0.15	< 0.15
Compaction degree	Very dense	Dense	Medium	Loose	Very loose

6.3.2 Monotonic triaxial tests on crushed granite

In practice, granular layers of bituminous pavements are designed in such a way that water can easily flow way. Therefore, crushed granite used in this research was tested under consolidated drained triaxial condition to obtain its Mohr-Coulomb parameters. In addition, only dry and fully-saturated specimens were tested in the present study, even though granular materials in real pavements can be partially-saturated.

6.3.2.1 *The equipment*

Triaxial conditions are achieved by placing cylindrical specimens into a cell that can be pressurised. The general set-up of the triaxial cell is illustrated in Figure 6-6. The function of each component is specified in Rees (2013).

The stresses applied to a soil specimen during a triaxial compression test are illustrated in Figure 6-7. The confining stress σ_c (i.e. minor principal stress σ_3) is applied by pressurising the cell fluid surrounding the specimen. The deviator stress q is generated by applying an axial strain ε_a on the top of the soil specimen. The sum of the deviator stress q and the confining stress σ_c is the major principal stress σ_1 . A stress state with $\sigma_1 = \sigma_3$ is termed as an isotropic state; otherwise it will be considered as an anisotropic state.

The GDS triaxial automated system is shown in Figure 6-8. The cell pressure controller is capable of adjusting the magnitudes of the confining stress. The back pressure controller aims to adjust the back pressure to a specific value. The data acquisition unit converts analogue readings from the load cell and axial displacement transducers to digital data which are then recorded by the GDS Lab control and acquisition software.

The triaxial cell used in the present study was a Bishop and Wesley (1975) cell which possesses a safe working pressure of 1700kPa. Upward and downward movements of the base pedestal correspond to loading and unloading to the specimen respectively. The load ram can provide an axial load of up to 2MPa. A 2kN internal submersible load cell is installed with an accuracy of 2N. The axial

deformation (strain) is measured using an external linear variable differential transformer (LVDT) mounted on the load ram with a range of 40mm and an accuracy of 0.1mm (Figure 6-6 and Figure 6-8). In addition, a pore pressure transducer with a measuring range of 2000kPa and an accuracy of 2kPa is connected to the pore pressure valve on the base pedestal of the chamber.

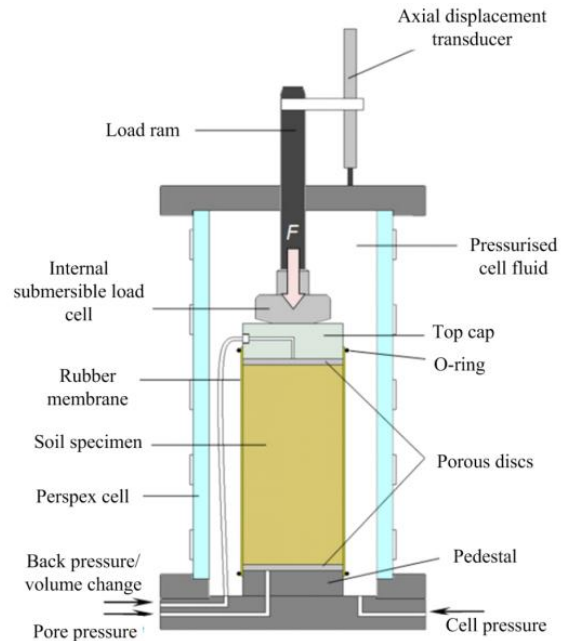


Figure 6-6 General set-up of a soil specimen inside a triaxial cell (Rees 2013)

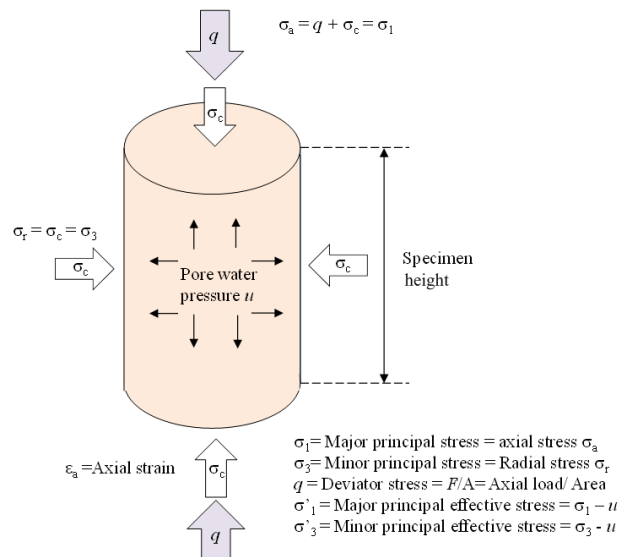
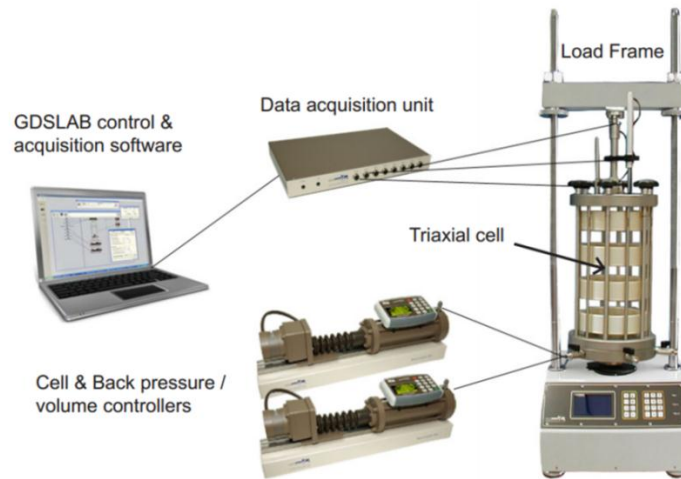


Figure 6-7 Illustration of triaxial test



(a) GDS Triaxial automated system (Rees 2013)



(b) photography of the GDS triaxial system at the University of Nottingham (Taken by author 2015)

Figure 6-8 GDS triaxial automated system

6.3.2.2 Specimen preparation

The granular specimen was formed and sealed with the assistance of a split-part mould (50mm in diameter and 100mm in height) and an inner rubber membrane. Two porous discs were placed at the top and the bottom of the specimen (Figure

6-9). The soil samples were divided into five portions and heavily compacted into the mould layer by layer.

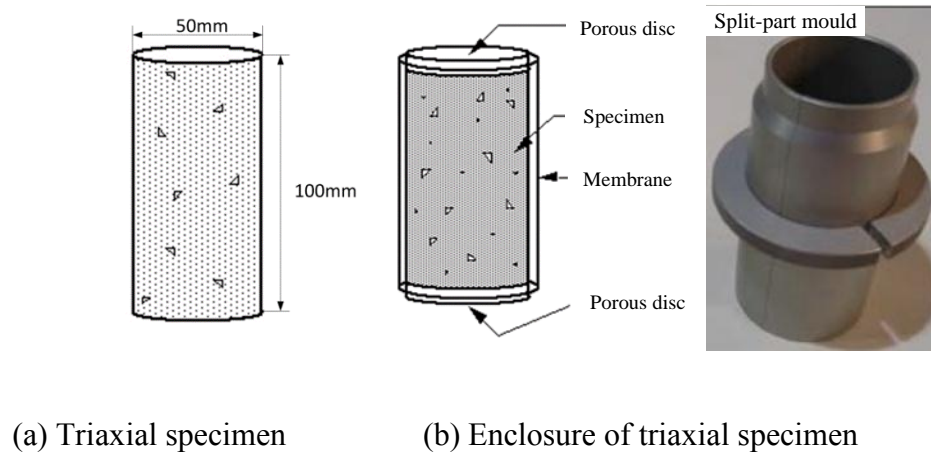


Figure 6-9 Preparation of the specimen

6.3.2.3 Determination of the loading rate

Loading rates of triaxial tests have a salient effect on the strength properties of granular materials. For drained tests, sufficient time must be provided for water movement so that the excess pore pressure can be totally dissipated. Seed and Lundgren (1954) performed drained and undrained tests on densely compacted saturated sands under 200 kPa confining pressure with strain rates up to 1000%/s. They revealed that transient drained tests act more like an undrained test since the pore water does not have sufficient time to drain adequately. Yanamuro and Lade (1993) found when the strain rate increased from 0.0517%/min to 0.74%/min, the shear strength increased around 2% for drained tests and 7% for undrained tests. Svoboda (2013) did consolidated drained tests on oven-dry sand with axial strain rates ranging from 1.1%/min to 4.4%/min. Additionally, Juspi (2007) conducted consolidated drained tests on unsaturated crushed granite and limestone with a strain rate of 0.167%/min. In light of all the previous work, the

consolidated drained triaxial tests in the present study were conducted with a strain rate of 1%/min on dry specimens and 0.1% /min on saturated specimens.

6.3.2.4 Consolidated drained (CD) monotonic triaxial test on dry samples

Procedures of CD triaxial test on dry specimens are summarised as below:

(1) The specimen was vacuumed at the beginning. This process could also help to check if the specimen was well-sealed.

(2) The consolidation process was achieved by applying a 200kPa cell pressure on the specimen after the cell was infused by de-aired water. To accelerate the consolidation process, the hydraulic pump kept vacuuming the specimen during the consolidation period. The specimen was supposed to be fully consolidated by maintaining this condition for four hours. It should be noticed that the load ram should be just in touch with the top-cap of the specimen to ensure that it is consolidated isotropically.

(3) The confining pressure was set to a specified value (40kPa, 100kPa or 300kPa in the present work) after the consolidation process. The base pedestal was raised at a velocity of 1mm/min until an axial strain of 20% was achieved. All the data were obtained using the GDS Lab Control and Acquisition software.

Three specimens were tested under confining pressures of 40kPa, 100kPa and 300kPa respectively. The void pressure of the fully-vacuumed and fully-consolidated dry specimens was 0, hence the total stresses can be assumed to be equal to the effective stresses. The stress and strain responses under different confining pressures are showed in Figure 6-10. In the present work, stiffness

moduli of granular materials and asphalt were estimated from the slope of the line connecting the origin and the point corresponding to one-half of the peak deviator stress (Lambe and Whitman 2008). The results are given in Table 6-2. A propotional (linear) relation is observed between the stiffness modulus and the confining pressure (Figure 6-11), which agrees with Kohata et al. (1997)'s statement. However, for either the wheel tracking tests considered in the present study or the practical engineering, the confining pressure is difficult to measure. Thus, the stiffness modulus estimated under an unconfined condition is finally selected as the input stiffness parameter for lower bound shakedown analysis (i.e. 18.3MPa for dry specimen).

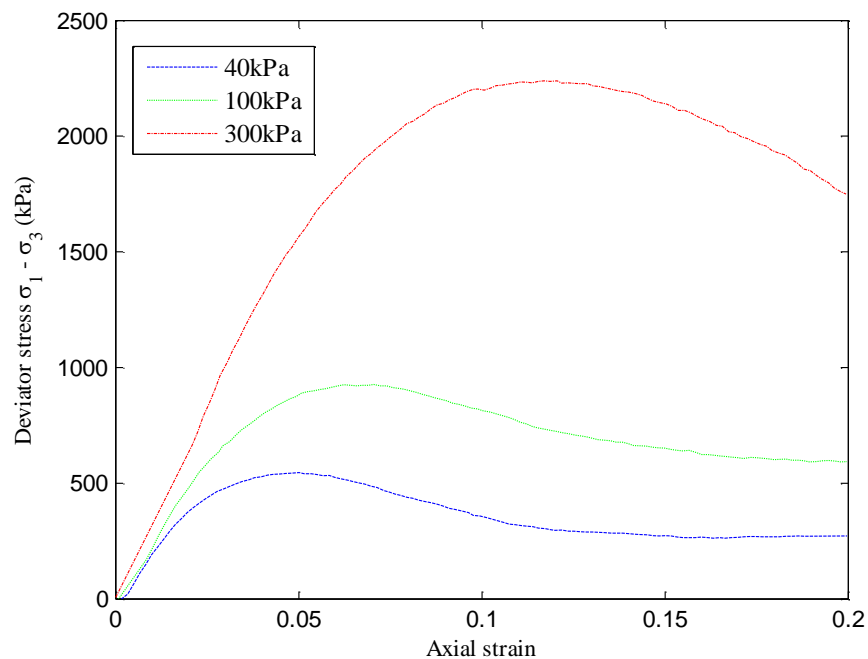


Figure 6-10 Stress and strain responses for dry specimens under different confining pressures

The plastic (Mohr-Coulomb) parameters were determined by seeking failure line well matched with the three Mohr circles plotted according to the confining

pressures and their corresponding peak axial pressures (Figure 6-12). The failure line was determined by using the matching method reported by Chen et al. (2010). Figure 6-12 illustrates that the friction angle of the dry crushed granite sample was around 50.9° and the cohesion was about 45.6kPa.

Table 6-2 Stiffness moduli and peak axial stresses during shear under different confining pressures for dry specimens

Confining pressure σ_3 (kPa)	Stiffness modulus E (MPa)	Axial stress σ_1 (kPa)
40	19.86	594
100	24.03	1026
300	33.44	2643

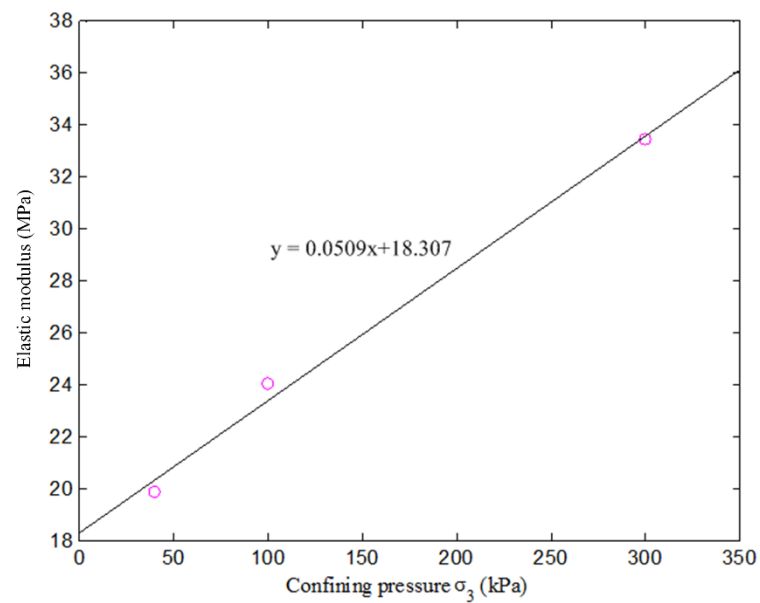


Figure 6-11 Confining pressures against stiffness moduli for dry specimens

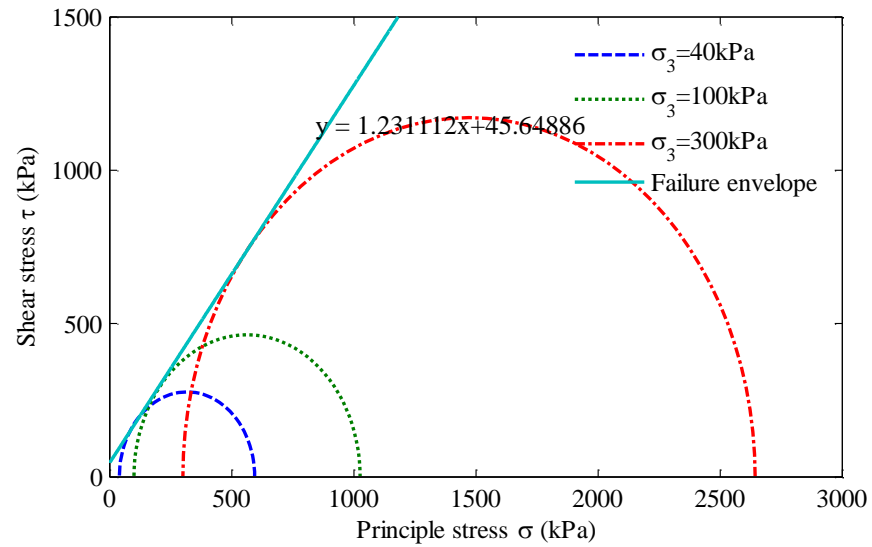


Figure 6-12 Mohr circles and the failure line for dry specimens

6.3.2.5 Consolidated drained (CD) monotonic triaxial test on fully-saturated samples

Procedures of the CD triaxial test on fully-saturated specimens are summarised as below:

- (1) The specimen was vacuumed at the beginning.
- (2) De-aired water was flushed through the specimen for at least 90 minutes until a highly saturated condition was achieved. A confining pressure of 20kPa was applied before and during the flushing process to avoid collapse caused by excess pore pressure.
- (3) The cell pressure and back pressure were increased to 420kPa and 400kPa respectively in 90 minutes. When the targets were met, the specimen was left overnight for saturating. Skempton's B-value assessment method was applied to check the degree of saturation. When the back pressure valve was switched off,

if the increase of cell pressure from 420kPa to 520kPa led to an increase of pore pressure larger than 96kPa (i.e. the B-value is larger than $96 / (520-420) = 0.96$), the specimen was considered as a fully-saturated specimen.

(4) Then, the fully-saturated specimen was left for isotropic consolidation overnight by decreasing the back pressure to 400kPa and increasing the cell pressure to 600kPa.

(5) During the triaxial compressing process, the back pressure (400kPa) was kept unchanged. The effective confining pressure was adjusted to a specified value of 40kPa, 100kPa and 200kPa. The base pedestal was gradually raised at a rate of 0.1mm/min. Each test was terminated when the axial strain reached 20% of the specimen height. All the data were outputted from GDS Lab Control & Acquisition software.

Figure 6-13 illustrates the stress and strain responses obtained under different confining pressures. The stiffness modulus can be obtained using the same method introduced before. According to Figure 6-14, the stiffness moduli changed linearly with the confining pressure. The stiffness modulus under the unconfined condition is around 11.1MPa, which is lower than that of the dry specimen. This agrees with Lu and Kaya (2014)'s finding, which indicated that the stiffness modulus of granular materials decreases with increasing water contents. By using the data given in Table 6-3, three Mohr circles were plotted in Figure 6-15. Results show that the friction angle of the fully-saturated sample was around 46.1° , and the cohesion was around 68.1kPa.

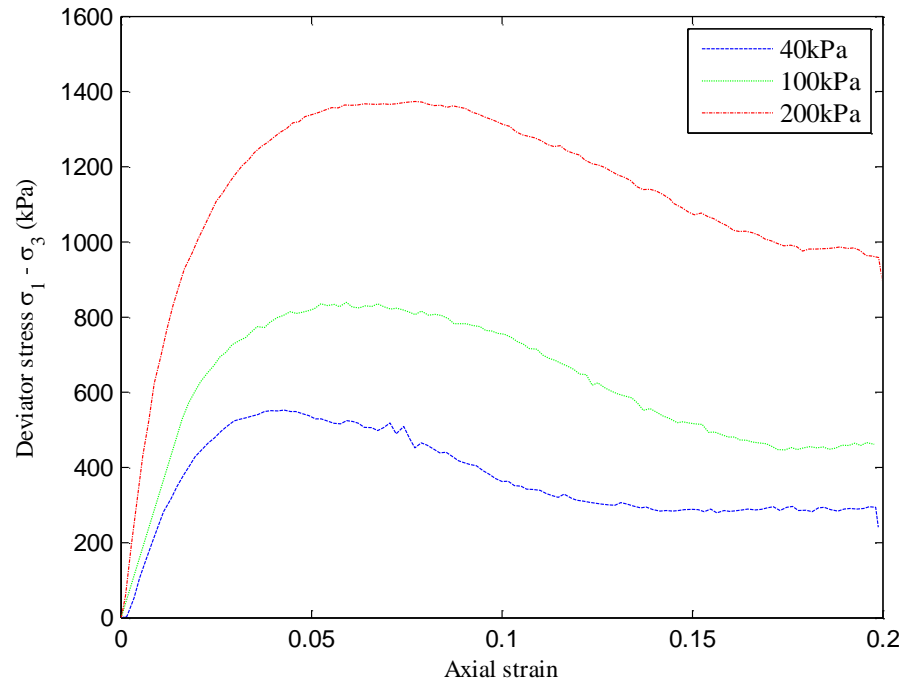


Figure 6-13 Stress and strain responses for fully-saturated specimens under different magnitudes of confining pressure

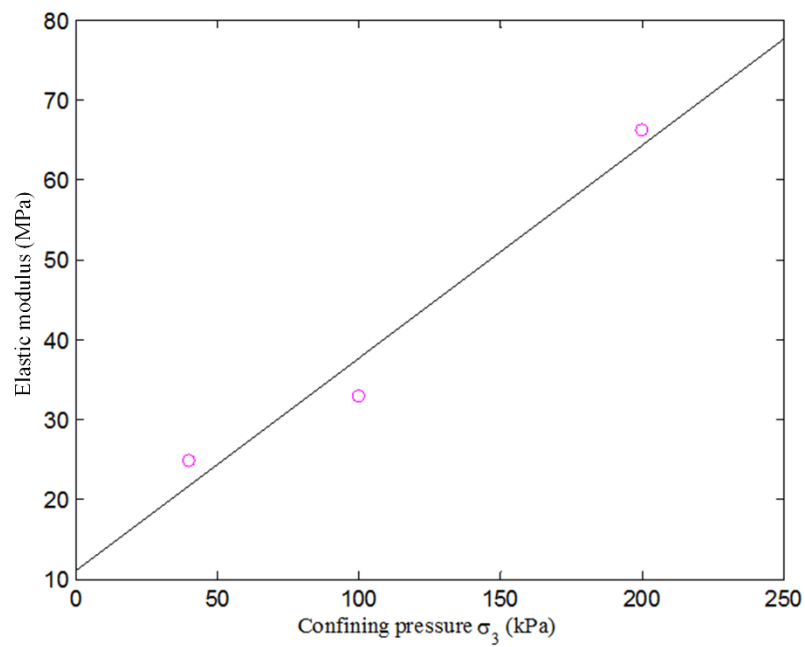


Figure 6-14 Confining pressures against stiffness moduli for fully-saturated specimens

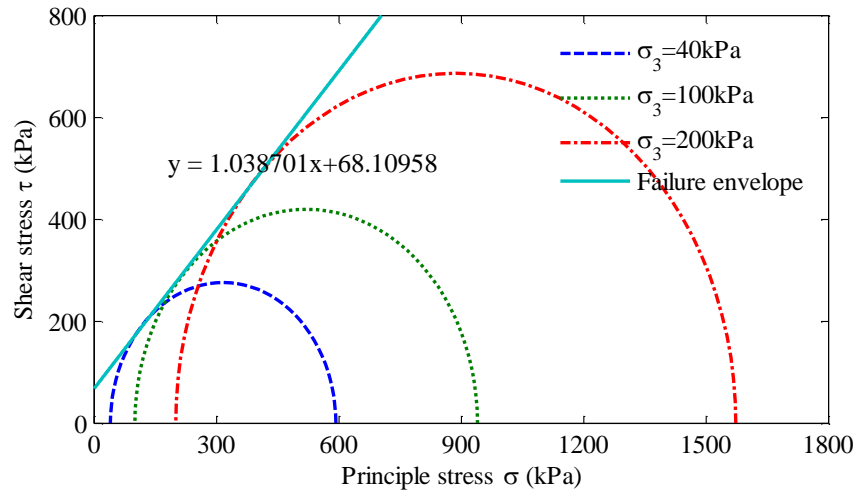


Figure 6-15 Mohr circles and the failure line of fully-saturated specimens

Table 6-3 Stiffness moduli and axial stresses for fully-saturated specimens under different magnitudes of confining pressure

Confining pressure σ_3 (kPa)	Stiffness modulus E (MPa)	Axial stress σ_1 (kPa)
40	24.8	592.0
100	32.9	939.7
200	66.2	1573.4

6.3.3 Monotonic triaxial tests on asphalt

In the present study, triaxial tests were conducted on cylindrical specimens of asphalt mixture at a relatively high temperature to obtain corresponding Mohr-Coulomb parameters.

6.3.3.1 The equipment

An Instron test equipment was used to evaluate the mechanical properties of materials and components (Figure 6-16). Compared with the standard triaxial

apparatus introduced in the subsection 6.3.2, the Instron is more versatile. It can be used for tensile and compressive strength tests, fatigue tests, flexural strength tests and so on. An Instron 1332 loading frame with a temperature-controlled cabinet (-5°C to 50°C) and a servo-hydraulic actuator with a load capacity of $\pm 100\text{kN}$ and $\pm 50\text{mm}$ axial stroke was used in the present testing programme. A triaxial chamber with a confining pressure capacity of 1.7MPa was installed into the Instron cabinet. The confining pressure was applied by filling the triaxial chamber (cell) with gas. The operational mechanisms for the other components were very similar to those for a standard triaxial apparatus.

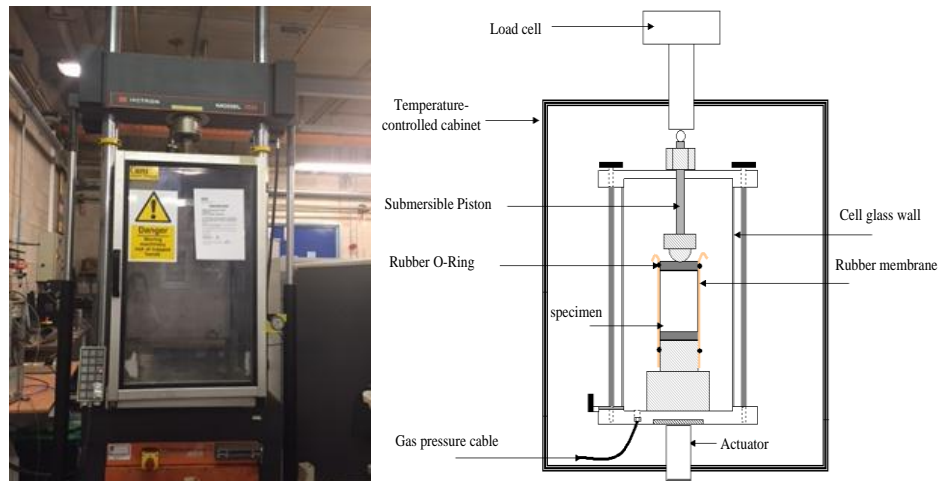


Figure 6-16 Instron apparatus at the University of Nottingham

6.3.3.2 Test procedure

Cylindrical specimens, 100mm in diameter and 110mm in height, were prepared. The triaxial cell was mounted in the Instron cabinet with a membrane sealing the asphalt specimen inside (Figure 6-17). The temperature of the cabinet was adjusted to 40°C and left overnight for preheating. An air pressure gauge attached to the triaxial chamber was used to control the value of the applied cell

pressure. The axial pressure was applied by lifting up the base pedestal gradually at a rate of 1mm/min and the loading process was stopped manually after the peak axial load was reached.



Figure 6-17 Photographs of the triaxial chamber for the Instron apparatus at the University of Nottingham (Taken by author 2015)

6.3.3.3 Test results

Table 6-4 presents the peak axial stresses obtained under confining pressures of 50kPa, 150kPa and 200kPa. Figure 6-18 illustrates that the friction angle was around 34.1 °and the cohesion was around 315.1kPa.

Table 6-4 Maximum axial stress under different confining pressure for asphalt

Confining pressure (kPa)	Maximum axial stress(kPa)
50	1363.8
150	1723.5
200	1895.0

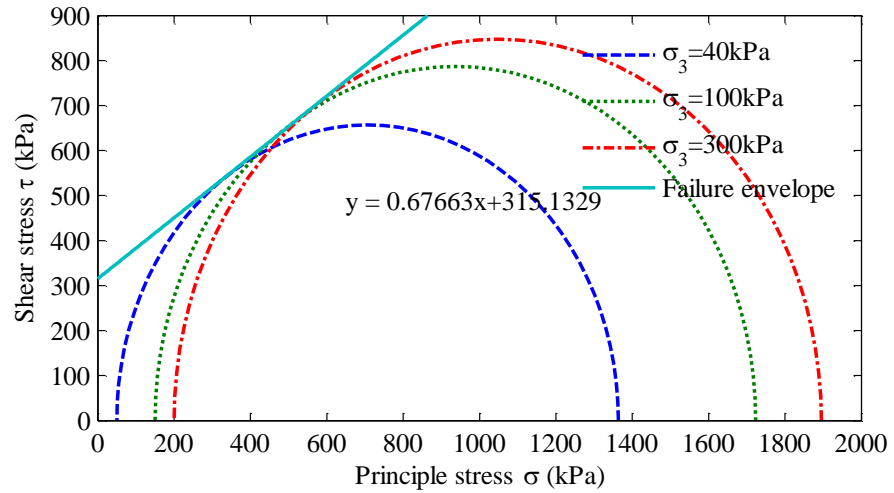


Figure 6-18 Mohr circles and the failure line of asphalt mixture

6.3.4 Unconfined uniaxial tests on asphalt

The uniaxial compression test (Figure 6-19) has been recognised as one of the most commonly-used methods for stiffness modulus estimation of asphalt by many researchers due to its least complex stress conditions (Road Research Laboratory Report 1962, Thom 2008, Harran and Shalaby 2009, Van Velsor et al. 2011, Mohammad et al. 2008). Details of this test are specified in AASHTO 2011.

Stiffness modulus of asphalt depends on both temperature and loading history. In the present study, the uniaxial tests on asphalt were carried out under a temperature-controlled condition (40 °C) and with a reasonable loading rate. Deng (2000) indicated that asphalt behaves more elastically at a low temperature or under very quick loading period (10^{-8} s to 10^{-6} s). Thom (2008) suggested that a pulse of load from a vehicle typically takes about 0.01s-0.015s to reach the peak stress. However, tests are generally conducted at a relatively slow rate due

to the limitation of test equipment. A loading period lasting 0.125s to the peak was recommended by Thom (2008) from which the stiffness modulus measured is typically 70% of that obtained under fast-moving traffic. A dynamic load with a frequency ranging from 0.1Hz to 25Hz was used to obtain the dynamic stiffness modulus of asphalt by Mohammad et al. (2008) and Van Velsor et al. (2011). In the present study, the effects of the loading mode on stiffness modulus were investigated by applying static and dynamic uniaxial stress. For static cases, the duration of the loading time (defined as t_s during which the axial stress increases from 0 to the peak) varied from 0.05s to 0.3s, while for dynamic load cases, the load frequency (f_d) varied from 1Hz to 10Hz. It should be noticed that there exists a congruent relationship between t_s and f_d . For example, for the case with $f_d = 10$ Hz, it takes 0.1s for the entire process of loading and unloading, therefore corresponding to a loading time (t_s) of 0.05s. According to Harran and Shalaby (2009), the maximum uniaxial stress applied on the top of the specimen should be controlled within a specified range ensuring the final permanent strain does not exceed 1500 microstrain. To meet the requirement, 200kPa was selected as the peak value of the axial load. Average readings were taken from two LVDTs positioned on the top platen (Figure 6-19).

6.3.4.1 Theoretical prediction on stiffness modulus of asphalt

The stiffness modulus of asphalt can be estimated based on the Equation presented below (Brown and Brunton 1985).

$$E_m = 1.157 \times 10^{-7} \times t^{-0.368} \times 2.718^{-Plr} (SP_r - T)^5 \times \left[1 + \frac{257.5 - 2.5VMA}{n(VMA - 3)} \right]^n, \quad (6.4)$$

where

t is the loading time,

T is the temperature,

PI_r is recovered Penetration index relating to the nominal initial penetration of the material (P_i), satisfying

$$PI_r = \frac{27 \log P_i - 21.65}{76.35 \log P_i - 232.82}, \quad (6.5)$$

SP_r is the softening point, which can be expressed as:

$$SP_r = 98.4 - 26.35 \log(0.65 P_i), \quad (6.6)$$

$$n = 0.83 \log \left[\frac{4 \times 10^4}{1.157 \times 10^{-7} \times t^{-0.368} \times 2.718^{-PI_r} (SP_r - T)^5} \right], \quad (6.7)$$

VMA is the voids in the mixed aggregate which can be written as:

$$VMA = V_B + V_V \quad (6.8)$$

where V_B is the volume of the binder in the asphalt and V_V is the volume of air voids.

Therefore, the stiffness modulus of the asphalt employed in the present study with $P_i = 50$, $V_B = 10.6$ and $V_V = 7.3$ can be roughly estimated.

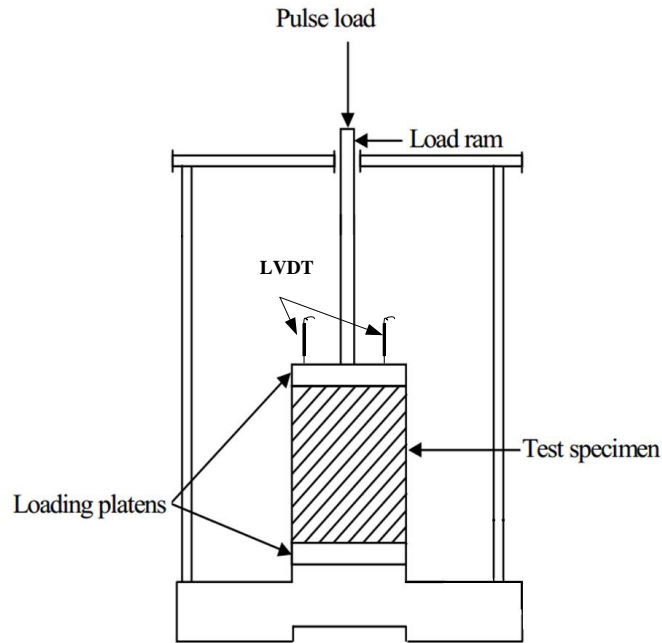


Figure 6-19 Asphalt specimen set-up for axial compression test

6.3.4.2 Unconfined axial compression tests under static load

Similar to granular materials, the secant modulus can be taken as the stiffness modulus for asphalt (Harran and Shalaby 2009). The stress and strain responses of a specimen tested under a static load ($t_s = 0.05s$) is given as an example in Figure 6-20. The slopes of two secant lines (red dash lines in Figure 6-20) are taken as the stiffness modulus under loading and unloading. In the present study, each test was performed at least twice until the difference between the obtained stiffness modulus was less than 15%. Average values were taken finally. The results are summarised in Table 6-5. Figure 6-21 shows that the stiffness moduli obtained from loading and unloading periods all decreased with increasing t_o . Besides, it can be seen that the stiffness moduli obtained for the unloading period are always larger than those obtained from the loading period, which is consistent with the finding in the Road Research Laboratory Report (1962). In

addition, it is notable that the differences between the loading and unloading periods become larger with the increase of t_s , which means that the effect of visco-elasticity becomes ever more obvious. Comparisons with theoretical solutions are also given in Figure 6-21. It can be seen that the unloading stiffness moduli obtained in the experiments are higher than the theoretical solutions at 40 °C, but closer to the theoretical solutions obtained under a relatively low temperature (e.g. 35 °C).

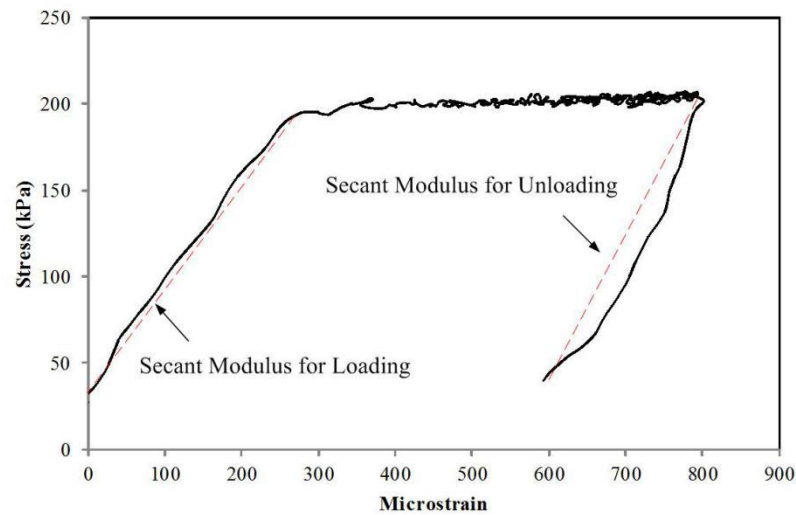


Figure 6-20 Determination of the stiffness modulus of asphalt during loading or unloading period when $t_s = 0.05s$

Table 6-5 Summary of the stiffness moduli for asphalt specimens tested under static loads

Loading time	Loading			Average (MPa)	Unloading			Average (MPa)
	Stiffness modulus (MPa)		Difference (%)		Stiffness modulus (MPa)		Difference (%)	
	1 st	2 nd			1 st	2 nd		
0.05	719.2	629.5	14.25	674.4	862.7	864.5	-0.21	863.6
0.1	541.3	550.1	-1.60	545.7	777.3	788.9	-1.47	783.1
0.2	370.6	357.4	3.69	364.0	723.8	689.2	5.02	706.5
0.3	354.3	321.5	10.20	337.9	650.7	646.5	0.65	648.6

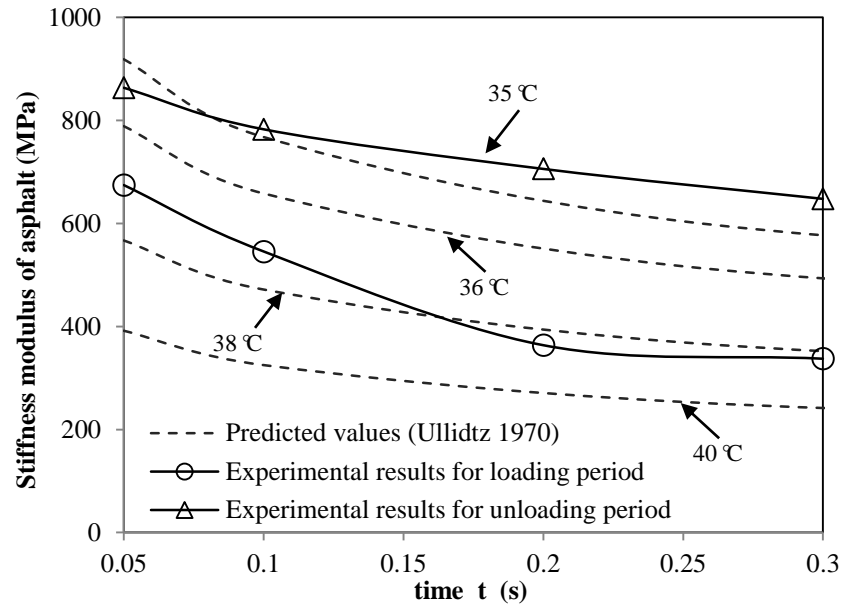


Figure 6-21 Effect of loading and unloading time on stiffness modulus of asphalt

6.3.4.3 Unconfined axial compression tests under dynamic loads

In reality, the pavement is subjected to repeated load rather than a static load, therefore the stiffness modulus measured under dynamic loads could be more reliable. The stress-strain response curve of asphalt under a dynamic load with $f_d = 2\text{Hz}$ is given as an example in Figure 6-22 in which the stiffness modulus becomes almost constant eventually. The stiffness modulus is taken as the slope of the secant connecting the zenith and the nadir in one cycle (refer to the red dash line in Figure 6-22). This makes the loading stiffness modulus identical to the unloading stiffness modulus. Each test was conducted at least twice. The results are listed in Table 6-6. Average values are taken and plotted in Figure 6-23 for comparisons with the theoretical solutions. The experimental results are higher than the theoretical results calculated at 40 °C, but close to those at 35 °C. This agrees with the finding in the static cases. In addition, comparisons can be

also made between the static load cases and dynamic load cases. For example, the dynamic stiffness modulus for 10Hz cyclic load corresponds to the static stiffness modulus for $t_s = 0.05s$. The value of the dynamic stiffness modulus is similar to that of the static stiffness modulus for unloading, with a minor difference of only 3.27%. The dynamic stiffness modulus will be used in the theoretical shakedown analysis below. Also, considering the wheel velocity, the frequency of 10Hz will be used.

Table 6-6 Measurements of the stiffness of asphalt specimens with different load frequencies

Frequency (Hz)	Stiffness of specimen (MPa)		Difference (%)	Average (MPa)
	1 st	2 nd		
1	558.3	563.5	0.92	560.9
2	661.4	634.5	-4.24	648.0
5	814.1	809.0	-0.63	811.6
10	896.7	886.9	-1.11	891.8

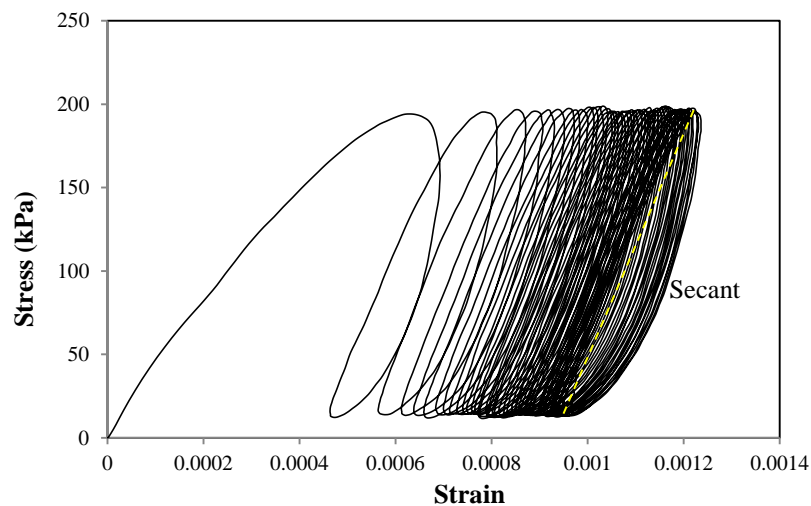


Figure 6-22 Stress-strain response of asphalt under dynamic load with a frequency of 2Hz

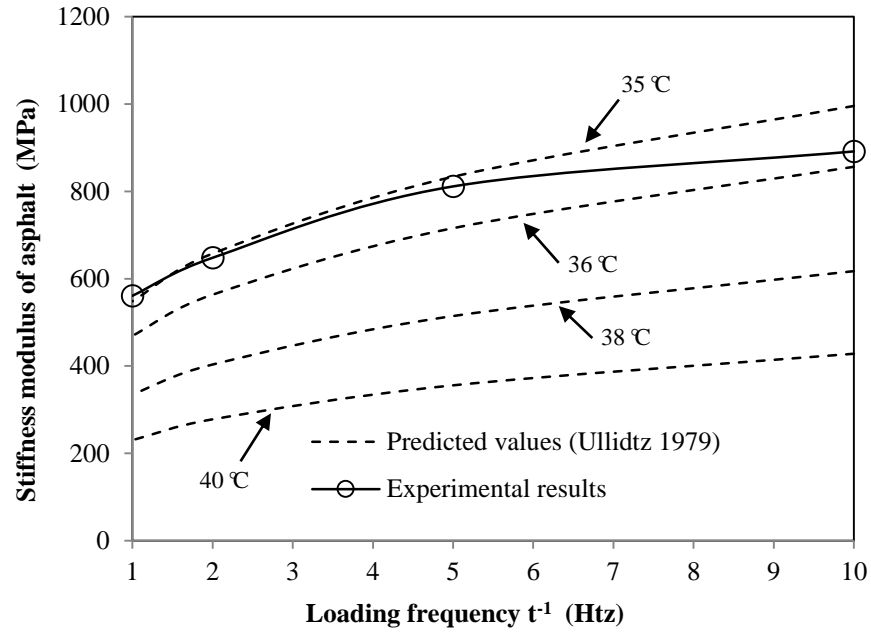


Figure 6-23 Effect of loading frequency on stiffness modulus of asphalt

6.4 Wheel Tracking Test

6.4.1 Wheel tracking facility

The Nottingham wheel tracking facility as shown in Figure 6-24 was used. The surface load was applied by a solid rubber wheel ($r = 100\text{mm}$) mounted between a pair of beams. During tests, the wheel remained at the same location. The motor driven shaft spun anti-clockwise to drive the reciprocating table forward and backward on which a mould (filled with the specimen) was mounted. Therefore the relative velocity of the specimen to the wheel is the velocity of the wheel load. In the present work, the velocity of the wheel load was around 0.98km/hr .

The magnitude of the load was controlled by adding weight on the load hanger. The wheel load on the specimen surface was measured by replacing the mounted mould with a digital scale as shown in Figure 6-25. Some rigid slabs were matted

under the scale to ensure that the top surface of the scale is as high as the specimen surface. Table 6-7 shows the relation between the wheel load and the applied weights on the loading hanger.

Table 6-7 transformational relation between the wheel load and the applied weights on the loading hanger

Weights(Kg)	0	2	4	5	6	7	9	10
Weight reading (Kg)	48.3	61.9	75.4	82.4	89.0	96.1	109.7	116.3
Wheel load (N)	473.3	606.6	738.9	807.0	872.2	941.4	1074.6	1139.5

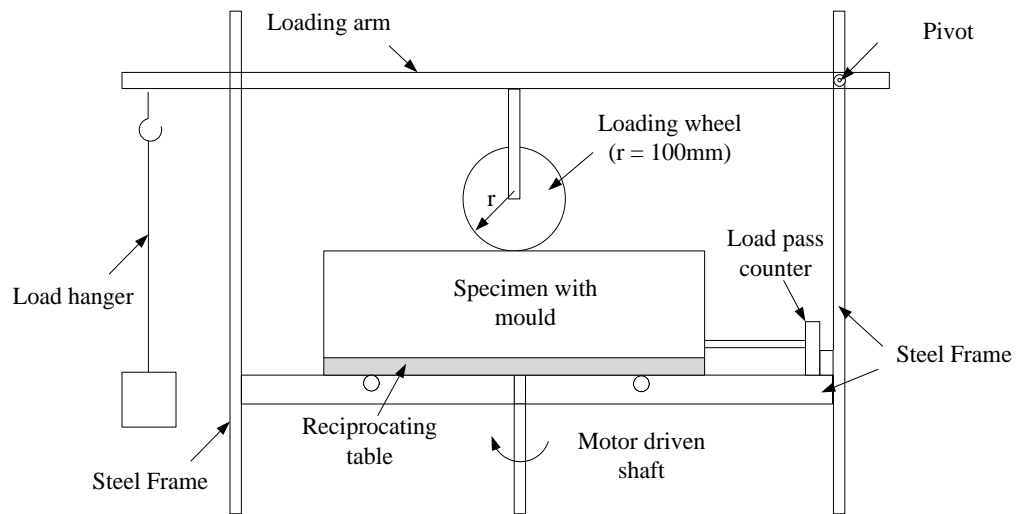
A specially designed LVDT (Figure 6-26), which can move horizontally, was used to measure the asphalt slab surface deformation. It was not mounted on the wheel tracking facility or the mould; therefore the reciprocating table had to be stopped at intervals for the measurement of surface displacement.

6.4.2 Specimen preparation

The dimension of the two-layered specimen is given in Figure 6-27. Specimen density in the granular layer remains the same as that in triaxial tests, i.e. $\rho = 1885 \text{ kg/m}^3$. Thus, 13.15 kg dry crushed granite was compacted into the mould layer by layer. The granular layer surfaces were levelled off and overlaid by an asphalt slab on the top. All the screws on the mould were tightened to ensure the specimen was properly bounded.



(a) Nottingham wheel tracking facility



(b) Schematic of Nottingham small wheel tracking facility

Figure 6-24 Nottingham wheel tracking facility



Figure 6-25 Measurement of the wheel load applied on the specimen surface
(Taken by author 2015)



Figure 6-26 Photographic of special designed LVDT (Taken by author 2015)

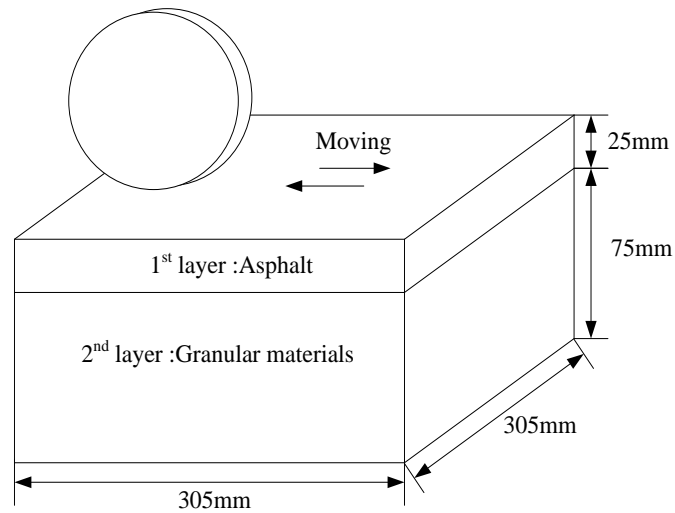


Figure 6-27 Bituminous pavement structure

6.4.3 Test procedures

(1) The wheel tracking tests were conducted in a temperature-controlled room (set to 40 °C during the test). The specimen with mould was stored in an oven before the test every day.

(2) During the test, the vertical displacement of the centre point of the specimen surface was measured by LVDT at time intervals.

(3) Due to the large number of load repetitions considered in the present study, tests usually lasted more than one day (2 to 11 days in the present study). At the end of each day, the specimen was removed from the temperature-controlled room and restored in the 40 °C oven till the next day morning for the subsequent tests. The influence of overnight storage on the specimen will be investigated in subsection 6.4.5.

(4) The tests were terminated if one of the following situations was observed: a) the surface displacement barely changes in two sequential days (approximately

20000 load passes); b) the accumulative surface displacement is large (say 8 mm).

6.4.4 Determination of contact area and contact pressure

The contact patches were measured under different load magnitudes. It was found that the shapes of the contact patches are more like rectangles. The width of the contact area always equals the width of the wheel (0.05m), and the length of the contact area changes almost linearly with the magnitude of the wheel load (Figure 6-28).

Five groups of wheel tracking tests were conducted by applying different magnitudes of wheel load on the specimens. The dimensions of the contact areas were estimated by using the trend line function in Figure 6-28. Accordingly, the contact pressures under different contact loads can be calculated as shown in Table 6-8.

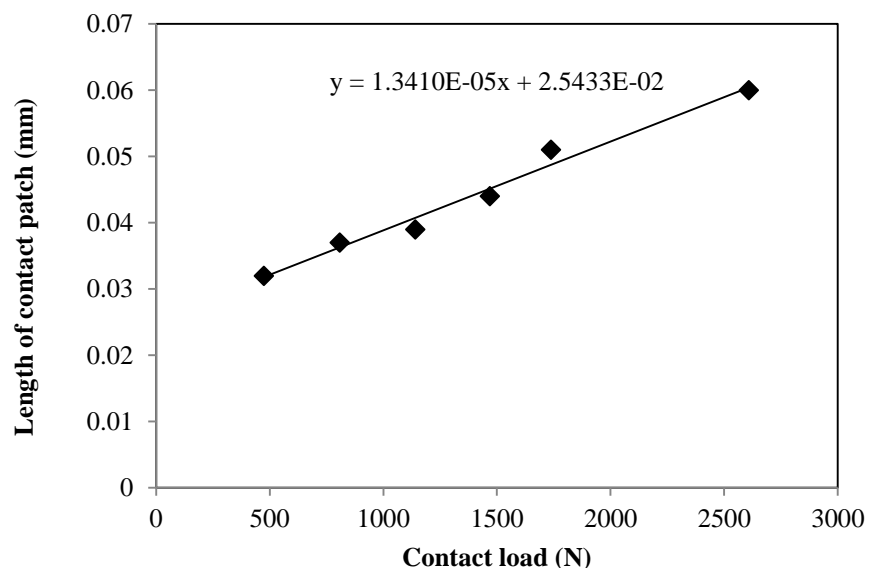


Figure 6-28 Length of contact patch against contact load

Table 6-8 Calculations of the contact length under different magnitudes of load

	Test 1	Test 2	Test 3	Test 4	Test 5
Load Applied (kN)	473.3	606.6	807.0	941.4	1139.5
Length of contact length $2a$ (m)	0.0320	0.0337	0.0364	0.0381	0.0407
Wide of contact area (m)	0.05	0.05	0.05	0.05	0.05
Contact pressure (kPa)	296	360	444	494	560

6.4.5 Experimental results

The development of the surface downward deformation along with the number of load passes for different magnitudes of contact pressure is presented in Figure 6-29(a). For the specimen subjected to 360kPa surface pressure, identical numbers of load passes (8000 load passes each day) was used to investigate the effect of overnight interruption. Generally speaking, some deformation recovered due to the visco-elastic property of the asphalt. It was found that the maximum difference between the pre-storage deformation and post-storage deformation was below 3%, and it did not affect the general developing tendency, as shown in Figure 6-29(a).

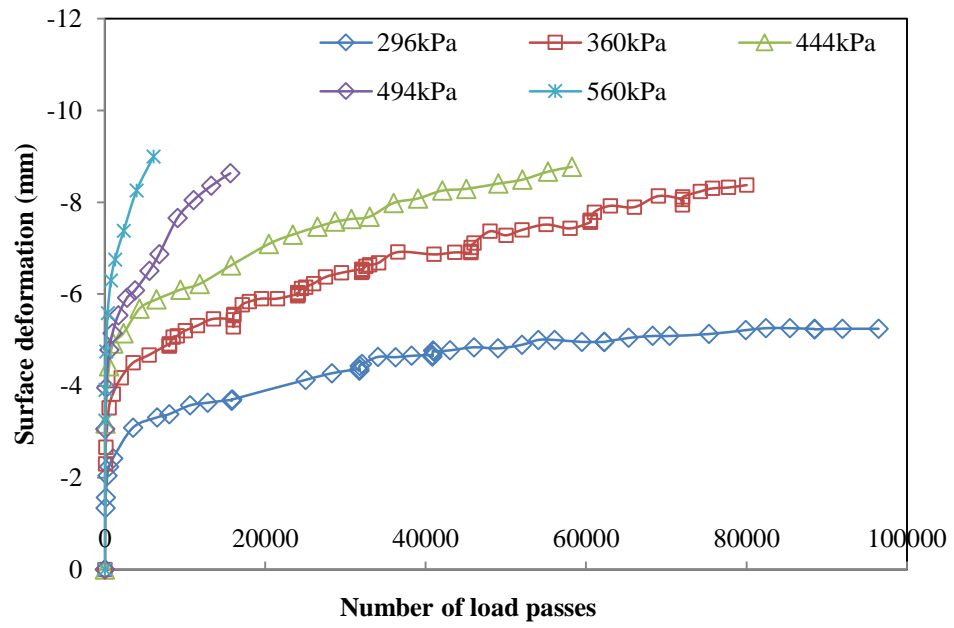
Figure 6-29(a) shows that when the load level is relatively high (i.e. 360kPa, 444kPa, 494kPa and 560kPa), the surface deformation gradually grows with the increasing number of load passes and reached more than 8mm. However, when the load level is relatively small (296kPa), the surface deformation barely changes after 40000 load passes; and there was nearly no increase of surface deformation in the last two days. Figure 6-29(b) was further plotted with the horizontal axis on a logarithmic scale. The final stage of the curve for 296kPa is shown as a convex-downward curve, while the other four curves demonstrate an

obviously different trend. This discrepancy of the trends due to different load levels can be explained by using shakedown theory. Therefore, this bituminous pavement structure is in a shakedown state when the load is at 296kPa, whereas it is in a non-shakedown state when the load is at or above 360kPa. The experimental shakedown limit should be between 296kPa and 360kPa.

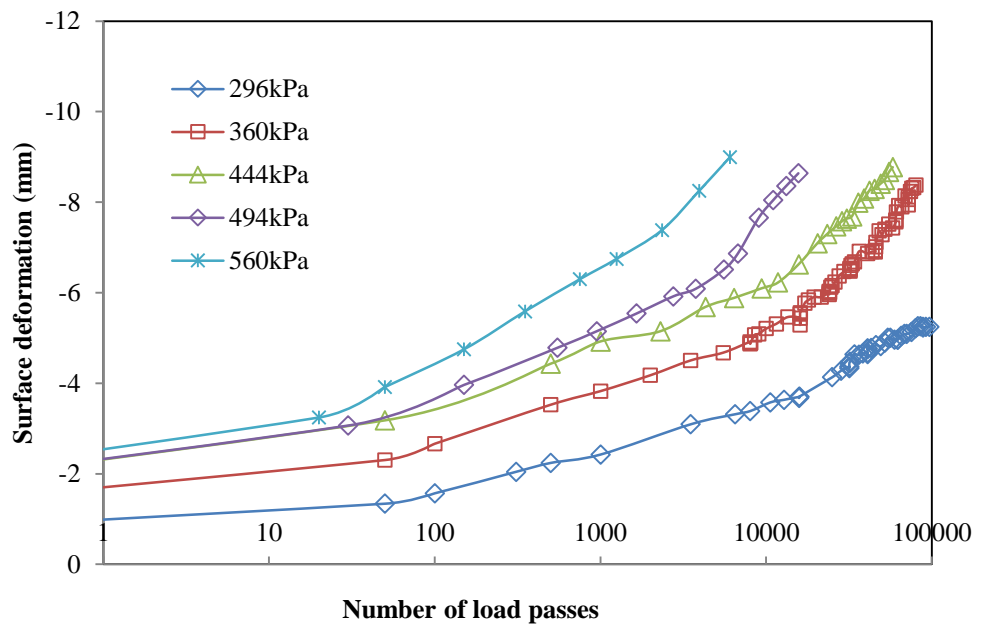
The shakedown status of the 296kPa case can be further demonstrated in Figure 6-30, where the change of permanent vertical strain rate is plotted against the surface permanent deformation. At 296kPa the surface deformation almost ceases to increase after 5mm. The measured ratio can reach 0 or even be slightly negative, shown as discontinuities in the curve. Fluctuations in those curves could be induced by measurement error and overnight storage.

6.4.6 Comparisons with theoretical solutions

Table 6-9 shows the shakedown limits calculated using the theoretical shakedown approach. Both 2D and 3D analyses were carried out. In the 2D problems, a contact length of 0.032 was used. In the 3D problems, a rectangular contact area (0.032m long, 0.05m wide) was assumed. Four sets of material parameters were used. The first two sets used the asphalt material parameters obtained directly from the triaxial and uniaxial compression tests where the temperature was 40 °C. Saturated and dry granular materials were considered in Set 1 and Set 2 respectively. In the third and fourth set, the stiffness modulus of asphalt was calculated from Equation (6.4) at 40 °C and 32 °C and the granular materials were considered to be dry. 32 °C is the minimum room temperature measured during the test due to the room sealing problem.



(a)



(b)

Figure 6-29 Development of surface deformation under different magnitudes of moving surface load

According to the wheel tracking tests, the experimental shakedown limit is between 296kPa and 360kPa for the current pavement structure. As can be seen, the 2D shakedown limits of Set 2 fall into this range. 2D shakedown limits for Set 1 and Set 3 are below this range while all 3D shakedown limits are above this range. The real pavement problem is a 3D problem. The difference between the 3D theoretical shakedown limits and the experimental results may be due to several reasons. First, the assumption of standard materials (i.e. following associated plastic flow) may overestimate the shakedown limit as discussed in the previous chapters. For example, it has been found that the use of a non-associated plastic flow rule instead of an associated plastic flow rule could lead to a 22% reduction in shakedown limit. Second, as mentioned before, the real pavement temperature may not reach 40 °C during the whole test process. If the asphalt stiffness at 32 °C is used (Set 4), the 2D shakedown limit is within the range of experimental results. Finally, measurement errors in the tests and the methods for determining the material parameters could also affect shakedown limits.

Table 6-9 Theoretical shakedown solutions obtained from the present study for comparison with the experimental results

Parameter sets	E_1 (MPa)	c_1 (kPa)	$\phi_1(^{\circ})$	ν_1	E_2 (MPa)	c_2 (kPa)	$\phi_2(^{\circ})$	ν_2	Shakedown limit (kPa)	
									2D	3D
Set 1	891.8	315.1	34.1	0.3	11.1	68.1	46.1	0.3	287.9	609.9
Set 2	891.8	315.1	34.1	0.3	18.3	45.6	50.9	0.3	351.4	688.0
Set 3	355.5	315.1	34.1	0.3	18.3	45.6	50.9	0.3	537.4	918.3
Set 4	1262.6	315.1	34.1	0.3	18.3	45.6	50.9	0.3	304.5	632.0

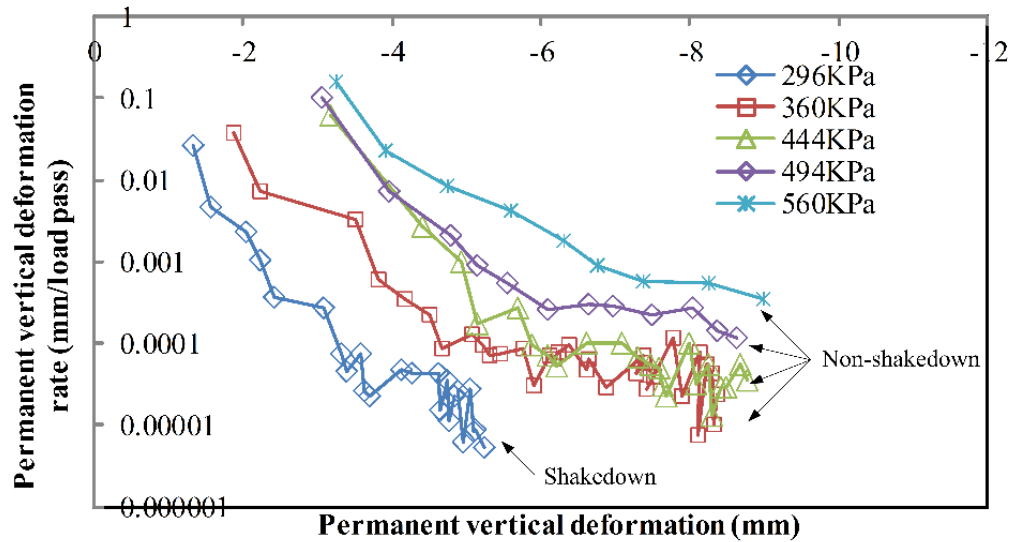


Figure 6-30 Change of permanent vertical strain rate against surface deformation

6.4.7 Summary

This chapter has reported the test procedures and results for the responses of a two-layered bituminous pavement structure under repeated wheel loads. Two distinct pavement responses due to different load magnitudes have been identified. The tests verified the existence of the shakedown and non-shakedown phenomena in bituminous road pavements. Triaxial tests and uniaxial compression tests were also conducted on asphalt and granular materials to obtain the stiffness and strength parameters and accordingly the theoretical shakedown limits could be calculated. Comparisons between the theoretical predictions and the experimental results suggest that current 3D shakedown analysis for standard materials may overestimate the shakedown limits for bituminous pavements.

CHAPTER 7

A COMPARISON BETWEEN THE SHAKEDOWN DESIGN APPROACH AND THE ANALYTICAL DESIGN APPROACH IN THE UK FOR FLEXIBLE PAVEMENTS

7.1 Introduction

As expressed in Chapter 2, the current design methods for flexible pavements can be divided into two categories: one is the empirical approach which utilizes design charts or empirical equations developed from experimental work and field tests, such as the standard design method in the UK; the other is the mechanistic-empirical approach (also called analytical design approach in the UK), in which elastic stresses or strains at critical points are related to pavement life considering principal failure modes of pavements. The latter approach can maximize the whole life value by choosing different materials and layer thicknesses and therefore has become increasingly popular around the world. However, one major limitation of this analytical design approach is that strength properties of pavement materials are not well considered, especially for the rutting failure which is attributed to material plasticity. In this Chapter, the

shakedown approach will be directly compared with the analytical approach (Equation 2.4-2.6) in the UK through a typical thickness design.

7.2 A typical pavement problem

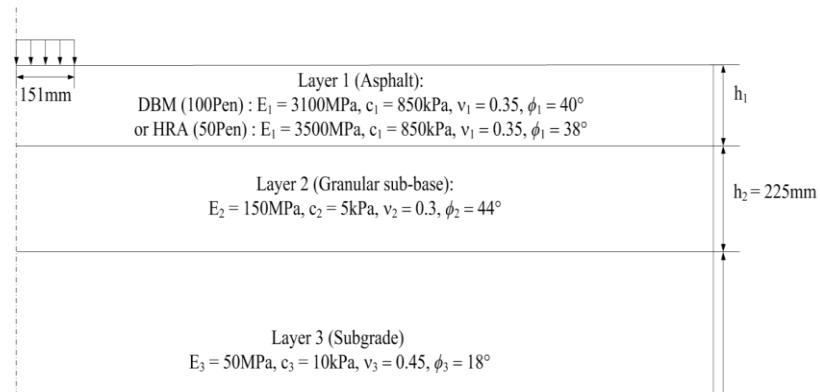


Figure 7-1 A flexible pavement structure and material properties

Figure 7-1 shows a typical flexible pavement structure which was used as an example in LR1132 (Powell et al. 1984). E_n , v_n , c_n , ϕ_n and h_n represent stiffness modulus, Poisson's ratio, cohesion, friction angle and thickness of materials at the n^{th} layer. The first layer is either dense bitumen macadam (100pen) or hot rolled asphalt (50pen) with stiffness modulus 3100MPa and 3500MPa respectively under a temperature of 20°C. CBR value of the subgrade soil is chosen as 5 percent and therefore its stiffness modulus is 50MPa (Highways Agency 2009) and no capping layer is needed. Also, stiffness modulus of the subbase granular layer should be 150MPa with a maximum layer thickness 225mm. In the shakedown approach, friction angle and cohesion of each material are also required. Selection of the values of the cohesion and friction angle of asphalt can refer to Table 2-1. Considering the deformation resistance of DBM

is usually higher than HRA (Thom 2008), a slightly smaller friction angle is chosen for HRA while the same value of cohesion is used.

In both methods of design, it is also necessary to know the contact area between tire and pavement. It is usually assumed that each tire has a circular contact area. In LR1132, a contact radius of 0.151m and a standard wheel load of 40kN are used. Therefore, an average contact pressure of 558kPa should be applied in the analytical design method. It should be noted that the contact pressure is generally considered to be equal to the inflation pressure of the tire, the value of which can vary from 250kPa for a car to 3000kPa for aircraft (Huang 2004; Thom 2008). In spite of that, most pavements take the highest axle loads from truck tires, the inflation pressure of which can be reach 860kPa for both single and dual configurations according to Michelin product specifications (e.g. XTE2). This means that the maximum contact pressure on most pavements could be 860kPa.

7.3 Thickness design

Contour plots Figure 7-2 and Figure 7-3 show the number of standard axle loads that the pavement can withstand (i.e. pavement life N) for various values of the contact pressure and asphalt thickness. In the analytical design approach, the contact pressure should be chosen as 558kPa which corresponds to the standard axle load 80kN. Figure 7-4 further shows the required asphalt thicknesses for various pavement lives when the design pressure is 558kPa. By the way, in the cases studied here, the pavement rutting criterion is always more critical than the fatigue criterion according to Equations 2.4-2.6.

The shakedown limit (expressed as contact pressure) against the asphalt thickness is also displayed as dash lines in Figures 7-4. The shakedown limit represents the maximum contact pressure that the pavement can withstand. Given the maximum possible pressure as 860kPa, the corresponding asphalt thickness should be at least 315mm for DBM and 300mm for HRA. One should highlight that a pavement shakes down or not is controlled by the maximum applied load; therefore the contact pressure used here is 860kPa instead of 558kPa. In addition, it is interesting to notice that the shakedown design curve is very close to the analytical design curve when the pavement life is 3.5×10^6 standard axles.

The shakedown-based thickness designs are also marked in Figure 7-4. It demonstrates that these designs (i.e. 315mm for DBM and 300mm for HRA) are identical with those from the analytical approach if the pavement life is 18msa. That is to say, in the case of 20°C, if the design life is at or below 18msa, the shakedown-based approach is safer; otherwise, the analytical design approach is more conservative.

By using the shakedown approach, it is also possible to identify which layer is more critical (i.e. more susceptible to rutting). It is found that the shakedown limit of the granular layer is always the minimum among all layers as shown in Tables 7-1 and 7-2. In other words, the granular layer is more critical in the current problem. However, one should bear in mind that for comparison purposes the temperature was kept as 20 °C throughout the study. The real pavements would be subject to changes of air temperature which would alter material properties and thus the capacity of the pavements. For this reason, the

effect of temperature on the shakedown-based designs will be discussed in the following subsection.

7.4 Influence of temperature

The analytical design approach was conducted under a temperature of 20 °C which may be sufficient in its context. However, the shakedown-based design approach does not have that privilege. The change of air temperature will change the pavement responses to repeated moving loads. It is commonly known that pavements rut more under higher temperature. In order to guarantee a pavement will shakedown within its service life, designs must be undertaken by considering the most critical situation (i.e. at the highest temperatures).

The increase of temperature obviously changes the asphalt stiffness modulus and cohesion, while its effect on asphalt friction angle may be minor (Chen et al. 2009). In this study, the friction angle of asphalt was decreased slightly to 35 degrees and the layer thickness was fixed as 315mm. Equation (7.1) (Ullidtz 1979) was used to calculate stiffness modulus of asphalt at various temperatures. Results are plotted in Figure 7-5 for both DBM and HRA.

$$\log(E_T) = \log(E_{20C}) - 0.0003 \times (20 - T)^2 + 0.022 \times (20 - T), \quad (7.1)$$

where E_T is the stiffness of asphalt at a specified temperature (T) and E_{20C} is the stiffness of asphalt at 20 °C.

The interactive influence of asphalt cohesion and stiffness modulus on the pavement shakedown limit is exhibited in Figure 7-6. On the lower side of the

dashed line (i.e. asphalt cohesion is relatively low), the asphalt layer is more critical, and the shakedown limit drops markedly with reducing cohesion and increases slightly with decreasing stiffness. On the upper side of the dashed line, the granular layer is more critical, and the pavement shakedown limit will not change with asphaltic cohesion. If the maximum possible contact pressure is 860kPa, shakedown can only be reached when the cohesion is above 145kPa and the stiffness is above 3100MPa which means 20 °C in DBM and 22 °C in HRA.

In other words, the current design cannot carry a pressure above 860kPa, and a thicker DBM layer or a stronger granular sub-base is needed to carry the load under a higher temperature. The reason why the HRA pavement can survive at a higher temperature (22 °C) is that its layer thickness is 315mm (300mm at 20 °C).

The increase of the asphalt layer thickness can definitely increase the pavement shakedown limit as shown in Figure 7-7 for various values of asphalt stiffness modulus. Therefore at a relatively high temperature in the UK (say 30 °C), the asphalt stiffness modulus is reduced to 1800MPa, so a minimum thickness of 390mm is required to support the maximum contact pressure 860kPa. According to Figure 7-4, this thickness can withstand around 8×10^7 standard axle loads which is also the pavement life suggested by highways England for interminate life flexible pavements (refer to report LR1132).

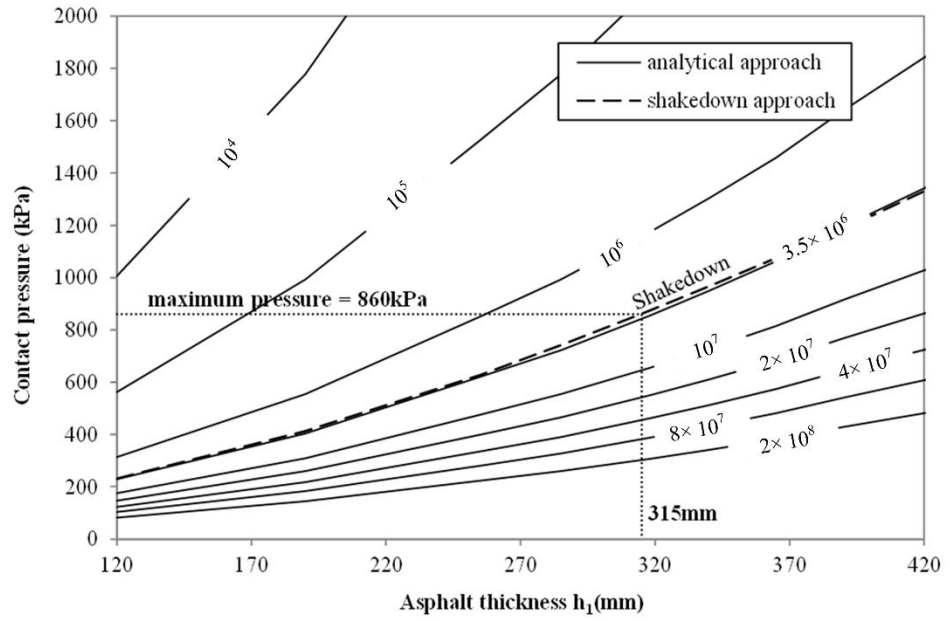


Figure 7-2 Comparison of DBM thickness designs

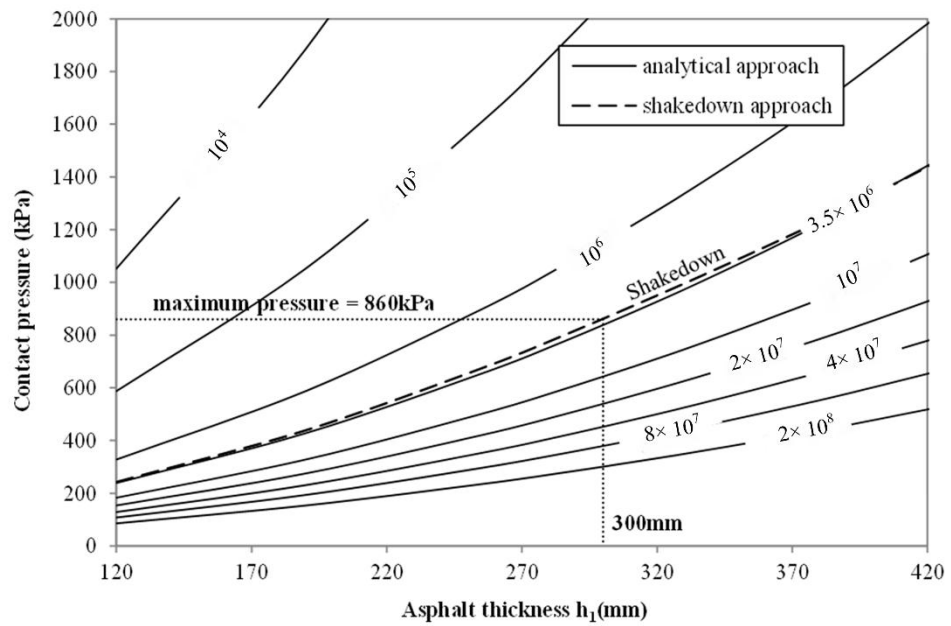


Figure 7-3 Comparison of HRA thickness designs

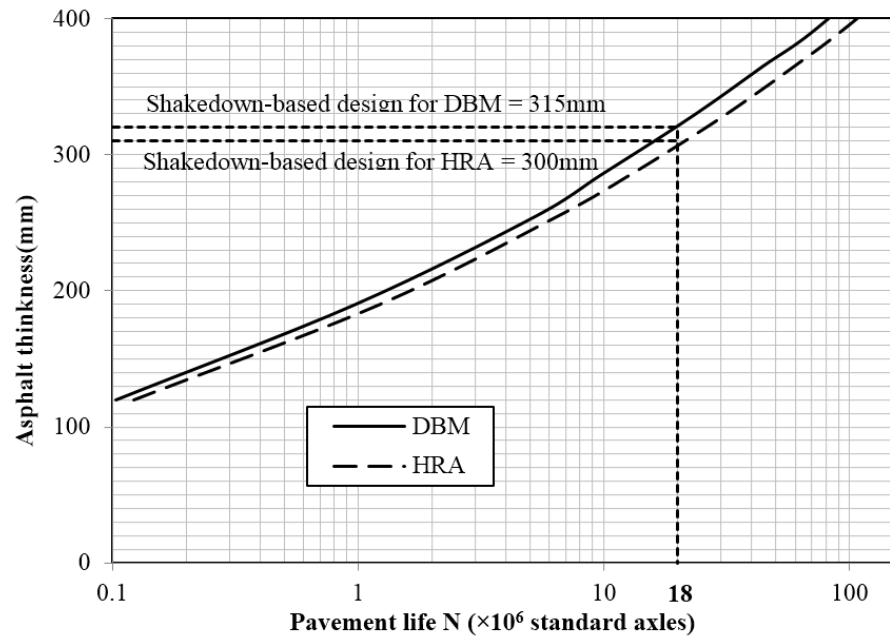


Figure 7-4 Comparison between analytical design curves and shakedown-based design

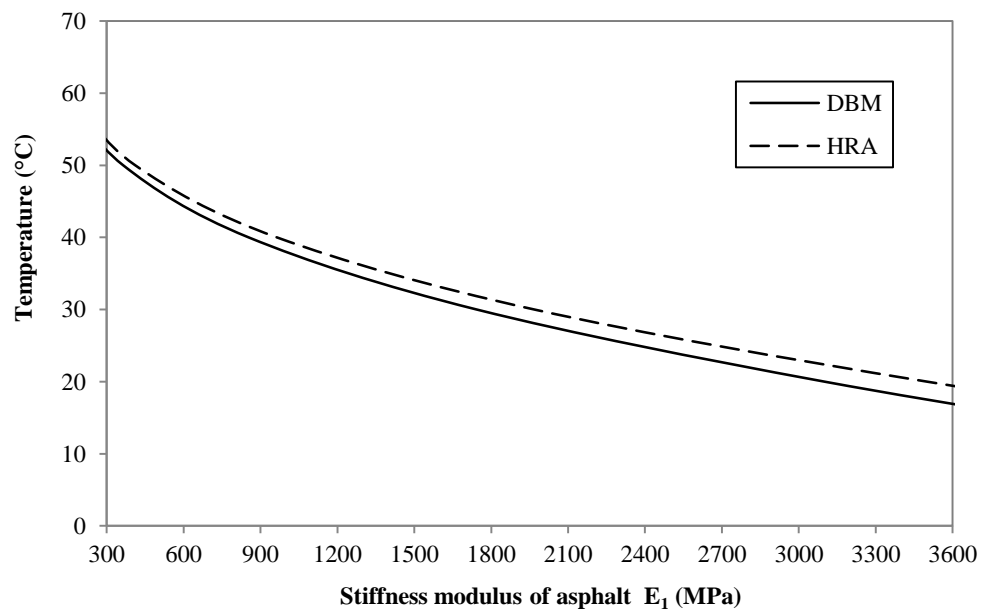


Figure 7-5 Influence of temperature on asphalt stiffness

Table 7-1 Shakedown limit of each layer for a DBM pavement

Thickness h_1 (mm)		120	190	255	285	340	365	390	440
Shakedown limit (kPa)	DBM layer	1598	2618	3901	4607	5355	5576	5788	6205
	Granular layer	231	412	628	742	967	1075	1187	1426
	Soil Subgrade	1968	3554	5479	6505	8593	9620	10686	12929

Table 7-2 Shakedown limit of each layer for a HRA pavement

Thickness h_1 (mm)		120	190	255	285	340	365	390	440
Shakedown limit (kPa)	HRA layer	1462	2431	3638	4301	5355	5602	5840	6298
	Granular layer	243	439	674	797	1042	1158	1280	1544
	Soil Subgrade	2066	3796	5908	7035	9327	10449	11611	14072

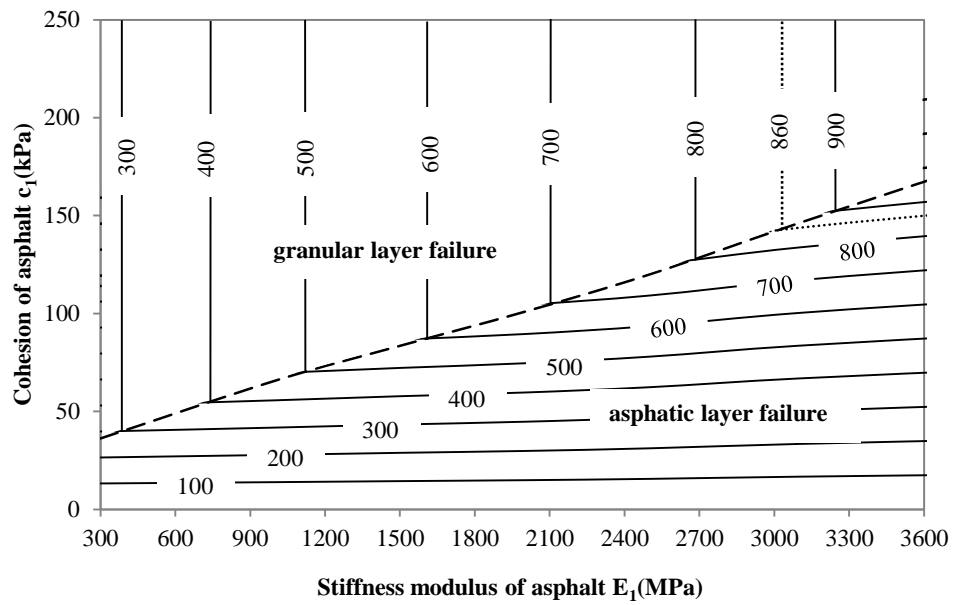


Figure 7-6 Pavement shakedown limits for various values of asphalt cohesion and stiffness (kPa)

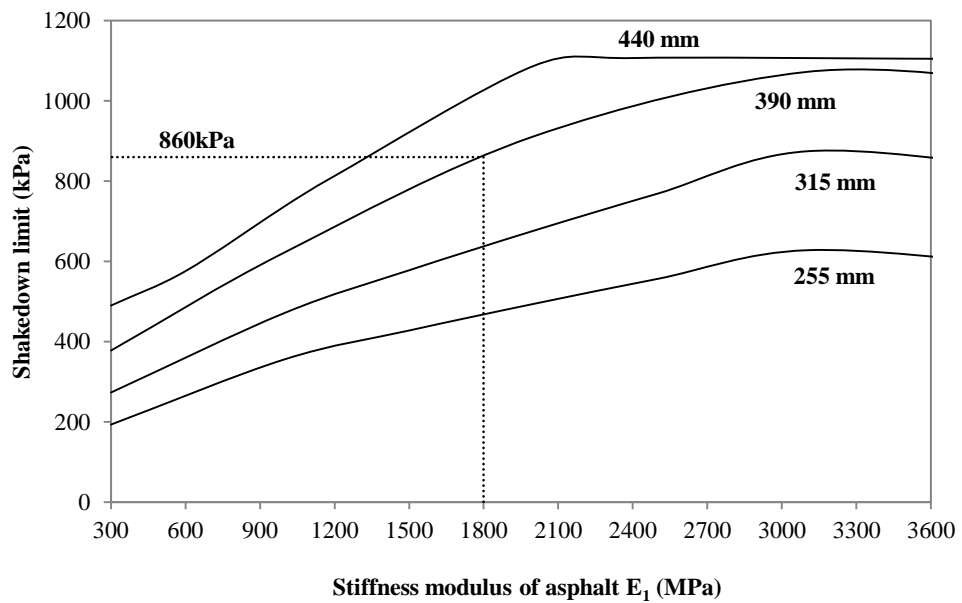


Figure 7-7 Influences of asphalt stiffness and layer thickness on the shakedown limit ($c_1 = 150$ kPa)

7.5 Summary

In this section, thickness designs using both the analytical approach in the UK and the shakedown approach of Wang and Yu (2013a) have been compared in detail. It is found that if the standard temperature is 20 °C, the analytical design approach is more conservative for a busy road (more than 18msa in the present study). If a relatively high temperature (e.g. 30 °C) is used in the shakedown design, the designed asphaltic layer will be as thick as the one obtained by the analytical approach for a pavement life around 80msa. Further increase of temperature will require thicker asphalt which is even safer than the analytical approach. Therefore, the shakedown approach for flexible pavement design should be conducted considering the maximum contact pressure and a high air temperature (at least 30 °C in the UK). Such a design then will be able to withstand long-term traffic loading without rutting failure.

CHAPTER 8

CONCLUDING REMARKS

8.1 Conclusions

The step-by-step numerical approach has been proved to be an appropriate method for shakedown analysis of both single-layered and multi-layered pavement structures. Both 2D and 3D pavements with standard materials were examined in detail. The obtained numerical shakedown limits and the distributions of residual stresses were compared with theoretical solutions and good agreements between the numerical and theoretical results were obtained.

Numerical shakedown analyses were also carried out considering non-associated plasticity of pavement materials (i.e. the material follows a non-associated plastic flow rule). It was found that the use of a non-associated flow rule obviously affects the distribution of residual stress fields as compared to associated cases and therefore leads to smaller shakedown limits. A static shakedown approach was also developed by assuming fictitious materials with reduced strength. The theoretical shakedown solutions agree well with the numerical findings in most cases; however the theoretical solutions are lower than numerical shakedown limits when the dilation angle is much smaller than

the friction angle. Nevertheless, the static shakedown approach is useful for conservative pavement design.

In addition, the existing static shakedown approach was further developed to study the effects of material cross-anisotropy and heterogeneity on the 2D and 3D shakedown limits for both single-layered and multi-layered problems. In the case of anisotropic materials, the shakedown limit varies with the frictional coefficient μ and the peak value may not occur at $\mu=0$ (i.e. normal load only). For a two-layered pavement system, the increase of anisotropic or heterogeneous factor in one layer reduces the shakedown limit of that layer but increases the shakedown limit of the other layer.

The shakedown concept in bituminous pavements was validated by undertaking wheel tracking tests on a two-layered bituminous pavement structure. Triaxial tests and uniaxial compression tests were also carried out to obtain stiffness and strength parameters so that the theoretical shakedown limits could be calculated. The comparison between the theoretical predictions and the experimental results suggested that current 3D shakedown analysis for standard materials may overestimate the shakedown limits for bituminous pavements.

Finally, the static shakedown approach was used to design layer thickness for a typical bituminous pavement structure considered in the analytical approach in the UK. The influence of temperature on the design was also discussed in detail. It was found that if the shakedown design is conducted at a relatively high temperature and against the maximum wheel pressure, the resulting pavement

structure will probably not fail due to excessive rutting within the design life suggested in the report.

8.2 Suggestions for future research

Future work could be conducted on the following aspects:

- Extend the step-by-step numerical approach to other similar geotechnical problems, such as tunnels and railway foundations.
- The step-by-step numerical approach could be further applied to a 3D half-space with Mohr-Coulomb materials so that the residual stresses in all the directions can be investigated. The numerical shakedown limits can be further compared with Wang and Yu (2013c, 2014)'s results in which only the horizontal residual stress in the central plane along the wheel moving direction was considered. The effects of the residual stresses in all the other directions on the shakedown limits and the most critical locations need to be assessed.
- As only the maximum stress in the loading history was considered in the static shakedown approach, the effect of loading history on the development of residual stress fields and the shakedown limits could be studied in detail by using the step-by-step numerical approach.
- Large scale wheel tracking tests which can simulate the real moving loads are highly suggested for the validation of the pavement shakedown solutions. However, very limited experimental work was conducted in this aspect and more research efforts are required.

Additionally, the influences of air temperature and loading frequency on the shakedown limits of bituminous pavements need to be further studied.

REFERENCE

- AASHTO. (1972). *Guide for Design of New and Rehabilitated Pavement Structures*. American Association of State Highway and Transportation Officials, America.
- AASHTO. (2007). *Standard method of test for resilient modulus of subgrade soils and untreated base/sub-base materials*. American Association of State Highway and Transportation Officials, America.
- AASHTO. (2011). *Standard Method of Test for Dynamic Modulus of Hot-Mix Asphalt Concrete Mixtures*. American Association of State Highway and Transportation Officials, America.
- Adlinge, S. S. and Gupta, A. K. (2013). Pavement Deterioration and Its Causes. *International Journal of Innovative Research and Development*, 2 (4), 437-450.
- Airey, D. and Prathapa, R. (2013). Triaxial Testing of Asphalt. *18th International Conference on Soil Mechanics and Geotechnical Engineering*, Paris.
- Arthur, J. R. F. and Menzies, B. K. (1972). Inherent Anisotropy in a Sand. *Geotechnique*, 22 (1), 115-128.
- Bindu, C. S. and Beena, K. S. (2013). Comparison of Shear Strength Characteristics of Stone Matrix Asphalt Mixture with Waste Plastics and Polypropylene. *Internation journal of strucural and civil engineering research*, 2 (4), 13-21.
- Bishop, A. W. and Wesley, L. D. (1975). A Hydraulic Triaxial Apparatus for Controlled Stress Path Testing. *G éotechnique*, 25, 657-670
- Boswell, L. F. and Scott, C. R. (1975). A Flexible Circular Plate on a Heterogeneous Elastic Half-Space: Influence Coefficients for Contact Stress and Settlement. *G éotechnique*, 25 (3).
- Boulbibane, M., Collins, I. F., Weichert, D. and Raad, L. (2000). Shakedown Analysis of Anisotropic Asphalt Concrete Pavements with Clay Subgrade. *Canadian geotechnical journal*, 37 (4), 882-889.
- Boulbibane, M., Collins, I. F., Ponter, A. R. S. and Weichert, D. (2005). Shakedown of Unbound Pavements. *Road Materials and Pavement Design*, 6 (1), 81-96.

- Boulbibane, M. and Ponter, A. R. S. (2005a). Extension of the Linear Matching Method to Geotechnical Problems. *Computer Methods in Applied Mechanics and Engineering*, 194 (45–47), 4633-4650.
- Boulbibane, M. and Ponter, A. R. S. (2005b). Linear Matching Method for Limit Load Problems Using the Drucker-Prager Yield Condition. *Géotechnique*, 55, 731-739.
- Boulbibane, M. and Ponter, A. R. S. (2006). The Linear Matching Method for the Shakedown Analysis of Geotechnical Problems. *International Journal for Numerical and Analytical Methods in Geomechanics*, 30, 157-179.
- Boulbibane, M. and Weichert, D. (1997). Application of Shakedown Theory to Soils with Non Associated Flow Rules. *Mechanics Research Communications*, 24 (5), 513-519.
- Boulbibane, M., Weichert, D. and Raad, L. (1999). Numerical Application of Shakedown Theory to Pavements with Anisotropic Layer Properties. *Transportation Research Record: Journal of the Transportation Research Board*, 1687 (1), 75-81.
- Briaud, J. L. (2001). Introduction to Soil Moduli. *Geotechnical News*, June 19.
- Brown, D. N. and Ahlvin, R. G. (1961). *Revised Method of Thickness Design for Flexible Highway Pavements at Military Installations*. Technical Report, US Army Engineer Waterways Experiment Station, Vicksburg, Mississippi, 3-582, 46.
- Brown, S. F. (1978) Stiffness and fatigue requirements for structural performance of asphaltic mixes. *Proceedings of Eurobitumen Seminar*, London, 141-145.
- Brown, S. F. and Brunton, J. M. (1985). *An Introduction to the Analytical Design of Bituminous Pavements*, University of Nottingham.
- Brown, S. F., Juspi, S. and Yu, H. S. (2008). Experimental Observations and Theoretical Predictions of Shakedown in Soils under Wheel Loading. *Advances in Transportation Geotechnics*, Nottingham, UK.
- Brown, S. F., Yu, H. S., Juspi, H. and Wang, J. (2012). Validation Experiments for Lower-Bound Shakedown Theory Applied to Layered Pavement Systems. *Géotechnique*, 62(10), 923-932.
- Brown, S. F. (1996). Soil Mechanics in Pavement Engineering. *Géotechnique*, 46, 383-426.
- BS1377:2. (1990). *Methods of Test for Soils for Civil Engineering Purposes. In Classification tests*. British Standard.
- BS1377:4. (1990). *Soil for Civil Engineering Purposes. In part 4: Compaction-related tests*. British Standard.

- BS EN 13286-7. (2004). *Unbound and Hydraulically Bound Mixtures-Cyclic Load Triaxial Test for Unbound Mixtures*. British Standard Institution.
- BS EN 12697-5. (2009). *Bituminous mixtures – Test methods for hot mix asphalt – Part 5: Determination of the maximum density*. British Standards Institution,
- Carrier, G. F. (1964). The Propagation of Waves in Orthotropic Media. *Quarterly Applied Mathematics*, 4 (2), 160-165.
- Carrier, W. D. and Christian, J. T. (1973). Rigid Circular Plate Resting on a Non-Homogenous Elastic Half-Space. *Geotechnique*, 23 (1).
- CEN. (2004) *BS EN 13286-7:2004 Unbound and hydraulically bound mixtures. Test methods for triaxial test for unbound mixtures*. BSI, London.
- Chen, L. H., Tang, S. T. and Zhang, H. T. (2010). Excel Method in Triaxial Test Data. *Processing of Journal of Beijing Jiaotong University*, Beijing, China, 34 (1), 54-57.
- Chen, W. F. (2013). *Limit Analysis and Soil Plasticity*, Elsevier.
- Chen, Z., Yang, J. and Zhu, H. (2009). Evaluation on the Shear Performance of Asphalt Mixture through Triaxial Shear Test. In *Advanced Testing and Characterization of Bituminous Materials*, CRC Press.
- Christensen, D. W., Bonaquist, R. and Jack, D. P. (2002). *Evaluation of Triaxial Strength as a Simple Test for Asphalt Concrete Rut Resistance*. Pennsylvania Transportation Institute, The Pennsylvania State University, PA.
- Collins, I. F. and Boulbibane, M. (1998). The Application of Shakedown Theory to Pavement Design. *Metals and Materials*, 4 (4), 832-837.
- Collins, I. F. and Boulbibane, M. (2000). Geomechanical Analysis of Unbound Pavements Based on Shakedown Theory. *Journal of Geotechnical and Geoenvironmental Engineering*, 126 (1), 50-59.
- Collins, I. F. and Cliffe, P. F. (1987). Shakedown in Frictional Materials under Moving Surface Loads. *International Journal for Numerical and Analytical Methods in Geomechanics*, 11 (4), 409-420.
- Collins, I. F., Wang, A. P., and Saunders, L. R. (1993a). Shakedown in Layered Pavements under Moving Surface Loads. *International Journal for Numerical and Analytical Methods in Geomechanics*, 17 (3), 165-174.
- Collins, I. F., Wang, A. P. and Saunders, L. R. (1993b). Shakedown Theory and the Design of Unbound Pavements. *Road and Transport Research*, 2 (4), 28-39.

- Corps of Engineers. (1945). *The California Bearing Ratio Test as Applied to the Design of Flexible Pavements for Airports*, Technical Memorandum, US Army Engineer Waterways Experiment Station, 231-1.
- Croney, D. and Croney, P. (1991). *The Design and Performance of Road Pavements (2nd Ed.)*, McGraw-Hill Professional.
- Davis, E. H. (1968). Theories of Plasticity and the Failure of Soil Masses. In *Soil Mechanics*, Chapter 6, Butterworths, London.
- De Pont, J., Steven, B. and Pidwerbesky, B. (1999). *The Relationship between Dynamic Wheel Loads and Road Wear. Research Report, California Transit Association*, 144.
- Djellali, A., Ounis, A. and Saghafi, B. (2012). Behavior of Flexible Pavements on Expansive Soils. *International journal of Transportation engineering*, 1 (1), 2-14.
- Drescher, A. and Detournay, E. (1993). Limit Load in Translational Failure Mechanisms for Associative and Non-Associative Materials. *Géotechnique*, 43, 443-456.
- Elliot, R.P., Thornton, S.I. (1988). Resilient Modulus and AASHTO Pavement Design. *Transportation Research Record*, 1192, 1-7.
- Endersby, V. (1951). *The History and Theory of Triaxial Testing, and the Preparation of Realistic Test Specimens*. ASTM Special Technical Publication, Philadelphia, 106, 112-137.
- Finn, F., Saraf, C., Kulkarni, R., Nair, K., Smith, W. and Abdullah, A. (1977). The Use of Distress Prediction Subsystems for the Design of Pavement Structures. *Proceedings of 4th International Conference on Structural Design of Asphalt Pavements*, Michigan.
- Fwa, T. F., Tan, S. A. and Zhu, L. Y. (2001). Reexamining C- ϕ Concept for Asphalt Paving Mix Design. *Journal of Transportation Engineering*, 127 (1), 67-73.
- Fwa, T. F., Tan, S. A. and Zhu, L. Y. (2004). Rutting Prediction of Asphalt Pavement Layer Using Model. *Journal of Transportation Engineering*, 130 (5), 675-683.
- Gazetas, G. (1980). *Deformational Anisotropy of Soil experimental investigation and mathematical modeling*. Research Report, Department of Civil Engineering, Case Western Reserve University, Cleveland.
- Gazetas, G. (1981). Strip Foundations on a Cross-Anisotropic Soil Layer Subjected to Dynamic Loading. *Géotechnique*, 31, 161-179.
- Giannakopoulos, A. E. and Suresh, S. (1997). Indentation of Solids with Gradients in Elastic Properties: Part II. Axisymmetric Indentors. *International Journal of Solids and Structures*, 34 (19), 2393-2428.

- Gibb, J. M. (1996). *Evaluation of Resistance to Permanent Deformation in the Design of Bituminous Paving Mixtures*, Ph.D. thesis, The University of Nottingham, UK.
- Gibson, R. E. (1967). Some Results Concerning Displacements and Stresses in a Non-Homogeneous Elastic Half-Space. *Geotechnique*, 17 (1), 58-67.
- Goetz, W. H. (1989). The Evolution of Asphalt Concrete Mix Design. Asphalt concrete mix design: development of more rational approaches. *American society for testing and materials*, Philadelphia, STP 1041, 5-14.
- Graham, J. and Houlsby, G. T. (1983). Anisotropic Elasticity of a Natural Clay. *Geotechnique*, 33 (2), 165-180.
- Guo, P. (2008). Modified Direct Shear Test for Anisotropic Strength of Sand. *Journal of Geotechnical and Geoenvironmental Engineering*, 134 (9), 1311-1318.
- Haas, R., Hudson, W. R. and Zaniewski, J. P. (1994). *Modern Pavement Management*, Malabar Florida.
- Harran, G. and Shalaby, A. (2009). Improving the Prediction of the Dynamic Modulus of Fine-Graded Asphalt Concrete Mixtures at High Temperatures. *Canadian Journal of Civil Engineering*, 36 (2), 180-190.
- Highways Agency (2006). Pavement design (HD26), Design manual for roads and bridge Vol: Pavement design and maintenance – pavement design and construction. Stationery Office, London.
- Highways Agency (2009). Pavement design (HD25), Design guidance for road pavement foundations. Stationery Office, London.
- Hoque, E., Tatsuoka, F. and Sato, T. (1996). Measuring Anisotropic Elastic Properties of Sand Using a Large Triaxial Specimen. *ASTM geotechnical testing journal*, 19 (4), 411-420.
- Huang, Y. H. (2004). *Pavement Design and Analysis*, Pearson/ Prentice Hall.
- Hveem, F. N. and Carmany, R. M. (1949). The Factors Underlying the Rational Design of Pavements. *Proceedings of 28th annual meeting*, Highway Research Board, Washington, 101-136.
- Jameson, G. and Sharp, K. G. (2004). Technical Basis of Austroads Pavement Design Guide, Austroads Publications Online, Australian.
- Jiang, G. L., Tatsuoka, F., Flora, A. and Koseki, J. (1997). Inherent and Stress-State-Induced Anisotropy in Very Small Strain Stiffness of a Sandy Gravel. *Geotechnique*, 47 (3), 509-521.

- Jiang, Y., Xu, B. and Sehitoglu, H. (2002). Three-Dimensional Elastic-Plastic Stress Analysis of Rolling Contact. *Journal of Tribology*, 124 (4), 699-708.
- Johnson, K. L. (1962). A Shakedown Limit in Rolling Contact. *Proceedings of the 4th US National Congress of Applied Mechanics*, Berkeley, California, 971-975.
- Johnson, K. L. (1985). *Contact Mechanics*, Cambridge University Press.
- Jones, A. (1962). Tables of Stresses in Three-Layer Elastic Systems. *Highway research board bulletin*, 342.
- Juspi, S. (2007). *Experimental Validation of the Shakedown Concept for Pavement Analysis and Design*, Ph.D. thesis, University of Nottingham, UK.
- Kapoor, A. and Williams, J. A. (1996). Shakedown Limits in Rolling-Sliding Point Contacts on an Anisotropic Halfspace. *Wear*, 191 (1-2), 256-260.
- Khanzada, R. (2000). *Permanent Deformation in Bituminous Mixtures*, Ph.D. thesis, The University of Nottingham, UK.
- Kohata, Y., Tatsuokaj, F., Wang, L., Jiang, G. L., Hoque, E. and Kodaka, T. (1997). Modelling the Non-Linear Deformation Properties of Stiff Geomaterials. *Geotechnique*, 47 (3), 563-580.
- Koiter, W. T. (1960). General Theorems for Elastic-Plastic Solids. In *Progress in Solid Mechanics*, edited by R. Hill. eds I. N. Sneddon. North-Holland, Amsterdam.
- Kootstra, B. R., Ebrahimi, A., Edil, T. B. and Benson, C. H. (2010). Plastic Deformation of Recycled Base Materials. *Proceedings of GeoFlorida*, 2682-2691.
- Krabbenhøft, K., Lyamin, A. V. and Sloan, S. W. (2007). Shakedown of a Cohesive-Frictional Half-Space Subjected to Rolling and Sliding Contact. *International Journal of Solids and Structures*, 44 (11-12), 3998-4008.
- Kulkarni, S. M., Hahn, G. T., Rubin, C. A. and Bhargava, V. (1990). Elastoplastic Finite Element Analysis of Three-Dimensional, Pure Rolling Contact at the Shakedown Limit. *Journal of Applied Mechanics*, 57 (1), 57-65.
- Kurukulasuriya, L. C., Oda, M. and Kazama, H. (1999). Anisotropy of Undrained Shear Strength of an over-Consolidated Soil by Triaxial and Plane Strain Tests. *Soils and Foundations*, 39 (1), 21-29.
- Kuwano, R. and Jardine, R. J. (2002). On the Applicability of Cross-Anisotropic Elasticity to Granular Materials at Very Small Strains. *Géotechnique*, 52 (10), 727-749.

- Lade, P. V., Nelson, R. B. and Ito, Y. M. (1987). Nonassociated Flow and Stability of Granular Materials. *Journal of Engineering Mechanics*, 113 (9), 1302-1318.
- Lade, P. V., Nelson, R. B. and Ito, Y. M. (1988). Instability of Granular Materials with Nonassociated Flow. *Journal of Engineering Mechanics*, 114 (12), 2173-2191.
- Lade, P. V. and Pradel, D. (1990). Instability and Plastic Flow of Soils. I: Experimental Observations. *Journal of Engineering Mechanics*, 116 (11), 2532-2550.
- Lambe, T. W. and Whitman, R. V. (2008). *Soil Mechanics Si Version*, John Wiley & Sons.
- Larew, H. G. and Leonards, G. A. (1962). A Strength Criterion for Repeated Loads. *Highway Research Board Proceedings*, 41, 529-556.
- Lashine, A. K. F. (1971). *Some Aspects of the Behaviour of Keuper Marl under Repeated Loading*, Ph.D. thesis, The University of Nottingham, UK.
- Lekarp, F. and Dawson, A. (1998). Modelling Permanent Deformation Behaviour of Unbound Granular Materials. *Construction and Building Materials*, 12 (1), 9-18.
- Lekarp, F., Isacsson, U. and Dawson, A. (2000). State of the Art.I: Resilient Response of Unbound Aggregates. *Journal of Transportation Engineering*, 126 (1), 66-75.
- Li, H. X. (2010). Kinematic Shakedown Analysis under a General Yield Condition with Non-Associated Plastic Flow. *International Journal of Mechanical Sciences*, 52 (1), 1-12.
- Li, H. X. and Yu, H. S. (2006). A Nonlinear Programming Approach to Kinematic Shakedown Analysis of Frictional Materials. *International Journal of Solids and Structures*, 43 (21), 6594-6614.
- Liu, S., Wang, J., Yu, H. S. and Wanatowski, D. (2016). Shakedown Solutions for Pavements with Materials following Associated and Non-associated Plastic Flow Rules. *Computers and Geotechnics*, 78, 218-266
- Liu, S., Wang, J., Yu, H. S. (2015). Shakedown of multi-layered pavements under repeated moving surface loads. XVI ECSMGE Geotechnical Engineering for Infrastructure and Development. Edinburgh, 307-312.
- Liu, S., Wang, J., Yu, H. S. and Wanatowski, D. (2015). 正交异性道路的安定分析. *土木工程学报*, 48(S2), 6-11.
- Liu, S., Wang, J., Yu, H. S. and Wanatowski, D. (2014). Shakedown of Layered Pavements under Repeated Moving Loads. *Geo-Shanghai 2014*. Shanghai, 179-188.

- Lings, M. L., Pennington, D. S. and Nash, D. F. T. (2000). Anisotropic Stiffness Parameters and Their Measurement in a Stiff Natural Clay. *Geotechnique*, 50 (2), 109-125.
- Lister, N. W. (1972). The Transient and Long Term Performance of Pavements in Relation to Temperature. *3rd International Conference on the Structural Design of Asphalt Pavements*, England.
- Lo, K. Y. (1965). Stability of Slopes in Anisotropic Soils. *Journal of the soil mechanics and foundations division*, 91 (4), 85-106.
- Loe, J. A. (1965). Full-Scale Pavement Design Experiment on A1. *Proceedings of the Institution of Civil Engineers*, Alconbury Hill, Huntingdonshire, 30 (2), 225-270.
- Lu, N. and Kaya, M. (2014). Power Law for Elastic Moduli of Unsaturated Soil. *Journal of Geotechnical and Geoenvironmental Engineering*, 140 (1), 46-56.
- Maji, A. and Das, A. (2005) Concepts of reliability in mechanistic-empirical bituminous pavement design. *Road Engineering Association of Asia and Australasia Journal*, 12(1), 24-30.
- McLeod, N. W. (1952). Rational Design of Bituminous Paving Mixtures with Curved Mohr-Coulomb Envelopes. *Proceeding of the Association of Asphalt Paving Technologists*, 21, 349-437.
- McLeod, N. W. and Ricketts, W. C. (1950). The Rational Design of Bituminous Paving Mixtures. *Highway Research Board Proceedings*, 29.
- Melan, E. (1938). Der Spannungszustand eines Hencky-Mises'schen Kontinuums bei veränderlicher Belastung. *Sitzungsberichte der Akademie der Wissenschaften Wien*, 147 (73).
- Menéndez, P. and Willam, K. J. (1995). Triaxial Failure Criterion for Concrete and Its Generalization. *Structural Journal*, 92 (3), 311-318.
- Michalowski, R. (1997). An Estimate of the Influence of Soil Weight on Bearing Capacity Using Limit Analysis. *Soils and foundations*, 37 (4), 57-64.
- Mohammad, L., Saadeh, S., Obulreddy, S. and Cooper, S. (2008). Characterization of Louisiana Asphalt Mixtures Using Simple Performance Tests. *Journal of Testing and Evaluation*, 36 (1), 490.
- Najm, W. A. S. (1987). *Numerical Application of Shakedown Theory to Multilayer Systems*, Ph.D. thesis, American University of Beirut.
- Nguyen, A. D. (2008). *Lower-Bound Shakedown Analysis of Pavements by Using the Interior Point Method*, Ph.D. thesis, RWTH Aachen University.

- Nova, R. and Wood, D. M. (1978). An Experimental Programme to Define the Yield Function for Sand. *Soils and Foundations*, 18 (4), 77-86.
- Nunn, M. E. (2004). *Development of a More Versatile Approach to Flexible and Flexible Composite Pavement Design*. Transport Research Laboratory (TRL) Report 615, 32.
- Nunn, M. E., Brown, A., Weston, D. and Nicholls, J. C. (1997). *Design of Long-Life Flexible Pavements for Heavy Traffic*. Transport Research Laboratory (TRL) Report 250.
- Paute, J. L., Horny, P. and Benaben, J. P. (1996). Repeated Load Triaxial Testing of Granular Materials in the French Network of Laboratories Des Ponts Et Chaussées. *Proceedings of the European Symposium Euroflex*, Portugal.
- Peutz, M. G. F. (1968). BISTRO: Computer Program for Layered Systems Under Normal Surface Loads. *Koninklijke/Shell Laboratorium*, Amsterdam, Holland.
- Ponter, A. R. S., Chen, H. F., Ciavarella, M. and Specchia, G. (2006). Shakedown Analyses for Rolling and Sliding Contact Problems. *International Journal of Solids and Structures*, 43 (14-15), 4201-4219.
- Ponter, A. R. S. and Engelhardt, M. (2000). Shakedown Limits for a General Yield Condition: Implementation and Application for a Von Mises Yield Condition. *European Journal of Mechanics A/Solids*, 19 (3), 423-445.
- Ponter, A. R. S., Hearle, A. D. and Johnson, K. L. (1985). Application of the Kinematical Shakedown Theorem to Rolling and Sliding Point Contacts. *Journal of the Mechanics and Physics of Solids*, 33 (4), 339-362.
- Porter, C. O. (1950). Development of Cbr Flexible Pavement Design Method for Airfields: A Symposium: Development of the Original Method for Highway Design. *Transactions of the American Society of Civil Engineers*, 115 (1), 461-467.
- Poulos, H. G. and Davis, E. H. (1980). *Pile Foundation Analysis and Design*. Krieger.
- Powell, W. D., Potter, J. F., Mayhew, H. C. and Nunn, M. E. (1984). *The Structural Design of Bituminous Roads*. Transport and Road Research Laboratory Report LR1132.
- Puppala, A. J., Mohammad, L. N., Allen, A. (1996). Engineering Behaviour of Lime-Treated Louisiana Subgrade Soil. *Transportation Research Record*, 1546, 24-31
- Raad, L. and Weichert, D. (1995). Stability of Pavement Structures under Long Term Repeated Loading. In *Inelastic Behaviour of Structures under Variable Loads*, 473-496. Springer.

- Raad, L., Weichert, D. and Haidar, A. (1989a). Analysis of Full-Depth Asphalt Concrete Pavements Using Shakedown Theory. *Transportation Research Record 1227*, 53-65.
- Raad, L., Weichert, D. and Haidar, A. (1989b). Shakedown and Fatigue of Pavements with Granular Bases. *Transportation Research Record 1227*, 159-172.
- Raad, L., Weichert, D. and Najm, W. (1988). Stability of Multilayer Systems under Repeated Loads. *Transportation Research Record 1207*, 181-186.
- Radovsky, B. S. and Murashina, N. V. (1996). Shakedown of Subgrade Soil under Repeated Loading. *Transportation Research Record: Journal of the Transportation Research Board*, 1547 (1), 82-88.
- Ranjan, G. and Rao, A. S. R. (2007). *Basic and Applied Soil Mechanics*. New Age International Publishers.
- Ravindra, P. S. and Small, J. C. (2008). Shakedown Analysis of Road Pavement Performance. Advances in Transportation Geotechnics. *Proceedings of the International Conference held in Nottingham*, Nottingham, UK, 25-27.
- Rees, S. (2013). Introduction to Triaxial Testing. Published on the GDS website: www.gdsinstruments.com.
- Road Research Laboratory (1962). Bituminous Materials in Road Construction, H. M. Stationery Off, London.
- Rowe, R. K. and Booker, J. R. (1981). The Behaviour of Footings Resting on a Non-Homogeneous Soil Mass with a Crust. Part I. Strip Footings. *Canadian Geotechnical Journal*, 18 (2), 250-264.
- Sangrey, D. A., Henkel, D.J. and Esrig, M. I. (1969). The Effective Stress Response of a Saturated Clay Soil to Repeated Loading. *Canadian Geotechnical Journal*, 6 (3), 241-252.
- Scott, C. R. (2013). *An Introduction to Soil Mechanics and Foundations*. Springer.
- Seed, H. B. and Lundgren, R. (1954). Investigation of the Effect of Transient Loading on the Strength and Deformation Characteristics of Saturated Sands. *Proceedings of American Society for Testing and Materials*, West Conshohocken, 54, 1288-1306.
- Seeds, S. B. (2000). Flexible Pavement Design Summary of the State of the Art. *A2B03: Committee on Flexible Pavement Design Millennium paper*, Transportation Research Board (TRB), Washington.
- Serigos, P.A., Prozzi, J. A., Nam, B. H. and Murphy, M. R. (2012). *Field Evaluation of Automated Rutting Measuring Equipment*, Technical

Report. Center for Transportation Research at The University of Texas at Austin (CTR).

- Sharma, P., Mahure, N. V., Gupta, S. L., Dhanote, S. and Singh, D. (2013). Estimation of Shear Strength of Prototype Rockfill Materials. *International Journal of Engineering Sciences*, 2 (8), 421-426.
- Sharp, R. W. and Booker, J. R. (1984). Shakedown of Pavements under Moving Surface Loads. *Journal of Transportation Engineering, ASCE*, no. 110: 1-14.
- Shiau, J. S., Lyamin, A. V. and Sloan, S. W. (2003). Bearing Capacity of a Sand Layer on Clay by Finite Element Limit Analysis. *Canadian Geotechnical Journal*, 40 (5), 900-915.
- Shiau, S. H. (2001). *Numerical Methods for Shakedown Analysis of Pavements under Moving Surface Loads*, Ph. D. Thesis, The University of Newcastle, Australia.
- Shiau, S. H. and Yu, H. S.(2000). Load and Displacement Prediction for Shakedown Analysis of Layered Pavements. *Transportation Research Record: Journal of the Transportation Research Board* no. 1730 (1):117-124.
- Silvestri, V. (2003). A Limit Equilibrium Solution for Bearing Capacity of Strip Foundations on Sand. *Canadian Geotechnical Journal*, 40 (2), 351-361.
- SIMULIA. (2010). Abaqus 6.10 User's Manual.
- Sloan, S. (2013). Geotechnical Stability Analysis. *Géotechnique*, 63 (7), 531-571.
- Smith, V. R. (1951). *Application of the Triaxial Test to Bituminous Mixtures*. ASTM Special Technical Publication, Philadelphia, 106, 112-137
- Stark, R. F. and Booker, J. R. (1997). Surface Displacements of a Non - Homogeneous Elastic Half - Space Subjected to Uniform Surface Traction. Part I: Loading on Arbitrarily Shaped Areas. *International journal for numerical and analytical methods in geomechanics*, 21 (6), 361-378.
- Svoboda, J. (2013). *Impact of Strain Rate on the Shear Strength and Pore Water Pressure Generation of Clays and Sands*, Ph.D. thesis, Oregon State University.
- Tang, L. S., Chen, H. K., Sang, H. T., Zhang, S. Y. and Zhang, J. Y. (2015). Determination of Traffic-Load-Influenced Depths in Clayey Subsoil Based on the Shakedown Concept. *Soil Dynamics and Earthquake Engineering*, 77, 182-191.
- Thom, N. (2008). *Principles of Pavement and Engineering*. Thomas Telford.

- Ullidtz, P. (1979). A Fundamental Method for the Prediction of Roughness, Rutting and Cracking in Asphalt Pavements. *Proceedings of the Association of Asphalt Paving Technologists*, 48: 557–586.
- Van Velsor, J. K., Premkumar, L., Chehab, G. and Rose, J. L. (2011). Measuring the Complex Modulus of Asphalt Concrete Using Ultrasonic Testing. *Journal of Engineering Science and Technology Review*, 4 (2), 160-168.
- Wang, J. (2011). *Shakedown Analysis and Design of Flexible Road Pavements under Moving Surface Loads*, Ph.D. thesis, The University of Nottingham, UK.
- Wang, J. and Yu, H. S. (2014). Three-dimensional Shakedown Solutions for Anisotropic Cohesive-Frictional Materials under Moving Surface Loads. *International Journal for Numerical and Analytical Methods in Geomechanics*, 38 (4), 331-348.
- Wang, J. and Yu, H. S. (2013a). Residual Stresses and Shakedown in Cohesive-Frictional Half-Space under Moving Surface Loads. *Geomechanics and Geoengineering*, 8 (1), 1-14.
- Wang, J. and Yu, H. S. (2013b). Shakedown Analysis for Design of Flexible Pavements under Moving Loads. *Road Materials and Pavement Design*, 14 (3), 703-722.
- Wang, J. and Yu, H. S. (2013c). Shakedown Analysis and Design of Layered Road Pavements under Three-dimensional Moving Surface Loads. *Road Materials and Pavements Design*, 14, 703-722.
- Wang, L., Hoyos, L. R., Wang, J., Voyiadjis, G. and Abadie, C. (2005). Anisotropic Properties of Asphalt Concrete: Characterization and Implications for Pavement Design and Analysis. *Journal of materials in civil engineering*, 17 (5), 535-543.
- Werkmeister, S. (2003). Permanent Deformation Behaviour of Unbound Granular Materials in Pavement Constructions, Ph.D. thesis, Technical University of Dresden, Germany.
- Werkmeister, S., Dawson, A. and Wellner, F. (2001). Permanent Deformation Behavior of Granular Materials and the Shakedown Concept. *Transportation Research Board: 80th Annual Meeting*, Washington D.C.
- Werkmeister, S. Dawson, A. R. and Wellner, F. (2004). Pavement Design Model for Unbound Granular Materials. *Journal of Transportation Engineering*, 130 (5), 665-674.
- Werkmeister, S., Dawson, A. R. and Wellner, F. (2005). Permanent Deformation Behaviour of Granular Materials. *Road materials and pavement design*, 6 (1), 31-51.

- Witczak, M. W., Von Quintus, H. L. and Schwartz, C. W. (1997). Superpave support and performance models management: Evaluation of the SHRP performance models system. *Proceeding of Eighth International Conference on Asphalt Pavements*, 3, 175-195.
- Witczak, M. W., Kaloush, K., Pellinen, T., El-Basyouny, M. and Von Quintus, H. (2002). *Simple Performance Test for Superpave Mix Design*. National Cooperative Highway Research Program (NCHRP) Report 465, Transportation Research Board, National Research Council, Washington.
- Wong, R. K. S. and Arthur, J. R. F (1985). Induced and Inherent Anisotropy in Sand. *Geotechnique*, 35 (4), 471-481.
- Yamamuro, J. A. and Lade, P. V. (1993). Effects of Strain Rate on Instability of Granular Soils. *Geotechnical Testing Journal*, 16 (3), 304-313.
- Yimsiri, S. and Soga, K. (2011). Cross-Anisotropic Elastic Parameters of Two Natural Stiff Clays. *Geotechnique*, 61 (9), 809-814.
- Yoder, E. J. and Witczak, M. W. (1975). *Principles of Pavement Design*. John Wiley & Sons.
- Yu, H. S. (2005). Three-Dimensional Analytical Solutions for Shakedown of Cohesive-Frictional Materials under Moving Surface Loads. *Proceedings of the Royal Society A: Mathematical, Physical and Engineering Science*, 461 (2059), 1951-1964.
- Yu, H. S. (2006). *Plasticity and Geotechnics*. Springer.
- Yu, H. S. and Dakoulas, P. (1993). General Stress-Dependent Elastic Moduli for Cross-Anisotropic Soils. *Journal of Geotechnical Engineering*, 119 (10), 1568-1586.
- Yu, H. S. and Hossain, M. Z. (1998). Lower Bound Shakedown Analysis of Layered Pavements Using Discontinuous Stress Fields. *Computer Methods in Applied Mechanics and Engineering*, 167 (3-4), 209-222.
- Yu, H. S. and Sloan, S. W. (1994). Limit Analysis of Anisotropic Soils Using Finite Elements and Linear Programming. *Mechanics Research Communications*, 21 (6), 545-554.
- Yu, H.S., Wang, J. and Liu, S. (2015). Three-dimensional shakedown solutions for cross-anisotropic cohesive-frictional materials under moving loads. *Direct Methods for Limit and Shakedown Analysis of Structures*. Oxford, 299-313.
- Yu, H. S. and Wang, J. (2012). Three-Dimensional Shakedown Solutions for Cohesive-Frictional Materials under Moving Surface Loads. *International Journal of Solids and Structures*, 49 (26), 3797-3807.
- Zhao, J., Sloan, S. W., Lyamin, A. V. and Krabbenhøft, K. (2008). Bounds for Shakedown of Cohesive-Frictional Materials under Moving Surface

Loads. *International Journal of Solids and Structures*, 45 (11-12), 3290-3312.

Zhao, J., Lyamin, A. and Sloan, S. (2008). Shakedown of Cohesive-Frictional Non-Homogeneous Soils under Moving Surface Loads. *The 12th International Conference of International Association for Computer Methods and Advances in Geomechanics*, India.

Zofka, A., Bernier, A., Josen, R. and Maliszewski, M. (2014). Advanced Shear Tester for Solid and Layered Samples. *Contact Urticaria Syndrome*, 397.